Permeation studies of hydrogen in 304 and 316 stainless steel: the influence of surface oxides

Thesis

PERMEATION STUDIES OF HYDROGEN IN 304 AND 316 STAINLESS STEEL: THE INFLUENCE OF SURFACE OXIDES.

A Thesis submitted for the degree of

Doctor of Philosophy of

The Open University.

By

DAVID M. GRANT, B.Sc.

Oxford Research Unit,

The Open University

November, 1984.

Author's number : HDK 64513

Date of submission : November 1984

Date of award : 10 December 1984

CONTENTS

LIST OF FIGURES AND TABLES

factor ς_1, for specified values of B, in the parallel diffusion model, [4.117].

Fig 4.7 Variation of relative amplitude modulation ratio , Λ, with the frequency factor ς_1, for specified values of B, in the parallel diffusion model,[4.120].

Fig 5.1 Variation of the cycle time Θ with frequency factor ς.

Fig 5.2 Variation of temperature T with Ξ for various thicknesses of foils of AISI 304.

Fig 5.3 Variation of the output chamber pressure $p\dot{s}$ with temperature T for $\ell = 1\times10^{-4}$m, AISI 304.

Fig 5.4 Sketch of the accessible experimental volume as an isometric drawing.

Fig 5.5 This graph typifies the variation of the phase lag Φ with square root frequency $\nu^{1/2}$ for a range of temperatures, 699 - 923, at a single input pressure, 83.5torr.

Fig 5.6 This graph typifies the variation of the modulation amplitude ratio $|R|^{-1}$ with square root frequency $\nu^{1/2}$ for a range of temperatures, 699 - 923K for

a single input pressure, 83.5torr.

Fig 5.7 This graph typifies the iso-thermal variation of the phase lag, Φ amplitude, with square root frequency $\nu^{1/2}$, for a range of pressures, 63.6 - 0.0885torr, at 674K.

Fig 5.8 Variation of the diffusion cofficient D with inverse temperature 1/T for an AISI 304, 2.5×10^{-4}m, foil which was ion beam cleaned.

Fig 5.9 Variation of the permeation cofficient Pm with inverse temperature 1/T for an AISI 304, 2.5×10^{-4}m, foil which was ion beam cleaned.

Fig 5.10 Variation of the diffusion cofficient D with inverse temperature 1/T for an AISI 304, 3.0×10^{-4}m, foil which was cleaned by activation.

Fig 5.11 Variation of the permeation coefficient Pm with inverse temperature 1/T for an AISI 304, 3.0×10^{-4}m, foil which was cleaned by activation.

Fig 5.12 Variation of the rate constant k_1 with inverse temperature for AISI 304.

Fig 5.13 Variation of the diffusion cofficient D with inverse temperature 1/T for an AISI 304, 2.5×10^{-4}m, foil

which was oxidised on the input surface.

Fig 5.14 Variation of the permeation coefficient Pm with inverse temperature 1/T for an AISI 304, 2.5×10^{-4}m, foil which was oxidised on the input surface.

Fig 5.15 Variation of the diffusion coefficient D with inverse temperature 1/T for an AISI 316, 1.0×10^{-4}m, foil which was cleaned by an ion beam.

Fig 5.16 Variation of the permeation coefficient Pm with inverse temperature 1/T for an AISI 316, 1.0×10^{-4}m, foil which was cleaned by an ion beam.

Fig 5.17 Variation of the diffusion coefficient D with inverse temperature 1/T for an AISI 316, 5.0×10^{-5}m, foil which was cleaned by an ion beam.

Fig 5.18 Variation of the permeation coefficient Pm with inverse temperature 1/T for an AISI 316, 5.0×10^{-5}m, foil which was cleaned by an ion beam.

Fig 5.19 Variation of the rate constant k_1 with inverse temperature 1/T for AISI 316.

Fig 5.20 Variation of the diffusion coefficient D with inverse temperature 1/T for an AISI 316, 5.0×10^{-5}m, foil

for a symmetric oxide.

Fig 5.21 Variation of the permeation coefficient Pm with inverse temperature 1/T for an AISI 316, 5.0×10^{-5}m, foil for a symmetric oxide.

Fig 5.22 Iso-frequency, isothermal variation of the phase lag Φ with input pressure ps. Temperature was 791K for an AISI 304, $\ell = 2.5\times10^{-4}$m, foil which was cleaned by an ion beam.

Fig 5.23 Iso-frequency, isothermal variation of the phase lag Φ with input pressure ps. Temperature was 810K for an AISI 316, $\ell = 1.0\times10^{-4}$m, foil which was cleaned by an ion beam.

Fig 5.24 Iso-frequency, isothermal variation of the phase lag Φ with input pressure ps. Temperature was 573K for an AISI 316, $\ell = 5\times10^{-5}$m, foil which was cleaned by an ion beam.

Fig 5.25 Iso-frequency, isothermal variation of the phase lag Φ with input pressure ps. Temperature was 833K for an AISI 304, $\ell = 3.0\times10^{-4}$m, foil which was cleaned by activation.

Fig 5.26 Iso-frequency, isothermal variation of the phase

lag Φ with input pressure ps. Temperature was 792K for an AISI 304, ℓ = 2.5×10^{-4}m, foil which was oxidised on the input surface only.

Fig 5.27 Iso-frequency, isothermal variation of the phase lag Φ with input pressure ps. Temperature was 574K for an AISI 316, ℓ = 5.0×10^{-5}m, foil subjected to a symmetric oxidation.

Fig 5.28 Iso-frequency, isothermal variation of the phase lag Φ with input pressure ps. Temperature was 674K for an AISI 316, ℓ = 1.0×10^{-4}m, foil which was cleaned by an ion beam.

Fig 5.29 Variation of phase lag Φ with square root frequency $\nu^{1/2}$ for flux that is modulated by ion beam injection.

Fig 5.30 The variation of the phase lag Φ with square root frequency $\nu^{1/2}$ illustrating parallel diffusion.

Fig 5.31 The variation of the relative amplitude modulation ratio $\dot{\Lambda}$ with square root frequency $\nu^{1/2}$ illustrating parallel diffusion.

Fig 6.1 The variation of diffusion coefficient with reciprocal temperature for all 304 stainless steel data.

oxide layer. (a) - atomic flow. (b) - molecular flow.

Fig 6.11 The variation of oxide permeation coefficient for molecular flow, Pmox, with reciprocal temperature.

Fig 6.12a Sketch of the variation of chemical potential with position co-ordinate for diffusion limited permeation.

Fig 6.12b Sketch of the variation of chemical potential with position co-ordinate for permeation incorporating finite surface rates.

6.13 The variation of phase lag, Φ, with ζ for the reversible trap model, equation [6.45], and for specified values of A and B.

6.14 The variation of Λ with ζ for the reversible trap model, equation [6.46], and for specified values of A and B.

6.15 Schematic diagram of a three stage process involving a surface phase with six independent surface rate constants.

6.16 The variation of the permeation power law index with Js/JR, equation [6.52] for μ = 1,0 and -1.

TABLES

Table 5.1 AISI 304, thickness ℓ = 2.5×10^{-4}m, cross-sectional area γ = $5.0\times10^{-4}m^2$ and cleaned by an ion beam on both surfaces.

Table 5.2 AISI 304, thickness ℓ = 3.0×10^{-4}m, cross-sectional area γ = $5.0\times10^{-4}m^2$ and activated on both surfaces.

Table 5.3 AISI 304, thickness ℓ = 2.5×10^{-4}m, cross-sectional area γ = $5.0\times10^{-4}m^2$ and oxidised on input surface.

Table 5.4 AISI 316, thickness ℓ = 1.0×10^{-4}m, cross-sectional area γ = $5.0\times10^{-4}m^2$ and ion beamed clean on both surfaces.

Table 5.5 AISI 316, thickness ℓ = 5.0×10^{-5}m, cross-sectional area γ = $5.0\times10^{-4}m^2$ and ion beamed clean on both surfaces.

Table 5.6 AISI 316, thickness ℓ = 5.0×10^{-5}m, cross-sectional area γ = $5.0\times10^{-4}m^2$ and oxidised on both surfaces.

Symbol	Description	Dimension
c	free diffusant concentration	ML^{-3}
z	trapped diffusant concentration	ML^{-3}
J	flux	$ML^{-2}T^{-1}$
p	pressure	$ML^{-1}T^{-2}$
x	position	L
t	time	T
ω	angular frequency	T^{-1}
D	diffusion coefficient	L^2T^{-1}
K_{sm}	Sievert's coefficient	$M^{\frac{1}{2}}L^{-5/2}T$
P_m	permeability	$M^{\frac{1}{2}}L^{-\frac{1}{2}}$
n	permeation pressure law exponent	0
l	thickness	L
γ	cross sectional area	L^2
σ	γRT	L^4T^{-2}
V	output chamber volume	L^3
S	pump speed	L^3T^{-1}
Q_{og}	outgassing load	ML^2T^{-3}
k_A	rate constant : trapping	T^{-1}
k_B	rate constant : release	T^{-1}
$k_1, \bar{k}_1$	rate constant : absorption	$L^{-1}T^1$
$k_2, \bar{k}_2$	rate constant : desorption	$M^{-1}L^4T^{-1}$
e,f,g,h	abbreviating parameters	L^2T^{-2}
y,y'	principal experimental variables	-
	phase delay between y and y'	0
ε	equipment response lag	0
Λ	relative modulation amplitude ratio	0
ζ	dimensionless frequency parameter	0
A	dimensionless trapping parameter	0
B	dimensionless release parameter	0
μ	surface symmetry parameter	0
$\underset{\sim}{a}, \underset{\sim}{b}$	complex wave numbers	L^{-1}
ξ, χ	$Re(\underset{\sim}{b}l)$, $Im(\underset{\sim}{b}l)$	0
$\underset{\sim}{R}$	entry:exit modulation amplitude ratio	0
$\mathcal{N}$	condition vector, 1 x 2	
$\mathcal{V}$	translation matrix, 2 x 2	
$\mathcal{Z}, \mathcal{Z}'$	phase boundary matrices at entry, exit surfaces, 2 x 2	
$\mathcal{Q}, \mathcal{Q}'$	entry, exit matrices 2 x 1	

g	[variable] gas phase, entry side
g'	[variable] gas phase, exit side
s	[subscript] steady state term
o	[subscript] modulation term
'	primed quantities indicate exit side variables
Re, Im	indicate real and imaginary parts of complex variables
*	complex conjugate

ACKNOWLEDGEMENTS

Thanks are due to:

The Open University and Culham for providing finance for myself and my equipment.

Ted, Peter, Alan, Ian, for technical help and endurance. Dawn, for reprographic work beyond the call of duty. Naomi and Richard for the SEM work. Castle Wall. All those who provided encouragement and cups of tea.

Derek Cummings, for large doses of patience, theoretic help and not least, friendship.

David Blackburn, for fund-raising, ideas and thoughts, and hospitality.

EX35

HIGHER DEGREES OFFICE

LIBRARY AUTHORISATION

STUDENT: DAVID MALCOLM GRANT SERIAL NO: HDK 64513

DEGREE: PHD Doctor of Philosophy

TITLE OF THESIS: PERMEATION STUDIES OF HYDROGEN IN 304 AND 316 STAINLESS STEEL: THE INFLUENCE OF SURFACE OXIDES

I confirm that I am willing that my thesis be made available to readers and may be photocopied, subject to the discretion of the Librarian.

Signed: D M Grant Date: 19/12/85

ABSTRACT

A time varying harmonically modulated flow method, analysed with a two rate constant surface reaction model, provides a series of permeation, P_m, diffusion, D, and surface rate coefficients, k_1,k_2, for hydrogen passing through 304 and 316 stainless steel. The method developed here allows the evaluation of a consistent set of bulk metal values of D and P_m, in the temperature range 502 < T/K < 963, despite wide ranging surface conditions, and are described by:

$D_{304}=(1.22\pm0.06)\times10^{-6}\exp\{[-(6.596\pm0.049)\times10^{3}/T]/K^{-1}\}\ m^2s^{-1}$

$P_{m304}=(4.82\pm0.21)\times10^{-7}\exp\{[-(7.990\pm0.044)\times10^{3}/T]/K^{-1}\}\ molm^{-1}s^{-1}Pa^{-½}$

$D_{316}=(7.28\pm0.94)\times10^{-7}\exp\{[-(6.296\pm0.109)\times10^{3}/T]/K^{-1}\}\ m^2s^{-1}$

$P_{m316}=(8.09\pm0.70)\times10^{-7}\exp\{[-(8.189\pm0.076)\times10^{3}/T]/K^{-1}\}\ molm^{-1}s^{-1}Pa^{-½}$

When surfaces are treated to form a stable oxide layer, the surface reaction rate constants are found to be interpretable in terms of molecular flow of hydrogen through the oxide. The permeation coefficients, P_{mox}, describing this flow are as follows:

$P_{mox304}=(1.43\pm0.29)\times10^{-11}\exp\{[-7.661\pm0.081)\times10^{3}/T)/K^{-1}\}\ molm^{-1}s^{-1}Pa^{-1}$

$P_{mox316}=(5.36\pm2.68)\times10^{-11}\exp\{[-6.967\pm0.228)\times10^{3}/T)/K^{-1}\}\ molm^{-1}s^{-1}Pa^{-1}$

CHAPTER 1: INTEREST OF THIS WORK

Today when physically surrounded by gas pipes, canisters, cylinders and the like, it is natural to assume that the metals which convey or store gases are wholly impermeable to them. However gas does enter metals and pass through them. As early as 1866 Thomas Graham observed that hydrogen can permeate palladium membranes and he used this as a method to purify hydrogen. Other studies dating back to that time established that such physical properties as their electrical resistivity and magnetic susceptibility may be changed by absorption of hydrogen.

It was a technological problem that drove early interest in the presence of hydrogen in metals, for hydrogen makes steels brittle. The same is true today. Suprisingly, after one hundred years there is still interest in the mechanisms by which hydrogen is transported through metals and the way the presence of hydrogen degrades certain physical properties.

However, the centre of interest has changed. Problems tend to be concerned with hydrogen in the metal hydrides to be used in storage systems or in possible battery electrodes. In addition there is one problem that is a direct follow on from the traditional work in hydrogen embrittlement. Fusion reactor components are subject to irradiation which leaves hydrogen and its isotopes embedded in them. These must be released if the components are to have a working life of useful duration. It is this problem that prompts the present work

which is an investigation of hydrogen flow in two stainless steels which are of potential interest for the construction of fusion reactors.

CHAPTER 2: INTRODUCTION

The diffusion of hydrogen and its isotopes in metals has been widely studied, but reviews such as that by Volkl and Alefeld (1) show notable anomalies. Data on some materials, nickel in particular, are consistent; data on other materials, notably iron and its alloys, are dispersed. Volkl and Alefeld, in describing diffusion in niobium, tantalum and vanadium were forced to accept data only from surface independent techniques: Gorsky effect, Mossbauer effect, quasi-elastic neutron scattering and relaxation of resistivity. They inferred that the macrosopic flow of diffusant across a surface causes data scatter in surface dependent techniques. While the surface independent approach may give a good estimate of rates of atomic motion, it is unhelpful for a number of technological problems, such as the design of hydrogen storage cells or of containment vessels for fusion reactor fuels and reaction products, since for these it is the macroscopic flow which is of consequence. There remains, therefore, a need for experimental techniques which will identify the individual processes which influence macroscopic diffusant flow.

This thesis details an experimental study of the permeation of hydrogen through stainless steel foils with the objective of investigating and separating those surface effects which are responsible for the reduction of diffusion fluxes through bulk material. To explain in more detail why this investigation was thought necessary the following sections:

2.1, review measurements of the diffusion coefficient in iron and

stainless steel using macroscopic methods; 2.2, review work with stainless steel on oxide inhibition of permeation, on surface rate coefficients and on the permeation power law index; 2.3, present a brief description of macroscopic methods, the experimental approach for the present work, and the objectives set; 2.4, presents a summary of the chapter.

2.1 A REVIEW OF HYDROGEN DIFFUSION DATA IN IRON AND STAINLESS STEEL

Volkl and Alefeld (1) showed that the α-iron hydrogen diffusion data for forty-six separate investigations is scattered over an order of magnitude over the temperature range accessible to experiment. Yet the consistency for nickel, which, like iron, has a low solubility in comparison with highly soluble materials such as palladium, is extremely good. This is shown in their review of twenty-five investigations using comparable techniques to those used with α-iron. The difference led Volkl and Alefeld to the conclusion that imperfections such as impurities, grain boundaries and dislocation precipitates do not play an important part in the diffusion of hydrogen since it would be expected that nickel would show similar scatter if this was so. They suggested that surface effects are the prime cause of the error although they did not discount the possibility of internal trapping effects.

The conclusion is supported in a more recent review on the solubility and diffusion of hydrogen in iron by Kiuchi and McLellan (2). This showed, from sixty-two investigations covering the range 300 - 1750K, that the "diffusivity D of hydrogen through b.c.c iron exibits a large degree of mutual inconsistancy" and that "statistical analysis of this large data mass has shown that only those data obtained by electro-chemical methods and H_2-gas equilibration methods using ultra high vacuum techniques and palladium coated membranes are reliable".

For this reason macroscopic flow measurements are claimed to be acceptable only if surface independent methods are employed. Unfortunately such measurements sidestep the real problem, that of estimating macroscopic flow rates. Though diffusion and permeation coefficients may well be interesting for an oxideless iron, they are not useful in the real world without some estimate of surface reaction coefficients.

The following sub-section reviews hydrogen diffusion data in stainless steel as estimated by macroscopic methods. This data might be expected, for the reasons detailed above, to be diverse by virtue of the very feature that it that provides its name; its protective oxide coat.

2.1.2 The current interest in stainless steel and recent work

One specific interest in hydrogen permeation through stainless steel is derived from the possibility of using this material in the fabrication of the containment vessel of a fusion reactor.

Recent work on the diffusion of hydrogen, deuterium and tritium in some of the stainless steels, (3) - (13), used macroscopic methods, the temperature covering the range 400 - 1100K. As in iron the data shows scatter with, typically, a band of values differing by an order

of magnitude.

Work on the permeation coefficient, of hydrogen in stainless steel was recently reviewed by Le Claire (14) in a survey covering forty investigations. Although Le Claire found scatter to exceed an order of magnitude over the 400 - 1173K temperature range he showed that a majority of the data are quite consistent and so he was able to derive a mean value for the permeation based on an Arrhenius equation.

In the following section, data on the variation of permeation flux caused by surface oxide inhibition is discussed as further evidence of the need for a macroscopic technique to separate surface reactions from bulk material permeation and to provide data on surface rate constants.

2.2 EVIDENCE OF THE EFFECT OF THE SURFACE OXIDE ON THE HYDROGEN PERMEATION OF STAINLESS STEELS

This section details: 2.3.1, evidence of surface oxide inhibition in hydrogen permeation of stainless steel; 2.3.2, data incorporating surface rate coefficients; 2.3.3, variations of the permeation power law index from its expected value of one half.

2.2.1 Surface oxide inhibition of hydrogen permeation of stainless steel

Several authors have attributed reductions of the permeation of hydrogen and its isotopes through stainless steel to the surface oxide layer. Earwaker, Ross and Farr (15) investigated the oxidation of stainless steel AISI 321. They demonstrated a five-fold reduction in the permeation, for their particular specimen geometry, as the oxide thickness was increased from 0.2μm to 0.6μm. The experiment was repeated for AISI 316 and "the oxide was found to have only a very slight effect even though it was the same thickness". They attributed this difference in the properties of the oxides to the fact that titanium is not present in the AISI 316 steel. Their suggestion is that the titanium may form an oxide barrier which does not inhibit the growth of other oxides.

Heubaum and Berkowitz (16) found an oxide surface to "have a considerable influence on hydrogen permeability" in 4130 steel. Their

comment typifies the view that surface oxides play a significant role in the hydrogen permeation of steels. Piggot and Siarkowski (17) showed the variation of hydrogen flux with increasing oxide thickness first to fall and then to rise for 302 and 307 stainless steels. The rise in flux was attributed to the oxide cracking.

In response to this reduction of permeation due to surface conditions, several investigators sputter clean and then sputter coat their specimens with a thin , ≈ 100nm, film of palladium. The process is described by Kumnick and Johnson (18). Their view is that the palladium has a very high and reproducible hydrogen diffusivity and permeability which protects the freshly cleaned surface from oxidation and leads to high and reproducible coefficients from diffusion and permeation experiments. Swansiger and Bastasz (19) exemplify this approach and detail the reduction in permeation of hydrogen by 2-3 orders of magnitude between a 309S stainless steel specimen coated with palladium and a specimen with a thin, 4nm, oxide coat. Interestingly Swansiger *et al* (20), in an earlier report on the same steel, using similar specimens and thicker oxides, stated: "the oxides investigated were found to have only minor effects on the measured permeabilities". It should be noted, however, that this earlier report covered the differences in permeation for oxides in the range 10 - 250nm and suggested that the lack of variation of permeation with thickness of oxide was perhaps due to cracking of the oxide.

2.2.2 Surface rate coefficients

The basic processes that together constitute permeation are the following:

(1) adsorption of molecules onto a surface from the gas phase and their desorption from that surface;

(2) molecular dissociation on the surface to atoms and their recombination to molecules;

(3) absorption of adsorbed atoms into solution in the surface layers of the the solid and their reverse passage out of solution.

In some cases dissociation may occur simultaneously with adsorption so that processes (1) and (2) become a single process. There is then no identifiable molecular phase on the surface. This is known as direct dissociative chemisorption and is generally believed to occur for hydrogen adsorption on many transition metal surfaces. Le Claire in a recent review (21), described three investigations (8), (22) and (23) in which the rate constant associated with this direct dissociative chemisorption was obtained; two of them, (22) and (23), were interpreted by Le Claire from the flux-pressure data. He could only conclude from these sparse results that the experimental measurements of this rate constant: were always orders of magnitude from the maximum possible values; seem to increase with temperature; change with alloying; and, in 304 stainless steel, can yield values that differ from one another by many orders of magnitude from specimen to specimen.

In the reverse process to direct dissociative chemisorption, atoms recombine to form molecules out of solution and are then desorbed from the surface. It is known as recombination. This recombination rate was measured for deuterium in 304 stainless steel by Braun *et al* (24). The rate constant was determined by relating the near surface deuterium concentration, on a membrane, to the release rate of deuterium from the membrane. The surface concentration itself was determined by the $D(^3He^+,p)^4He$ reaction. The rate constant was seen to increase with increasing temperature but no Arrhenius relationship was found. There is some uncertainty about the experimental method in this work since measurements may be influenced by radiation damage, oxides, and the adsorption of deuterium gas from the downstream vessel.

Clearly, direct information on surface rate coefficients is limited. For this reason the following sub-section reviews data on the permeation power law index as an alternative source of information on oxide permeation effects.

2.2.3 Surface oxides and the permeation power law index

Usually, experimental conditions are such that direct dissociative chemisorption is assumed to be infinitely fast. Permeation through a metal is then limited by Richardson's law, Richardson (25), with flux

proportional to the square root of the input gas pressure, $p^{½}$. However, if pressures are low or temperatures are high, dissociation at the surface of the metal may become the rate limiting process and the flux then becomes directly proportional to p. This change in the power index was estimated by Le Claire (21) to cover a range of 3 - 4 orders of magnitude in input gas pressure.

Suprisingly few reports demonstate a power law index of one-half as confirmation of diffusion limited permeation. Those that do are varied in their interpretation of the value they measure. For example: Matsuama and Redman (26), for an index of 0.58, state "these data indicate that tritium permeation through 304L is half power dependent on the T_2 pressure". A more cautious approach is provided by Katsuta and Furukawa (9), again on 304 stainless steel, who describe themselves as puzzled that they consistantly obtained a power index of 0.57 despite coating their specimens with palladium. This is in contrast to Kass and Andrzejewski (27) who measured a $p^{½}$ dependence for a palladium coated stainless steel 309S. However, for the same pressure range, they claimed a p^{1} dependence for uncoated specimens. This last variation is in agreement with Swansiger and Bastasz (19) who, for the same material, noted a reduction of 2 - 3 orders of magnitude in permeation for a non-palladium coated specimen. Van Deventer and Maroni (28) also noted "a closer to first power dependence" at low pressures.

Assesments of the power law index can be complicated further by considering oxides which may have cracked, as mentioned earlier.

Zarchy and Axtman (29) provided evidence for a model first proposed by Strehlow and Savage (30). This model requires that molecules impinging on the surface either:

(1) diffuse through the oxide coating

or

(2) pass directly through the cracks or pores to the metal surface.

This model predicts a half-order pressure dependence at high pressures. As the driving pressure is lowered the rate limiting step becomes transport through the oxide coating, with first order dependence. As the pressure is reduced further, transport through the cracks and pores becomes rate limiting and hence the pressure dependence should return to half-order. The ultimate low pressure limit is dissociative chemisorption and first order pressure dependence.

It is clear that the problem of oxide inhibition of permeation is complex, so useful experiments must cover a wide range of temperatures, pressures and hydrogen impurity levels. Tanabe *et al*, (12) and (31), have done interesting work. They show that the stability of surface oxides is a crucial factor in the determination of permeation fluxes. In consequence of the above information, the following section includes a review of surface dependent experimental techniques with a view to finding a reliable method of measuring surface coefficients.

2.3 POSSIBLE MACROSCOPIC METHODS AND THE OBJECTIVES OF THIS WORK

This section details:

2.3.1, a brief description of macroscopic experimental methods and the method chosen to enable a separation of the surface coefficients from those of bulk permeation; 2.3.2, the materials to be investigated and the objectives of this work.

2.3.1 Macroscopic experimental methods of interest

As pointed out earlier, it is the macroscopic flow across a surface which is of experimental interest so consideration is limited to the methods which are affected by surface conditions. Conventional descriptions of macroscopic flow in the solid state relate phenomenological coefficients to two series of measurements: one is of the steady flows through a foil produced by specified pressures of gaseous diffusant; the other is of the time varying flows which follow a step change in diffusant pressure.

The steady state permeation of hydrogen through a metal foil yields only the product of the diffusion and solubility coefficient, Richardson (25), Wang (32). Time varying flows are therefore studied to provide an estimate of the diffusion coefficient. Normally one of two surface dependent techniques is used. They depend on gaseous

permeation or on electrochemistry. These methods are described below along with a description of the recent variation using modulations which has been applied to them both.

(1) Permeation method

Time varying flows which follow a step change in the driving pressure were first described by Daynes (33), and by Barrer (34). Their experiment is known as the time lag method since the diffusion coefficient is deduced from the relaxation time to the steady state. Usually, two vacuum chambers are separated by an experimental membrane. Diffusant gas, admitted rapidly to one chamber, is detected in the second after a delay which is the subject of experimental measurement: in a complementary form of experiment, gas is removed rapidly from one chamber and the delay preceding the consequential drop in the second is measured. Delays are interpreted as dependent on the diffusion coefficient and the membrane thickness alone.

Delays may in part be due to trapping or to slow surface reactions, but this is difficult to detect since such processes leave no strong and characteristic signature on the output trace. For this reason a detailed fit is rarely sought. A report by Shah *et al* (35), illustrates the use of a generalised time-lag method when phase boundary processes are rate limiting.

(2) Electrochemical method

Electrochemical techniques are variations of the permeation methods with measurements derived from the passage of a hydrogen current through a cell. The time constants are measured for the redistribution of hydrogen in a specimen membrane separating two electrolytic cells. The electrochemical method has the advantage of versatility in the setting of its boundary conditions. For example: the entrance side can be polarised cathodically, by hydrogen precipitation, by a constant current, or by a short pulse. At the detection side, the time variation of the hydrogen potential can be followed directly, or it can be followed by the time variation of the compensating, anodic, current required to maintain the potential constant.

(3) Variation by modulation.

A recent variation common to both electrochemical and gaseous permeation methods, uses periodic modulation of the driving pressure or current, (36) - (41).

This modulation method has much to commend it over the time lag method. The diffusion coefficient can be derived from the phase difference between the input and output waveforms and the permeation constant can be determined from the relative amplitudes, Reuben, Cummings and Blackburn (40). Also, repeated modulations

using signal averaging enables accurate measurements of a kind not possible with the featureless time-lag curve. This makes it realistic to attempt an assessment of flux measurements in systems where permeation may be inhibited by surface reactions of some complexity.

2.3.2 Objectives of this work

Current interest lies in 304 and 316 stainless steel (42) and, as found in 2.2.1, in the effect of oxides on the permeation of hydrogen through these two materials. Therefore the objectives set in this work were to: investigate 304 and 316 stainless steel specimens in an industrial as received condition, with no special coating treatments; to develop an analysis for the separation of diffusion and permeation coefficients from the intrusive effects of surface inhibition of flows; to obtain data covering the widest possible range of pressure, temperature and surface conditions. The starting point for the work was to be the pressure modulation technique already in use, in a primitive form, at the Oxford Research Unit of the Open University.

2.4 SUMMARY

Diffusion and permeation data on iron and stainless steels shows large anomalies. Scatter in the data is attributed to surface effects. There is substantial evidence to support the view that oxide layers impede bulk material permeation. Data on surface rate coefficients is limited and reports on the permeation power law index are diverse and show deviations from the expected value of one half. The recent underdeveloped pressure modulation method is thought to be capable of separating surface rate coefficients from bulk diffusion and permeation coefficients.

CHAPTER 3: EXPERIMENTAL EQUIPMENT AND METHOD

The objectives of the experimental work were to measure permeation, diffusion and surface rate constants by measurements of macroscopic flow. In consequence the general requirements of the equipment were to:

(1) deliver to one side of the specimen a range of time dependent pressures.

(2) detect time dependent flows emerging from the other side of this specimen.

Specific requirements were to: construct an ultra high vacuum system with input and output chamber separated by a foil specimen; to obtain a frequency range such that the diffusion time(ℓ^2/D) would be an appreciable fraction of the period of oscillation over a wide range of temperatures and pressures, ensuring sufficient structure for a curve fit analysis; to devise a control system to modulate the input side pressure over the frequency and temperature range.

The following sections provide a description of the experimental rigs designed to meet these requirements. Two rigs were constructed but in the interests of clarity only only one will be described in detail. Variations between their various parts will be brought to notice as seems appropriate.

These sections describe:

3.1, the vacuum system; 3.2, the control, modulation and measurement

of pressure in this system; 3.3, the specimen and furnace configuration, and temperature control; 3.4, the preparation of specimens and ion beam cleaning; 3.5, the system control of the complete rig, the waveform Fourier coefficients and the calibration of the equipment. The chapter is summarised in section 3.6 together with some comments on experimental limitations in the use of the equipment. The topic of experimental constraints is taken up again in 5.1 where the concept of an experimental phase space is introduced.

3.1 THE VACUUM SYSTEM

It was essential to construct a vacuum system to meet requirements (1) and (2). The two experimental rigs constructed are shown in figs 3.1a and 3.1b. Their common features are illustrated in fig 3.2 and are detailed below.

Fig 3.2 illustrates the double ultra high vacuum system, in which a foil specimen separates two chambers. In this system the input chamber volume may be changed so providing a means to control the diffusant flux. The output chamber, of fixed volume, is continuously pumped into an ion pump via a calibrated leak (0.714 ± 0.002 ls^{-1}), this leak acting as a choke to minimise pressure variations arising from ion pump fluctuations.

The ultra high vacuum components were constructed of stainless steel and sealed with with copper ofc gaskets on conflat knife-edges. This ultra high vacuum system was outgassed by baking at 453K for 36 hours. This is the maximum *safe* temperature for the ceramic feedthroughs. During bakeout, gas released from this system was taken through twin, (water and liquid N_2), traps to a diffusion pump. After bakeout the input and output chambers were pumped by their separate $25ls^{-1}$ ion pumps, the diffusion pump being shut off from the system. The residual partial pressure after bakeout was typically $(1 - 5)\times10^{-9}$ torr.

The positioning of the quadrupole mass spectrometer enabled gas

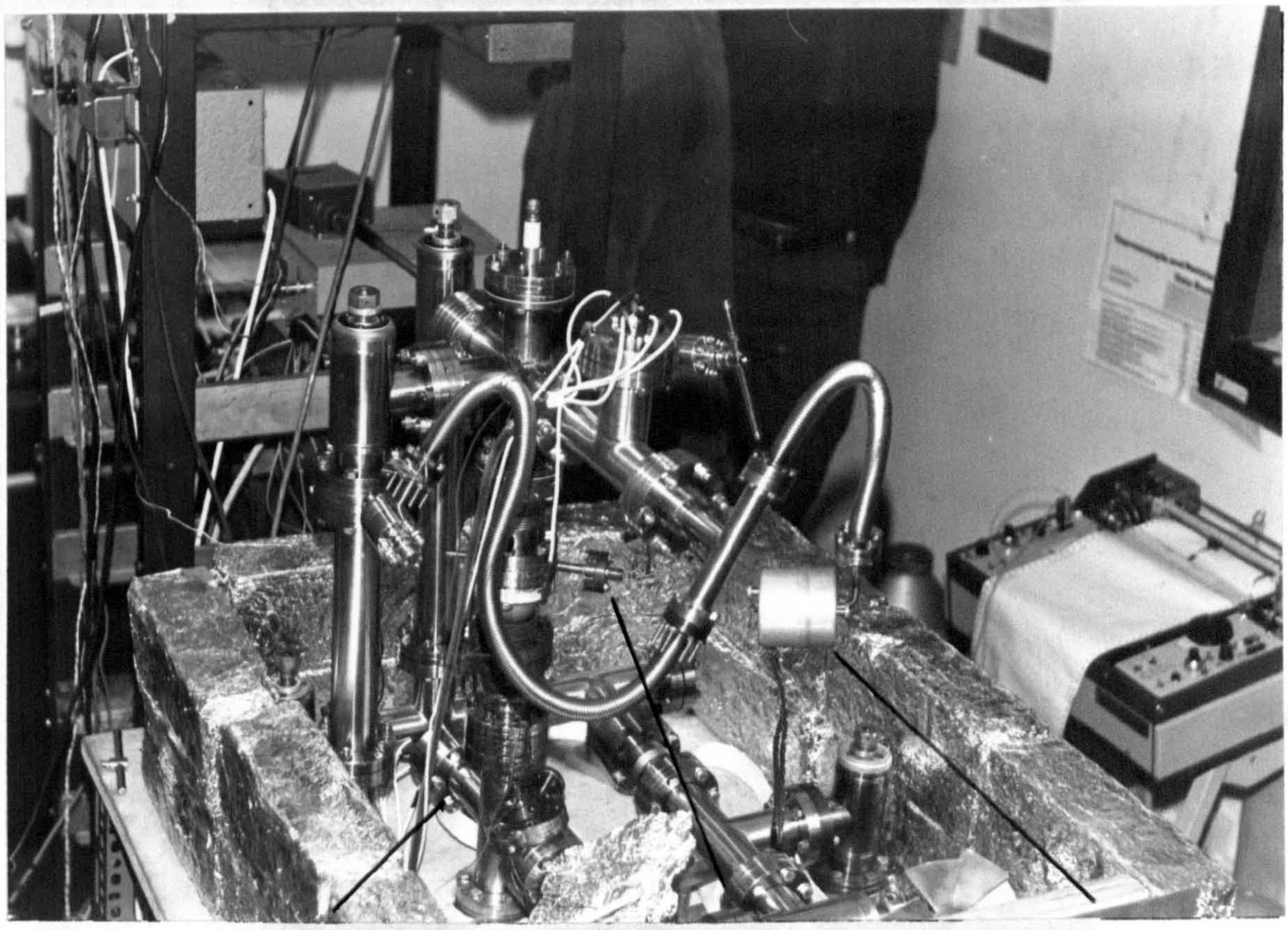

Fig 3.1a Photograph of the early rig showing part of the vacuum system, section 3.1. Some of the more visible features are indicated and are referred to in the text. A schematic diagram of the whole vacuum system is shown in fig 3.2.

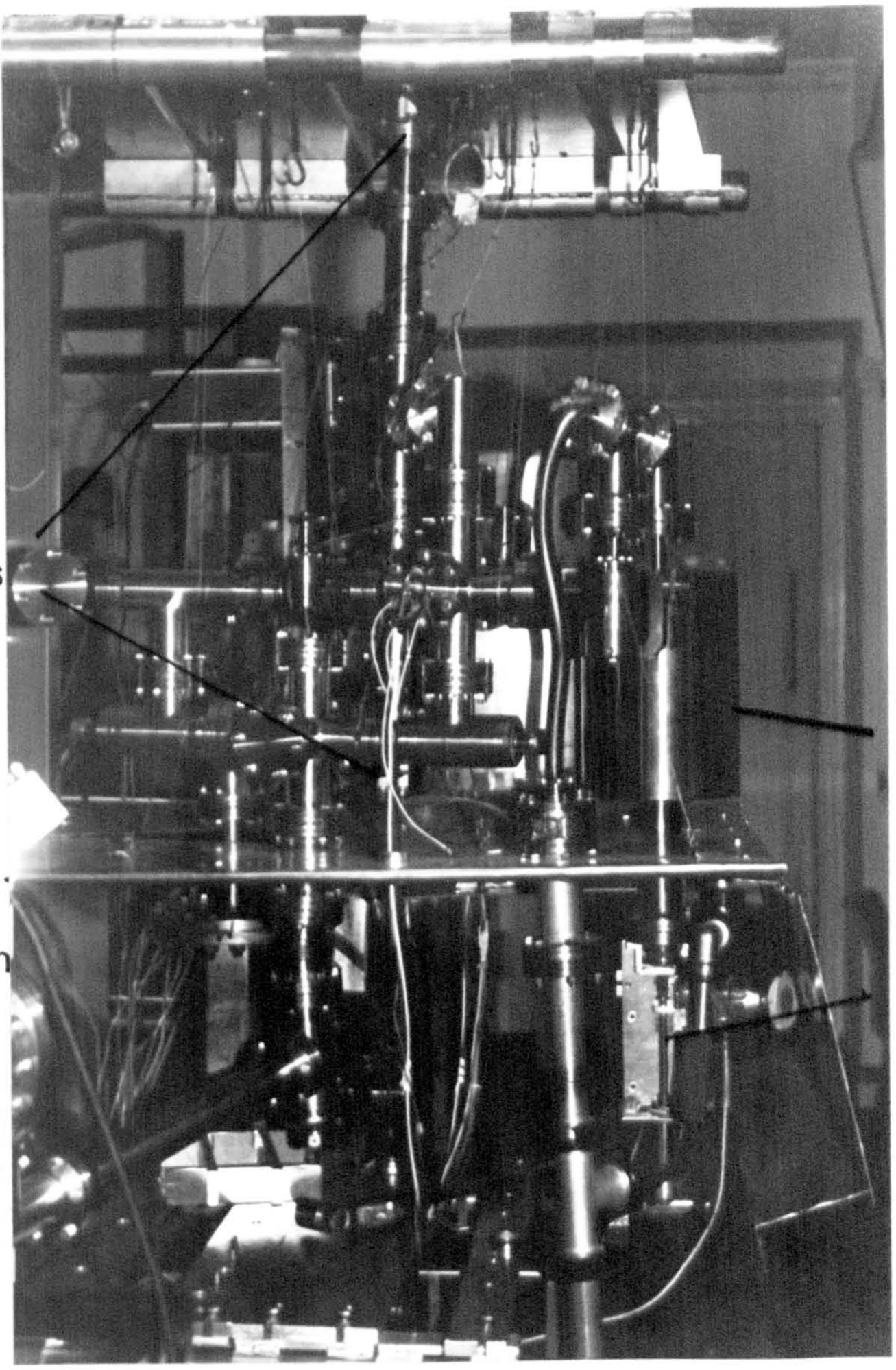

Fig 3.1b Photograph of the later rig showing part of the vacuum system. The vacuum system is supported by skyhooks enabling design to be truly three-dimensional. Some of the more visible features are referred to in the text. A schematic diagram of the whole vacuum system is shown in fig 3.2.

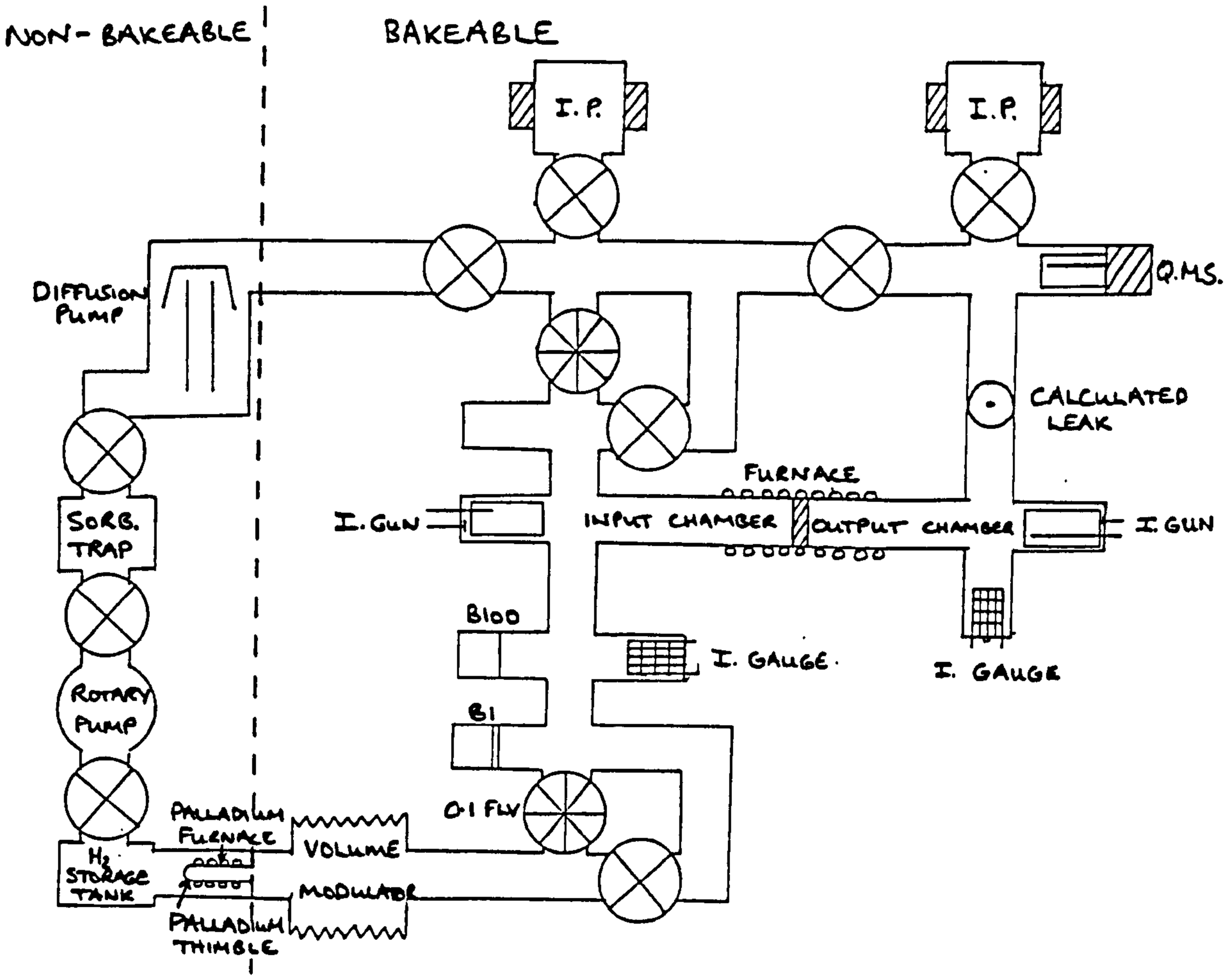

Fig 3.2 Simplified diagram of the vacuum system showing the ultra high vacuum bakeable, region and the low-vacuum, non-bakeable region.

Key:

I - Ion; I.P. - Ion Pump; 0.1FLV - 0.1 ls^{-1} fine leak valve; Q.M.S - quadrupole mass spectrometer; B1 - 1torr Baratron, capacitance manometer; B100 - 100torr Baratron.

purity checks to be made in either the input or the output chamber. Checks were made at experimental pressures and temperatures and with the equipment cold. The gas purity may be described in the following ways:

(1) Checks cold give the output chamber impurity partial pressure to be in the range $(1 - 10)\times10^{-10}$torr.

(2) At the optimum pressure of 10^{-4}torr, the apparent impurity content is 1 - 10ppm. This seems a common method of impurity measurement. However, this is not particularly satisfactory since smaller signal pressures and experimental temperatures both increase the impurity level.

(3) Other checks were made at experimental temperatures and pressures and the ratio of hydrogen to all other impurities was found not to fall below 500:1. This does not seem to be particularly good, but when compared with other experimenters who checked at experimental temperatures, it compares favourably. For example, Sherman and Birnhaum (44) describe a ratio of 300:1 for their apparatus.

(4) The input chamber was thought to have significantly better purity ratio but this was not measured directly because mass spectrometers cannot operate at such high pressures. Indirect measurements were made of purities greater than 2000:1 at 10^{-4}torr of hydrogen and this ratio was expected to increase with increasing pressures.

Components, such as the palladium diffuser, stainless steel bellows

and pressure meters, will be detailed with respect to the control, calibration and measurement of the partial pressure of hydrogen, in the following section.

3.2 PRESSURE CONTROL, MODULATION AND MEASUREMENT

This section has three sub-divisions. These are:

3.2.1, the input of H_2 gas, the maintenance of a steady base pressure of this gas and the measurement of the input chamber pressure; 3.2.2, the modulation of the input chamber pressure by a deformable stainless steel bellows and the limitations of this method; 3.2.3, the measurement and calibration of the output chamber pressure meter.

3.2.1 Measurement and control of input chamber base pressure

The input chamber pressure was monitored using a Baratron capacitance manometer with full scale of either 1 torr or 100 torr. The 100torr Baratron (B100) was readable to a precision of three and a half digits while the 1torr Baratron (B1) was readable to four and a half digits. Thus the B100 was used in the range 100 to 1 torr ± 0.05torr, while the B1 was used from 1 to 10^{-3}torr ± 5×10^{-5}torr. Both baratrons were calibrated against a NBS standard.

To provide a diffusant of suitable purity, hydrogen was bled into the input chamber, fig 3.3b, from a supply reservoir, using a palladium diffuser. The diffuser was surrounded by a small thermocoax furnace and was heated to ≈ 500K. Conductance at this temperature and for a supply pressure of 500 torr was ≈ $10^{-4}ls^{-1}$. The analogue output voltage from either baratron was set up so that it simulated a

thermocouple and was fed into the palladium furnace temperature controller. This provided the feedback required for the maintenance of the base pressure.

3.2.2 Modulation of the input chamber pressure

Modulation of the input pressure was provided by harmonic variation of the chamber volume. A large stainless steel bellows fitted to the input chamber provided the means of change, fig 3.3a. To change the volume, an A.C. motor was used to drive a linear motion vacuum feedthrough. This feedthrough was connected to a transducer to provide a feedback signal for the control of the system. The bellows was contained within a low vacuum cylinder maintained at a pressure close to that inside the bellows thus reducing the power required of the motor. The transducer followed a sinusoidal reference signal generated by the computer program and fed via a 12 bit digital to analogue converter. This signal was also inverted, floated and fed, at a suitable amplitude, to the palladium furnace control loop so that the palladium furnace controller would respond only to base pressure fluctuations, and would make no response to the imposed pressure modulations.

Fig.3.3.b is a schematic view of the input chamber. Here C_{in} is the input conductance of the palladium diffuser and C_{out} is that of the fine leak valve. Control of C_{out} was required to maintain the base

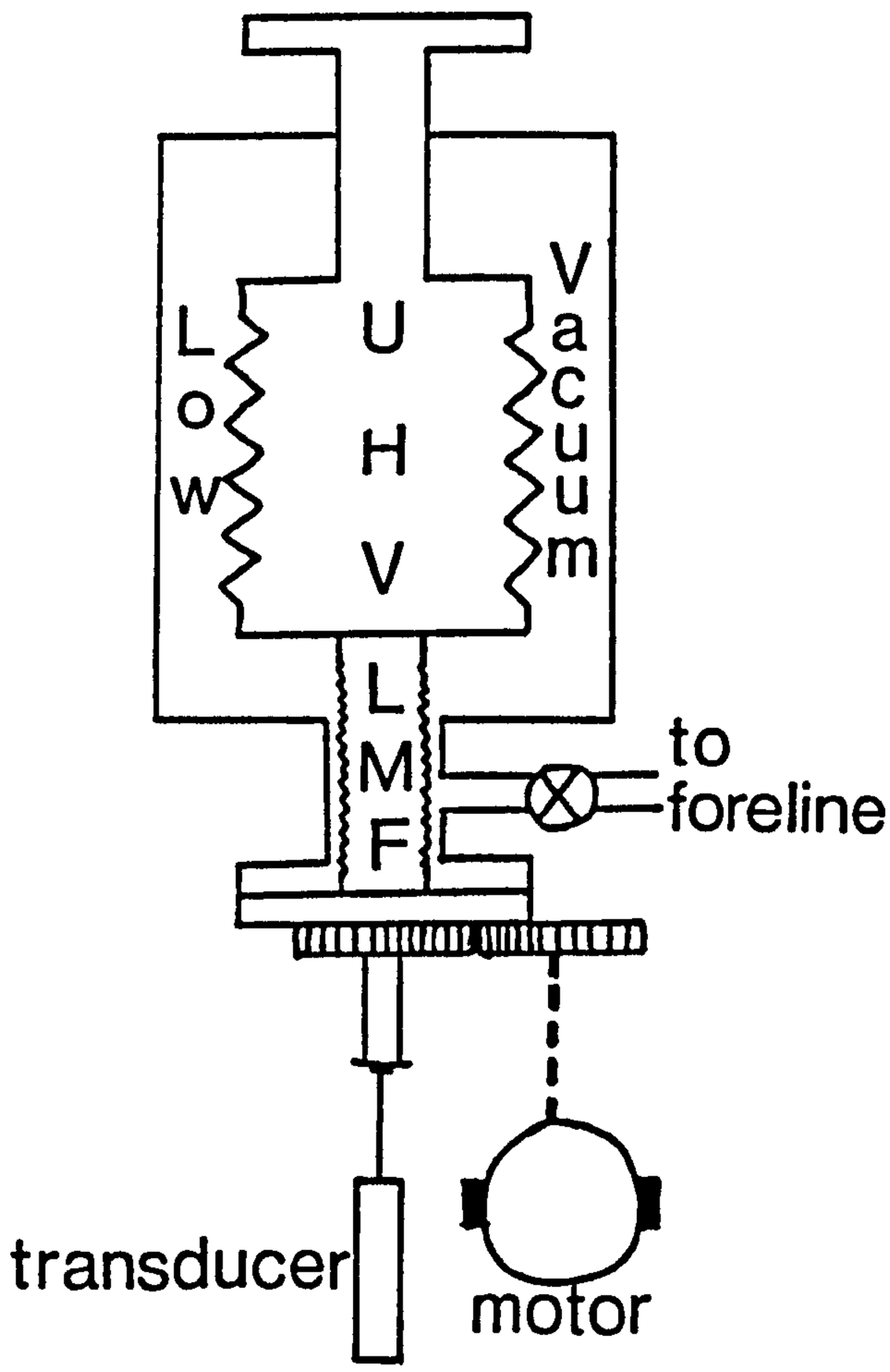

a

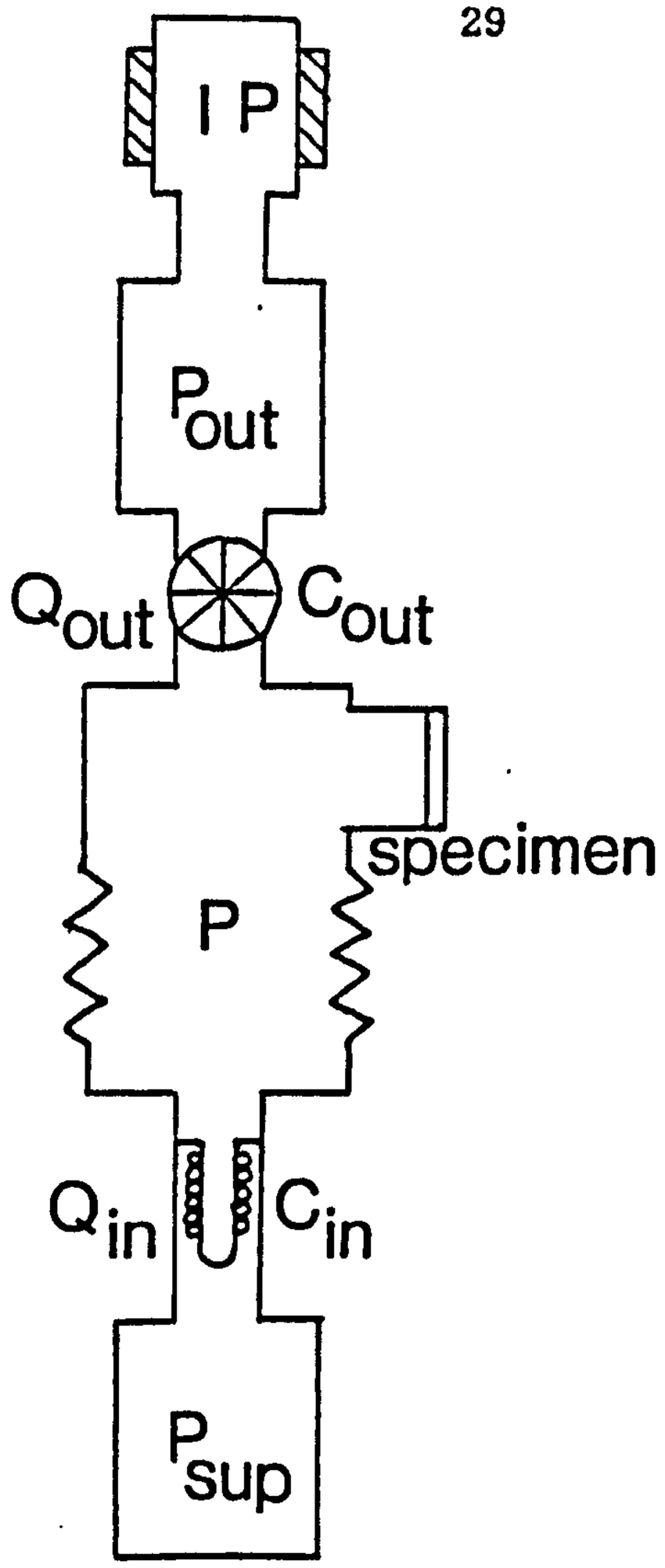

b

Fig 3.3a Schematic diagram of the stainless steel bellows, linear motion feedthrough, A.C. motor and transducer.

Fig 3.3b Simplified diagram of the input chamber. P_{sup} is the supply reservoir separated from the input chamber, P, by the palladium diffuser. P_{out} is maintained by the fine leak valve and the input chamber ion pump. P_{out} is not the pressure in the specimen output chamber.

pressure and purity of the gas by providing a dynamic flow through the chamber.

The need to stream gas sets a lower limit on the experimental pressure. With the volume modulator described here, this may be estimated as follows:

$$PV = nRT$$

where n ≡ molar moles of gas.

$$\frac{dV}{Vdt} + \frac{dP}{Pdt} = \frac{RTdn}{PVdt}$$

$$\frac{dn}{dt}RT = (Q_{in} - Q_{out})$$

where Q is throughput ($torr ls^{-1}$).

$$\frac{1dV}{Vdt} + \frac{dP}{Pdt} = \frac{1}{PV}(Q_{in} + Q_{out})$$

where:

$$Q_{in} = C_{in}(P_{sup} - P) \quad : \quad Q_{out} = C_{out}(P - P_{out})$$

If P and V are split into their respective steady state and oscillatory parts such that:

$$P = P_s + P_o \quad \text{and} \quad V = V_s + V_o$$

and defining:

$$\frac{V_o}{V_s} = A_v.\exp(i\omega t) \qquad \text{and} \qquad \frac{P_o}{P_s} = A_p.\exp[i(\omega t - \Phi)]$$

where Φ is the phase lag between the pressure and volume oscillations, then for $C_{in} \ll C_{out}$ and $P_{out} \rightarrow 0$:

$$\exp(i\Phi) = \left[-1 + i\frac{(C_{in} + C_{out})}{\omega V_s}\right] \frac{A_p}{A_v} \qquad [3.1]$$

For the amplitude:

$$\left[\frac{A_v}{A_p}\right]^2 = 1 + (C_{out}T_{osc}/2\pi V_s)^2 \qquad [3.2]$$

where T_{osc} is the period of oscillation. Imposing the restriction that the pressure amplitude must not fall to half of its maximum value, $A_p > A_v/2$, then:

$$C_{out}T_{osc}/2\pi V_s < \sqrt{3} \qquad [3.3]$$

$$C_{out} < 10V_s/T_{osc} \qquad [3.4]$$

Hence, for a 2 litre system of maximum oscillation period 10000s, the corresponding maximum conductance is:

$$C_{out\ max} \approx 2\times10^{-3}ls^{-1}. \qquad [3.5]$$

3.2.3 Measurement and calibration of the output chamber pressure.

The output chamber pressure was monitored using an ion gauge. This gauge was calibrated for hydrogen against a Baratron by measurement of the rate of rise of pressure in a measured volume through a calibrated leak. The result was 3.1 ± 0.1, and is in good agreement with the multiplier, 3.1, predicted by Dennis and Heppell(45). The gauge head was of a Bayard Alpert type, range (10^{-2} to 10^{-11}torr), with a sensitivity 25 per torr and an X-ray limit of 2×10^{-11} torr. After amplification and signal averaging the true minimum detectable fluctuation due to background pressure and system noise was found to be ≈ 10^{-10} torr.

3.3 SPECIMEN, FURNACE CONFIGURATION AND TEMPERATURE CONTROL

This section deals with the design of specimen mounts and the arrangements for temperature measurement and control. Its sub-sections describe:

3.3.1, the constraints on furnace and specimen and the resulting designs; 3.3.2, the system of temperature measurement and furnace control; 3.3.3, the system of program control for temperature.

3.3.1 Furnace and specimen mount design

Criteria for the specimen mount and furnace design were:

(1) to support a 2.54×10^{-2}m diameter specimen disc.

(2) to deliver greater than 600 watts to the specimen area over the required temperature range, 300 - 1200K.

(3) to enable the ion gun to have a clear *view* of the specimen area for cleaning purposes.

Figures 3.4a and 3.4b show the two designs used. Each met the above criteria. The sole difference is in the position of the furnace. Fig 3.4a shows a furnace located within the input chamber: internal configuration. Fig 3.4b shows a furnace external to the input chamber: external configuration.

The furnace heating element took the form of 4m of 1mm diameter

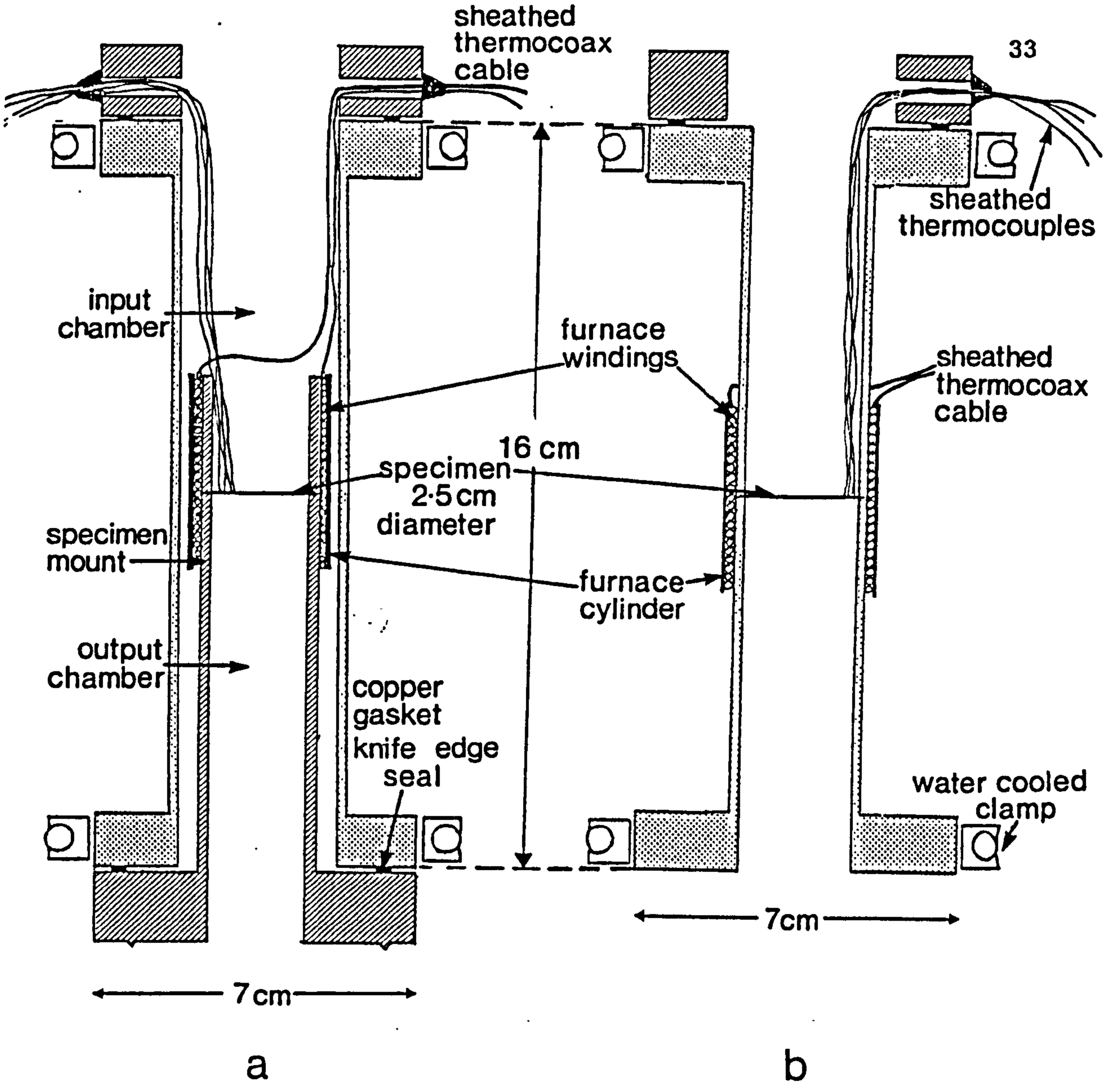

Fig 3.4a Schematic diagram of the furnace located within the input chamber with the specimen mount: internal configuration.

Fig 3.4b Schematic diagram of the furnace external to the input chamber: external configuration.

Notice the modular furnace design. The water cooled clamps were to minimise outgassing of the chamber walls.

thermocoax cable - a nickel resistance wire surrounded by an insulant and enclosed within an inconel sheath - fitted with cold junctions at each end. This was wound onto the inside of a cylindrical holder. The design was capable of delivering ≈ 1000 watts to the specimen region. Notice that the furnace design is modular so it could be used in either configuration.

The thermocoax cable in the internal configuration was brazed into a double sided FC70 conflat flange. Welding the thermocoax cable to the flange was not possible because the inconel sheath is too thin.

3.3.2 Temperature measurement and furnace control

Temperatures were measured using chromel/alumel thermocouples, each calibrated against an NPL Pt/PtRh standard. Four thermocouples were used, all being insulated and sheathed in inconel, of 0.5mm or 1mm diameter. As with the thermocoax cable the thermocouples were brazed into a conflat flange, fig. 3.4a and 3.4b.

The thermocouples were arranged as follows:

2 on specimen to measure

1 on specimen to control

1 on furnace to check thermocoax specification

On later runs when the furnace design was proven the configuration was modified to:

2 on specimen to measure

1 on specimen to control

1 on specimen as backup

The reference junction for all thermocouples was a continuously maintained triple point cell (Delrister Icell). The control thermocouple was connected to a Viscount, three term controller; when adjusted this was able to control temperature to 0.1K.

Temperature measurments were derived from two thermocouples. In normal operation these were consistent to less than 1K. Temperatures quoted for experimental runs were derived from the mean of these two experimental values.

Stability of measurement was dependent on the following:

(1) the temperature controller

(2) the 0°C cold cell

(3) the reference signal to the controller

A complete set of frequencies runs took typically six hours. Over this time drift from the reference signal corresponded to an error of less than 0.1K. Temperature fluctuations during a run were also less than 0.1K. Therefore, with the thermocouple differences, uncertainty

of absolute measurement can be statistically estimated as 0.55K. Fortunately hydrogen diffusivities in metals have a low activation energy so uncertainties of this magnitude are not intolerable.

3.3.3 Temperature control program

The requirements of temperature control were to:

(1) ramp the temperature under computer control to any temperature in the range 300 - 1200K.

(2) maintain the temperature precisely throughout each set of frequency modulation runs.

These requirements were met by the use of a 12 bit digital to analogue converter to provide the reference signal for the specimen furnace temperature controller. This signal was floated, divided and sent to the furnace controller in such a way that 1 bit ≈ 10μV. Therefore the temperature could be ramped in steps of 0.25K. Since a digital to analogue conversion took ≈ 100ms the time increments were limited to the response of the furnace controller. This limit is in excess of $1Ks^{-1}$ but was never found since the prime concern was to limit the ramp rate to $0.1Ks^{-1}$ to avoid problems associated with rapid thermal expansion of vacuum seals.

The temperature control signal provided by the two specimen thermocouples, was measured with a six digit volt meter calibrated to

1μV. This voltage was interpreted as a temperature using a Lagrange interpolating polynomial of degree three with a stored calibrated table of values; accuracy by this method was better than 0.1K. The digital to analogue bit value was adjusted so that the set temperature was centred on the nearest bit value.

3.4 SPECIMEN PREPARATION AND *IN SITU* ION BEAM CLEANING

This section deals with the preparation and cleaning of the specimens and is sub-divided into: 3.4.1, the specimen materials and preparation; 3.4.2, the cleaning of the specimen *in situ* by an ion beam.

3.4.1. Specimen materials and preparation

Two specimen materials were used: 304 and 316 stainless steels. The specimens were checked for composition on a scanning electrode microscope with a 10 - 100amu, energy dispersive system, EDS, analysing head, and were within the suppliers stated composition tolerances. The analysis for specimens of supposedly similar steels were consistant to a degree that just two analyses are presented below, one for each type of stainles steel.

(1) Stainless Steel AISI 316; annealed; thickness 1.0×10^{-4}m,5.0×10^{-5}m.

Analysis:

ELEMENT	% ELEMENT
Fe	71.3
Cr	18.0
Ni	8.8
Mn	1.4
C	(less than 1200ppm, not measured)

(2) Stainless Steel AISI 304;thickness (3.0, 2.5 and 1.25)$\times 10^{-4}$m.

Analysis:

ELEMENT	% ELEMENT
Fe	65.8
Cr	17.8
Ni	11.9
Mn	1.7
Mo	2.1
C	(less than 800ppm, not measured)

Small amounts of silicon were present, 0.3 - 0.7%, but in varying amounts from sample to sample and were attributed to the preparation and handling of the specimens. No silicon was present according to the suppliers analysis. Thicknesses were checked with a micrometer screw gauge.

All materials were cleaned using a method similar to that used for the ultra high vacuum components. That is: cleaned in detergent → ultrasonic bath(UB) in detergent → UB in distilled water → washed acetone → UB acetone → washed distilled water → UB distilled water → blown dry.

The specimen foil was then welded into the specimen mount and the above cleaning process repeated.

No mechanical cleaning of the specimen was undertaken but all were annealed in atmosphere of hydrogen in preparation for the experiment: typically the anneal was at 1000K for 24 hours at hydrogen pressures of 50 torr. This annealing process is known as the *activation* of a specimen. The purpose of this anneal was to *condition* the specimen to the flow of hydrogen. Just what this process entails is not known but it is thought to reduce the surface oxide on the steels and is certainly an established procedure among authors (5),(22),(23),(49) and (50). The grain sizes after such treatment were found to be in the region 5 - 20μm as exemplified by figs 3.5a and 3.5b.

Unfortunately as pointed out in chapter 2, specimens prepared in this way are not particularily reproducable, so specimens were further cleaned by using a hydrogen ion beam, except for one specimen which was left activated as a control experiment to the effectiveness of this ion beam as a surface cleaning method. The topic of ion beam cleaning is detailed in the following section.

3.4.2 Ion beam removal of surface oxides

The primary function of the ion guns was *in situ* cleaning of the specimen surfaces. They were also used, section 5.5, for an interesting confirmatory experiment in which the input chamber ion beam was used to inject hydrogen into the specimen foils.

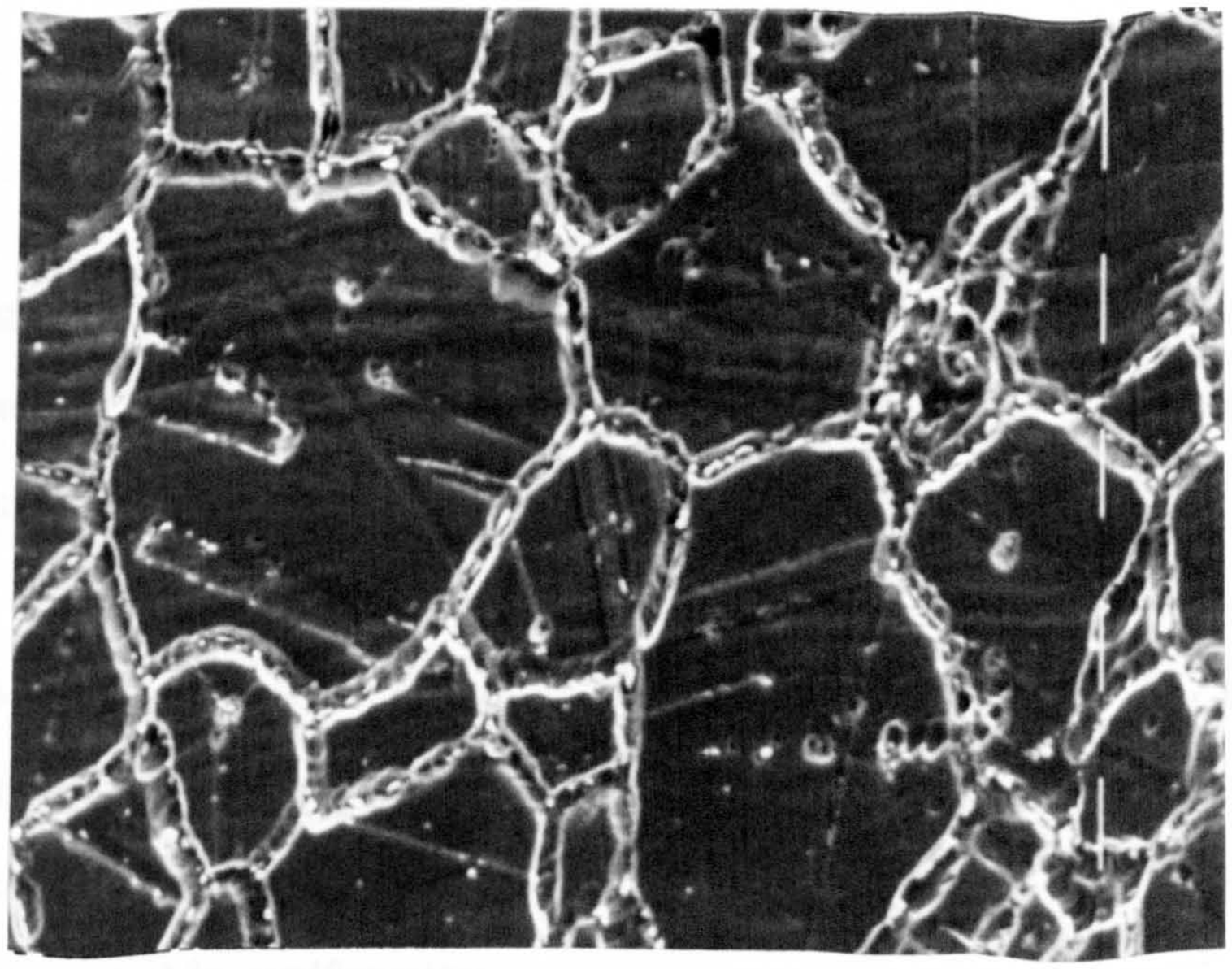

a

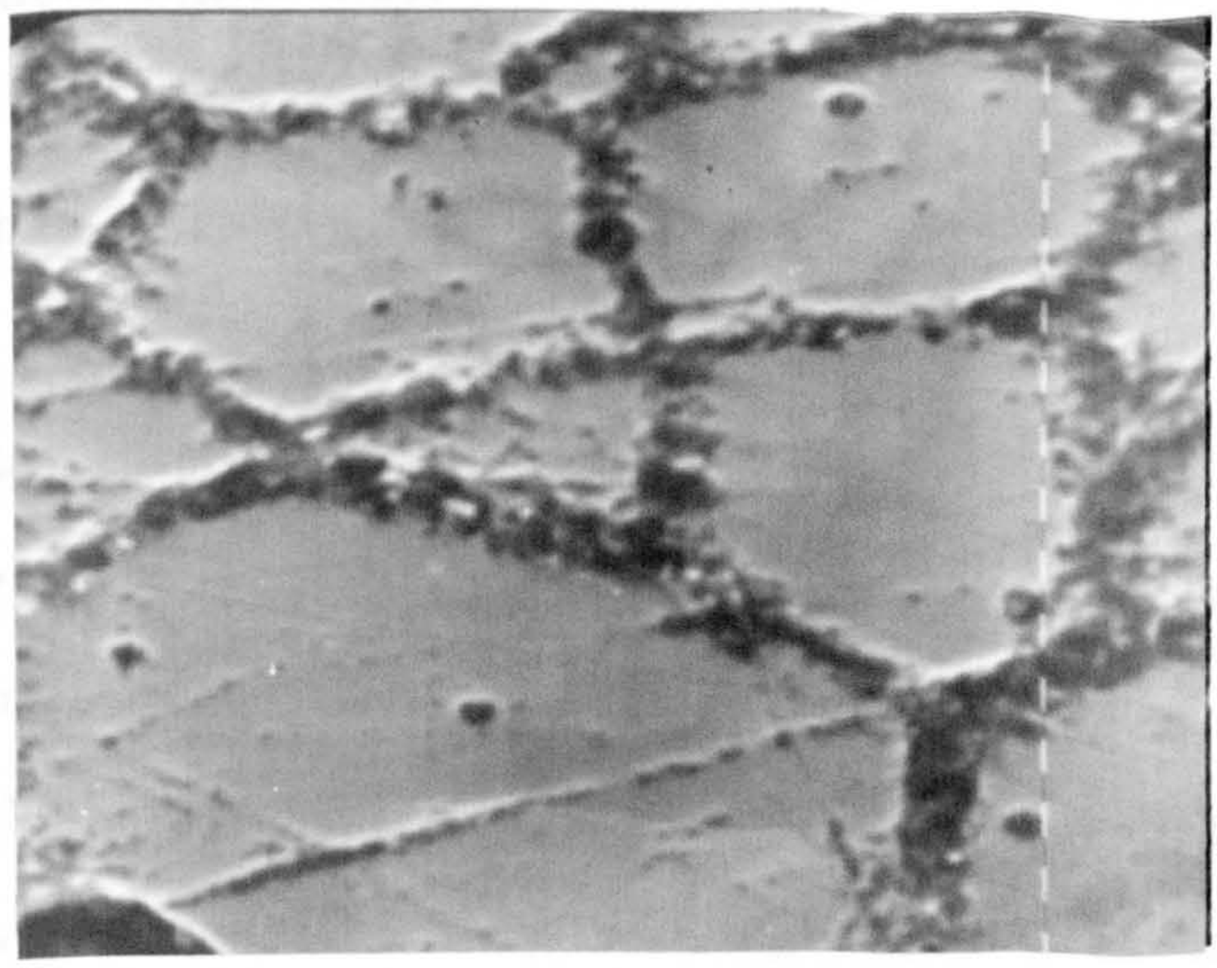

b

Fig 3.8 Scanning electron microscope photographs for 304 stainless steel, 3.0×10^{-4}m, (a), and 316 stainless steel, 5.0×10^{-4}m, (b), after annealing in the experimental rig. The marker represents 10μm and 1μm for (a) and (b) respectively.

The guns used a saddle field source configuration, Franks (46) and McIlraith (47) and were designed to satisfy the following requirements:

(1) to be of ultra high vacuum construction using stainless steel and ceramic components only.

(2) the beam divergence to be sufficient to cover the specimen area with reasonable uniformity.

(3) surface oxides within to be removed within a reasonable length of time, less than one week.

Requirements (1) and (2) were readily met by the design shown in fig 3.5. Typically a tube voltage of 4KV and a tube current of 5mA would produce > 100μA on the Faraday cup and > 25μA on the specimen ≈ 18cm away. Characteristics of a typical gun are shown in figs 3.6a, 3.6b and 3.6c for various pressures of hydrogen. Notice the ion current density is reasonably uniform over a distance approximately equal to the foil diameter.

Requirement (3) was difficult to quantify in advance since no data is available on cutting rates for diffuse hydrogen beams on stainless steel oxides. A method of checking the effectiveness of the gun was clearly necessary. This was done as follows:

An AISI 316 1.0×10^{-4}m thick specimen was cleaned by exposure to the gun current for over 100 hours. Hydrogen permeation through that

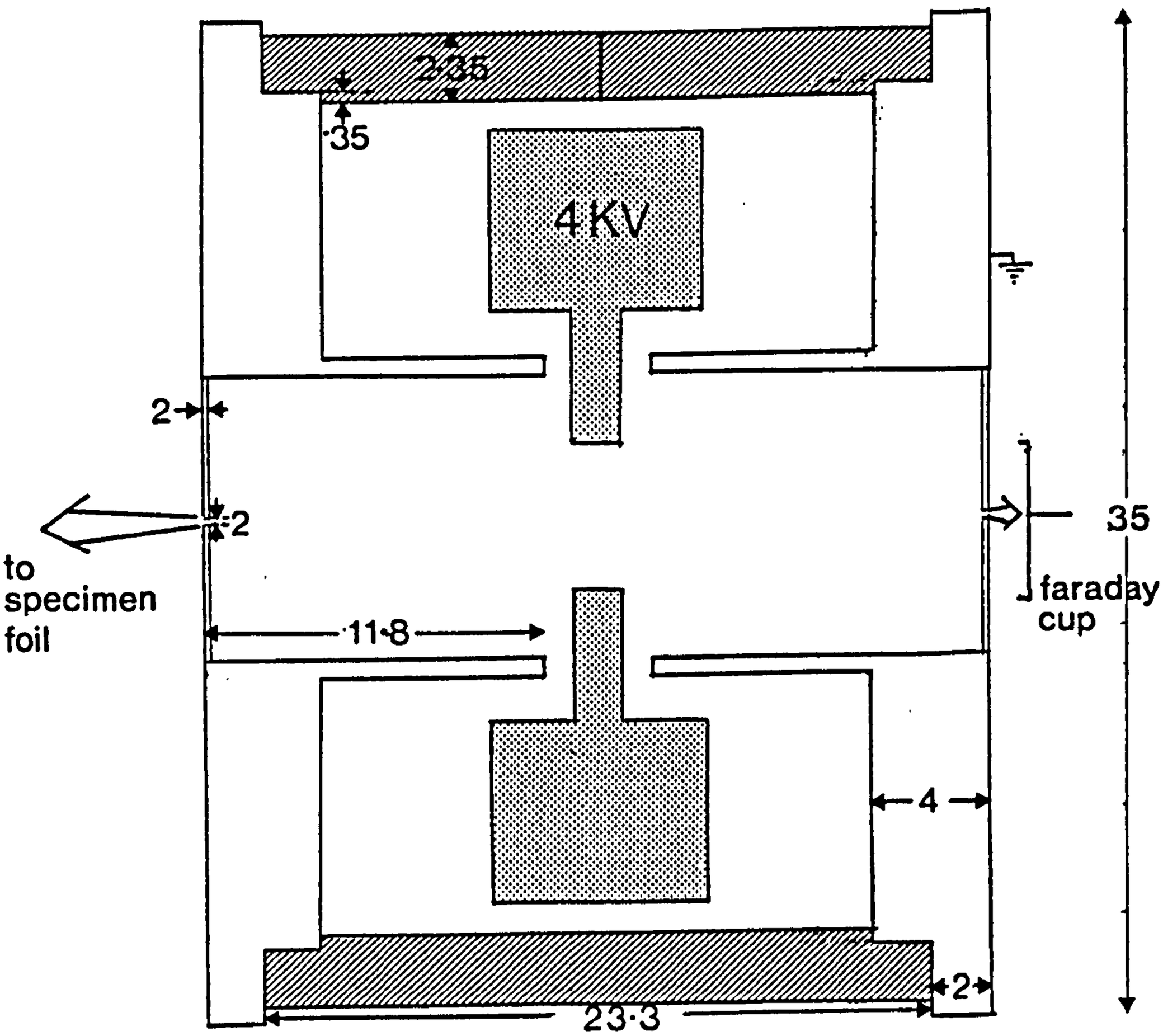

Fig 3.5 Diagram of the basic features of the ion gun. All measurements are in mm. The gun is cylindical and the high voltage feedthrough and ceramic spacers are omitted for reasons of clarity. The symmetric nature of the gun enabled a Faraday cup to be used to monitor the ion current. Vacuum feedthroughs for the high voltage and faraday cup were welded into a FC70 flange.

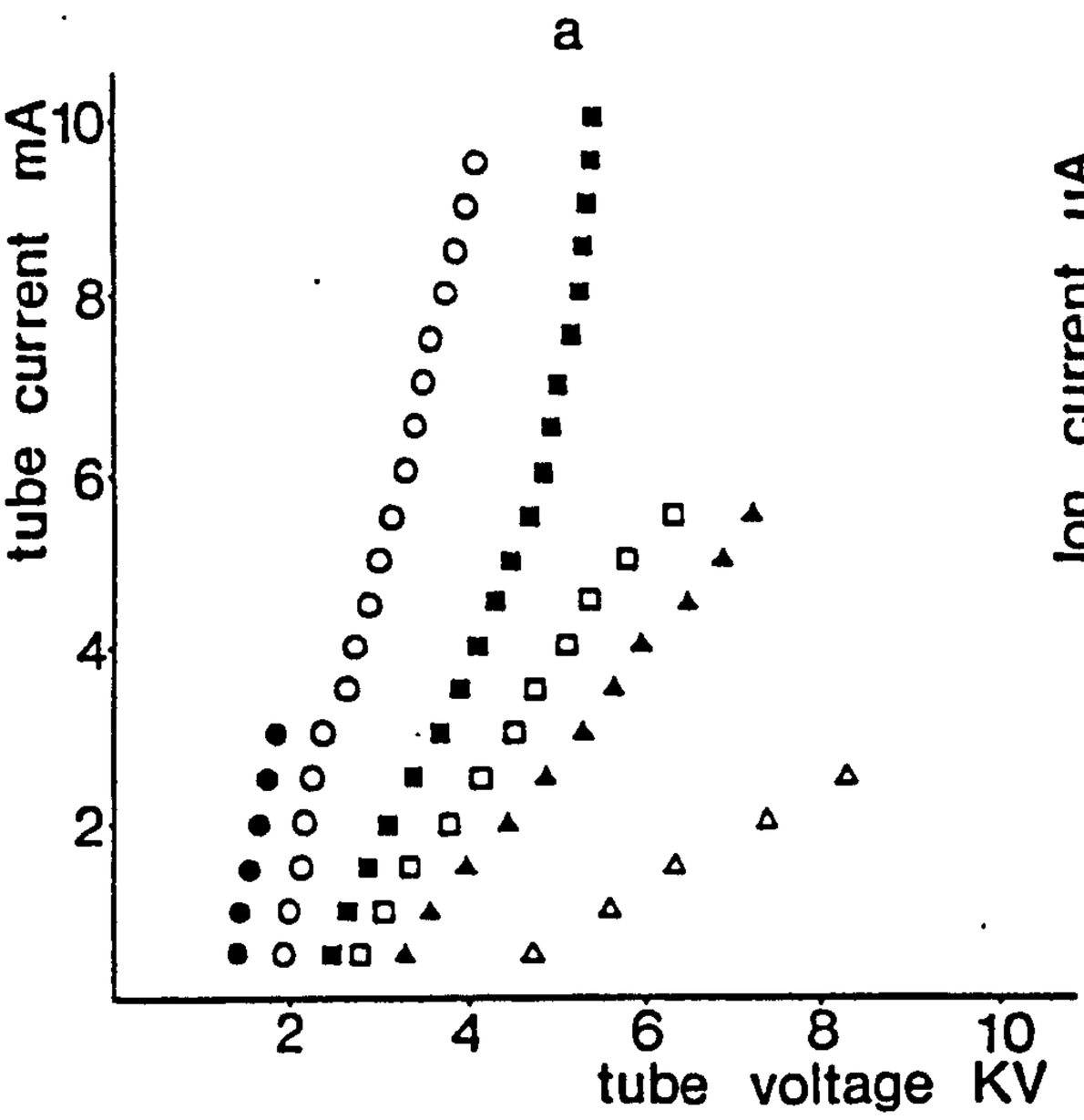

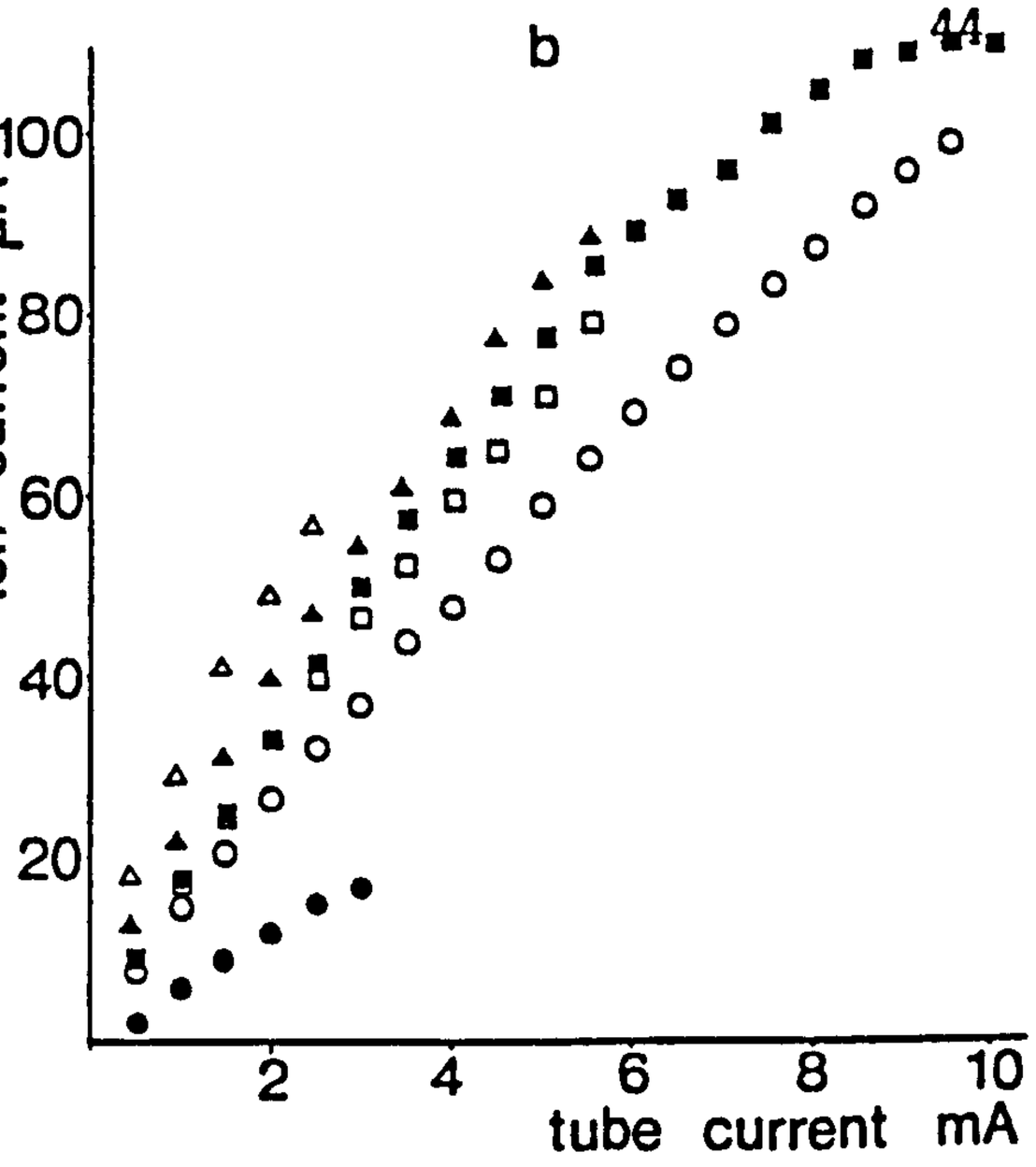

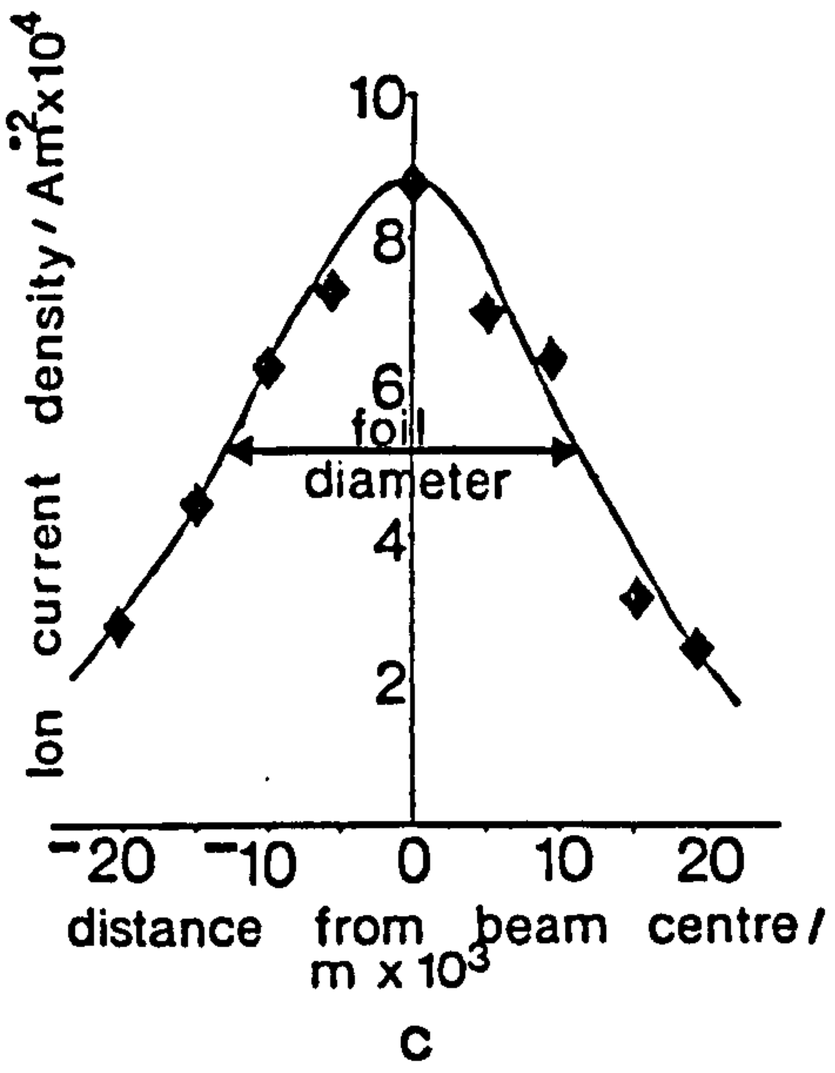

c

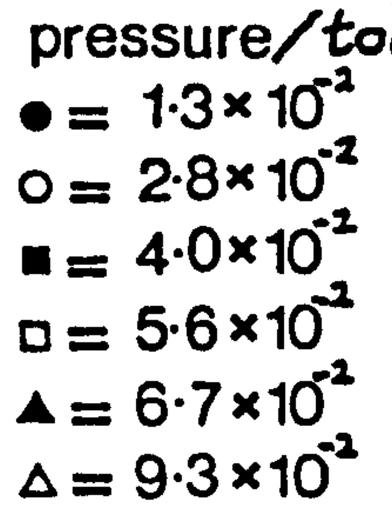

Fig 3.6a Variation of ion gun tube current with tube voltage for various operating pressures.

Fig 3.6b Variation of ion current with tube current for various operating pressures.

Fig 3.6c Variation of ion current density with position from beam centre at a distance of 0.2m from the gun.

specimen was then measured; at an input pressure of 50torr and a temperature of 873K. Following this, 0.9torr of air was introduced to one chamber and the specimen was annealed at 973K for 12hrs. This produced a 48% reduction in the permeation. It was found that a futher 84Hrs exposure to the ion beam recovered the permeation to within 2% of its original value, the uncertainty in the measurement being due mainly to a badly positioned thermocouple which shadowed part of the specimen.

Interestingly, the old method of activating a specimen produced a permeation approximately 10% down on that of the ion gunned specimen. This is presumably why, as shown in chapter 6, the final data on permeation is above Le Claire's reviewed values of permeations for steels(14).

All specimens were ion beam cleaned on both sides *in situ* unless otherwise stated.

3.5 CONTROL SYSTEM

Control of the equipment during an experiment was fully automated. Similar control programs were written for the two rigs, but there were differences in method and hardware. To illustrate the control system and data collection an experimental run will be detailed, 3.5.1. In sub-section 3.5.2 the method of obtaining the Fourier coefficients of the input and output waveform is described. Details of equipment calibration are given in 3.5.3.

3.5.1. An experimental run

The control system is illustrated in fig 3.7. For a specific pressure the variables of temperature range, number and ramp rate, frequency range and number and plateau time were fed into the program. The temperature was ramped up to the first set temperature using the digital to analogue converter described in section 3.3. The set temperature was held for a period of about 50 minutes, to allow the temperature, input and output pressures and gauges to stabilise. Measurements of the input and output gauges, for this steady state condition, were then taken using the 6-digit volt meter.

For analysis of the time varying flux the signal from these gauges was offset, amplified and fed into a ±1V 12 bit analogue to digital converter. The reference signal for the first frequency was sent to

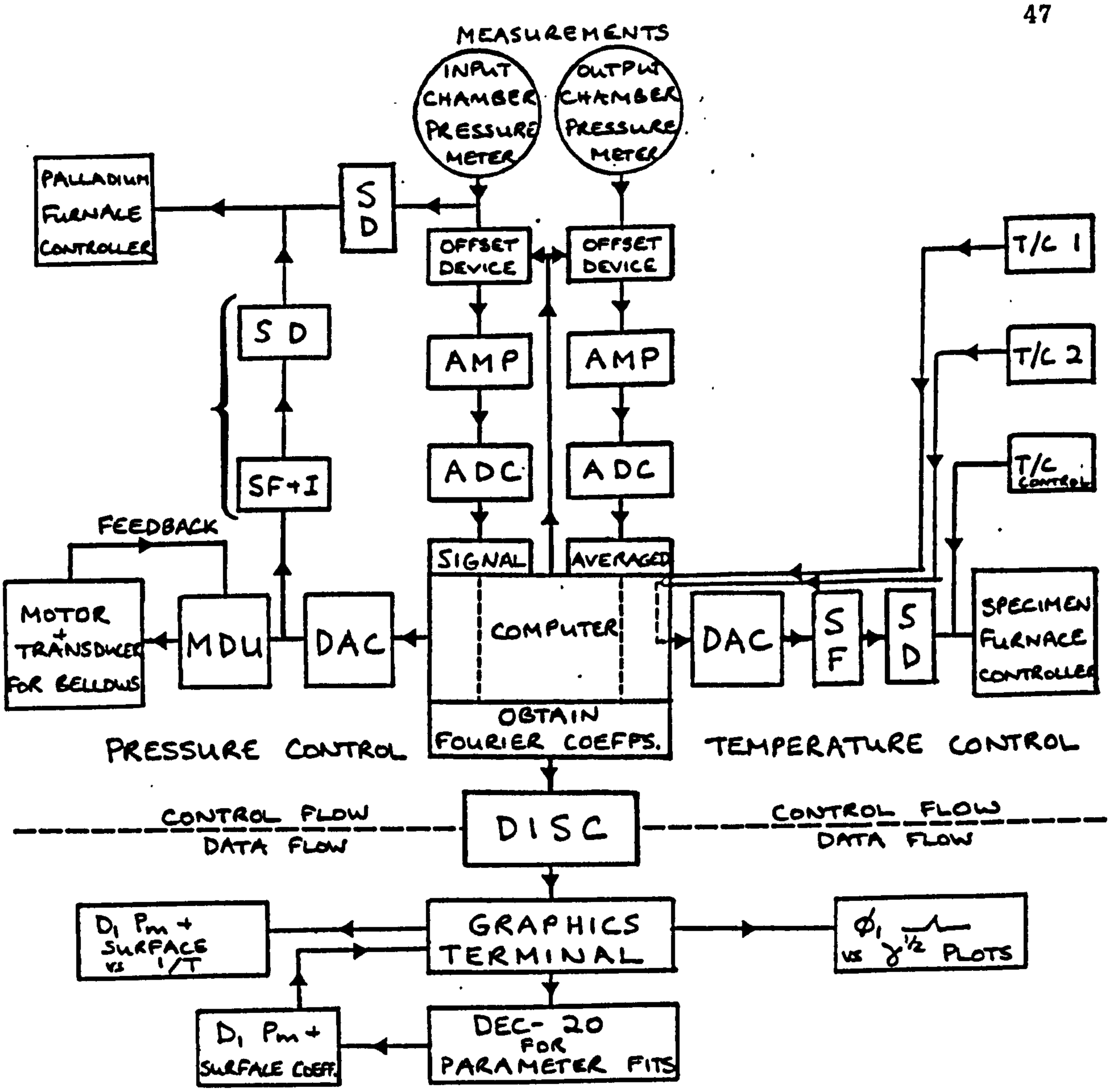

Fig 3.7 Control diagram of the experimental system. Key:

DAC - digital to analogue converter; ADC - analogue to digital converter; MDU - motor drive unit; T/C - Thermocouple; DVM - digital volt meter; SF - signal floated; I - signal inverted; SD - signal divided; AMP- amplifier.

the motor drive unit of the volume modulator via a 12 bit digital to analogue converter as described in section 3.2. The computer controlled the frequency by using its own internal clock. After 10 minutes, to allow transients to disappear, measurements of the pressure waveform in the input and output chambers were taken. A minimum of 1000 measurements was taken for each cycle. These were then signal averaged over several scans the number depending on the cycle time. The data was stored in the I/O buffer of the computer.

In the ten minutes allowed for the next frequency to stabilise :

(1) the buffer was read

(2) the data was signal averaged if more than one scan was measured

(3) a least squares fit was performed on the resulting waveforms, to give the Fourier coefficients and their standard errors.

(4) the Fourier coefficients were converted into terms of phase lag, Φ, relative amplitude modulation ratio, Λ, and amplitude modulation ratio $|R^{-1}|$ (chapter 4).

(5) this data was then dumped to disc.

(6) the signal averaged waveforms were plotted on the VDU.

(7) a hard copy of the refined data and the VDU waveforms were dumped to the printer.

(8) if the signal to noise ratio (S/N) was less than 2 an extra scan was called for the next frequency studied.

Following analysis the I/O buffer was cleared and the sequence

repeated for a new frequency. After all the frequencies at a given temperature were run, the temperature was ramped to the next set value and the process repeated.

The total time taken for an experiment using 6 pressures, each pressure run at 10 temperatures and each temperature run for 14 frequencies was about 3 weeks (C.E.G.B permitting).

There were minor differences between the control and data handling systems in the two experimental rigs. In the older rig the control system was more dispersed. For example, the alternative method used of generating a reference signal for the volume modulator was to store a harmonic signal on a 12 bit eprom and to call this signal by timed pulses from an internal clock. The central computer was used to select the pulse interval but the clock was left to *play* the eprom at the chosen frequency. This unit, with the clock and eprom, was known as an Eprom Player. The reference signal was sent to the motor drive unit and used as in the other rig.

The corresponding method of data collection was to use a hardware analogue to digital converter and signal averager (Datalab DL4000 series). This provided an averaged waveform which was dumped to disc and analysed in the normal way. The advantage of this method is that data from a run at one frequency may be analysed while the rig is running at the next frequency of the series since the computer is no longer tied up receiving data in the course of a run. Unfortunately, the disadvantages of this approach far outweigh the

advantages since only a preset number of scans is available and the same number of measurements are taken in each scan whatever the frequency. In consequence useful measurement time is wasted.

After an experimental run, the refined data for each frequency, temperature and pressure, was transferred to a graphics terminal for plotting of the data. This data was then sent to a mainframe computer , via a modem, for least squares fitting of the parameters of the model being used.

3.5.2 The derivation of Fourier coefficients using a least squares method.

Analytic expressions for the input and output waveforms were obtained by a least squares fit of the data to the equation:

$$y_i = a\ \sin x_i + b\cos x_i + c \qquad [3.6]$$

It is useful to express this as:

$$(y_i - \bar{y}) = a[\sin x_i - \textstyle\sum(\sin x_i)/N] + b[\cos x_i - \sum(\cos x_i)/N] \qquad [3.7]$$

where the bar, $\bar{}$, refers to mean value of y. In matrix notation for all i; i = 1 to N, [3.7] may be written:

$$\begin{bmatrix} \\ y_i - \bar{y} \\ \\ \end{bmatrix} = \begin{bmatrix} & & \\ (\sin x_i - \sum \sin x_i) & & (\cos x_i - \sum \cos x_i) \\ & & \end{bmatrix} \begin{bmatrix} a \\ \\ b \end{bmatrix}$$

$$Y = J P \qquad [3.8]$$

Hence:

$$\tilde{J}Y = \tilde{J}JP \qquad [3.9]$$

Therefore:

$$P = (\tilde{J}J)^{-1}\ \tilde{J}Y \qquad [3.10]$$

Thus the parameter matrix P containing the Fourier coefficients a and b can be found. Also a variance co-variance matrix can be defined to obtain the standard error of a and b, such that:

$$\sigma_a^2 = (\tilde{J}J)^{-1}_{11}\ \sigma_y^2 \qquad [3.11]$$

$$\sigma_b^2 = (\tilde{J}J)^{-1}_{22}\ \sigma_y^2 \qquad [3.12]$$

where σ_a and σ_b are the standard errors on a and b and σ_y^2 is the residual sum of squares such that:

$$\sigma_y^2 = \sum (y^{obs} - y^{calc})^2/N \qquad [3.13]$$

By this method the Fourier coefficients a and b and their standard errors were found for both input and output waveforms. For further analysis the coefficients were put into phase and amplitude form. Notice that in addition to the coefficients a and b, this method obtains any offset, c, due to drift during a frequency run; this computed value of c was used for fine adjustment of the input and output base pressure measurements.

3.5.3 List of hardware and calibration of equipment

To demonstrate the precision expected in the experimental work this section includes a short list of the equipment used and of the associated calibration procedures.

Hardware

(1) HP-86 scientific computer - with - HP-IB/IEEE 488 bus interface, RS232 serial interface, 192k byte memory, two 5¼ inch floppy disc drives and a 9×9 dot matrix printer connected via a Centronics interface.

(2) Triton Trivector Z80 - with - simulated IEEE bus, RS232 serial interfaces, DLO and DLI, 20mA current loop, two 8 inch double sided floppy disc drives and a Texas 810 serial printer.

(3) Datalab DL4000 - was set up to provide - two 512 channel, ±1V 12 bit analogue to digital converters, signal averaged over a set number of cycle scans, typically 4, and advanced by an external trigger.

(4) 3-D Inlab rack and modules. Both computers were connected to an Inlab rack on the IEEE interface. The rack itself was given a primary address and the following modules were identified with a secondary address.

(1) 8-channel opto-isolators - function - enabling the auto-offset device, resetting the volume modulator to its central position and for various safety trips involved in the

bakeout program.

(2) 8-channel relay unit - function - as for (1)

(3) 4-channel 12 bit digital to analogue converters - function - temperature ramping and reference signal for volume modulator.

(4) 12 bit fast analogue to digital converter - function - to replace the Datalab hardware method of signal averaging.

(5) 16-channel single ended analogue multiplexor card - function - to enable more than one signal to use (4).

(5) Two Solatron digital volt meters were used and were linked by either the serial or 20mA loop interface. Both were 6 digit, calibrated to 1μV.

Calibration

The aforementioned digital volt meters were traceable to NPL standards. They were used to calibrate the analogue to digital converters, digital to analogue converters, amplification for the auto-offset device, signal floaters and dividers as well as for zeroing pressure meters and controllers.

The whole measurement system was checked from amplification to Fourier analysis using a measured sine wave signal which was substituted for both pressure signals into the auto-offset device. The cycle time of the dummy signal was that of the fastest frequency used in the experiment. Accuracy of the whole measurement system

was then found to be better than 0.5% of full scale, while comparison between the two identical input waveforms was better than 0.1% for phase lags and amplitudes.

3.6 SUMMARY

Two experimental rigs were designed and built. They were each capable of doing the following:

(1) support experimental foils of thickness upwards of 5×10^{-5}m.

(2) control temperatures in the range 300K-1200K.

(3) control and monitor hydrogen gas pressure in the range 10^{-4} - 5×10^{2}torr for the input chamber, 10^{-9} - 10^{-4}torr for the output chamber.

(4) modulate the input pressure up to ±10% for a frequency range 10^{-2} - 10^{-5} Hz.

(5) detect fluctuations in the output chamber pressure, down to 10^{-10} torr, corresponding to a flux of $\sim10^{-10}$ torrls^{-1}.

(6) signal average and calculate the Fourier coefficients of the waveforms.

(7) provide a total system accuracy of better than 0.5% from gauge head controller to Fourier coefficients.

CHAPTER 4 : THEORY

This chapter details a theoretical model which describes the progress of a modulated diffusant flux from one side of a material to the other. The model is a general one, based on a linear approximation, which expresses the ratio of the vector representing the experimental output to that representing the input as a matrix product. Since a separate matrix is used for each of the elementary processes which together produce flow, the model is readily adapted to the description of a variety of experimental configurations.

In the approach used here, this treatment is exemplified by using it to describe pressure modulations under circumstances of diffusion limited permeation. Having described this simplest of models, the approach is developed by consideration of the less tractable problem of how permeation is modified by surface processes of finite rate. Again the case treated is that of the pressure modulation.

An alternative form of flux modulation, specifically ion beam injection, is described in a later section. This shows the versatility of the matrix method and the facility with which it may be modified to describe different sorts of experiment. Finally, the question of parallel diffusion, which may cause a systematic error in some measurements, is considered and methods to overcome this problem are discussed.

The chapter is presented in sections, their functions being to:

4.1, describe a mathematical model of the system and define its parameters; 4.2, demonstrate a matrix notation that succinctly describes a wide range of experimental conditions; 4.3, describe in detail diffusion limited, *classical*, permeation as it applies to a modulation experiment; 4.4, show how the diffusion limited model may be modified to include surface rate constants; 4.5, describe flows modulated by ion beam injection of diffusant; 4.6, assess parallel diffusion as a possible experimental complication; 4.6, summarise the principal features of the analysis presented.

4.1 REPRESENTATION OF THE SYSTEM AND PARAMETERS USED

4.1.1 System

The experimental system to be modelled, is that described in chapter 3. It comprises, fig 4.1, three sections; the input chamber, the experimental membrane and the output chamber.

Consider the membrane to be a single solid phase of length ℓ and uniform cross-section γ in the plane perpendicular to the flow of the diffusing species. Diffusant enters the input surface of the membrane and propagates by diffusion to the exit surface. This diffusant flux is subject to modulations of angular frequency ω about a fixed central value. Diffusant leaves the membrane to enter the output chamber, of volume V, evacuated by a pump of constant speed S. Pressure within this chamber modulates with angular frequency ω about a central value p'_g whose magnitude is not maintained but represents a balance between the diffusant flux from the membrane, outgassing of diffusant from the walls of the chamber at a rate Q_{og} and the action of the pump.

Analysis is restricted to a condition of quasi-steady state such that all transient flows are supposed to have disappeared; the sole perturbation is the input modulation and its consequential variations downstream. The presence of the modulation is supposed not to alter the established steady state.

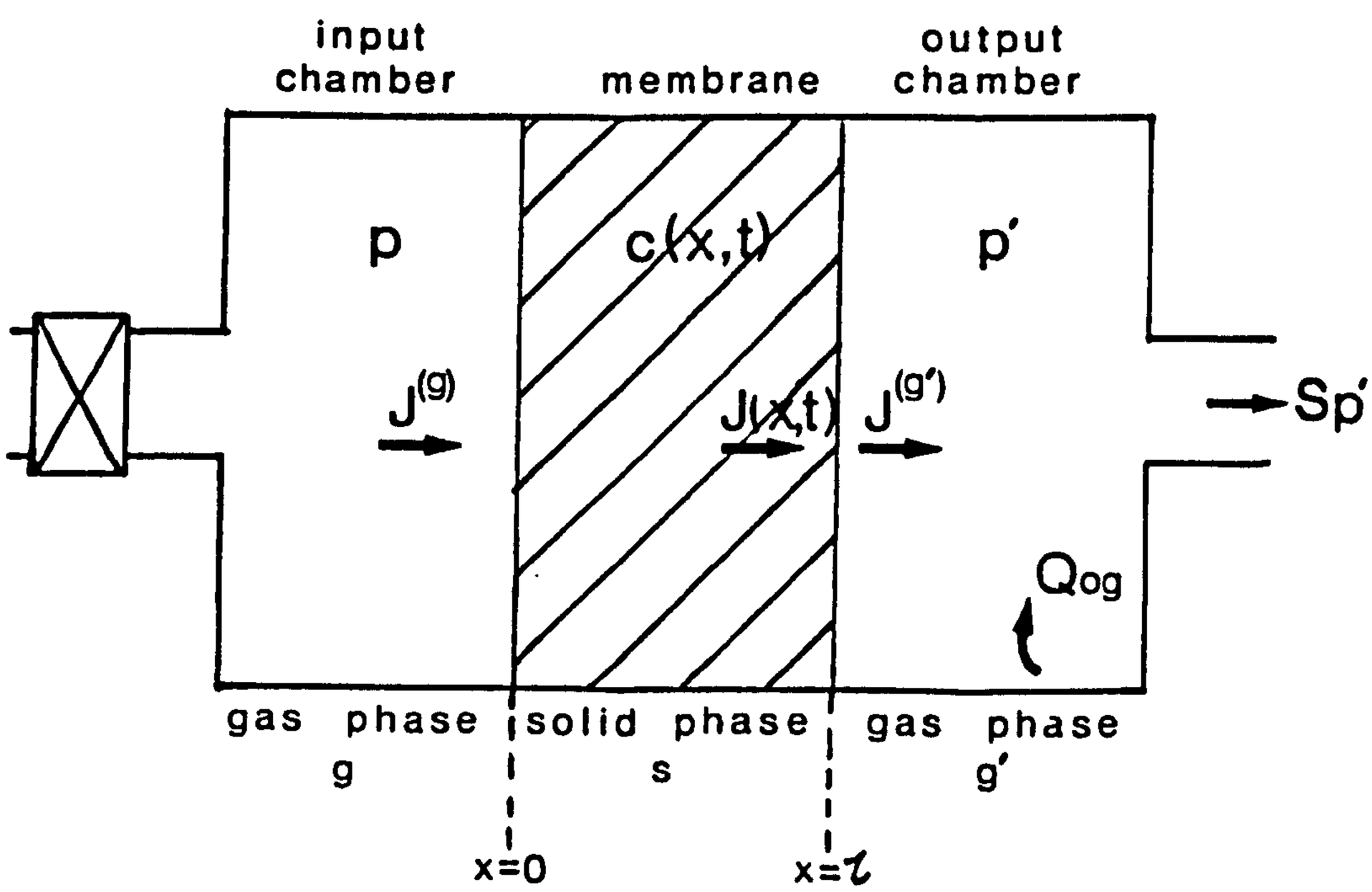

Fig 4.1 Schematic diagram of the experimental system to be modelled. It comprises three sections; the input chamber, the specimen membrane and the output chamber.

4.1.2 Parameters

Just two variables are required to specify the condition of each section. For a pressure modulation experiment these are, in the gas phases, the partial pressure and the flux of diffusant. Each of these variables is here split into a time-independent steady state term, denoted by the subscript s ,and an harmonic term denoted by the subscript o.At time t, the variables are defined as follows :

(1)in the membrane (solid phase s)

The concentration c(x,t), and the flux, J(x,t), of diffusant at position x,where $0 < x < \ell$ are:

$$\begin{aligned} c(x,t) &= c_s(x) + c_o(x,t) \\ J(x,t) &= J_s + J_o(x,t) \end{aligned} \qquad [4.1]$$

(2)in the input chamber (gas phase g)

The diffusant partial pressure, p(t), and the flux, $J^g(t)$, from the chamber to the membrane are:

$$\begin{aligned} p(t) &= p_s + p_o(t) \\ J^g(t) &= J^g_s + J^g_o(t) \end{aligned} \qquad [4.2]$$

(3)in the output chamber (gas phase g')

The diffusant partial pressure, p'(t), and the flux, $J^{g'}(t)$ from the membrane to the chamber are:

$$\begin{aligned} p'(t) &= p'_s + p'_o(t) \\ J^g(t) &= J^{g'}_s + J^{g'}_o(t) \end{aligned} \qquad [4.3]$$

The net throughput of the chamber, $Q_n(t)$, is:

$$Q_n(t) = Sp'(t) \qquad [4.4]$$

It is useful to consider these modulated variables as the real parts of a complex quantity, so that, for example:

$$p = |p|\exp[i(\omega t)] \; ; \; p' = |p'|\exp[i(\omega t - \Phi)] \qquad [4.5]$$

Thus:

$$p_o(t) = Re(p) = |p|\cos\omega t \qquad [4.6]$$

$$p'_o(t) = Re(p') = |p'|\cos(\omega t - \Phi) \qquad [4.7]$$

where Re(p) and Re(p') represent the real parts of the complex quantities p and p' and Φ represents the phase lag between the modulations of p and p'.

In general any harmonically varying quantity $y_o(t)$ with arbitary phase lag Φ_y will be written:

$$y = |y|\exp[i(\omega t - \Phi_y)]; \; y_o(t) = Re(y) \qquad [4.8]$$

The purpose of the following sections is to derive general expressions that relate the experimentally observable variables describing the input and output chamber in the general form of the ratio:

$$R = \frac{Y}{y}, \qquad [4.9]$$

and, for most work;

$$R = \frac{P}{p},$$

From this the phase lag Φ and the amplitude ratio $|p'|/|p|$, may be evaluated using the following relationships:

$$\Phi = Arg(R) = \tan^{-1}[Im(R)/Re(R)] \qquad [4.10]$$

$$\frac{|p'|}{|p|} = |R|^{-1} \qquad [4.11]$$

4.2 MATRIX NOTATION

A form of this matrix approach can be found in Carslaw and Jaeger "Heat conduction in solids" (52).

Classically it may be expected that the rate of entry to the solid of a diatomic diffusant gas will vary as $p^{1/2}$ but other variations are conceivable. Whatever relationship holds, it is not inherently linear. Here, to simplify the mathematical description, all experimental modulations are assumed to be fractionally small. Specifically:

$$p_o(t) \ll p_s \quad ; \quad c_o(x,t) \ll c_s(x) \qquad [4.13]$$

With this restriction the system may be treated as linear. In consequence the quotient R = y/y' may be written as a matrix product with a separate matrix to describe each process occurring from input to output chamber. To do this, the variables are first expressed in vector form.

In the solid phase the condition at any point, x, is defined by the concentration c(x) and flux J(x).The time dependent parts of these quantities are represented by a vector, the condition vector, N, where:

$$N = \begin{bmatrix} c(x) \\ J(x) \end{bmatrix} \qquad [4.14]$$

Analogous vectors are defined for the input and output chamber gas phases:

$$N^g = \begin{bmatrix} p \\ J^g \end{bmatrix} \quad ; \quad N^{g'} = \begin{bmatrix} p' \\ J^{g'} \end{bmatrix} \qquad [4.15]$$

In this linear model, conditions in the gas phases can be linked to those in the solid phase by introducing the general interphase matrices Z and Z', which have the properties:

$$N^g = ZN(0) \; ; \; N(\ell) = Z'N^{g'} \qquad [4.16]$$

N(0) and N(ℓ) are defined as the condition vectors just below the entry and exit surfaces of the solid phase. They are linked by a translation matrix, V, defined by:

$$N(0) = VN(\ell) \qquad [4.17]$$

To complete this matrix representation of the variables, the diffusant fluxes on the input and output surfaces of the membrane must be related to actual experimental observables. While p and p', for the input and output chamber, are readily measured, other combinations, for example J^g and p', are also of potential use. To preserve generality of treatment, the observables associated with the input and output chamber are designated y and y' respectively. This allows entry and exit matrices, Q and Q', to be defined, such that:

$$y = QN^g \; ; \quad N^{g'} = Q'y' \qquad [4.18]$$

It follows that:

$$R = \frac{y}{y'} = QZVZ'Q' \qquad [4.19]$$

In subsequent sections the matrix coefficients appropriate to particular experimental variables, and models incorporating diffusion

and surface reactions, will be introduced. Above is the required linear relationship in general form.

4.3 DIFFUSION LIMITED PERMEATION

The translation matrix describes flows in the region $0 < x < \ell$ within the metal and, in particular, it provides a means to relate concentration and flux at the $x = \ell$ surface to that at the $x = o$ surface. A model to describe $\mathbb{V}$ will be developed in sub-section 4.3.1. The phase boundary matrices, $\mathbf{Z}$ and $\mathbf{Z}'$, and the entry and exit matrices $\mathbb{Q}$ and $\mathbb{Q}'$, introduced in the previous section, will be described in 4.3.2 and 4.3.3, for the simplest case of diffusion limited permeation. This will enable a solution to be evaluated, 4.3.4, for when surface reactions are very rapid and permeation is rate limited uniquely by the process of diffusion. The solution so obtained applies to any combination of input and output conditions. The particular solution for a system that is rapidly pumped, that is for $p_S' \ll p_S$, will then be discussed in detail, 4.3.5, since it is of primary experimental interest.

4.3.1 The translation matrix $\mathbb{V}$

A modulation of diffusant concentration at one surface of the membrane will propagate by diffusion. For the region $0 < x < \ell$ Fick's laws are assumed to be valid, so that with the diffusion coefficient, D:

$$\frac{\partial c(x,t)}{\partial t} = D\frac{\partial^2 c(x,t)}{\partial x^2} \qquad [4.20]$$

$$J(x,t) = -D\frac{\partial c(x,t)}{\partial x} \qquad [4.21]$$

Splitting into steady state and harmonic parts:

(1) for the time independent part

$$D\frac{\partial^2 c_s}{\partial x^2} = 0 \quad ; \quad J_s = -D\frac{\partial c_s}{\partial x} \qquad [4.22]$$

Using [4.1] gives:

$$c_s(x) = c_s(0) - \frac{x}{\ell}[c_s(0) - c_s(\ell)] \qquad [4.23]$$

and

$$J_s = \frac{D}{\ell}[c_s(0) - c_s(\ell)] \qquad [4.24]$$

(2) for the harmonic part

$$\frac{\partial c_o(x,t)}{\partial t} = D\frac{\partial^2 c_o(x,t)}{\partial x^2} \qquad [4.25]$$

and

$$J_o(x,t) = -D\frac{\partial c_o(x,t)}{\partial x} \qquad [4.26]$$

which are contained in the following complex variable equations:

$$\frac{\partial c}{\partial t} = D\frac{\partial^2 c}{\partial x^2} \quad ; \quad J = -D\frac{\partial c}{\partial x} \qquad [4.27]$$

For this last equation the general solution is:

$$c(x) = [Ae^{a(\ell-x)} + Be^{a(x-\ell)}]e^{i\omega t} \qquad [4.28]$$

$$J(x) = Da[Ae^{a(\ell-x)} - Be^{a(x-\ell)}]e^{i\omega t} \qquad [4.29]$$

where:

$$a = (1+i)(\omega/2D)^{1/2} \qquad [4.30]$$

and A and B are parameters determined by the boundary conditions.

The coefficients A and B can be eliminated. Using [4.14], [4.28] and [4.29] can be expressed in matrix notation as:

$$N(x) = \begin{bmatrix} e^{a(\ell-x)} & e^{a(x-\ell)} \\ De^{a(\ell-x)} & -De^{a(x-\ell)} \end{bmatrix} \begin{bmatrix} A \\ B \end{bmatrix} e^{i\omega t} \quad [4.31]$$

thus at $x = \ell$:

$$N(\ell) = \begin{bmatrix} 1 & 1/Da \\ Da & -Da \end{bmatrix} \begin{bmatrix} A \\ B \end{bmatrix} e^{i\omega t} \quad [4.32]$$

Inverting shows:

$$\begin{bmatrix} A \\ B \end{bmatrix} = \frac{1}{2} \begin{bmatrix} 1 & Da \\ 1 & -1/Da \end{bmatrix} N(\ell) e^{i\omega t} \quad [4.33]$$

Substituting back into [4.31] then gives:

$$N(x) = \begin{bmatrix} \cosh a(\ell-x) & (1/Da)\sinh a(\ell-x) \\ Da\sinh a(\ell-x) & \cosh a(\ell-x) \end{bmatrix} N(\ell) \quad [4.34]$$

It is of primary interest to relate conditions at the input surface to those at the output surface. Thus by putting $x = 0$ and comparing with [4.17], the translation matrix **V** may be identified as:

$$\mathbf{V} = \begin{bmatrix} \cosh a\ell & (1/Da)\sinh a\ell \\ Da\sinh a\ell & \cosh a\ell \end{bmatrix} \quad [4.35]$$

4.3.2 The phase boundary matrices, **Z** and **Z'**, for diffusion limited permeation.

The function of a phase-boundary matrix is to relate the condition vector just inside a solid to that of the adjacent gas. Since the model under discussion in this section is for diffusion limited permeation, calculations are subject to the following conditions:

(1) The flux of diffusant entering or leaving the gas phase at all times equals the flux leaving or entering the adjacent solid phase; there is no surface accumulation. Thus at all times:

$$J^g(t) = J(0,t) \quad ; \quad J^{g'}(t) = J(\ell,t) \qquad [4.36]$$

hence for the steady state part:

$$J^g_S = J_S = J^{g'}_S \qquad [4.37]$$

and for the harmonic part:

$$J^g_o(t) = J_o(0,t) \; ; \; J_o(\ell,t) = J^{g'}_o(t) \qquad [4.38]$$

(2) The subsurface diffusant concentrations are those providing equilibrium with the adjacent gas. Following Sieverts' law this gives, for a diatomic gas:

$$c(0,t) = K_{sm}[p(t)]^{\frac{1}{2}} \qquad [4.39]$$

$$c(\ell,t) = K_{sm}[p'(t)]^{\frac{1}{2}} \qquad [4.40]$$

K_{sm} being the solubility coefficient.

Splitting into steady and harmonic components [4.39] gives, for the $x = 0$ surface:

$$[c_s(0) + c_o(0,t)]^2 = K_{sm}^2[p_s + p_o(t)] \qquad [4.41]$$

Remembering that harmonic components are fractionally small, [4.13], the steady and harmonic components may be written:

$$c_s(0) = K_{sm}p_s^{1/2}$$
$$2c_s(0)c_o(0,t) = K_{sm}^2 p_o(t) \qquad [4.42]$$

Hence :

$$c_o(0,t) = (K_{sm}/2\sqrt{p_s})p_o(t) \qquad [4.43]$$

Similarily for the $x = \ell$ exit surface , using [4.40]:

$$c_o(\ell,t) = (K_{sm}/2\sqrt{p'_s})p'_o(t) \qquad [4.44]$$

The above relationships are then contained in the following two matrix equations:

$$\begin{bmatrix} p \\ J^g \end{bmatrix} = \begin{bmatrix} 2\sqrt{p_s}/K_{sm} & 0 \\ 0 & 1 \end{bmatrix}\begin{bmatrix} c(0) \\ J(0) \end{bmatrix} = Z\begin{bmatrix} c(0) \\ J(0) \end{bmatrix} \qquad [4.45]$$

$$\begin{bmatrix} c(\ell) \\ J(\ell) \end{bmatrix} = \begin{bmatrix} K_{sm}/2\sqrt{p'_s} & 0 \\ 0 & 1 \end{bmatrix}\begin{bmatrix} p' \\ J^{g'} \end{bmatrix} = Z'\begin{bmatrix} p' \\ J^{g'} \end{bmatrix} \qquad [4.46]$$

from which the phase boundary matrices Z and Z' may be identified.

4.3.3. The entry and exit matices, Q and Q', for diffusion limited permeation.

(1) The entry matrix , Q:

In an experiment driven by pressure modulations the input variable y is the specified pressure variation p.Thus from [4.18]:

$$y = p = Q\begin{bmatrix} p \\ J^g \end{bmatrix} = [1\ 0]\begin{bmatrix} p \\ J^g \end{bmatrix} \qquad [4.47]$$

which identifies the entry matrix Q.

(2) The exit matrix Q':

Pressure modulations in the output chamber are influenced in amplitude and phase by the chamber volume,the characteristics of the pump used ,and outgassing from the chamber walls. Changes of pressure are modelled by:

$$V\frac{dp'}{dt} = \sigma J^{g'} + Q_{og} - Sp' \qquad [4.48]$$

where $\sigma = \gamma RT$.

Splitting [4.48] into steady state and harmonic parts as before gives:

$$p_s' = \frac{1}{S}(\sigma J_s + Q_{og}) \qquad [4.49]$$

and:

$$V\frac{dp'}{dt} = \sigma J^{g'} - Sp' \qquad [4.50]$$

so:

$$Jg' = \frac{1}{\sigma}(S + i\omega V)p' \qquad [4.51]$$

Using the exit pressure p' as the detection variable, it follows from [4.18] that the exit matrix, Q',is defined by:

$$N^{g'} = \begin{bmatrix} 1 \\ (S + i\omega V)/\sigma \end{bmatrix}(p') = Q'(p') \quad [4.52]$$

4.3.4 Solution for diffusion limited permeation.

Using the results obtained above the quotient R can be evaluated to describe a pressure modulation experiment:

$$R = p/p' = QZVZ'Q'$$

$$= [1\ 0]\begin{bmatrix} 2p_s^{1/2}/K_{sm} & 0 \\ 0 & 1 \end{bmatrix}\begin{bmatrix} \cosh a\ell & (1/Da)\sinh a\ell \\ Da\sinh a\ell & \cosh a\ell \end{bmatrix}$$

$$\cdot\begin{bmatrix} K_{sm}/2p_s'^{1/2} & 0 \\ 0 & 1 \end{bmatrix}\begin{bmatrix} 1 \\ (S + i\omega V)/\sigma \end{bmatrix}$$

$$= \left[\frac{p_s}{p_s'}\right]^{1/2}\cosh a\ell + \frac{2p_s^{1/2}}{\sigma DK_{sm}}(S + i\omega V)\frac{\sinh a\ell}{a} \quad [4.53]$$

This is a solution that applies for all pressures. Actual experiments will normally be conducted with $p_s \gg p_s'$ and in the present work this condition is always observed. The following sub-section shows a simplification which may be used when this condition prevails.

4.3.5 Particular solution for transmission of pressure modulations with a rapidly pumped output chamber.

When the output chamber pressure is low, that is when $p'_s < p_s$, the basic assumption of rapid surface reaction means that Richardson's law of permeation applies in the form:

$$J_s = \frac{P_m p_s^{1/2}}{\ell} ; \quad P_m = DK_{sm} \qquad [4.54]$$

where P_m is the permeability.

Together with the pumping equation [4.49], [4.53] may be written:

$$R = \left[\frac{p_s}{p'_s}\right]^{1/2}\left\{\cosh a\ell + 2\left[\frac{p_s}{p'_s}\right]^{1/2}\left[\frac{S + i\omega V}{S}\right]\right.$$

$$\left.\cdot\left[\frac{1}{1 - Q_{og}/Sp'_s}\right]\frac{\sinh a\ell}{a\ell}\right\} \qquad [4.55]$$

Since $p_s \gg p'_s$, the $\cosh a\ell$ term remains negligible and if $Q_{og} \to 0$ then:

$$R = \frac{2\sqrt{p_s}\ell}{\sigma P_m}.(S + i\omega V)\frac{\sinh(1 + i)\zeta}{(1 + i)\zeta} \qquad [4.56]$$

where the dimensionless frequency parameter ζ is introduced, such that:

$$\zeta = \ell(\omega/2D)^{1/2} \qquad [4.57]$$

The ratio R may then be written as:

$$R = \frac{p_s^{1/2}\ell}{DK_{sm}\zeta}\left[\frac{S + i\omega V}{\sigma}\right](1-i)$$

$$.(\sinh\zeta\cos\zeta + i\sin\zeta\cosh\zeta) \qquad [4.58]$$

This form of the equation will now be used, 4.3.5.1. and 4.3.5.2, for the interpretation of experimental data.

4.3.5.1 The variation of phase lag with frequency

From [4.10] the phase lag is $\Phi = Arg(R)$ so from [4.58]:

$$\Phi = \arctan\left[\frac{\tan\zeta}{\tanh\zeta}\right] - \frac{\pi}{4} + \text{arc tan}\left[\frac{\omega V}{S}\right] \qquad [4.59]$$

The final term, $\epsilon = \arctan(\omega V/S)$, is an equipment response time correction. By making the output chamber volume small and the pump speed sufficiently fast it is possible to ensure, even at the highest frequencies, that $\omega V \ll S$. For example: $T_{min} = 100s$; $V \approx 0.33$ l; and $S = 0.714\ ls^{-1}$ gives $\omega V \approx 0.02 \ll S$. The conditions, $\epsilon = 0$, is here referred to as the *hard pumping approximation* and it well describes the experimental conditions of the present work. In [4.59] it leads to:

$$\tan\Phi = \frac{\tan\zeta - \tanh\zeta}{\tan\zeta + \tanh\zeta} \qquad [4.60]$$

This functional relationship is of potential experimental importance since it is independent of K_{sm} and so allows direct experimental evaluation of a diffusion cofficient. The behaviour of the function is shown in fig 4.2, lower curve. Note that ζ has the value $\pi^{1/4}$ when the periodic time of the modulation equals the time ℓ^2/D, characterizing diffusion through the foil.

For higher frequencies, $\zeta > 3$, to a good approximation [4.60] reduces to:

$$\Phi = \zeta - \frac{\pi}{4} = \ell(\omega/2D)^{1/2} - \frac{\pi}{4} \qquad [4.61]$$

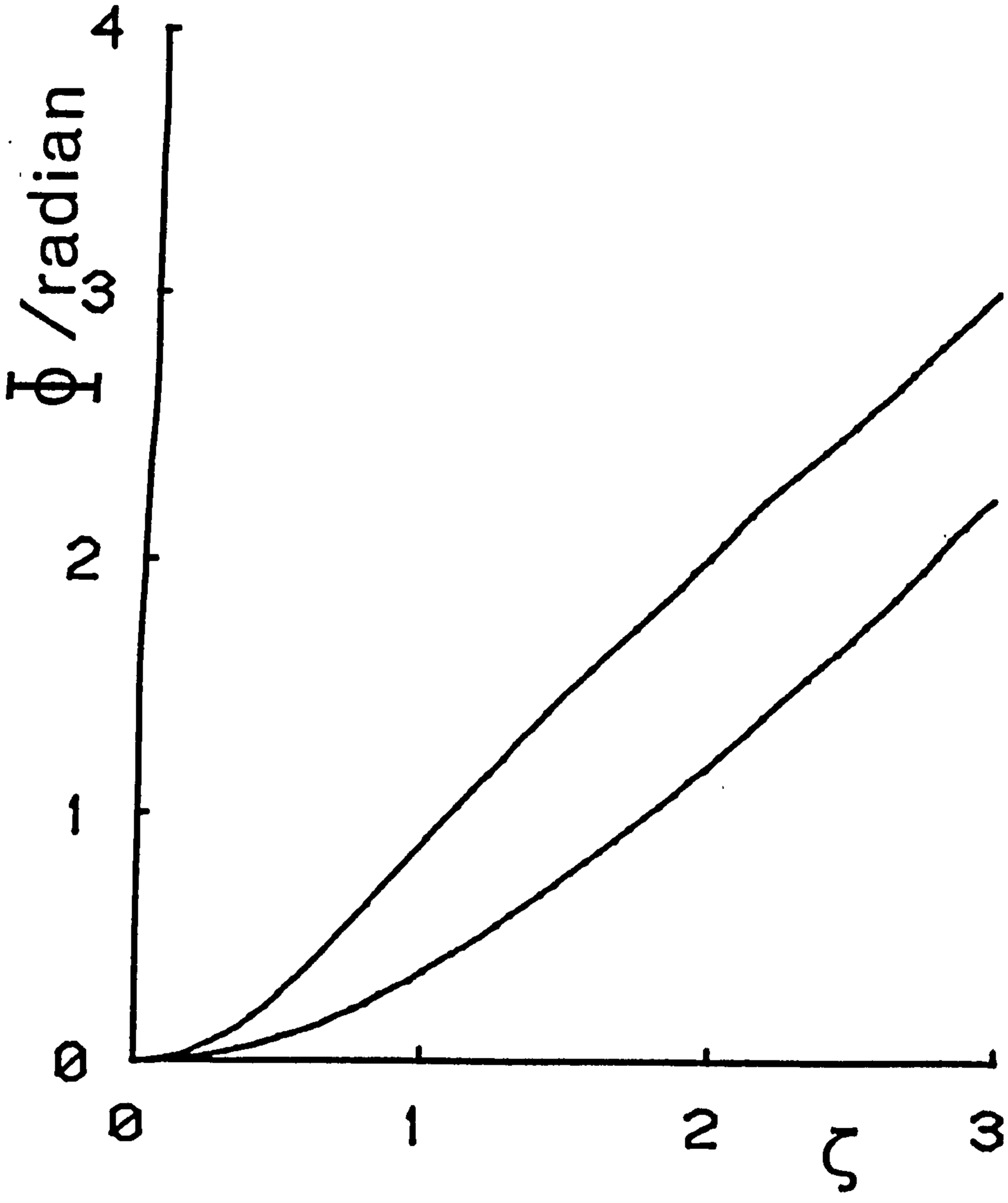

Fig 4.2 variation of phase lag Φ with frequency factor ς.
Lower curve : diffusion limited permeation for $p_g \gg p'_g$, zero backflow and $S \gg \omega V$, for pressure modulations, [4.60]. The high frequency region extrapolates back to $-\pi/4$ on the Φ-axis.
Upper curve : ion injection modulation for rapid pumping, $S \gg \omega V$, no backflow and fast surface reactions. The $+\pi/4$ phase shift, in comparison with the pressure modulatory case, at high frequencies,[4.128] and [4.60].

Thus, the phase lag varies linearly with $\omega^{1/2}$ at *high* frequencies and if this linear region is extrapolated back, it gives an intercept of $-\pi/4$ on the Φ axis. In the low frequency limit, expanding [4.60] in powers of ζ gives,to a good approximation, for values of $\zeta < 1/2$:

$$\Phi = \frac{\zeta^2}{3} = \frac{\ell^2\omega}{6D} \qquad [4.62]$$

Therefore the phase lag, Φ, varies linearly with ω for small phase angles.

4.3.5.2 The variation of modulation amplitude with frequency.

Measurement of pressure amplitudes also provides useful information about the permeation system. From [4.56]:

$$|R|^{-1} = \frac{DK_{sm}\zeta\sigma}{2p_s^{1/2}\ell}\left[\frac{1}{S^2 + (\omega V)^2}\right]^{1/4}\left[\frac{\sinh a\ell \sinh a^*\ell}{(1+i).(1-i)}\right]^{-1/2} \qquad [4.63]$$

It follows, using the hard pumping approximation $\omega V \ll S$:

$$|R|^{-1} = \frac{|p'|}{|p|} = \frac{DK_{sm}\sigma}{p_s^{1/2}S\ell}\,\frac{\zeta}{(\cosh 2\zeta - \cos 2\zeta)^{1/2}} \qquad [4.64]$$

This result is of importance in two ways. First, it provides a separate way of evaluating the diffusion coefficient and hence, by comparison with the phase data, gives an internal consistency check. Second, it allows evaluation of the permeability independent of the outgassing effects which can modify the precision of estimates based on the steady state pressures p_s and p'_s.

Equation [4.64] can be simplified. Introducing the variable Λ to represent the relative modulation amplitude ratio, then for $Q_{og} \to 0$:

$$\Lambda = \frac{|p'|}{p'_g}\frac{p_g}{|p|} = \frac{\zeta}{(\cosh 2\zeta - \cos 2\zeta)^{1/4}} \qquad [4.65]$$

This relationship is shown in fig 4.3: lower intercept. In the low frequency limit the right hand side of [4.65] reduces to ¼ and this constant value is a good approximation to the true curve over the range $0 < \zeta < \pi/4$. In the high frequency limit, [4.65] approaches the curve:

$$\Lambda = \zeta e^{(-\zeta)} \qquad [4.66]$$

The low frequency limit of the relative modulation amplitude ratio [4.65] has particular significance. Consider the permeation pressure law in the exponential form:

$$J^{g'} = kp^n$$

where the parameters k and n vary only slowly with pressure. On differentiating with respect to time, and taking the limit as $\omega \to 0$:

$$\frac{1}{J^{g'}}\frac{dJ^{g'}}{dt} = \frac{n}{p}\frac{dp}{dt}$$

therefore for sufficiently small modulation amplitudes:

$$\frac{|J^{g'}|}{J_g} = n\frac{|p|}{p_g}$$

Combining [4.49] and [4.51] in the limit $Q_{og} \to 0$, gives:

$$\Lambda = \frac{|p'|}{|p|}\frac{p_g}{p'_g} = n \qquad \text{(for } \omega \to 0\text{)} \qquad [4.67]$$

The relative modulation amplitude ratio, extrapolated back to zero frequency, is simply the exponent n in the generalized permeation pressure law. Thus for diffusion limited flow at small background

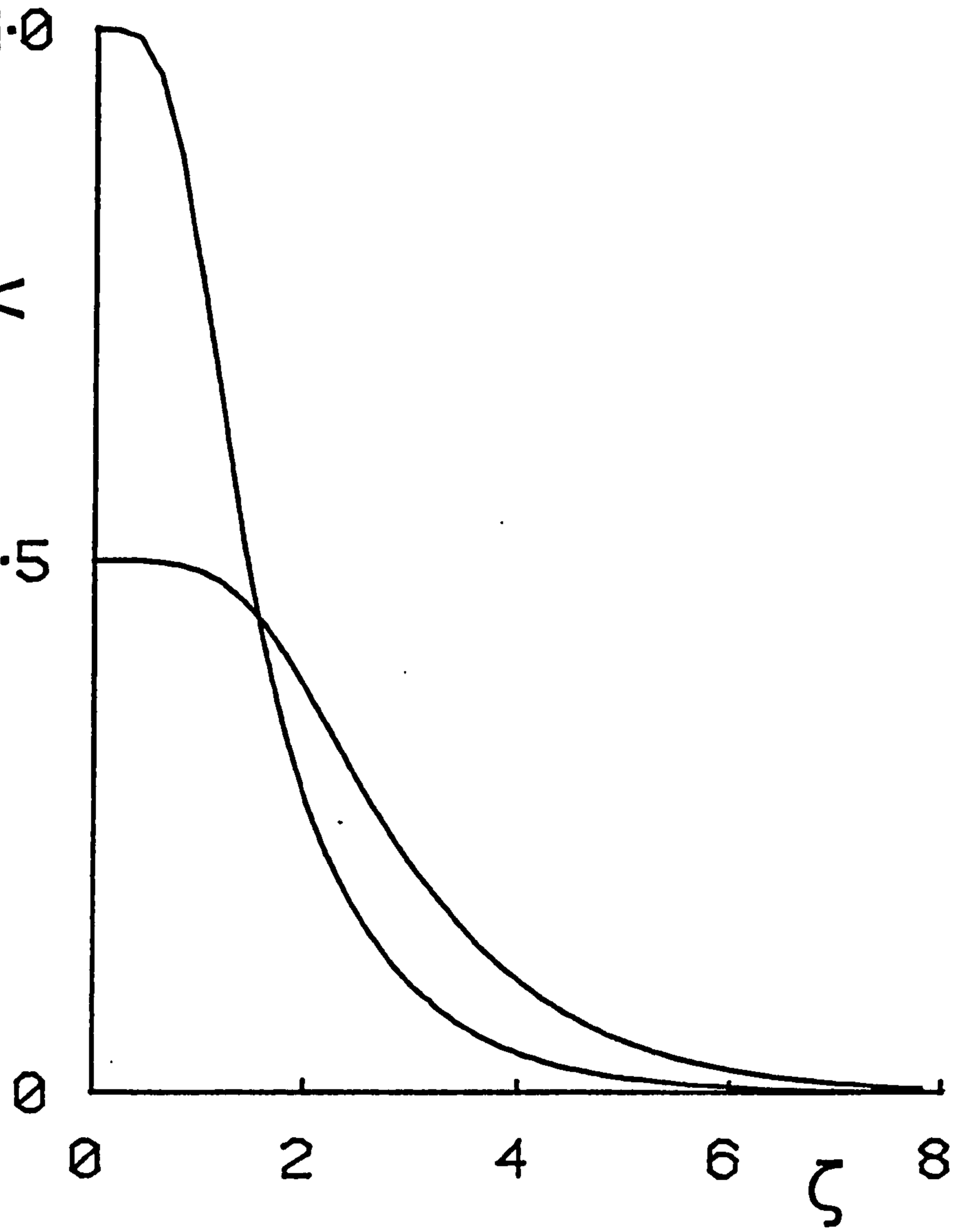

Fig 4.3 Variation of relative amplitude modulation ratio, $\Lambda = (|p'|p_g)/(p'_g|p|)$, with frequency factor ζ.
Lower intercept curve: diffusion limited permeation, rapid pumping, $p_g \gg p'_g$, $S \gg \omega V$, no backflow, $Q_{Og} \to 0$, for pressure modulations [4.65]. The intercept $\Lambda(\omega \to 0) = ½ = n$ where n is the exponent in the generalized permeation pressure law. Upper intercept curve: ion injection modulation for rapid pumping, $S \gg \omega V$, no backflow and fast surface reactions.

pressures, when Richardson's law of permeation applies, the extrapolation of Λ to the zero frequency axis should lead to the value $\frac{1}{2}$.

4.3.6 Summary of section 4.3.

Subject to the requirement that Fick's laws apply, the translation matrix coefficients are:

$$V = \begin{bmatrix} \cosh a\ell & (1/Da)\sinh a\ell \\ Da\sinh a\ell & \cosh a\ell \end{bmatrix}$$

A system in which the input pressure follows a specified harmonic pattern and surface reactions are so rapid that permeation is diffusion limited, may be described by the phase boundary matrices:

$$Z = \begin{bmatrix} 2\sqrt{p_s}/K_{sm} & 0 \\ 0 & 1 \end{bmatrix}$$

$$Z' = \begin{bmatrix} K_{sm}/2\sqrt{p'_s} & 0 \\ 0 & 1 \end{bmatrix}$$

and by the entry and exit matrices:

$$Q = [1\ 0]$$

$$Q' = \begin{bmatrix} 1 \\ (s + i\omega V)/\sigma \end{bmatrix}$$

The solution of prime experimental interest is that for a rapidly pumped output chamber, where $p_s \gg p'_s$. For this case the relationships between input and output pressures are:

$$R = \frac{p_s^{1/2}\ell}{DK_{sm}\zeta}\left[\frac{S + i\omega V}{\sigma}\right](1-i)$$

$$.(\sinh\zeta\cos\zeta + i\sin\zeta\cosh\zeta)$$

$$\tan\Phi = \frac{\tan\zeta - \tanh\zeta}{\tan\zeta + \tanh\zeta}$$

$$\Lambda = \frac{|p'|}{p'_s}\,\frac{p_s}{|p|} = \frac{\varsigma}{(\cosh 2\varsigma - \cos 2\varsigma)^{1/2}}$$

Points of interest which arise in considering these relationships are that:

(1) the phase lag, Φ,varies linearly with $\omega^{1/2}$ at high frequencies, $\varsigma > 3$. Extrapolating this linear region to the zero frequency axis gives an intercept of $-\pi/4$.

(2) the frequency variation of the relative modulation amplitude ratio, Λ, provides a separate method of determining the diffusion coefficient, D.

(3) the frequency variation of the amplitude ratio, $|R|^{-1}$, provides a method of evaluating P_m, completely independent of the output chamber background p'_s and hence free fom any background pressure problems.

(4) for $Q_{Og} \to 0$, $\Lambda(\omega \to 0) = n$ where n is the exponent in the generalized permeation pressure law.

4.4 TWO RATE CONSTANT SURFACE MODEL

The diffusion controlled permeation model described in the previous section owes its simplicity of analysis to the supposition that a continuing equilibrium exists between the solid and gas phase concentrations of diffusant; surface reactions are treated as having infinite speed. To incorporate the effect of finite reaction rates ,the following two rate constant model was devised. It has sufficient detail to describe deviations from equilibrium in the sub-surface concentrations and to describe the variation of permeation from a rate proportional to $p_g^{1/2}$ at high pressures, to one proportional to p_g at low pressures. However, it takes no account of any surface phase.

In this model the possible surface processes - adsorption, desorption, dissociation, association, solution and de-solution - are all described by the single reversible reaction:

$$H_2(\text{gas phase}) \underset{k_2c^2}{\overset{k_1p}{\rightleftharpoons}} 2H(\text{solid phase}) \quad [4.68]$$

where hydrogen is taken to be the diffusant gas and k_1 and k_2 are the rate constants.

In the formulation of earlier sections, a change in surface properties calls for a change only in the phase boundary matrices, Z and Z'. The coefficients describing the translation, V, entry, Q, and exit, Q', matrices are retained. In consequence following subsections will

describe the construction of new phase boundary matrices **Z** and **Z'**. These will then be used to provide a new expression for the vector pressure ratio, R, and derivative expressions for the frequency variations of the phase lag, Φ, the amplitude modulation ratio $|R|^{-1}$, and the relative amplitude modulation, Λ. The calculation will be made in the limit $p'_g/p_g \rightarrow 0$, which corresponds to the experimentally interesting condition of a rapidly pumped output chamber.

4.4.1 The phase boundary matrices Z and Z'.

From [4.68] the rate constants k_1, k_2, k'_1, k'_2 are such that at the entry surface:

$$J^g = k_1 p - k_2 c^2(0) = J(0) \qquad [4.69]$$

and at the exit surface:

$$J(\ell) = k'_2 c^2(\ell) - k'_1 p' = J^{g'} \qquad [4.70]$$

the, prime, being used to indicate that the exit surface coefficients may differ from those of the input.

At equilibrium, all fluxes are zero, $p = p'$, and for all x:

$$c(x) = K_{sm} p^{1/2}$$

specifically:

$$c(0) = c(\ell) = K_{sm} p^{1/2}$$

so, using [4.69] and [4.70], the rate constants are related by:

$$K_{sm} = (k_1/k_2)^{1/2} = (k'_1/k'_2)^{1/2} \qquad [4.71]$$

Since this model has only the two rate constants, it does not allow

surface accumulation. Therefore, in steady state flow, all the fluxes in [4.69] and [4.70] can be set equal to some particular value, J_s, giving:

$$c_s(0) = K_{sm}(p_s - J_s/k_1)^{1/2} \qquad [4.72]$$

$$c_s(\ell) = K_{sm}(p'_s + J_s/k'_1)^{1/2} \qquad [4.73]$$

Assuming Fick's law to hold, the flux within the foil is:

$$J_s = \frac{D}{\ell}[c_s(0) - c_s(\ell)] \qquad [4.74]$$

and so:

$$\frac{J_s\ell}{DK_{sm}} = (p_s - J_s/k_1)^{1/2} - (p'_s + J_s/k'_1)^{1/2} \qquad [4.75]$$

Consider now the flow equations [4.69],[4.70] modified by superposing a small modulation on the steady flow. Then with $|c(x)| \ll c_s(x)$ and $|J(x)| \ll J_s$ splitting into steady state and harmonic parts gives:

$$[J_s + J_o^g] = k_1(p_s + p_o) - k_2[c_s(0) + c_o(0)]^2$$
$$= [J_s + J_o(0)] \qquad [4.76]$$

$$[J_s + J_o(\ell)] = k'_2[c_s(\ell) + c_o(\ell)]^2 - k'_1(p'_s + p'_o)$$
$$= [J_s + J_o^{g'}] \qquad [4.77]$$

These last equations can be linearised to give, for the time dependent fluxes:

$$J^g = k_1 p - 2k_2 c_s(0)c(0) = J(0) \qquad [4.78]$$

$$J(\ell) = 2k'_2 c_s(\ell)c(\ell) - k'_1 p' = J^{g'} \qquad [4.79]$$

which, in matrix notation, is:

$$\begin{bmatrix} p \\ J^g \end{bmatrix} = \begin{bmatrix} 2k_2 c_s(0)/k_1 & 1/k_1 \\ 0 & 1 \end{bmatrix} \begin{bmatrix} c(0) \\ J(0) \end{bmatrix} \qquad [4.80]$$

and:

$$\begin{bmatrix} c(\ell) \\ J(\ell) \end{bmatrix} = \begin{bmatrix} k_1'/[2k_2'c_s(\ell)] & 1/[2k_2'c_s(\ell)] \\ 0 & 1 \end{bmatrix} \begin{bmatrix} p_g' \\ J^g \end{bmatrix} \quad [4.81]$$

Hence, using [4.16] and, [4.72] and [4.73] to substitute for $c_s(0)$ and $c_s(\ell)$, the phase boundary matrices, Z and Z', may be identified as:

$$Z = \begin{bmatrix} (2/K_{sm})(p_s - J_s/k_1)^{1/2} & 1/k_1 \\ 0 & 1 \end{bmatrix} \quad [4.82]$$

$$Z' = \begin{bmatrix} (K_{sm}/2)(p_s' + J_s/k_1')^{-1/2} & (K_{sm}/2k_1')(p_s' + J_s/k_1')^{-1/2} \\ 1 & 0 \end{bmatrix} \quad [4.83]$$

Using [4.35],[4.47],[4.52],[4.82] and [4.83] in [4.19] then, the solution for an input pressure modulated system with two surface rate constants is:

$$R = QZVZ'Q'$$

$$R = [1\ 0]\begin{bmatrix} 2/K_{sm}(p_s - J_s/k_1)^{1/2} & 1/k_1 \\ 0 & 1 \end{bmatrix}$$

$$\cdot\begin{bmatrix} \cosh a\ell & (1/Da)\sinh a\ell \\ Da\sinh a\ell & \cosh a\ell \end{bmatrix}$$

$$\cdot\begin{bmatrix} (K_{sm}/2)(p_s' + J_s/k_1')^{-1/2} & (K_{sm}/2k_1')(p_s' + J_s/k_1')^{-1/2} \\ 1 & 0 \end{bmatrix}$$

$$\cdot\begin{bmatrix} 1 \\ (S + i\omega V)/\sigma \end{bmatrix} \quad [4.84]$$

Before multiplying out terms, it is prudent to obtain Z' in a simplified form. This is detailed in the next subsection.

4.4.2 Pressure modulations when the output chamber is rapidly pumped and there is no backflow.

In experiments where the output chamber is pumped so rapidly that $p_s \ll p'_s$, it can be assumed that there is no significant backflow to the membrane from the diffusant in the output chamber. This allows [4.70] to be written as:

$$J(\ell) = k'_2 c^2(\ell) = J^{g'} \qquad [4.85]$$

This *no backflow* approximation also allows [4.73] to be written :

$$c_s(\ell) = K_{sm}(J_s/k'_1)^{1/2} \qquad [4.86]$$

so the steady state flow is now :

$$J_s\ell/P_m = (p_s - J_s/k_1)^{1/2} - (J_s/k'_1)^{1/2} \qquad [4.87]$$

therefore :

$$p_s = J_s\left[\frac{1}{k_1} + \frac{1}{k'_1} + \frac{2\ell}{P_m}(J_s/k'_1)^{1/2} + J_s(\ell/P_m)^2\right] \qquad [4.88]$$

Also [4.79] becomes :

$$J(\ell) = 2k'_2 c_s(\ell)c(\ell) = J^{g'} \qquad [4.89]$$

thus giving as the exit phase boundary matrix Z':

$$Z' = Z'_Z = \begin{bmatrix} 0 & (K_{sm}/2)(k'_1 J_s)^{-1/2} \\ 0 & 1 \end{bmatrix} \qquad [4.90]$$

where the suffix ,Z, is used to denote the zero backflow approximation.

To this approximation :

$$R = \mathbb{Q}\mathbb{Z}\mathbb{V}\mathbb{Z}'_Z\mathbb{Q}'$$

$$R = [1\ 0]\begin{bmatrix} 2/K_{sm}(p_s - J_s/k_1)^{1/2} & 1/k_1 \\ 0 & 1 \end{bmatrix}$$

$$\cdot\begin{bmatrix} \cosh a\ell & (1/Da)\sinh a\ell \\ Da\sinh a\ell & \cosh a\ell \end{bmatrix}$$

$$\cdot\begin{bmatrix} 0 & (K_{sm}/2)(k'_1 J_s)^{-1/2} \\ 0 & 1 \end{bmatrix}\begin{bmatrix} 1 \\ (S + i\omega V)/\sigma \end{bmatrix} \qquad [4.91]$$

Multiplying out terms shows R to have the general form:

$$R = [(e+if)\cosh a\ell + (g + ih)\sinh a\ell]\frac{S + i\omega V}{\sigma a\ell} \qquad [4.92]$$

with :

$$e = f = \zeta[(p_s - \frac{J_s}{k_1})^{1/2}(k'_1 J_s)^{-1/2} + \frac{1}{k_1}]$$

$$g = \frac{2\ell}{DK_{sm}}(p_s - \frac{J_s}{k_1})^{1/2} \qquad [4.93]$$

$$h = \zeta^2(\frac{DK_{sm}}{\ell k_1})(k'_1 J_s)^{-1/2}$$

Since $a\ell = (1+i)\zeta$, $\cosh a\ell$ and $\sinh a\ell$ can be expanded to give :

$$R = \frac{S + i\omega V}{\sigma a\ell}\begin{bmatrix} (e + if)(\cosh\zeta\cos\zeta + i\sinh\zeta\sin\zeta) \\ + (g + ih)(\sinh\zeta\cos\zeta + i\sin\zeta\cosh\zeta) \end{bmatrix} \qquad [4.94]$$

Using [4.10] for the phase shift ,Φ, the above gives :

$$\Phi = \arctan\left[\frac{e\tan\zeta\tanh\zeta + f + g\tan\zeta + h\tanh\zeta}{e - f\tan\zeta\tanh\zeta + g\tanh\zeta - h\tan\zeta}\right] + \epsilon - \frac{\pi}{4} \qquad [4.95]$$

where $\epsilon = \arctan(\omega V/S)$ is the equipment response time lag.

For the amplitude ratio, [4.94] gives:

$$|R| = \frac{|S + i\omega V|}{\sigma\zeta\sqrt{2}}\left[\begin{array}{l} (e^2 + f^2)|\cosh a\ell|^2 \\ + (g^2 + h^2)|\sinh a\ell|^2 + \\ 2\mathrm{Re}[(e+if)(g+ih)\cosh a\ell\sinh^* a\ell] \end{array}\right]^{1/2} \qquad [4.96]$$

hence :

$$|R| = \frac{(S^2 + \omega^2 V^2)^{1/2}}{2\sigma\zeta}\left[\begin{array}{l}(e^2+f^2+g^2+h^2)\cosh 2\zeta \\ +(e^2+f^2-g^2-h^2)\cos 2\zeta \\ +\ 2(eg + fg)\sinh 2\zeta \\ +\ 2(fg - eh)\sin 2\zeta\end{array}\right]^{1/2} \qquad [4.97]$$

Athough [4.95] and [4.97] with [4.93] are a complete description of the effect of surface rate constants on phases and amplitudes, they are not in a form which readily allows comparison. The difficulty is that, the coefficients e, f, g and h depend on *both* p_s and J_s.

To show how the transmitted modulation varies with pressure it is convenient to express the flux in dimensionless form and the rate constants in a form which describes those effects which vary with the symmetry of the foil surfaces.

To do this, mean rates $\overline{k_1}$, $\overline{k_2}$ are formed with :

$$\overline{k_1} = k_1 k_1'/(k_1 + k_1') \ ; \ \overline{k_2} = k_2 k_2'/(k_2 + k_2') \qquad [4.98]$$

and the symmetry of the surfaces is described by the dimensionless parameter, μ, defined by the equivalent expressions:

$$\mu = (k_1 - k_1')/(k_1 + k_1') = (k_2 - k_2')/(k_2+k_2') \qquad [4.99]$$

In this formulation the condition $\mu = 0$ corresponds to $k_1 = k_1'$, $k_2 = k_2'$ and identity in the properties of the surfaces of the foil. The condition $\mu = 1$ corresponds to $k_1 \gg k_1'$, and a flux determined by the exit surface; $\mu = -1$ corresponds to $k_1' \gg k_1$ and a flux determined by

the entry surface.

The flux is most conveniently put into dimensionless form, j, by dividing the steady state flux, J_s, by a reference flux, J_{ref}, such that :

$$j = J_s/J_{ref} \qquad [4.100]$$

To define J_{ref}, note first that in [4.87] at high pressures, $J_s \to \infty$, the steady state equation reduces to:

$$J_s(p \to \infty) = (P_m/\ell)p_s^{1/2} \qquad [4.101]$$

that is, to Richardson's law. At low pressures $J_s \to 0$, and [4.87] becomes:

$$J_s(p \to 0) = \overline{k_1}p_s \qquad [4.102]$$

Extrapolation of these two limiting curves [4.101], [4.102] shows them to intersect when $p_s^{1/2} = (P_m/\ell)/k_1$. The corresponding flux value is taken as the reference flux. That is:

$$J_{ref} = (P_m/\ell)^2/\overline{k_1} \qquad [4.103]$$

hence:

$$j = \overline{k_1}(\ell/P_m)^2 J_s \qquad [4.104]$$

Substitution into the steady state equation, enables the pressure to be written:

$$p_s = j(P_m/\overline{k_1}\ell)^2\{1 + [2j(1 + \mu)]^{1/2} + j\} \qquad [4.105]$$

and the parameters e, f, g, h become:

$$e = f = (\varsigma/2\overline{k_1})\{2 + [2j(1 + \mu)]^{1/2}\}$$

$$g = (1/\overline{k_1})\{2j + [2j(1 + \mu)]^{1/2}\} \qquad [4.106]$$

$$h = (\varsigma^2/2\overline{k_1})(1 - \mu)[(1 + \mu)/2j]^{1/2}$$

Of experimental interest is how the modulation amplitude and phase vary with frequency. The simplification of this section allows this readily to be done.

4.4.2.1 The variation of phase with frequency.

The phase-frequency relationship of [4.95] is illustrated in figure 4.4 for $\mu = 0$ and various values of j. Here, the principal characteristic is the increase in phase lag that accompanies a reduction in flux or pressure. This is a direct consequence of the changeover from n = ½ to n = 1 permeation. Analysis of the curves is simplified at high modulation frequencies for, with $\varsigma > 3$, $\sinh a\ell \approx \cosh a\ell \approx \exp(a\ell)$. From [4.94] it follows that :

$$R = [(e + g) + i(f+h)]\exp a\ell\frac{(S + i\omega V)}{(1 + i)\sigma\varsigma} \qquad [4.107]$$

Since this is in product form it again follows immediately that:

$$\Phi = \mathrm{Arg}[e + g + i(f + g)] + \mathrm{Arg}[\exp a\ell] + \epsilon - \frac{\pi}{4}$$

$$= \Phi_g + \varsigma + \epsilon - \frac{\pi}{4} \qquad [4.108]$$

where Φ_g represents phase changes within the surfaces at high

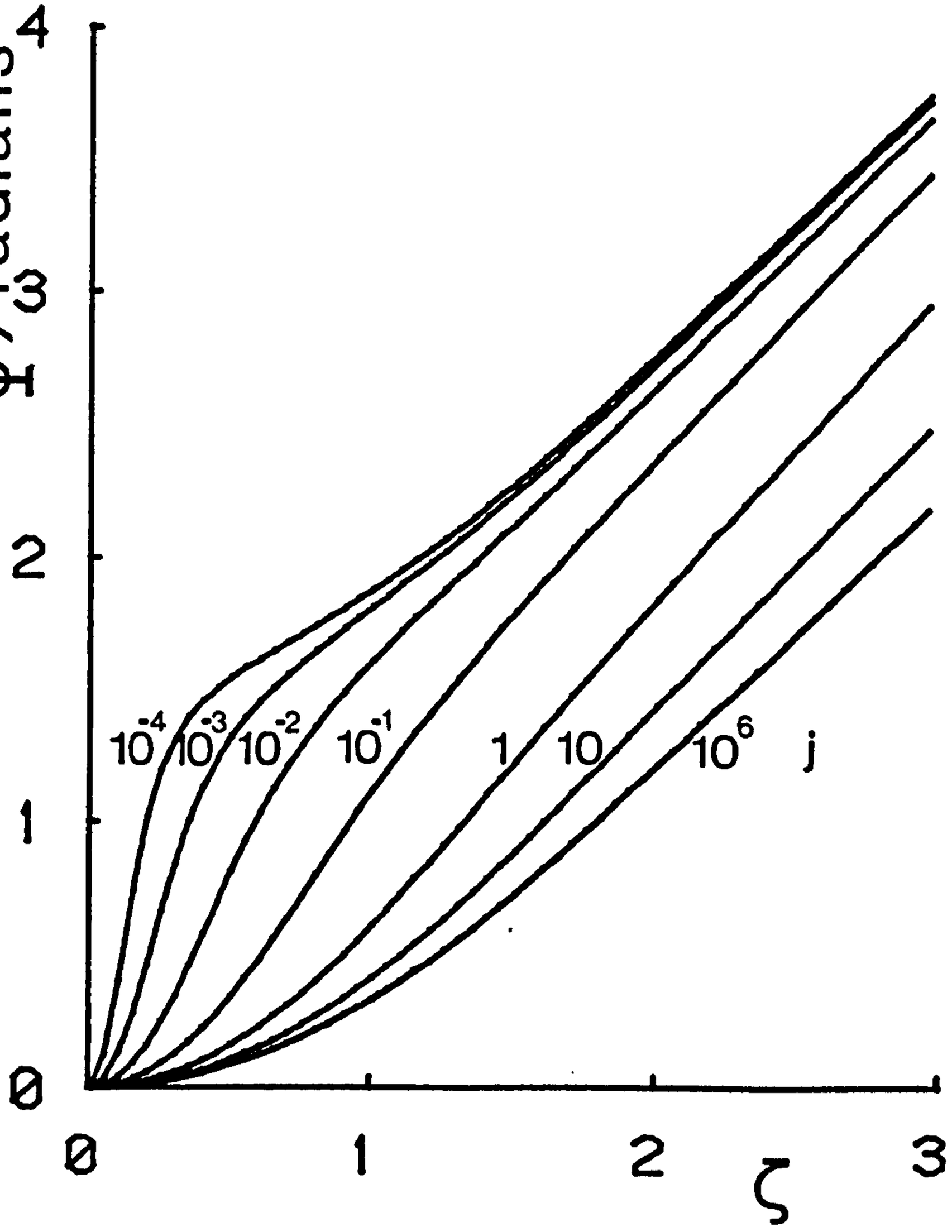

Fig 4.4 Variation of phase lag Φ with frequency factor ζ, [4.95], for the rapidly pumped two rate constant model. Curves are for symmetric surfaces, $\mu = 0$, and specified values of the dimensionless flux factor j. The curves demonstrate the $+\pi/2$ phase shift, $\pi/4$ per surface, from high flux diffusion limited permeation to low flux surface limited permeation.

frequencies. This surface phase lag may be evaluated for any specified surface condition.

To explore the pressure dependence of the surface phase, consider a flux limited by the input surface with $\mu = -1$. Then from [4.106] :

$$\Phi = \arctan[\varsigma/(\varsigma + 2j)] \qquad [4.109]$$

so at high pressures, when $j \gg 1$ and $n = \frac{1}{2}$, $\Phi_s = 0$: and at low pressures when $j \ll 1$ and $n = 1$, $\Phi_s = \pi/4$. Pressure reduction thus increases the phase lag by $\pi/4$. Other surface conditions result in other values for Φ_s. The principal point of note is that a single surface can produce a maximum phase change of $\pi/4$ on pressure variation whereas when both surfaces limit the flux a variation of $\pi/2$ is possible.

4.4.2.2 The variation of modulation amplitude with frequency.

The variation of modulation amplitude with frequency is best described in relative terms using the ratio, $\Lambda = |R|^{-1}(p_s/p_s')$. Neglecting equipment effects, $S \gg \omega V$, and assuming outgassing to be negligible, $Q_{og} \to 0$,it follows from [4.97] and [4.105] that :

$$\Lambda = \frac{2\varsigma/\sqrt{k_1}\{1 + [2j(1+\mu)]^{\frac{1}{2}} + j\}}{\left[\begin{array}{l}(e^2+f^2+g^2+h^2)\cosh 2\varsigma+(e^2+f^2-g^2-h^2)\cos 2\varsigma \\ +\ 2(eg + fh)\sinh 2\varsigma + 2(fg - eh)\sin 2\varsigma\end{array}\right]^{\frac{1}{2}}} \qquad [4.110]$$

This variation of relative amplitude modulation ratio, Λ, with frequency is shown in figure 4.5 for $\mu = 0$ and specified values of j.

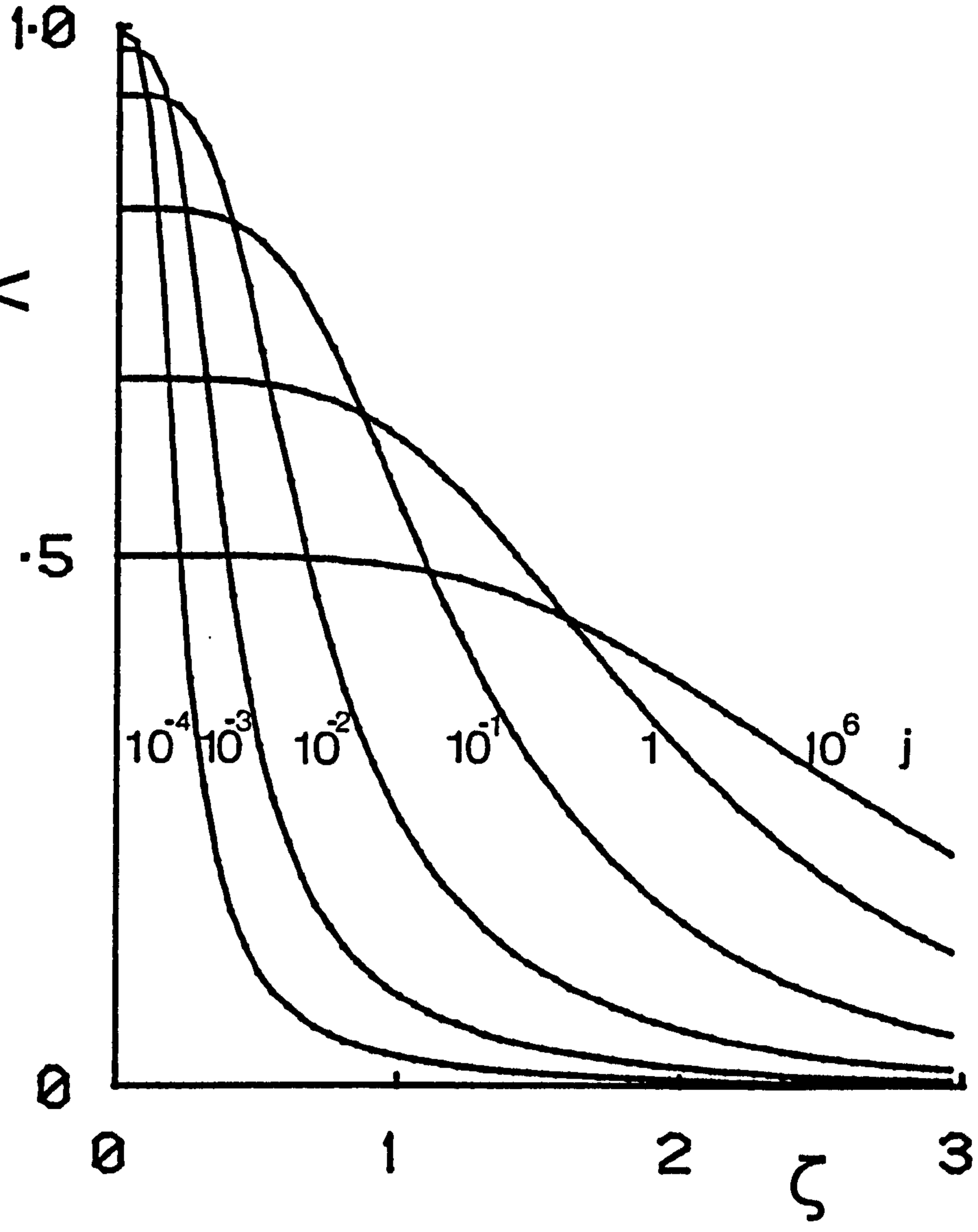

Fig 4.5 Variation of relative amplitude modulation ratio , Λ, with frequency factor ζ, [4.110], for the rapidly pumped two rate constant model. These curves are for symmetric surfaces, $\mu = 0$, and specified values of the dimensionless flux factor j and demonstrate the changeover of the power law index, at $\omega \to 0$, from ½ to 1 with decreasing flux. Notice the changeover in the low frequency region, where for increasing flux, Λ falls, while in the high frequency region Λ increases.

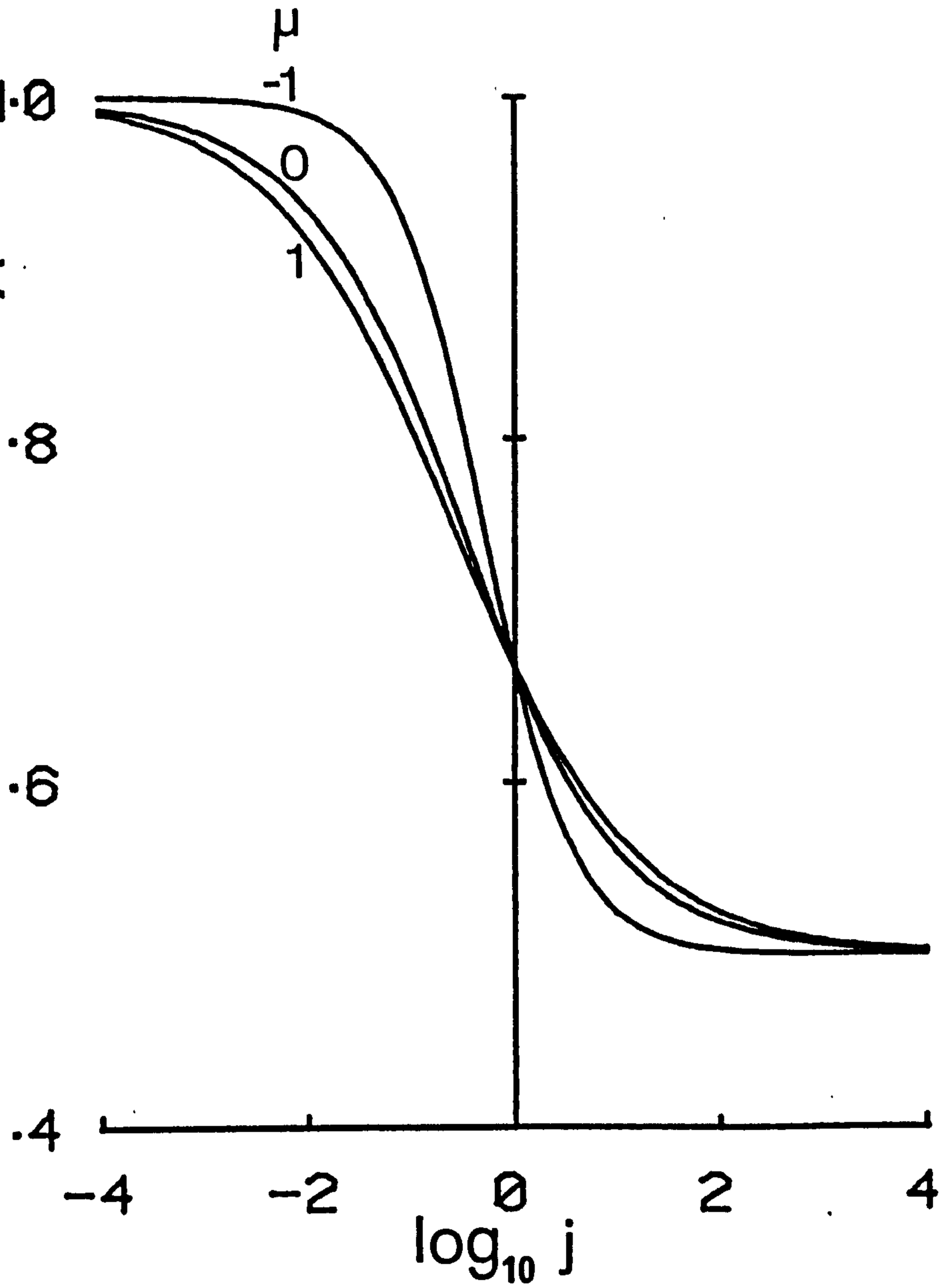

Fig. 4.6 Variation of relative modulation amplitude $\Lambda(\omega \to 0)$ with the dimensionless flux factor j,[4.104]. The curves are for specified μ and illustrate the fall of the power law index, n, from 1 to ½ as the flux is increased; this represents the approach to diffusion limited permeation.

Its characteristic feature is the changeover from a low frequency region where Λ falls with increasing pressure to a high frequency region when Λ increases with increasing pressure.

The value of Λ as $\omega \to 0$ is an especially useful indicator of the permeation process and, as described in the previous section, $\Lambda(\omega \to 0) = n$, where n is the power law index. This equality is subject to the condition that the outgassing terms can be ignored.

From [4.107] then, when $\omega \to 0$, one finds:

$$\Lambda(\omega \to 0) = \frac{\{1 + [2j(1+\mu)]^{1/2} + j\}}{\{1 + (3/2)[2j(1+\mu)]^{1/2} + 2j\}} \qquad [4.111]$$

The form of this variation is shown in figure 4.6 for $\mu = 0$ and $\mu = \pm 1$. It shows a gradual changeover in the power law index from the diffusion limited, high flux value of ½, when $j \gg 1$, to the surface limited, low flux value of 1, when $j \ll 1$. In passing it is of interest to note that when $j = 1$, that is when the flux is equal to the reference flux, $n = 2/3$ for all values of μ.

4.4.2 Summary of the two rate constant model.

For the two rate constant model, subject to the requirements that Fick's laws apply, the translation matrix coefficients remain as defined in section 4.3 and are :

$$\mathbf{V} = \begin{bmatrix} \cosh a\ell & (1/Da)\sinh a\ell \\ Da\sinh a\ell & \cosh a\ell \end{bmatrix}$$

When surface reaction rates are described by the single reaction H_2(gas phase) $\rightleftharpoons$ 2H(solid phase) the phase boundary matrices become:

$$\mathbf{Z} = \begin{bmatrix} (2/K_{sm})(p_s - J_s/k_1)^{1/2} & 1/k_1 \\ 0 & 1 \end{bmatrix}$$

$$\mathbf{Z'} = \begin{bmatrix} K_{sm}/2(p'_s + J_s/k'_1)^{-1/2} & K_{sm}/2k'_1(p'_s + J_s/k'_1)^{-1/2} \\ 0 & 1 \end{bmatrix}$$

When the input pressure follows a specific harmonic modulation and the output chamber is pumped at a fixed rate the entry and exit matrices return to the form:

$$\mathbf{Q} = [1 \quad 0]$$

$$\mathbf{Q'} = \begin{bmatrix} 1 \\ (S + i\omega V)/\sigma \end{bmatrix}$$

and the exit matrix may be simplified to :

$$\mathbf{Q'} = \begin{bmatrix} 1 \\ S/\sigma \end{bmatrix}$$

for $S \gg \omega V$. Under the conditions of zero backflow and rapid pumping the input and output pressures are related by:

$$R = \begin{bmatrix} (e + if)(\cosh\varsigma\cos\varsigma + i\sinh\varsigma\sin\varsigma) \\ + (g + ih)(\sinh\varsigma\cos\varsigma + i\sin\varsigma\cosh\varsigma) \end{bmatrix}$$

$$\Phi = \arctan\left[\frac{e\tan\varsigma\tanh\varsigma + f + g\tan\varsigma + h\tanh\varsigma}{e - f\tan\varsigma\tanh\varsigma + g\tanh\varsigma - h\tan\varsigma}\right] + \epsilon - \frac{\pi}{4}$$

$$\Lambda = \frac{2\varsigma/\overline{k_1}\{1 + [2j(1+\mu)]^{1/2} + j\}}{\left[\begin{matrix}(e^2+f^2+g^2+h^2)\cosh 2\varsigma + (e^2+f^2-g^2-h^2)\cos 2\varsigma \\ + 2(eg + fh)\sinh 2\varsigma + 2(fg - eh)\sin 2\varsigma\end{matrix}\right]^{1/2}}$$

It follows from these relationships that:

(1) for the phase lag, Φ, the flux frequency dependence shows that pressure variations can produce a maximum phase shift of $+\pi/4$ for a single surface at high frequencies. Thus as $p \rightarrow \infty$, the model predicts the same flux independent, diffusion limited, permeation described in the previous section and a high frequency extrapolation to $-\pi/4$ on the Φ-axis. At low pressures, $p \rightarrow 0$, when both surfaces limit flow, a $+\pi/2$ phase shift will occur and the high frequency variation extrapolates to $+\pi/4$ on the Φ-axis.

(2) for the relative amplitude modulation ratio Λ, the flux frequency dependence shows that $\Lambda(\omega \rightarrow 0)$,hence the power law index, rises from ½ to 1 with reduction of flux: the limit $\Lambda(\omega \rightarrow 0) = ½$ corresponds to $p \rightarrow \infty$ and flux independent, diffusion limited, permeation; $\Lambda(\omega \rightarrow 0) = 1$ corresponds to $p \rightarrow 0$ and surface dominated permeation. This change in the permeation law index is characterised by Λ falling with increased pressure in the low frequency region while Λ increases for increased pressure in the high frequency region.

The model described clearly represents a simplification of the possible surface processes. It has sufficient detail to describe deviations from equilibrium in the subsurface concentrations and to describe the variation of permeation from a $p^{½}$ law at high pressures, to a p^{1} law at low pressures. The model does not have sufficient structure to describe surface accumulation of diffusant and cannot be expanded to do so without a full re-evaluation of the interphase matrices with additional coefficients.

4.5 ION BEAM INJECTION

Ion guns provide an interesting alternative to pressure modulation as a means of producing a modulating flux of diffusant through a specimen. The main feature of a flux having this origin, is that diffusant may be expected to enter the specimen at a rate which is independent of chemical reactions at the input surface. This opens up the possibility of determining the rates of surface reaction for a single surface.

To model this possibility the following suppositions are made:

(1) The beam injects diffusant past the input surface but to a depth that is small relative to the specimen thickness.

(2) Ion injection does not affect the flow of diffusant inside the specimen or conditions on the exit surface.

(3) The usual condition of zero backflow applies.

In the following sub-sections, expressions are derived for Φ and Λ for an experiment in which the output surface rate coefficient is high; there are no surface hold ups.

4.5.1 The experimental values y,y'.

With ion beam injection the input variable y is now chosen to be the ion current, I, instead of the input pressure, such that:

$$y = I \qquad [4.121]$$

The output variable remains as before, y' = p.

4.5.2 The ion beam input matrix $\mathbb{Q}_{ion}$.

Since the beam is assumed to place diffusant straight into the body of the specimen, and provided that the input chamber pressure is sufficiently low, it is unnecessary to retain the usual input phase boundary matrix, $\mathbb{Z}$. Instead:

$$R = \frac{y}{y'} = \frac{I}{p'} = \mathbb{Q}_{ion}\mathbb{V}\mathbb{Z}'\mathbb{Q}' \qquad [4.122]$$

The matrix $\mathbb{Q}_{ion}$, now links the modulated ion beam current directly to the subsurface condition vector $\mathbb{N}(0)$. That is:

$$I = \mathbb{Q}_{ion}\begin{bmatrix} c(0) \\ J(0) \end{bmatrix} \qquad [4.123]$$

To construct $\mathbb{Q}_{ion}$ it is assumed that the flux just below the surface of this model, J(0), is equal to some fraction, α, of the total beam hitting the surface. That is:

$$\mathbb{Q}_{ion} = [\ 0 \quad 1/\alpha] \qquad [4.124]$$

4.5.3 The matrices $\mathbb{V},\mathbb{Z}',\mathbb{Q}'$.

Since the injection conditions should not affect the flow of diffusant

inside the specimen or conditions at the exit surface, the matrices $\mathbb{V},\mathbb{Z}',\mathbb{Q}'$ retain the coefficients found for the case of pressure modulation; [4.35],[4.46] and [4.52] respectively. This allows the quotient R to be evaluated as follows:

$$R = [0 \quad 1/\alpha]\begin{bmatrix}\cosh a\ell & (1/Da)\sinh a\ell \\ Da\sinh a\ell & \cosh a\ell\end{bmatrix}$$

$$\cdot\begin{bmatrix}K_{sm}/(2p'^{1/2}_s) & 0 \\ 0 & 1\end{bmatrix}\begin{bmatrix}1 \\ (S + i\omega V)/\sigma\end{bmatrix}$$

$$= \frac{1}{\alpha}\left[\frac{K_{sm}}{2p'^{1/2}_s}\right]Da\sinh a\ell + \frac{1}{\alpha\sigma}(S + i\omega V)\cosh a\ell \qquad [4.125]$$

This expression will be considered in detail in the following subsection.

4.5.4 The current-pressure ratio for a modulated ion injection experiment.

The characteristics of an ion injection experimont are best explored by comparison with the expression derived earlier for pressure modulations. Since the subsurface diffusant concentrations are supposed to maintain equilibrium with the adjacent gas, it follows that $c(\ell) \approx 0$. Thus $\mathbb{Z}'$ is:

$$\mathbb{Z}' = \begin{bmatrix}0 & 1 \\ 0 & 0\end{bmatrix}$$

and the $\sinh a\ell$ term in [4.125] disappears. Hence, for $S \gg \omega V$:

$$R = \frac{S}{\sigma\alpha}\cosh a\ell$$

which in terms of ς is:

$$R = \frac{S}{\sigma\alpha}(\cosh\varsigma\cos\varsigma + i\sinh\varsigma\sin\varsigma) \qquad [4.126]$$

4.5.4.1 Phase lag of output pressure with respect to gun current.

From [4.126] and [4.10] it follows that that:

$$\Phi = \arctan(\tanh\varsigma\tan\varsigma) \qquad [4.127]$$

and since for $\varsigma > 3$, $\tanh\varsigma \to 1$, then:

$$\Phi \simeq \varsigma = \ell(\omega/2D)^{1/2} \qquad [4.128]$$

At these high frequencies, therefore, Φ varies linearly with $\omega^{1/2}$, extrapolating back to 0 on the Φ-axis. Comparison with the pressure modulation case, for diffusion limited permeation at high frequencies [4.61],shows that the ion injection experiment causes a $+\pi/4$ phase shift, at these frequencies. This is illustrated in figure 4.2.

4.5.4.2 Ratio of output pressure to gun current.

From [4.126] and [4.11] it follows that a relative modulation amplitude ratio, Λ', may be derived. It may be written:

$$\Lambda' = \frac{|p'|}{p'_s}\frac{I_s}{|I|} = \frac{\sqrt{2}}{(\cosh 2\varsigma + \cos 2\varsigma)^{1/2}} \qquad [4.129]$$

This curve is shown in figure 4.3 along with that from the pressure modulation, diffusion limited, permeation curve. Notice that for $\omega \to 0$:

$$\Lambda(\omega \to 0) = 1 \qquad [4.130]$$

4.5.5 Summary of the ion gun injection section.

Ion injection experiments have the potential to provide measurements of diffusion coefficients and exit surface rate constants. Points of note are:

(1) The frequency variation of the phase lag and the modulation amplitude have characteristic forms that may be used to provide estimates of the diffusion coefficient which should be independent of input surface conditions.

(2) The ion injection experiment produces a $+\pi/4$ phase shift for high frequencies relative to pressure modulation experiments.

(3) The relative amplitude modulation ratio at zero frequency, $\Lambda(\omega \rightarrow 0)$ has a value of 1 as opposed to the value ½ for the diffusion limited pressure modulation experiment.

4.6 PARALLEL DIFFUSION

When specimens are mounted using the internal furnace configuration of section 3.3, there is inevitably a spurious diffusant flux, through the walls of the support tube, from the input to the output chamber. This flux is subject to modulation and so influences the observed phase and amplitude of the pressure in the output chamber. It is therefore prudent to calculate how such effects modify the measured values of Φ and Λ.

To model this effect suppose that:

(1) the flux passing through the support walls is confined to an area γ_2 which is maintained by the furnace at a uniform temperature.

(2) the thickness of the support walls is ℓ_2, where the subscript, $_2$, is used generally to denote variables related to the wall flux.

(3) the walls are the same material as the specimen and are at the same temperature as the specimen, thus $P_{m1} = P_{m2}$.

(4) permeation is diffusion limited.

(5) conditions are such that pumping is rapid, $p_g \gg p'_g$, with no backflow; outgassing is at a low rate, $Q_{og} \to 0$; and the equipment response time is negligible, $S \gg \omega V$.

With these conditions the pumping equation is:

$$\sigma_1 J_1{}^{g'} + \sigma_2 J_2{}^{g'} = Sp' \qquad [4.113]$$

From [4.56], it is easily shown that, for i = 1,2:

$$J_i^{g'} = pP_{mi}\left[2\ell_i\sqrt{P_s}\frac{\sinh(1+i)\zeta_i}{(1+i)\zeta_i}\right]^{-1} \qquad [4.114]$$

Therefore:

$$\left[\frac{\sigma_1 P_{m1}(1+i)\zeta_1}{\ell_1\sinh(1+i)\zeta_1} + \frac{\sigma_2 P_{m2}(1+i)\zeta_2}{\ell_2\sinh(1+i)\zeta_2}\right]\frac{p}{2p_s{}^{1/2}} = Sp' \qquad [4.115]$$

Rearranging and defining $\kappa_i = \sigma_i P_{mi}/(2Sp_s{}^{1/2}\ell_i)$ then:

$$R^{-1} = (1+i)\left[\frac{\kappa_1\zeta_1(\sinh\zeta_1\cos\zeta_1 - i\sin\zeta_1\cosh\zeta_1)}{\cosh^2\zeta_1 - \cos^2\zeta_1} + \frac{\kappa_2\zeta_2(\sinh\zeta_2\cos\zeta_2 - i\sin\zeta_2\cosh\zeta_2)}{\cosh^2\zeta_2 - \cos^2\zeta_2}\right] \qquad [4.116]$$

4.6.1 Effect of parallel diffusion on the phase lag, Φ.

Using [4.10], supposition (5) gives for Φ:

$$\Phi = \tan^{-1}\left[\frac{\kappa_1\Psi_1\sin\zeta_1\cosh\zeta_1 + \kappa_2\Psi_2\sin\zeta_2\cosh\zeta_2}{\kappa_1\Psi_1\sinh\zeta_1\cos\zeta_1 + \kappa_2\Psi_2\sinh\zeta_2\cos\zeta_2}\right] - \frac{\pi}{4} \qquad [4.117]$$

where $\Psi_i = \zeta_i/(\cosh^2\zeta_i - \cos^2\zeta_i)$.

In terms of an experiment ζ_1 is actually the conventional frequency parameter ζ, so if A and B are defined as:

$$A = \frac{\zeta_2}{\zeta_1} = \frac{\ell_2}{\ell_1} \qquad [4.118]$$

$$B = \frac{\kappa_2}{\kappa_1} = \frac{\sigma_2 P_{m2}\ell_1}{\sigma_1 P_{m1}\ell_2} = \frac{\sigma_2\ell_1}{\sigma_1\ell_2} \qquad [4.119]$$

the frequency variation of the phase lag may be evaluated for given A and B.

The variation of Φ with ς_1 is plotted in figure 4.8 using parameters appropriate to the range of experimental conditions considered. A is set at 5.33 which corresponds to the worst possible case experimentally envisaged, that of a 0.3mm thick specimen supported by a 1.6mm thick wall. The maximum and minimum, of figure 4.7 are characteristic and obviously affect the curve fitting procedure from which the correct diffusion coefficients derived. A point to note is that the correction is only important at low frequencies: for frequencies above the minimum point, ς_{min}, the curve returns to that of flow limited by the specimen alone. This can be seen in figure 4.7 where, for A = 5.33, the position of ς_{1min} is close to 1.4 irrespective of the value of B. Therefore analysis of this high frequency region, once identified, provides the correct single diffusion coefficient D.

4.6.2 Effect of parallel diffusion on Λ

Amplitude data is also changed by parallel flows. Using [4.116] and supposition (5) gives for Λ:

$$\Lambda = [(\Psi_1 \sinh\varsigma_1 \cos\varsigma_1 + B\Psi_2 \sinh\varsigma_2 \cos\varsigma)^2 + (\Psi_1 \sin\varsigma_1 \cosh\varsigma_1 + B\Psi_2 \sin\varsigma_2 \cosh\varsigma)^2]^{1/2} . [1/(1+B)] \qquad [4.120]$$

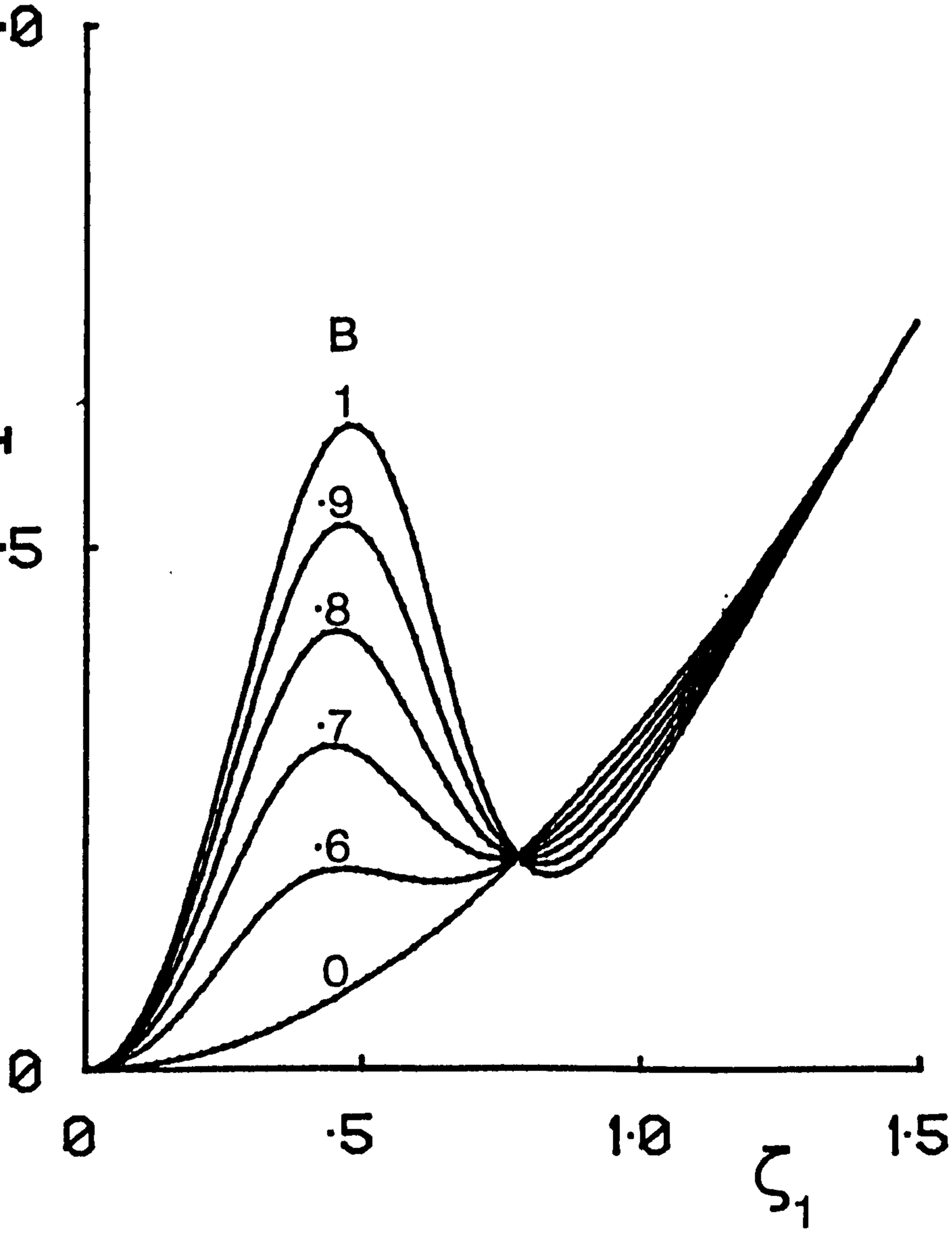

Fig 4.7 Variation of phase lag Φ with the frequency factor ζ_1, for specified values of B, in the parallel diffusion model, [4.117].

The parameter A is set at 5.33 typifying a 3×10^{-4}m thick specimen supported by a 1.6×10^{-3}m wall. The phase lag Φ returns to simple diffusion values for $\zeta_1 > 1.4$.

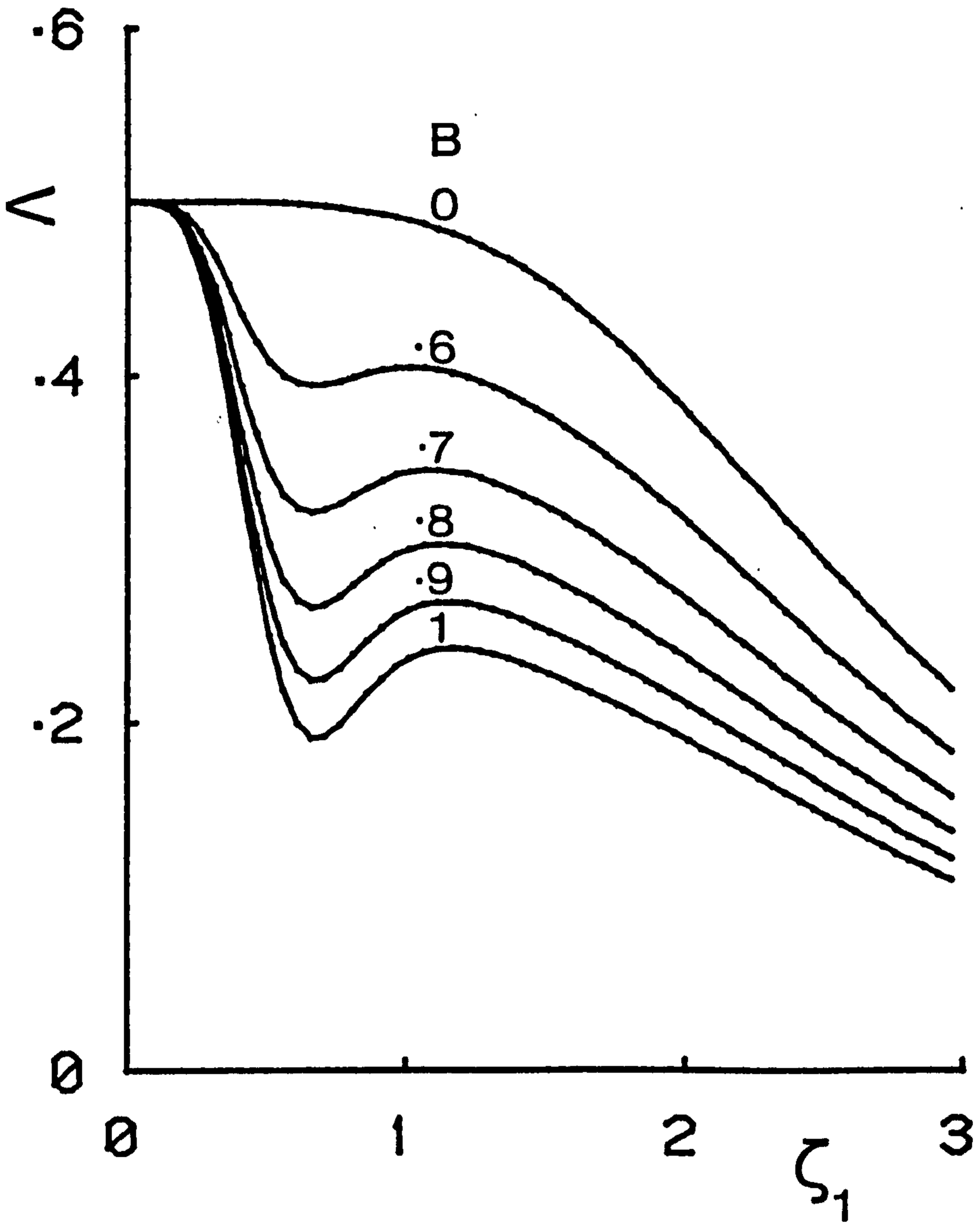

Fig 4.7 Variation of relative amplitude modulation ratio , Λ, with the frequency factor ζ_1, for specified values of B, in the parallel diffusion model,[4.120]. the parameter A is set at 5.33, typifying a 3×10^{-4}m thick specimen supported by a 1.6×10^{-3}m wall.

For this case the indicator of parallel diffusion is the minimum in the curve, figure 4.8.

An unfortunate effect of parallel diffusion is that the low frequency limit, $\Lambda(\omega \to 0) = n$, deviates from its conventional extrapolated value except at frequencies too low for experimental investigation. The variation of $|R|^{-1}$ with ς_1, however, is subject to simple diffusion limitation for $\varsigma_1 > \varsigma_{1min}$, and allows uncorrupted values of D and P_m to be obtained, for this high frequency region.

4.6.3. Discussion of parallel diffusion.

The clear characteristics of parallel diffusion enable it to be easily detected. The uncertainties of D and P_m, introduced by this effect, can be avoided by:

(1) taking steps to increase A and lower B such that the effect can be treated as negligible; increasing the ratio of the specimen to wall hot zone surface area and/or increasing the ratio of wall to specimen thickness ratio.

(2) conducting experiments within the high frequency region determined by $\varsigma_1 > \varsigma_{1min}$.

Confirmation that the above parallel diffusion model correctly predicts

phase and amplitude deviations is provided in chapter 5 where a specimen in the internal configuration and A = 5.33, with the cylindrical furnace displaced to create a large area, γ_2 at the specimen temperature was investigated at low frequencies. It showed all the predicted phenomena.

4.6.3 Summary of parallel diffusion.

Parallel diffusion processes may confuse data taken from modulation experiments. The characteristics of these processes allow experimental detection, and awareness of the phenomenon suggests how its effects may be reduced. Points of note are:

(1) The variation of Φ with ς_1 produces a maximum and minimum in the low frequency region. The magnitude and frequency span of this effect depends on the parameters contained within A and B. This curve reverts to that for simple diffusion for $\varsigma_1 > \varsigma_{1min}$.

(2) The variation of Λ with ς_1 produces a characteristic curve with a maximimum and a minimum. The absolute value of Λ does not return to that for simple diffusion for high ς but that for $|R|^{-1}$ does.

(3) When a specimen is to be used in the internal furnace configuration precautions should be taken to ensure that the parameters A and B are set to produce only minor effects. Even when parallel diffusion is significant, it is still possible to obtain the parameters of permeation from the high frequency region of the phase and amplitude curves.

4.7 SUMMARY OF CHAPTER 4

A matrix notation may be used to relate the input and output observables. It may be applied to the description of modulated fluxes generated by variations of pressure or ion beam bombardment.

For the particular case of rapid pumping and no backflow, simple theoretical relationships exist between the modulation vectors of the input and output chambers when using models based on diffusion limited flow, flows described by two surface rate constants and flows generated by ion injection.

4.7.1 Summary of Φversus ς

In the *classical* model of diffusion limited permeation the phase lag varies linearly with ς at high frequencies and extrapolates to $-\pi/4$ on the Φ axis. The shape of this curve is similar for ion injected flows and for flows described by a surface model; deviations in character occur at low frequencies.

A two rate constant surface model gives a phase shift of up to $+\pi/4$ per surface, in the high frequency region, as flux is reduced. Ion injection also provides a phase shift of $+\pi/4$, at high frequencies.

Parallel diffusion processes modify the frequency variation of both phase and amplitude. The curves are highly characteristic with developed maxima and minima. They should allow the phenomena to

be detected in the course of a careful experiment.

4.7.2 Summary of Λ and $|R|^{-1}$ versus ζ

The variation of Λ with ζ, provides a separate means to determine the diffusion coefficient D. The amplitude modulation ratio provides the permeation coefficient P_m, which can be evaluated independently of p_s and p_s' by analysing $|R|^{-1}$ versus ζ. This provides a useful measurement of P_m for comparison with that obtained by steady state measurements.

The two rate constant model describes the shift from $p^{1/2}$, diffusion limited permeation, to p^1,surface limited permeation, with reduction of flux. This is illustrated by $\Lambda(\omega \to 0) = n$, where n is the index of the input pressure in the permeation law.

CHAPTER 5: RESULTS

This chapter is divided into nine sections. These comprise: an initial section, 5.1, dealing with the ranges of the physical variables within which effective measurements can be made; a section describing the features of the observed data, 5.2; two sections dealing with the the detailed analysis of data on 304 and 316 stainless steel, 5.3 and 5.4; a further section concerning the variation of phase lag with pressure, 5.5; and sections describing ion beam modulation and parallel diffusion data, 5.6 and 5.7. In section 5.8 the oxide thickness determinations are described and the final section, 5.9, summarises this chapter. The results presented and assumptions made in the analysis are discussed in chapter 6.

5.1 EXPERIMENTAL PHASE SPACE AND DATA PRESENTATION.

Pressure, temperature, specimen geometry, pumping rate, data collection rates and available modulation drive rates all impose constraints on the measurement of flux to an acceptable ratio of signal to noise. To describe the capabilities of a particular equipment a useful concept is that of an experimental phase space within which an experiment must be conducted. Examination of this space can provide a useful guide to the range of conditions within which it is sensible to conduct experiments. A primary use of the concept in this work was to assess the accessible phase space for

specimens of defined geometry.

To demonstrate the construction of such a phase space, the case of 304 stainless steel is considerd. The suppositions for the mathematical model are:

(1) Permeation is diffusion limited, that is, surface reactions are rapid and Richardson's law holds.

(2) The diffusion and permeation coefficients are :

$$D = 1.2\times10^{-6}\exp(-6.60\times10^{3}/T)\,m^{2}s^{-1} \quad [5.1]$$

$$P_{m} = 4.8\times10^{-7}\exp(-7.99\times10^{3}/T)\,mol\ m^{-1}s^{-1}Pa^{-\frac{1}{2}} \quad [5.2]$$

(3) The relative amplitude modulation ratio, Λ, is greater than 0.05. This imposes an upper limit on the frequency factor such that $\varsigma_{max} = 5.5$.

(4) The frequency factor ς must span a sufficient range to enable satisfactory curve fitting of the data. This was set at $1 < \Delta\varsigma$.

To this must be added the equipment contraints on the phase space, previously defined in chapter 3, which are :

(1) Temperature range 300K - 1300K.

(2) The useful frequency range is 10^{-2} - 10^{-4}Hz. For cycle periods less than 100s the exit chamber phase lag and some instrumentation times become significant. For periods greater than 1000s the

experiment becomes too time consuming.

(3) Input chamber pressure range 760 - 10^{-4} torr.

(4) Output pressure range 10^{-8} - 10^{-4} torr.

Clearly the various constraints interact. thus for example, good analysis calls for an appreciable experimental range for the frequency parameter, this change in ς, $\Delta\varsigma$, was limited to greater than 1. At the high frequency end ς is limited by the need to have Λ large enough to preserve the signal to noise ratio and at the low frequency end by the time taken to collect data. For specimens of progressively increasing thickness these limits gradually approach until no useful data may be obtained and experiment becomes pointless. The series of such limitations together define the phase space within which experiments must be done.

To determine the form of the surface surrounding the accessible phase space a three stage calculation was used :

(1) The dimensionless frequency factor, ς, can be expressed in terms of the cycle time, Θ, with :

$$\Theta = \frac{\Xi^2}{\varsigma^2} \qquad [5.3]$$

where

$$\Xi = \ell(\pi/D)^{1/2} \qquad [5.4]$$

This awkward function, Ξ, which has dimensions of $[T]^{1/2}$, is extremely useful in defining the phase space. A plot of the variation of cycle time Θ with frequency factor ς for various Ξ is shown in fig 5.1.

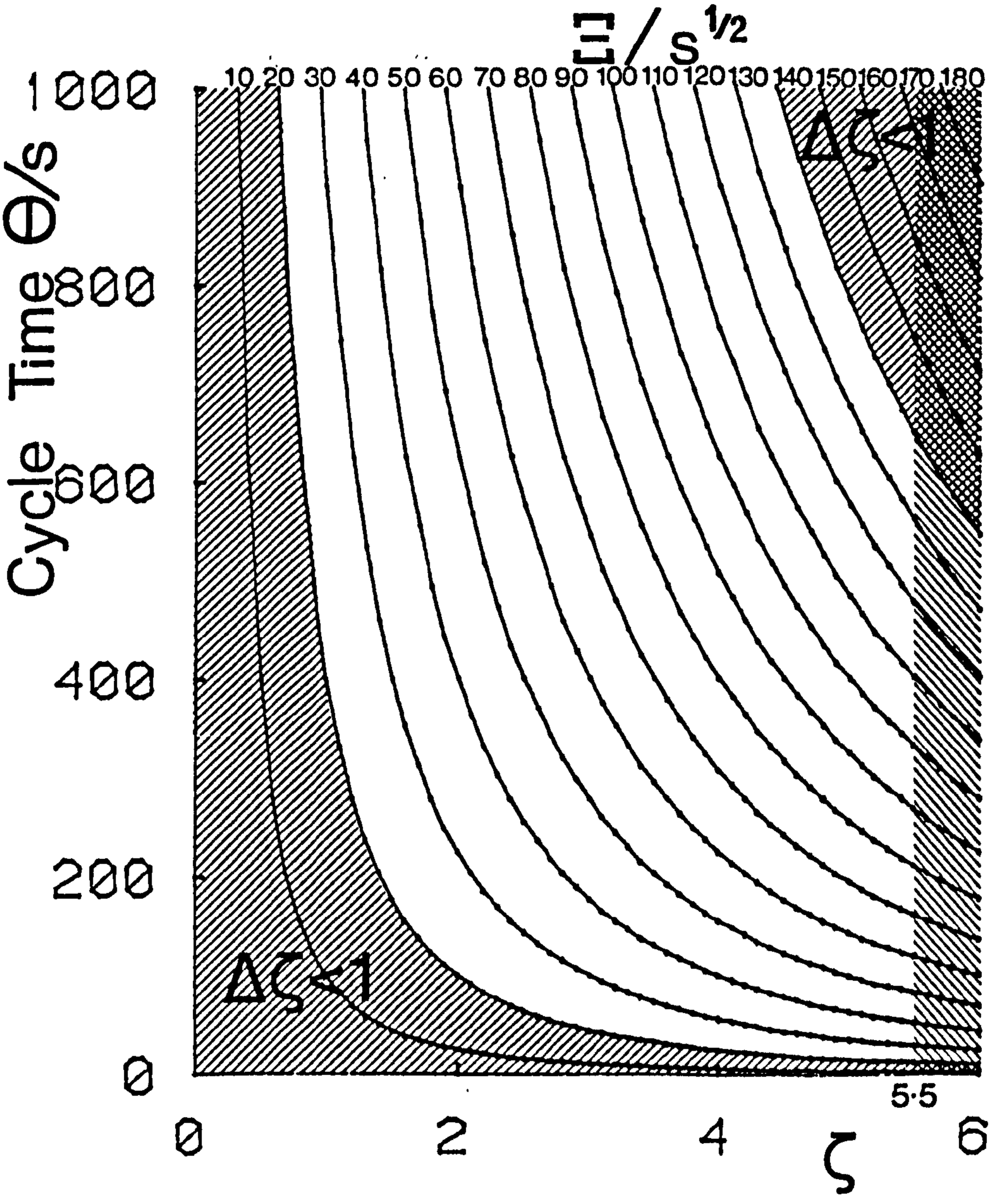

Fig 5.1 Variation of the cycle time Θ with frequency factor ς. This illustrates the first stage of the accessible experimental phase space calculation in which the range of values of Ξ are found.

When the constraints on ζ are applied to this plot a range of accessible values for Ξ are obtained. These are carried on to the next stage :

(2) If the diffusion coefficients are now expressed in terms of Ξ, using [5.1], then :

$$T = \frac{6.60\times10^{3}}{\ln[1.2\times10^{-6}\Xi^{2}/(\pi\ell^{2})]} \qquad [5.5]$$

This variation of temperature T with Ξ for various thicknesses of specimen is shown in fig 5.2, using the constraints on Ξ defined in the above stage. This enables a suitable specimen thickness to be chosen to give an acceptable temperature span. For the case shown: $\ell_{max} \sim 5\times10^{-4}$m, $\ell_{min} \sim 0.5\times10^{-4}$m.

(3) From Richardson's law of permeation with the coefficient defined in [5.2], and using [4.49] with negligible outgassing, then the steady state output pressure p'_s is :

$$p'_s = \frac{\sigma p_s^{1/2}}{S\ell}4.8\times10^{-7}\exp(-7.99\times10^{3}/T)\text{Pa} \qquad [5.6]$$

The variation of output chamber pressure p'_s with temperature T can now be found for a specified specimen thickness, ℓ, and input pressure, p_s. This allows the envelope of input pressures set by the constraints of the output chamber pressure to be found for a given specimen. This is illustrated in fig 5.3 for a 1×10^{-4}m thick specimen.

Stages (1),(2) and (3) provide a means to map out the accessible phase space. This approach is a general one. It may be adapted to

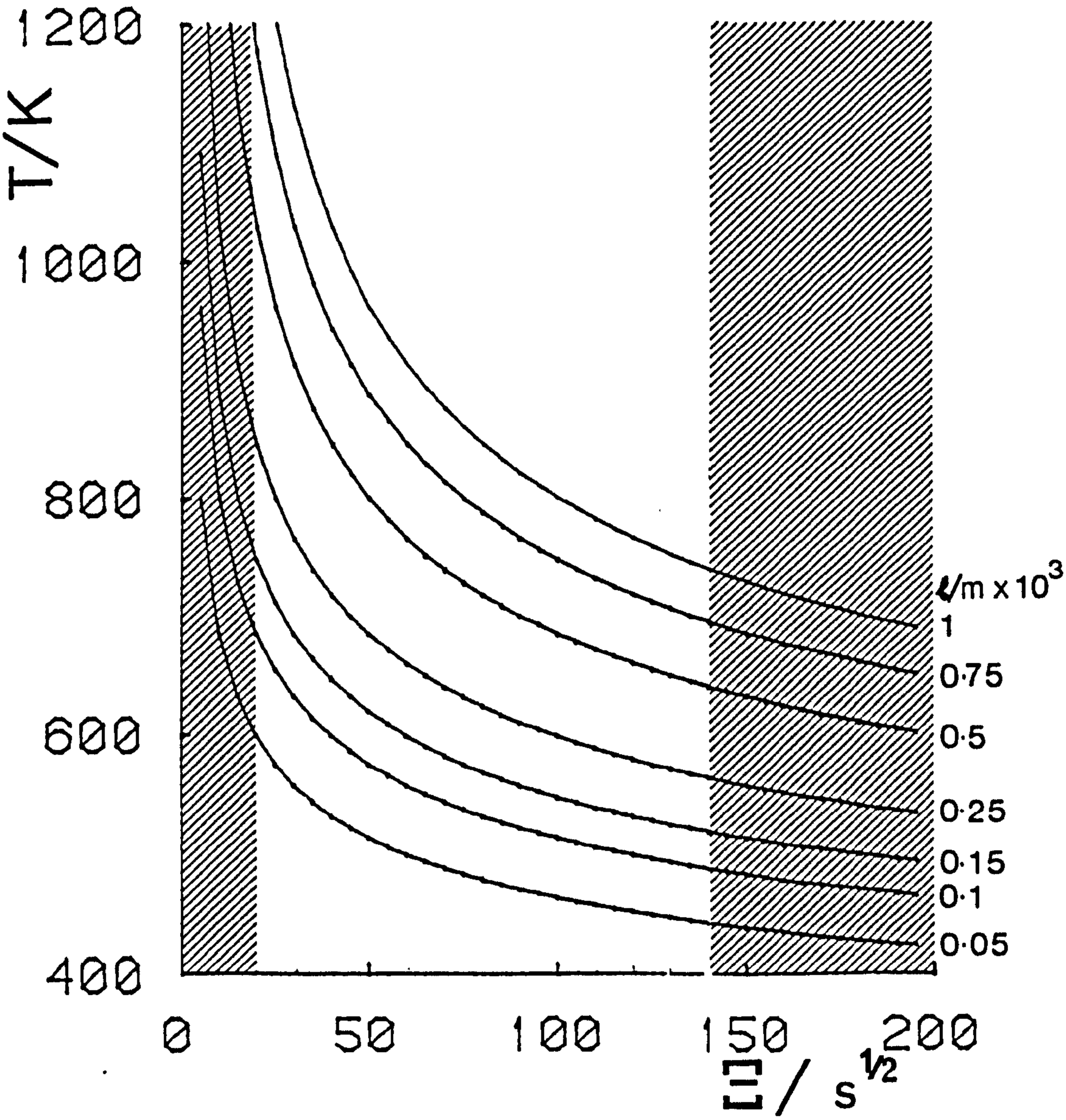

Fig 5.2 Variation of temperature T with Ξ for various thicknesses of foils of AISI 304. This illustrates the second stage in the calculation of the accessible experimental phase space.

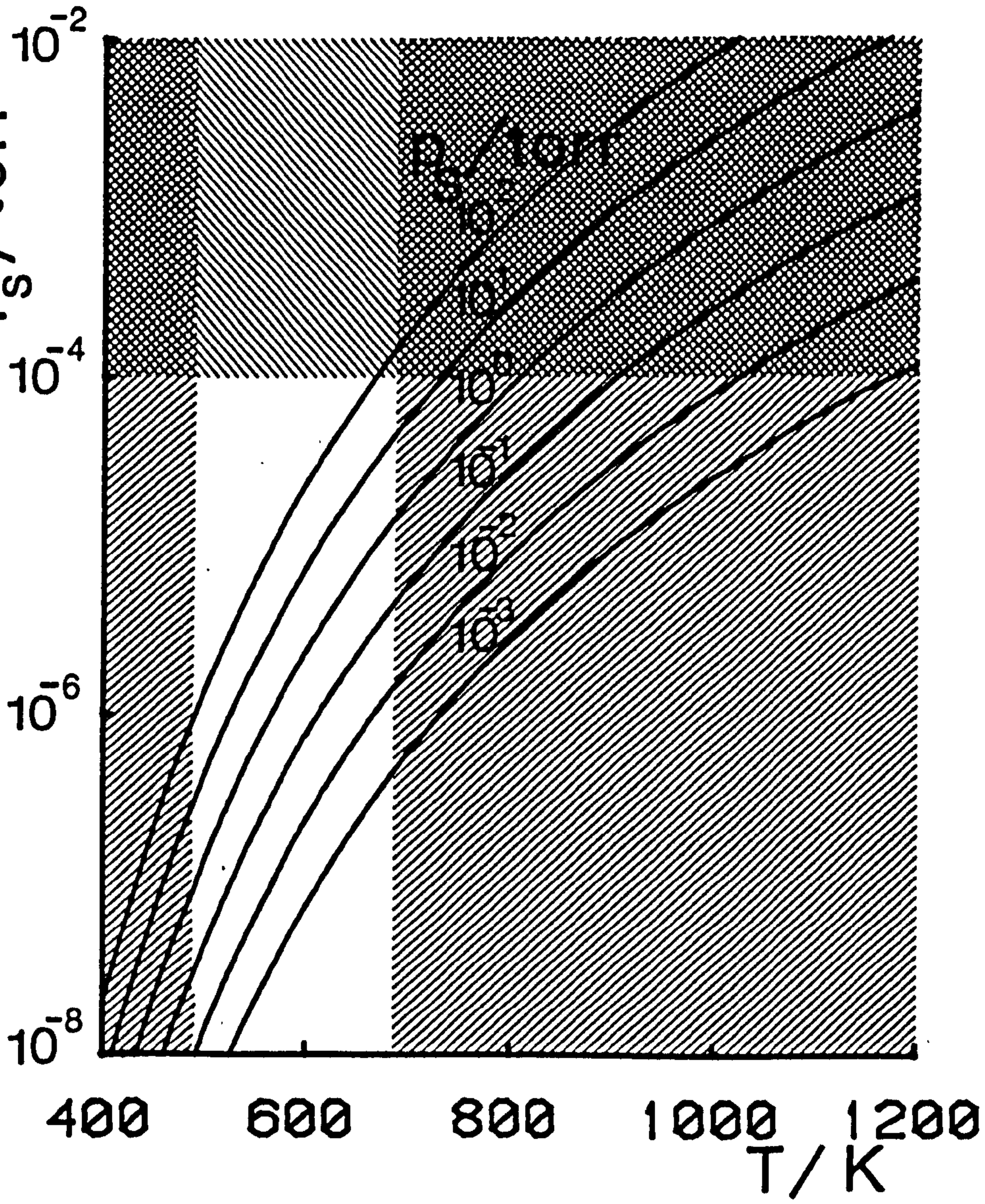

Fig 5.3 Variation of the output chamber pressure p_g', with temperature, T, for $\ell = 1\times10^{-4}$m, 304 stainless steel and of cross-sectional area, $\gamma = 5\times10^{-4}$m^2.

describe any experimental material and could well be extended to cover the analysis of surface effects. In this case, the thin end of the range of specimens would be of increased interest.

The accessible experimental value is illustrated in fig 5.4 as an isometric drawing. Shown in this way the relationships between the equipment constraints become clearer and in this way the sketch helps to show just where measurements should be concentrated.

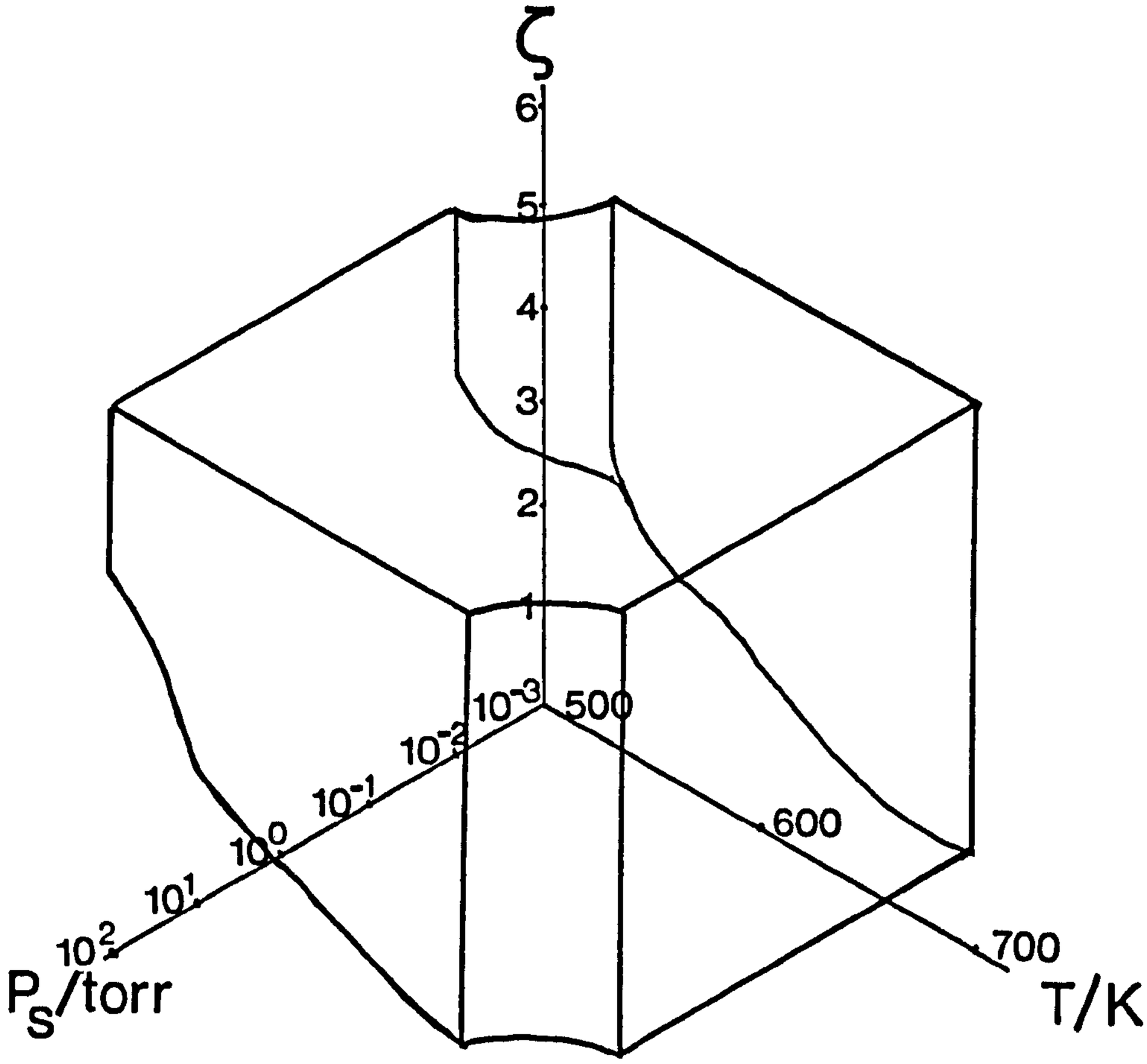

Fig 5.4 Sketch of the accessible experimental volume as an isometric drawing for a 1×10^{-4}m thick, 304 stainless steel of cross-sectional area $5\times10^{-4}m^2$.

5.2 GENERAL FEATURES OF THE OBSERVED DATA PATTERNS AND DATA PRESENTATION

The function of this section is to illustrate some general features of the experimental data obtained and describe the process by which it has been analysed in terms of diffusion, permeation and surface rate coefficients.

Fourier coefficients obtained by the methods detailed in chapter 3, provide estimates of phase lag, Φ, amplitude modulation ratio, $|R|^{-1} = |p'|/|p|$) and relative amplitude modulation ratio, $\Lambda = (|p'|p_s/(|p|p_s)$, for specified combinations of frequency, ν, temperature and pressure. Since ζ is proportional to $\nu^{1/2}$ it is convenient to show data graphically by plotting against the square root frequency.

The data are exemplified in figs 5.5 and 5.6. They show the variation of Φ and $|R|^{-1}$ with square root frequency $\nu^{1/2}$ for a range of temperatures at a single pressure. The specimen was AISI 304, of thickness 3.0×10^{-4}m. Notice the lack of structure at the high end of the temperature range.

The iso-thermal variation of phase lag, Φ, with square root frequency, $\nu^{1/2}$, for a range of pressures is typified in fig 5.7. The specimen was AISI 316, of thickness 1.0×10^{-4}m, at 674K. Notice the deterioration of the data at the lowest pressure as the signal begins to approach the noise level of the equipment.

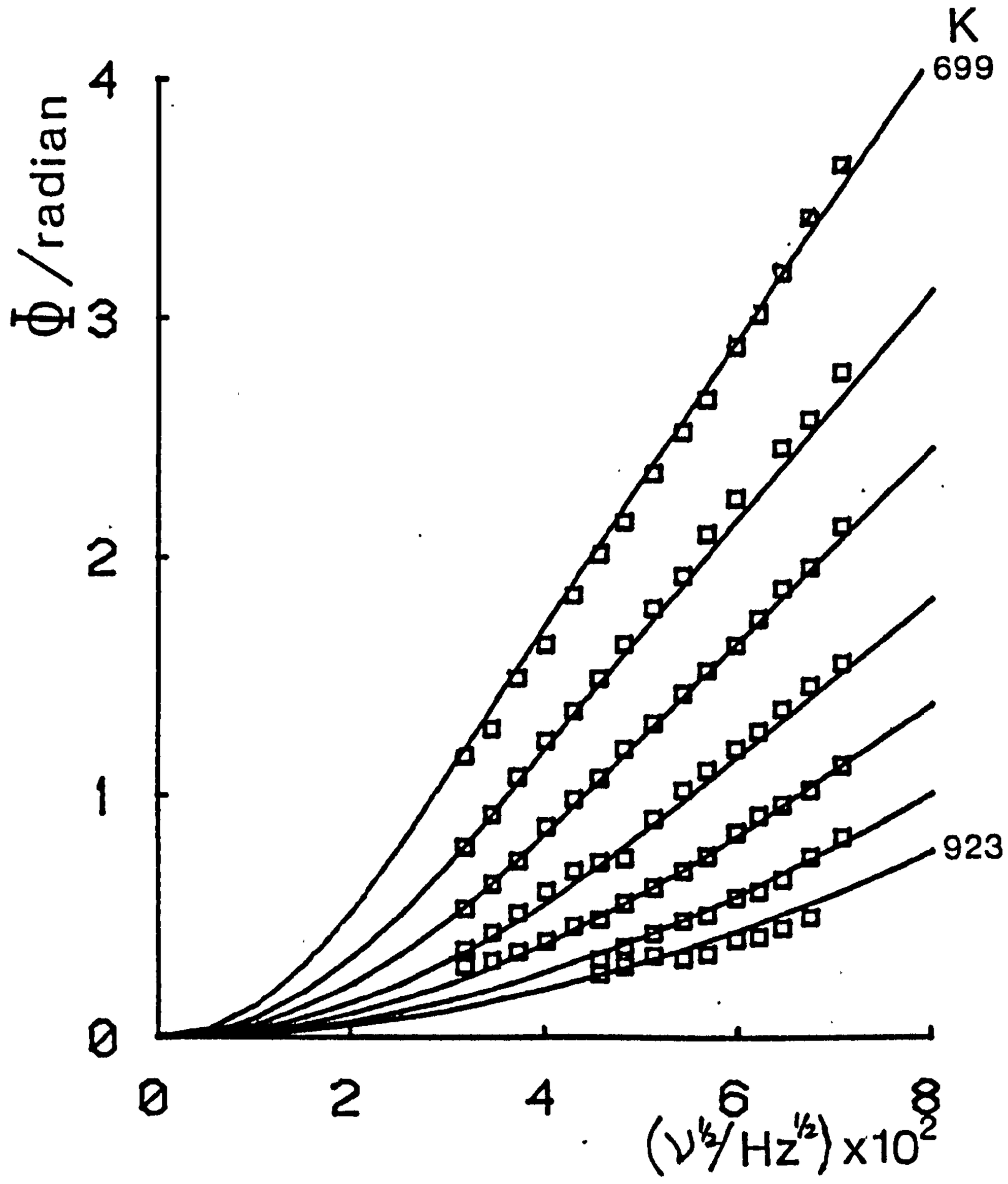

Fig 5.5 This graph typifies the variation of the phase lag Φ with square root frequency $\nu^{1/2}$ for a range of temperatures, 699 - 923K, at a single pressure, 83.5torr. The foil was stainless steel AISI 304 of thickness 3.0×10^{-4}m.

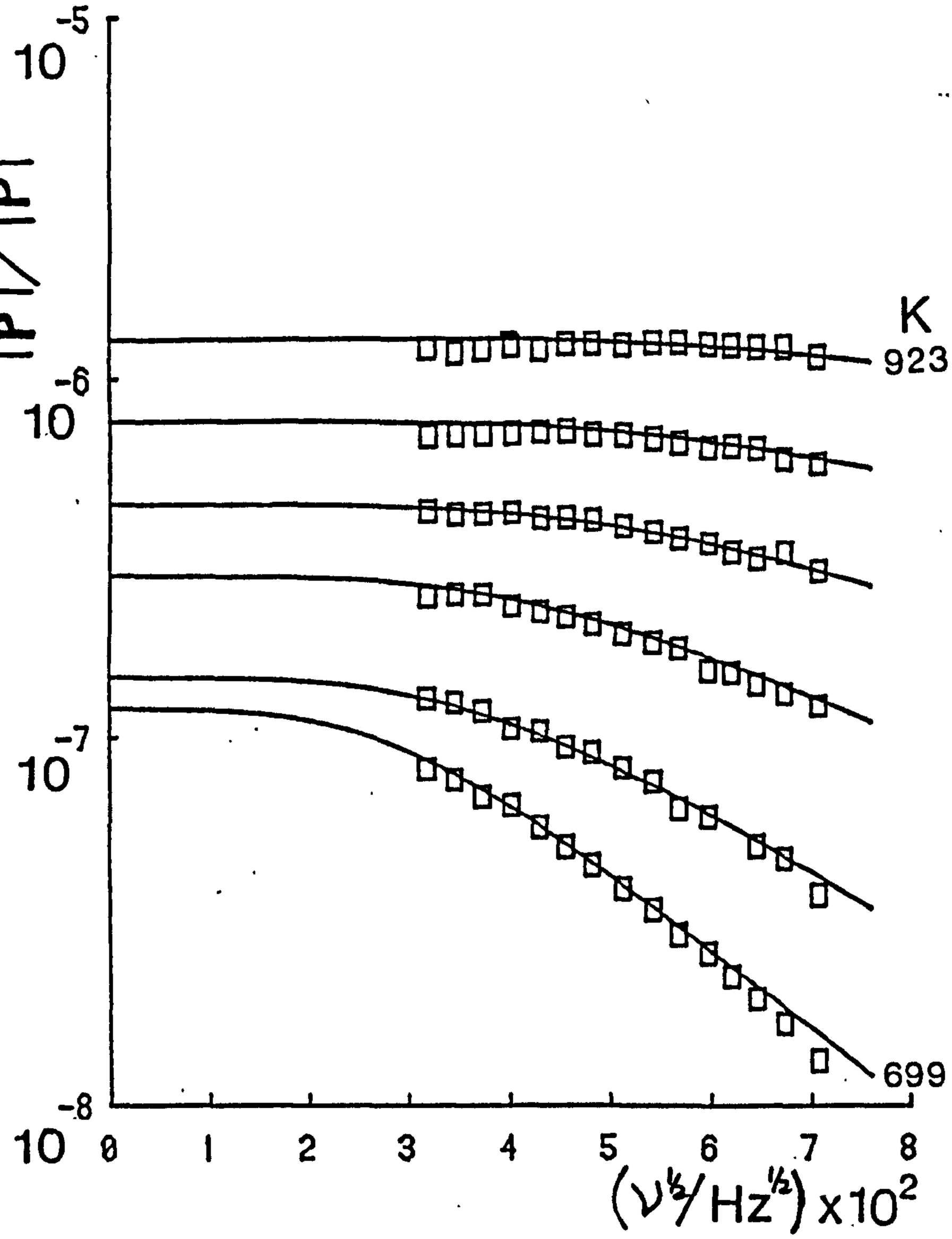

Fig 5.6 This graph typifies the variation of the modulation amplitude ratio $|R|^{-1}$ with square root frequency $\nu^{\frac{1}{2}}$ for a for a range of temperatures, 699 - 923K, at a single pressure, 83.5torr. The foil was stainless steel AISI 304 of thickness 3.0×10^{-4}m.

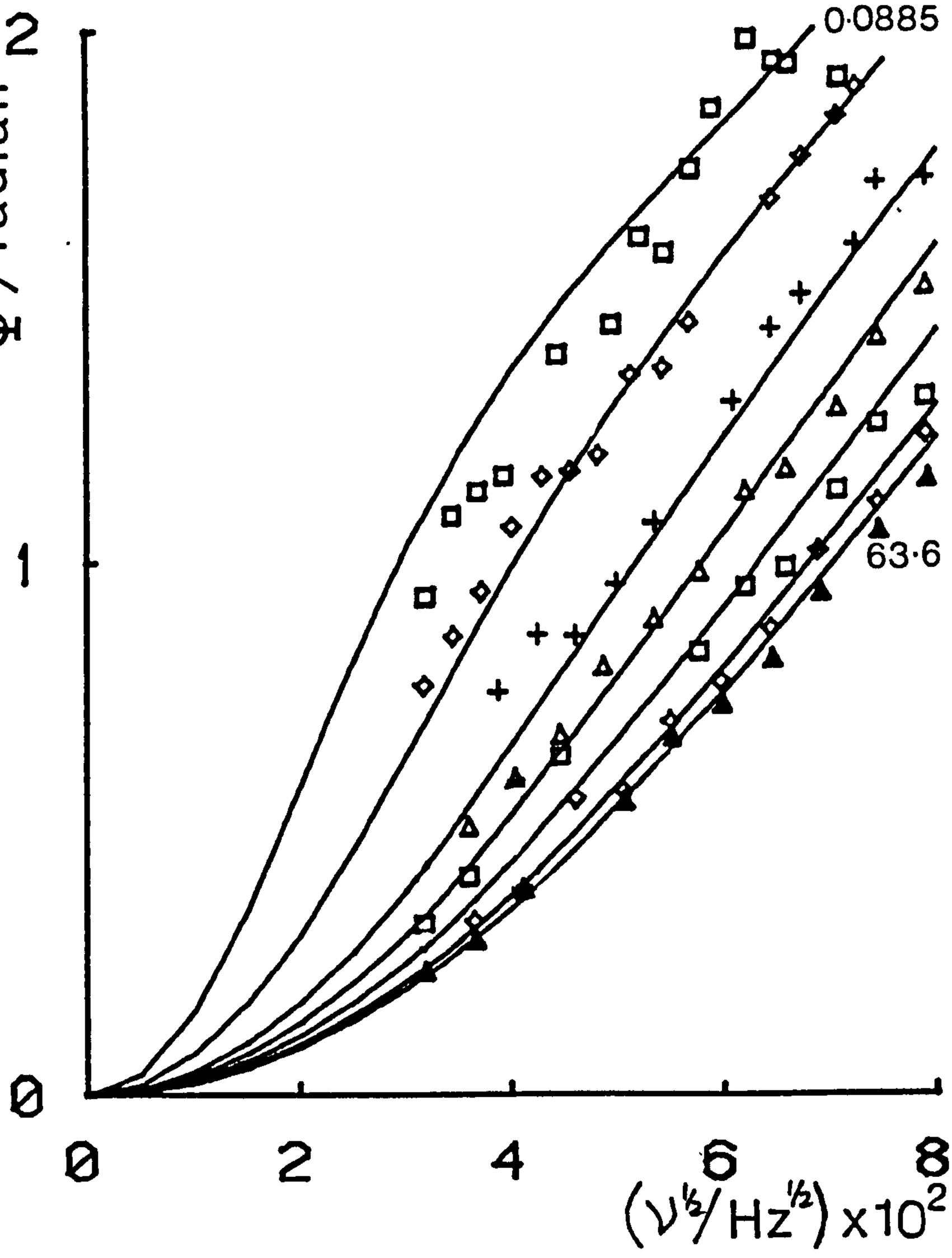

Fig 5.7 This graph typifies the iso-thermal variation of phase lag, Φ, with square root frequency, $\nu^{1/2}$ for a range of pressures, 63.6 - 0.0885torr, at 674K. Notice the deterioration of the data at the lowest pressure as the signal approaches the noise level of the equipment and the difficulty presenting data this way at high pressures.

The variation of Λ with $\nu^{1/2}$, although monitored, was not used for curve fitting of the parameters. The reason for this is two-fold:

(1) The Λ analysis requires the background pressure to approach zero which is not possible if a wide range of temperatures and pressures are to be investigated.

(2) The independent evaluation of the permeation coefficient comes from the evaluation of $|R|^{-1}$ and not Λ. Also, since $|R|^{-1}$ remains unaffected by the background pressure, it is the obvious choice for analysis.

For these reasons the data for Φ and $|R|^{-1}$ versus $\nu^{1/2}$ were grouped together and used as the principal basis for analysis.

A separate and interesting way of presenting the data is given in section 5.5. The figures in that section show the isothermal, iso-frequency variation of the phase lag Φ with pressure. They illustrate how surface reactions may produce an increase, of phase lag with reduction of pressure, corresponding to the changeover from $p^{1/2}$ to p^1 permeation.

As over 3000 data points are available, complete graphical presentation would be cumbersome and un-informative. In presentation therefore it is assumed that the data shown above typify the body of available data on the variation of Φ and $|R|^{-1}$

versus $\nu^{1/2}$ and provide the basis for a numerical analysis in which the parameters D, P_m and k_1 are fitted to measurements of phase and amplitude at given frequencies. In the two sections which follow, a detailed analysis of D, P_m and k_1 will be shown for the data from AISI 304 and 316 specimens respectively. The data is separated to show first the flux through specimens with cleaned surfaces and then specimens with imposed oxide layers.

5.3 STAINLESS STEEL : AISI 304

This section is divided into descriptions of results from clean surfaces, 5.3.1, and oxidised surfaces, 5.3.2. All 304 foils were mounted in the internal furnace configuration.

5.3.1. Clean surface results

A series of temperature, pressure and frequency runs were conducted on AISI 304 2.5×10^{-4}m and 3.0×10^{-4}m foils. The main distinguishing feature of these specimens is that they were cleaned *in situ* by two completely different proceedures. The 2.5×10^{-4}m foil was cleaned on both sides by an ion gun, while the 3.0×10^{-4}m foil underwent the surface preparation of *activation*, typical of the method used by several authors (5),(22),(23),(49) and (50) to reduce the surface oxide. Both methods are described in detail in 3.4.

The results are tabulated in tables 1 and 2. Figs 5.8, 5.9, 5.10 and 5.11 show these tabulated variations of D and P_m with 1/T for the 2.5×10^{-4}m and 3.0×10^{-4}m foils respectively. The variation of k_1 with 1/T for both foils is shown in fig 5.12. A least squares fit of these Arrhenius plots provides the following equations for D,P_m and k_1 for these two foils under clean surface conditions.

For the ion beam cleaned AISI 304, 2.5×10^{-4}m foil.

Table 5.1 AISI 304, thickness ℓ = 2.5×10^{-4}m, cross-sectional area γ = $5.0\times10^{-4}m^2$ and cleaned by an ion beam on both surfaces. Six pressures from 79.6 - 0.0886torr. Frequency range at each temperature and pressure, expressed as a cycle time θ, was 160 - 990s for typically fourteen frequencies.

T/K	D/m^2s^{-1}	$P_m/molm^{-1}s^{-1}Pa^{-½}$	$k_1/molm^{-2}s^{-1}Pa^{-1}$
965	1.49×10^{-9}	1.24×10^{-10}	***
915	9.94×10^{-10}	7.78×10^{-11}	***
869	6.17×10^{-10}	5.03×10^{-11}	2.27×10^{-7}
829	4.22×10^{-10}	3.09×10^{-11}	1.67×10^{-7}
791	2.92×10^{-10}	1.95×10^{-11}	8.33×10^{-8}
758	1.98×10^{-10}	1.21×10^{-11}	5.11×10^{-8}
727	1.39×10^{-10}	7.55×10^{-12}	2.78×10^{-8}
697	9.03×10^{-11}	4.91×10^{-12}	1.87×10^{-8}
672	6.29×10^{-11}	***	1.06×10^{-8}
646	4.83×10^{-11}	2.02×10^{-12}	5.95×10^{-9}

Table 5.2 AISI 304, thickness ℓ = 3.0×10^{-4}m, cross-sectional area γ = $5.0\times10^{-4}m^2$ and activated on both surfaces. Pressures were 83.5 and 9.20torr. Frequency range at each temperature and pressure, expressed as a cycle time θ, was 160 - 990s for typically fourteen frequencies.

T/K	D/m^2s^{-1}	$P_m/molm^{-1}s^{-1}Pa^{-½}$	$k_1/molm^{-2}s^{-1}Pa^{-1}$
923	9.40×10^{-10}	9.56×10^{-11}	1.17×10^{-7}
877	6.73×10^{-10}	5.56×10^{-11}	5.44×10^{-8}
833	4.71×10^{-10}	3.38×10^{-11}	2.82×10^{-8}
795	3.39×10^{-10}	2.07×10^{-11}	1.13×10^{-8}
760	2.20×10^{-10}	1.29×10^{-11}	7.02×10^{-9}
728	1.60×10^{-10}	7.05×10^{-12}	2.27×10^{-9}
699	9.91×10^{-11}	5.89×10^{-12}	1.55×10^{-9}

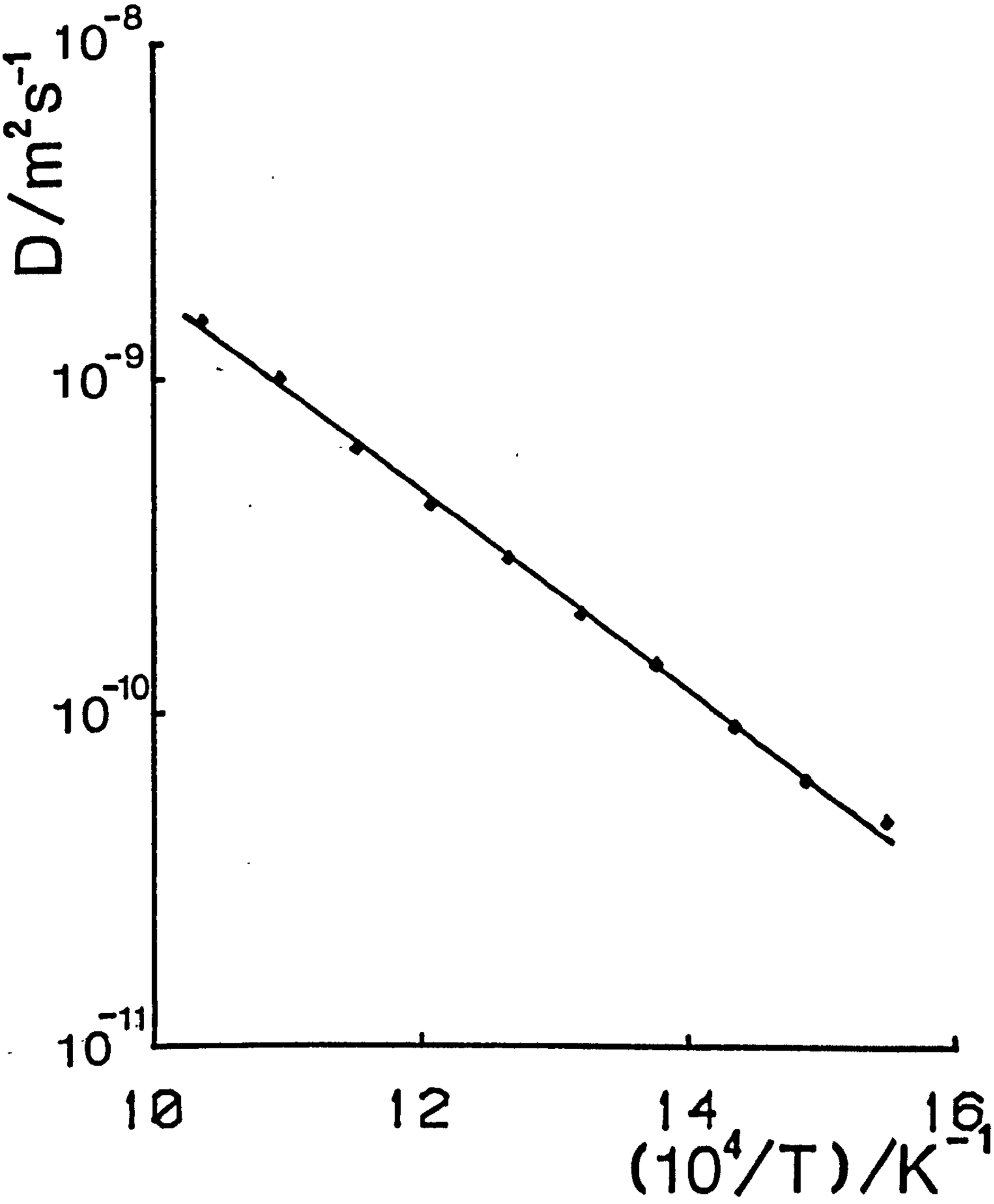

Fig 5.8 Variation of the diffusion cofficient D with inverse temperature 1/T for an AISI 304, 2.5×10^{-4}m, foil which was ion beam cleaned.

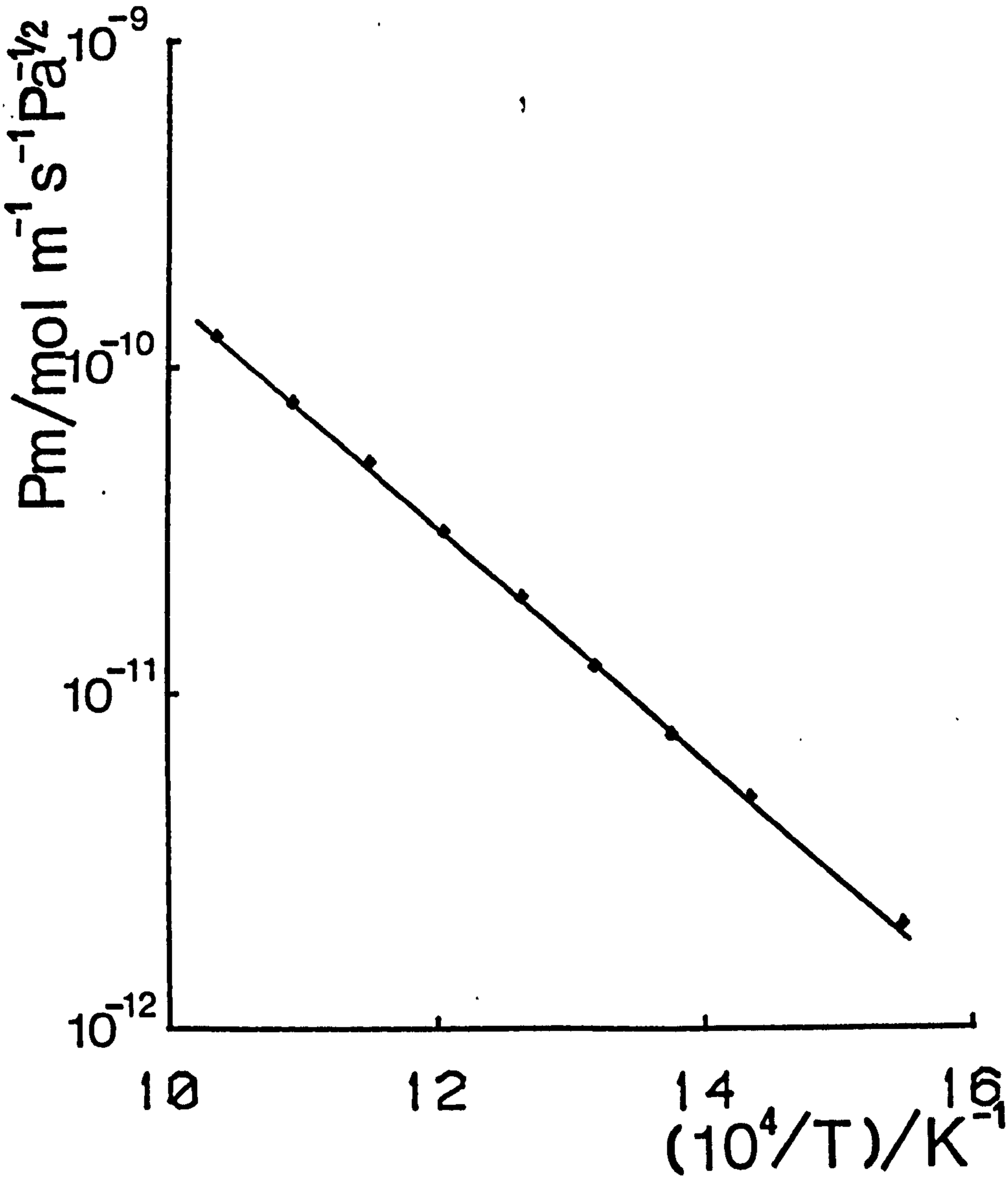

Fig 5.9 Variation of the permeation cofficient P_m with inverse temperature 1/T for an AISI 304, 2.5×10^{-4}m, foil which was ion beam cleaned.

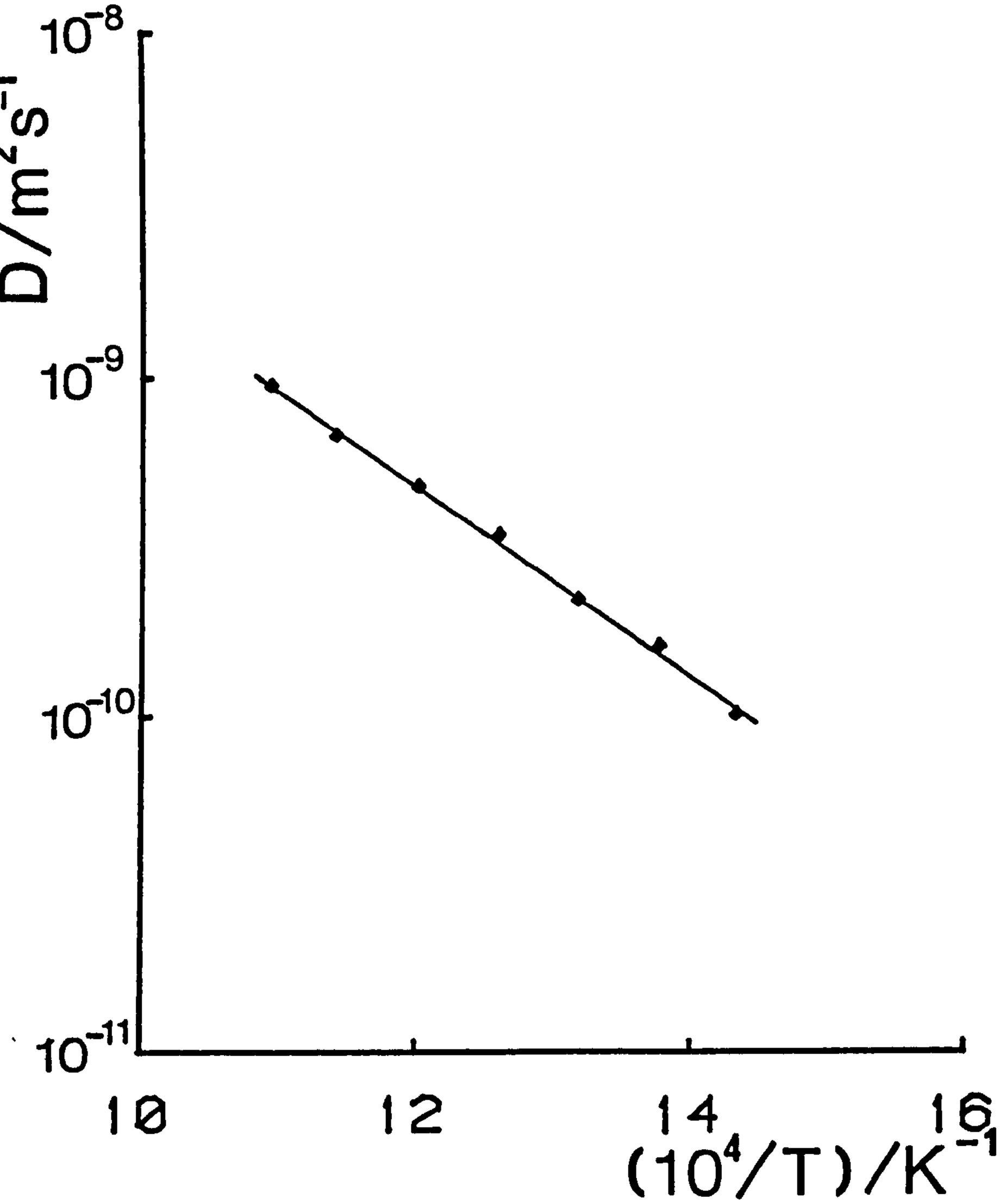

Fig 5.10 Variation of the diffusion cofficient D with inverse temperature 1/T for an AISI 304, 3.0×10^{-4}m, foil which was cleaned by activation.

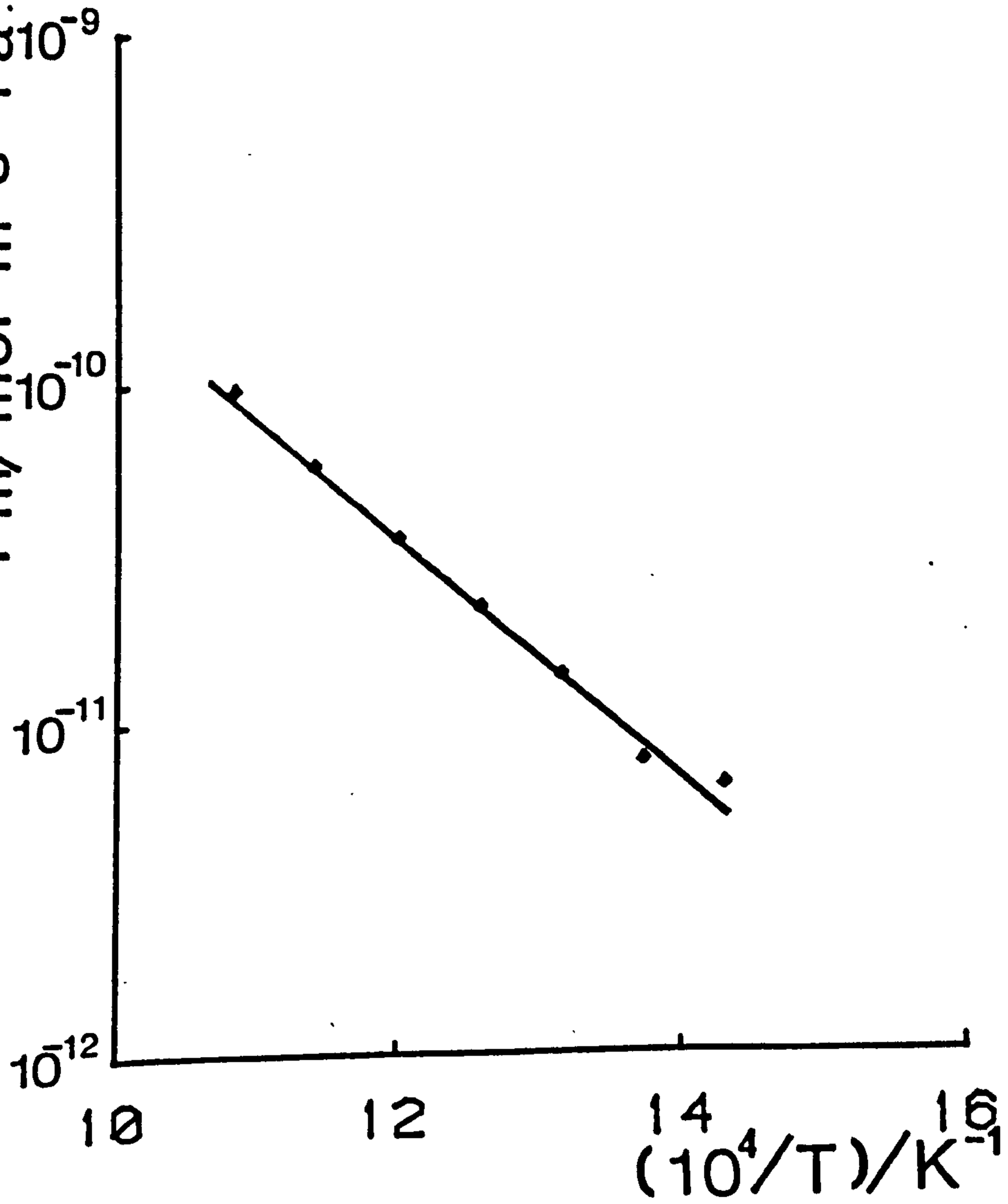

Fig 5.11 Variation of the permeation coefficient P_m with inverse temperature 1/T for an AISI 304, 3.0×10^{-4}m, foil which was cleaned by activation.

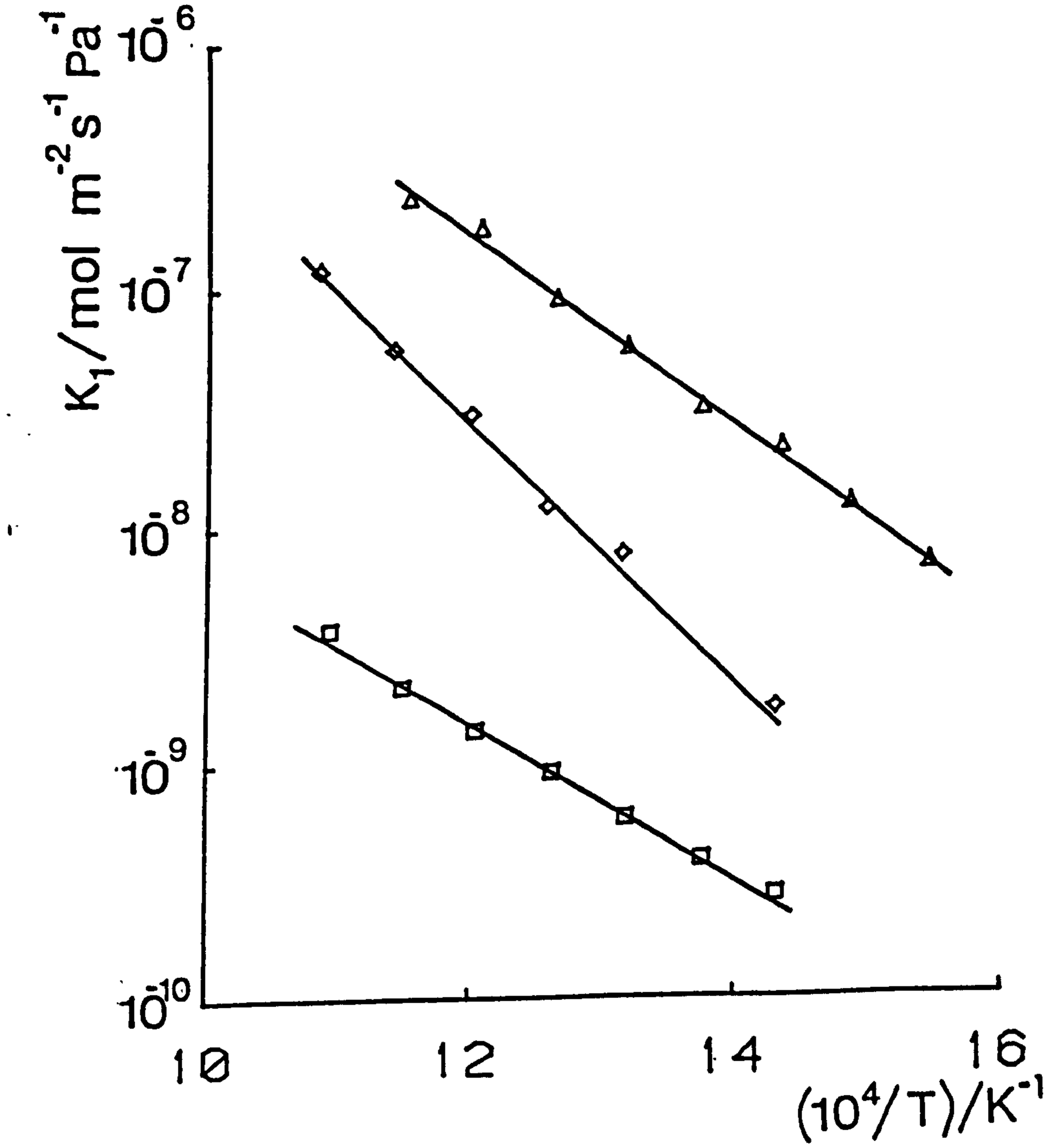

Fig 5.12 Variation of the rate constant k_1 with inverse temperature for AISI 304.

Upper curve: 2.5×10^{-4}m foil cleaned by an ion beam.

Middle curve: 3.0×10^{-4}m foil cleaned by activation.

Lower curve: 2.5×10^{-4}m foil oxidised on input surface.

$$D=(1.59\pm0.08)\times10^{-6}\exp\{-[(6.789\pm0.049)\times10^{3}/T]/K^{-1}\}m^{2}s^{-1} \quad [5.7]$$

$$P_m=(5.46\pm0.14)\times10^{-7}\exp\{-[(8.102\pm0.024)\times10^{3}/T]/K^{-1}\}molm^{-1}s^{-1}Pa^{-\frac{1}{2}} \quad [5.8]$$

$$k_1=(1.13\pm0.10)\times10^{-2}\exp\{-[(9.325\pm0.082)\times10^{3}/T]/K^{-1}\}molm^{-2}s^{-1}Pa^{-1} \quad [5.9]$$

For the activated AISI 304, 3.0×10^{-4}m foil:

$$D=(1.09\pm0.06)\times10^{-6}\exp\{-[(6.474\pm0.054)\times10^{3}/T]/K^{-1}\}m^{2}s^{-1} \quad [5.10]$$

$$P_m=(7.16\pm0.77)\times10^{-7}\exp\{-[(8.228\pm0.112)\times10^{3}/T]/K^{-1}\}molm^{-1}s^{-1}Pa^{-\frac{1}{2}} \quad [5.11]$$

$$k_1=(1.17\pm0.20)\times10^{-1}\exp\{-[(12.76\pm0.17)\times10^{3}/T]/K^{-1}\}molm^{-2}s^{-1}Pa^{-1} \quad [5.12]$$

Clearly the rate constant k_1 is more rapid by an order of magnitude for the ion beam cleaned foil than the activated one, fig 5.12. This and the consistency of D and P_m is discussed in chapter 6.

5.3.2 Oxidised surface results

Having established a difference between an ion beamed specimen and an activated one, the next step was to oxidise the input side of the cleaned 2.5×10^{-4}m foil. This was done by exposing the surface to 0.9torr of air at 1023K for 36 hours and caused a reduction in the permeation of ≈ 27%.

The reason for this approach was two-fold. With just one surface oxidised it was possible to analyse for $\mu \neq 0$, a case which had not been accessible till then. It also provided on a single specimen both a clean and an oxidised surface for analysis of oxide composition and

depth.

The data for the specimen given this single sided oxidation are tabulated in table 3. The oxide was assumed sufficiently thick that the parameter μ could be set to -1 for purposes of analysis. Figs 5.13, 5.14 and 5.12 show the consequential values of D, P_m and k_1 and their variation with 1/T for this oxidised foil. A least squares fit of these Arrhenius plots provides the following equations for D,P_m and k_1:

For the single oxodised AISI 304, 2.5×10^{-4}m foil:

$$D=(1.40\pm0.03)\times10^{-6}\exp\{-[(6.773\pm0.024)\times10^{3}/T]/K^{-1}\}m^{2}s^{-1} \quad [5.13]$$

$$P_m=(3.09\pm0.07)\times10^{-7}\exp\{-[(7.648\pm0.023)\times10^{3}/T]/K^{-1}\}molm^{-1}s^{-1}Pa^{-\frac{1}{2}} \quad [5.14]$$

$$k_1=(1.43\pm0.11)\times10^{-5}\exp\{-[(7.661\pm0.081)\times10^{3}/T]/K^{-1}\}molm^{-2}s^{-1}Pa^{-1} \quad [5.15]$$

The value of k_1 is lower for this oxidised foil than for the ion beam or activated clean foils, fig 5.12. As stated earlier these values of k_1 and the consistency of D and P_m is discussed in chapter 6.

Table 5.3 AISI 304, thickness ℓ = 2.5×10^{-4}m, cross-sectional area γ = $5.0\times10^{-4}m^2$ and oxidised on input surface. Four pressures from 83.6 - 2.42torr. Frequency range at each temperature and pressure, expressed as a cycle time θ, was 160 - 990s for typically fifteen frequencies.

T/K	D/m^2s^{-1}	$P_m/molm^{-1}s^{-1}Pa^{-½}$	$k_1/molm^{-2}s^{-1}Pa^{-1}$
915	8.63×10^{-10}	7.39×10^{-11}	3.66×10^{-9}
870	5.86×10^{-10}	4.63×10^{-11}	2.04×10^{-9}
830	3.95×10^{-10}	3.07×10^{-11}	1.32×10^{-9}
792	2.64×10^{-10}	1.94×10^{-11}	8.77×10^{-10}
758	1.80×10^{-10}	1.30×10^{-11}	5.64×10^{-10}
727	1.29×10^{-10}	8.18×10^{-12}	3.73×10^{-10}
699	8.69×10^{-11}	5.57×10^{-12}	2.67×10^{-10}

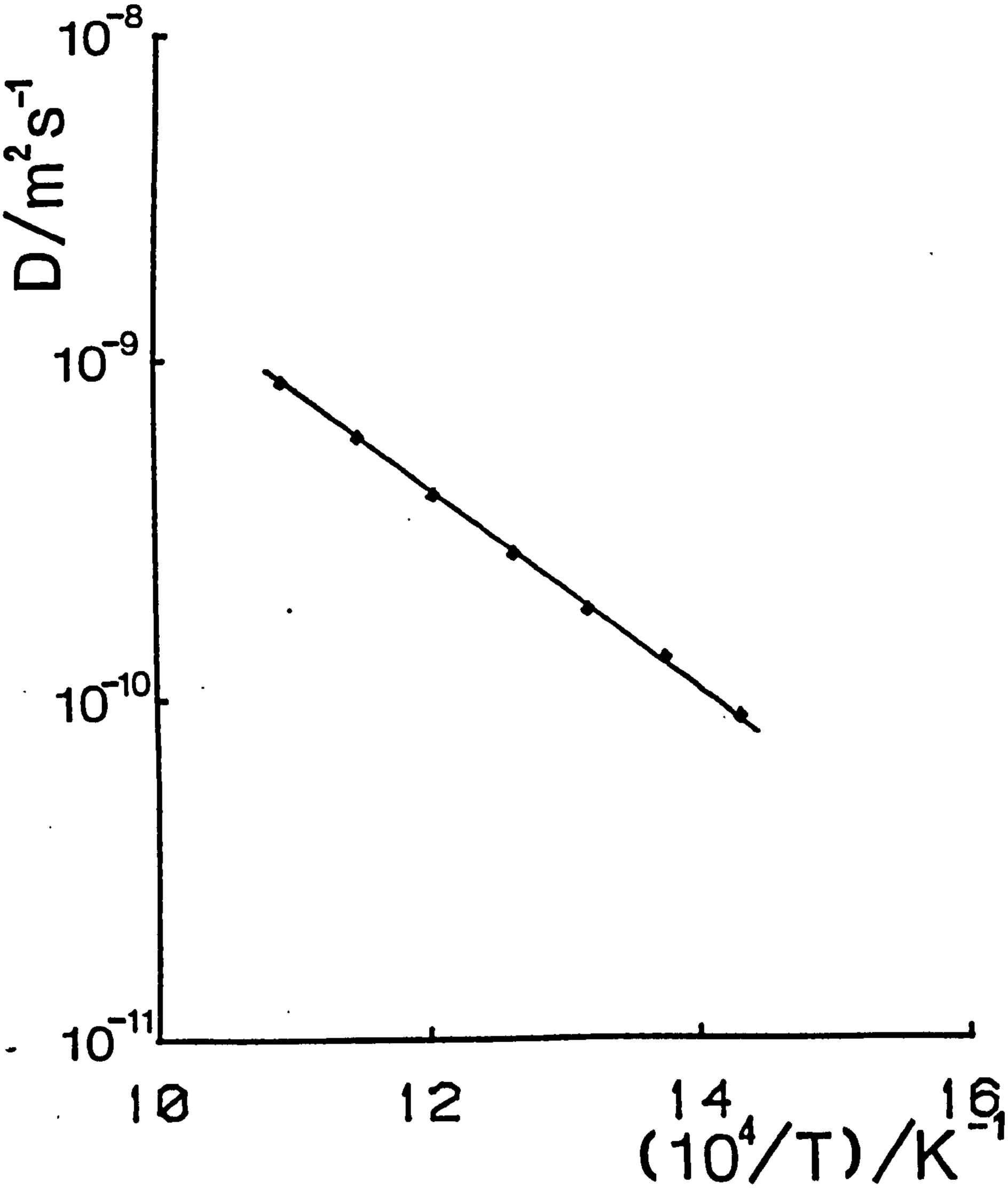

Fig 5.13 Variation of the diffusion cofficient D with inverse temperature 1/T for an AISI 304, 2.5×10^{-4}m, foil which was oxidised on the input surface.

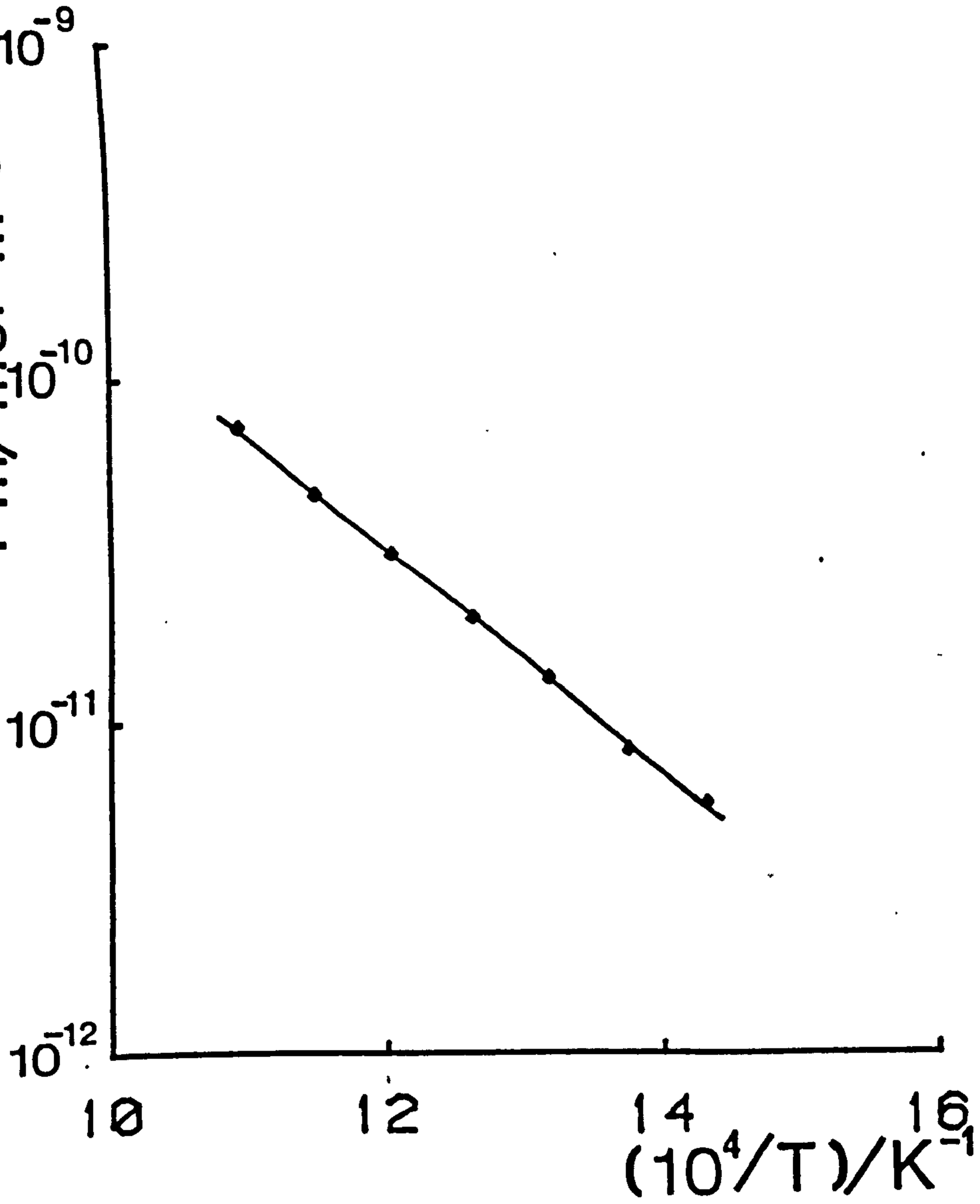

Fig 5.14 Variation of the permeation coefficient P_m with inverse temperature 1/T for an AISI 304, 2.5×10^{-4}m, foil which was oxidised on the input surface.

5.4 STAINLESS STEEL : AISI 316

As with the 304 stainless steel the descriptions of results for the AISI 316 specimens is divided into sections dealing with clean surface data, 5.4.1 and oxidised surface data, 5.4.2. The 1.0×10^{-4}m thick foil was run in the internal furnace configuration while the 5.0×10^{-5}m foil was run in the external configuration. All 316 foils had a cross-sectional area of $5.0\times10^{-4}m^2$.

5.4.1. clean surface results

Data from a comprehensive range of temperatures, pressures and frequencies were obtained for the 1.0×10^{-4}m and 5.0×10^{-4}m specimens. Each specimen was cleaned on both surfaces using an ion beam. Again, for purposes of analysis the parameter μ was set equal to zero. The results of the analysis are tabulated in tables 5.4 and 5.5 for the 1.0×10^{-4}m and 5.0×10^{-4}m foils respectively.

Figs 5.15, 5.16, 5.17 and 5.18 show the variation of D and P_m with 1/T for the two foils. The variation of k_1 with 1/T is shown in fig 5.19. Notice that the variation of D and P_m remain unaffected by the external configuration. This provides further confirmation that the experimental range was outside the irrecoverable effects of parallel diffusion descibed in section 4.6. This point is taken up again in section 5.7.

Table 5.4 AISI 316, thickness ℓ = 1.0×10^{-4}m, cross-sectional area γ = $5.0\times10^{-4}m^2$ and ion beamed clean on both surfaces. Seven pressures from 63.6 - 0.0885torr. Frequency range at each temperature and pressure, expressed as a cycle time θ, was 160 - 990s for typically twelve frequencies.

T/K	D/m^2s^{-1}	$P_m/molm^{-1}s^{-1}Pa^{-½}$	$k_1/molm^{-2}s^{-1}Pa^{-1}$
863	7.70×10^{-10}	7.66×10^{-11}	2.76×10^{-8}
800	3.70×10^{-10}	3.24×10^{-11}	1.67×10^{-8}
759	2.48×10^{-10}	1.64×10^{-11}	8.15×10^{-9}
714	1.25×10^{-10}	7.63×10^{-12}	4.94×10^{-9}
674	7.77×10^{-11}	3.89×10^{-12}	2.36×10^{-9}
638	4.04×10^{-11}	1.77×10^{-12}	1.51×10^{-9}
606	2.54×10^{-11}	1.15×10^{-12}	6.74×10^{-10}
576	1.38×10^{-11}	6.02×10^{-13}	3.77×10^{-10}
549	9.01×10^{-12}	2.24×10^{-13}	2.16×10^{-10}

Table 5.5 AISI 316, thickness ℓ = 5.0×10^{-5}m, cross-sectional area γ = $5.0\times10^{-4}m^2$ and ion beamed clean on both surfaces. Three pressures were investigated from 79.1 - 0.800torr. Frequency range at each temperature and pressure, expressed as a cycle time θ, was 160 - 990s for typically fourteen frequencies.

T/K	D/m^2s^{-1}	$P_m/molm^{-1}s^{-1}Pa^{-½}$	$k_1/molm^{-2}s^{-1}Pa^{-1}$
818	2.13×10^{-10}	3.62×10^{-11}	2.11×10^{-7}
776	1.50×10^{-10}	2.08×10^{-11}	1.41×10^{-7}
740	1.15×10^{-10}	1.29×10^{-11}	6.21×10^{-8}
706	8.85×10^{-11}	8.01×10^{-12}	3.30×10^{-8}
675	5.96×10^{-11}	4.77×10^{-12}	1.82×10^{-8}
647	4.30×10^{-11}	2.92×10^{-12}	9.56×10^{-9}
621	3.33×10^{-11}	2.01×10^{-12}	4.54×10^{-9}
597	1.89×10^{-11}	9.66×10^{-13}	***
573	1.39×10^{-11}	7.32×10^{-13}	1.57×10^{-9}

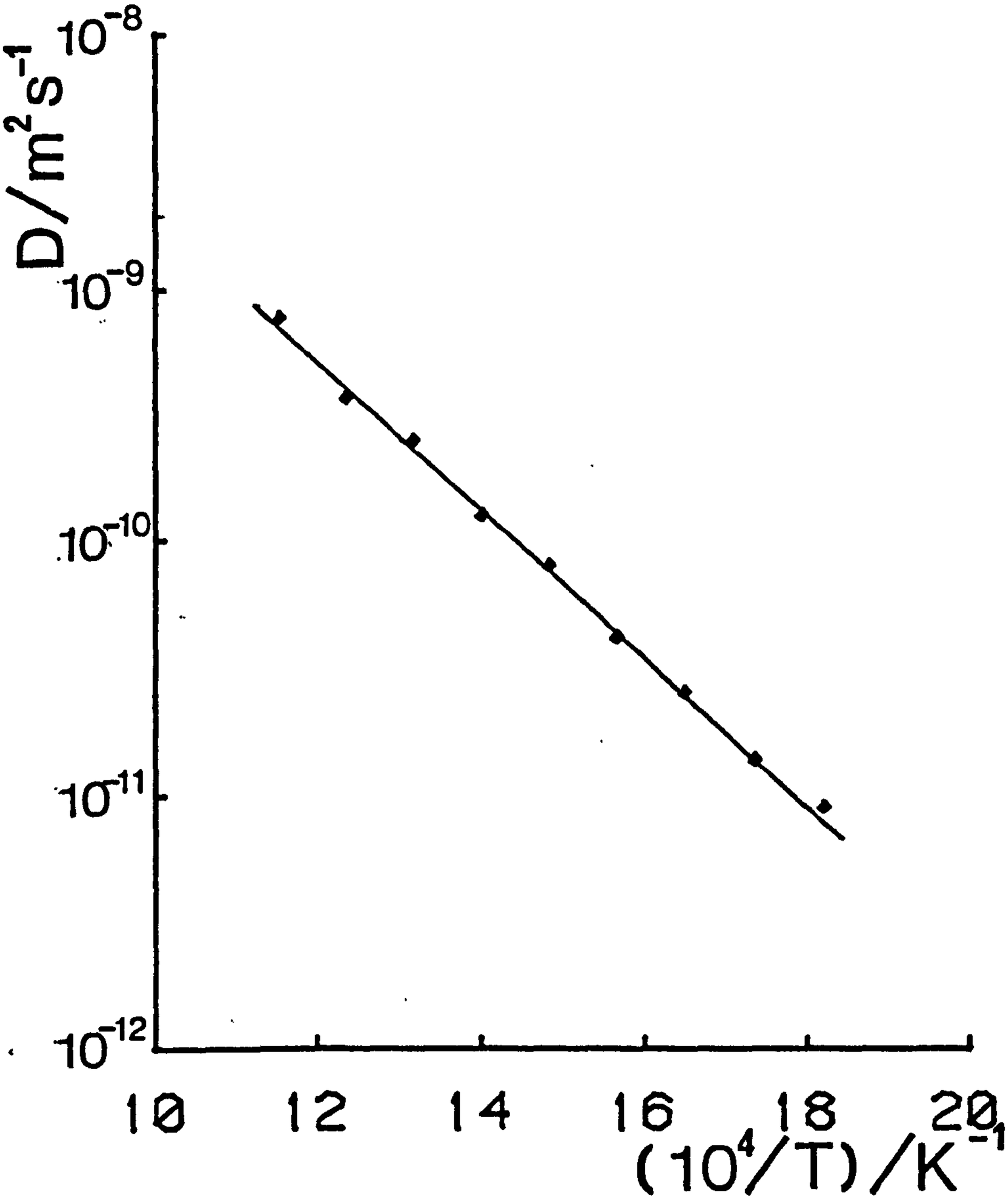

Fig 5.15 Variation of the diffusion coefficient D with inverse temperature 1/T for an AISI 316, 1.0×10^{-4}m, foil which was cleaned by an ion beam.

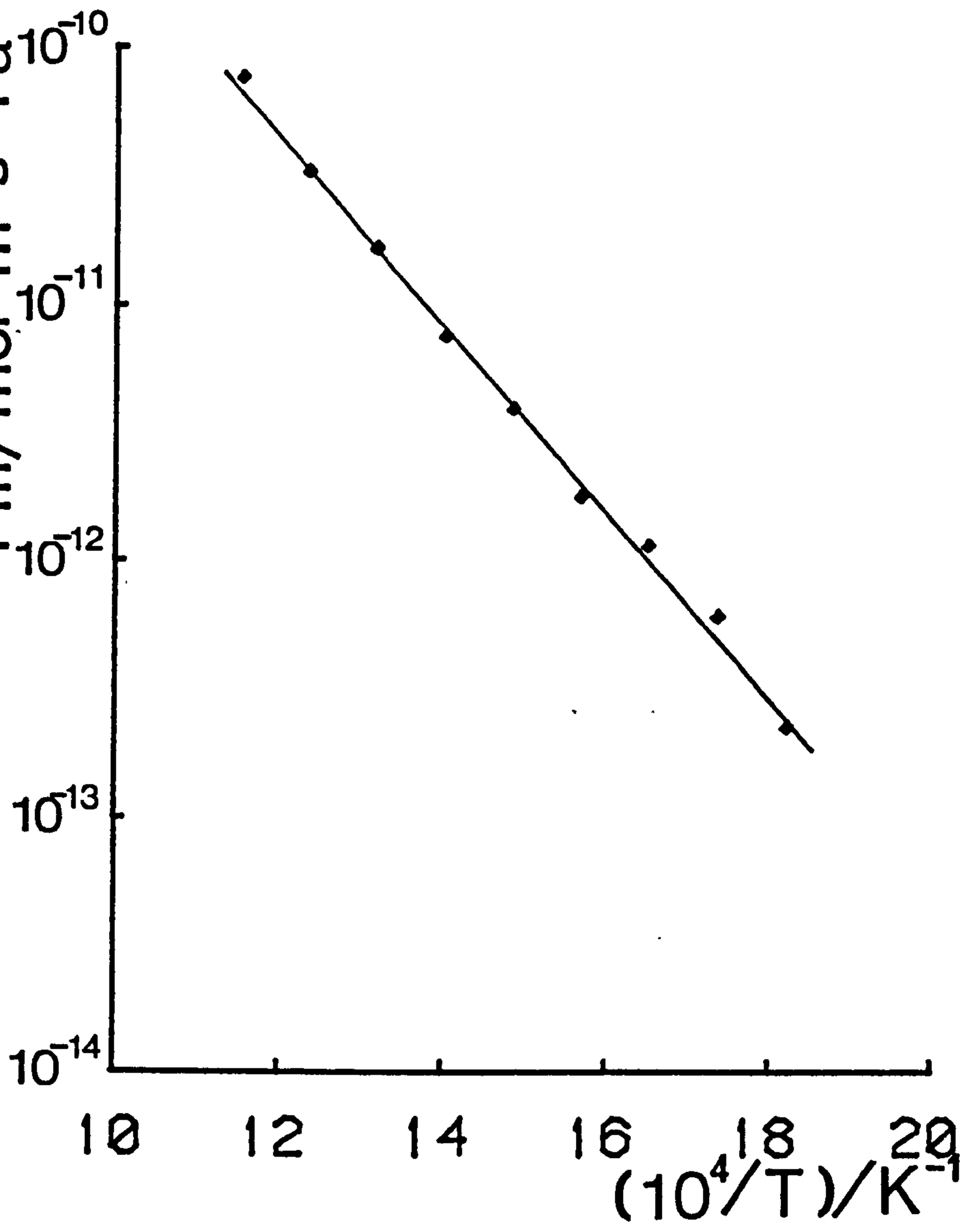

Fig 5.16 Variation of the permeation coefficient P_m with inverse temperature 1/T for an AISI 316, 1.0×10^{-4}m, foil which was cleaned by an ion beam.

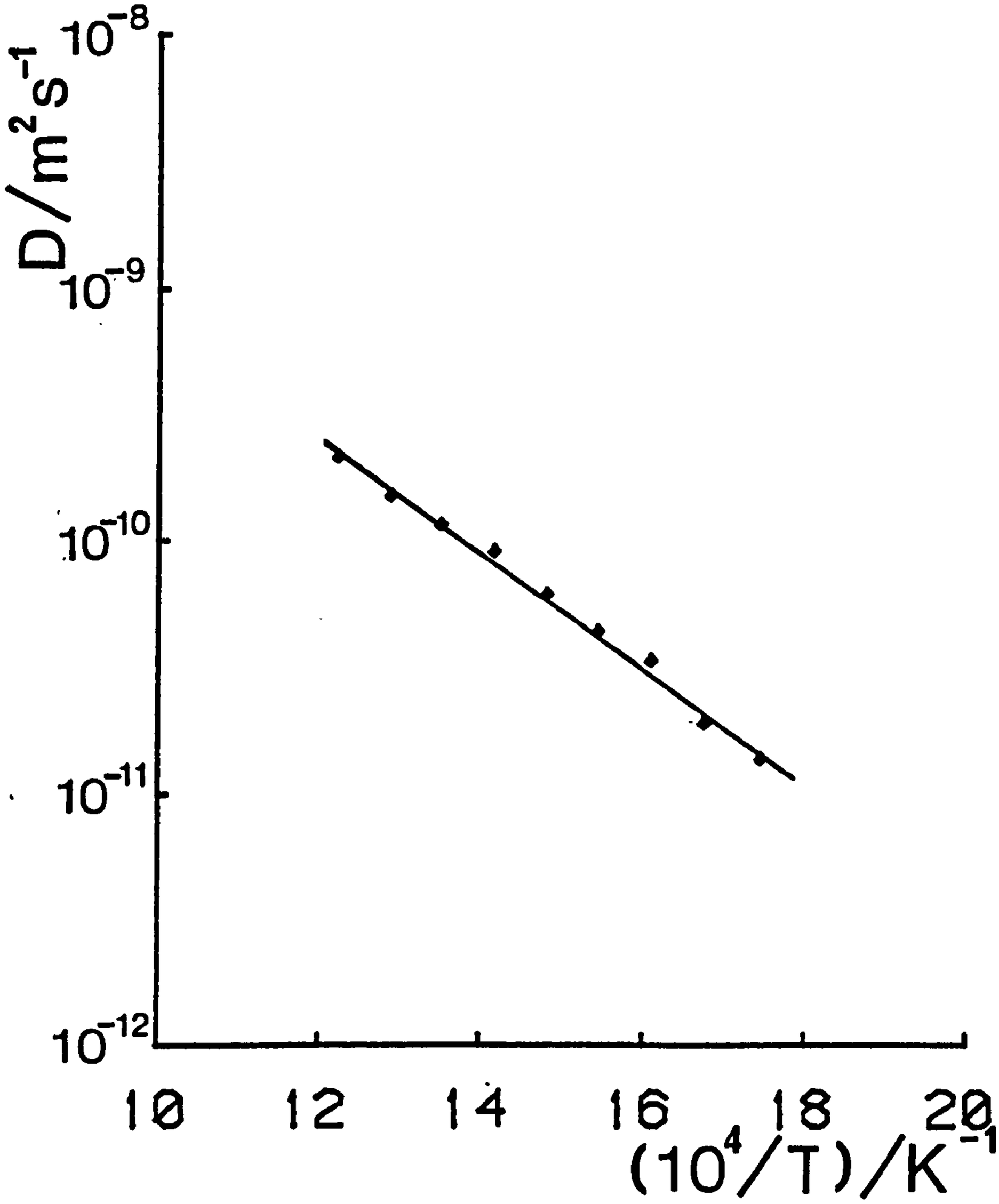

Fig 5.17 Variation of the diffusion coefficient D with inverse temperature 1/T for an AISI 316, 5.0×10^{-5}m, foil which was cleaned by an ion beam.

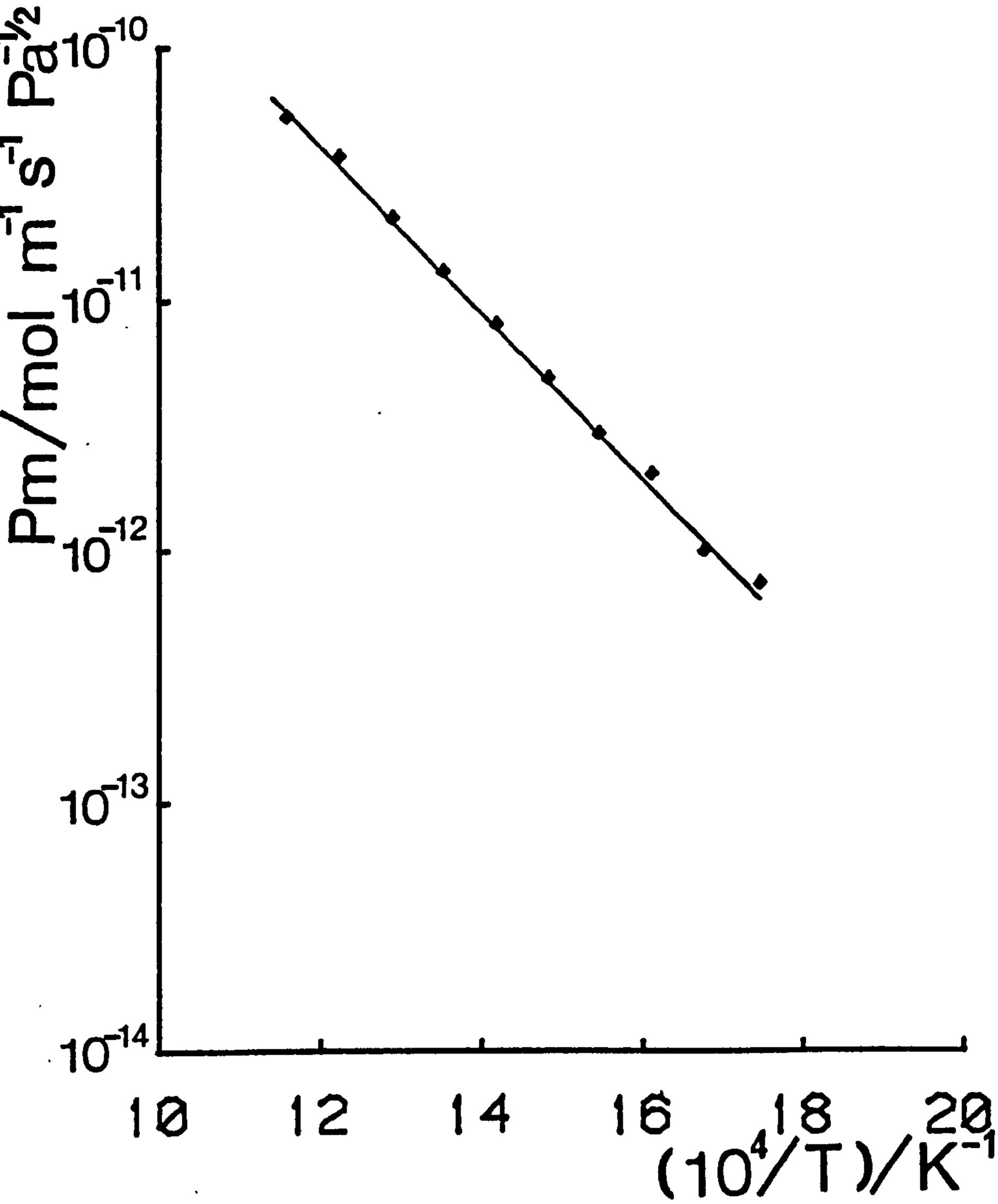

Fig 5.18 Variation of the permeation coefficient P_m with inverse temperature 1/T for an AISI 316, 5.0×10^{-5}m, foil which was cleaned by an ion beam.

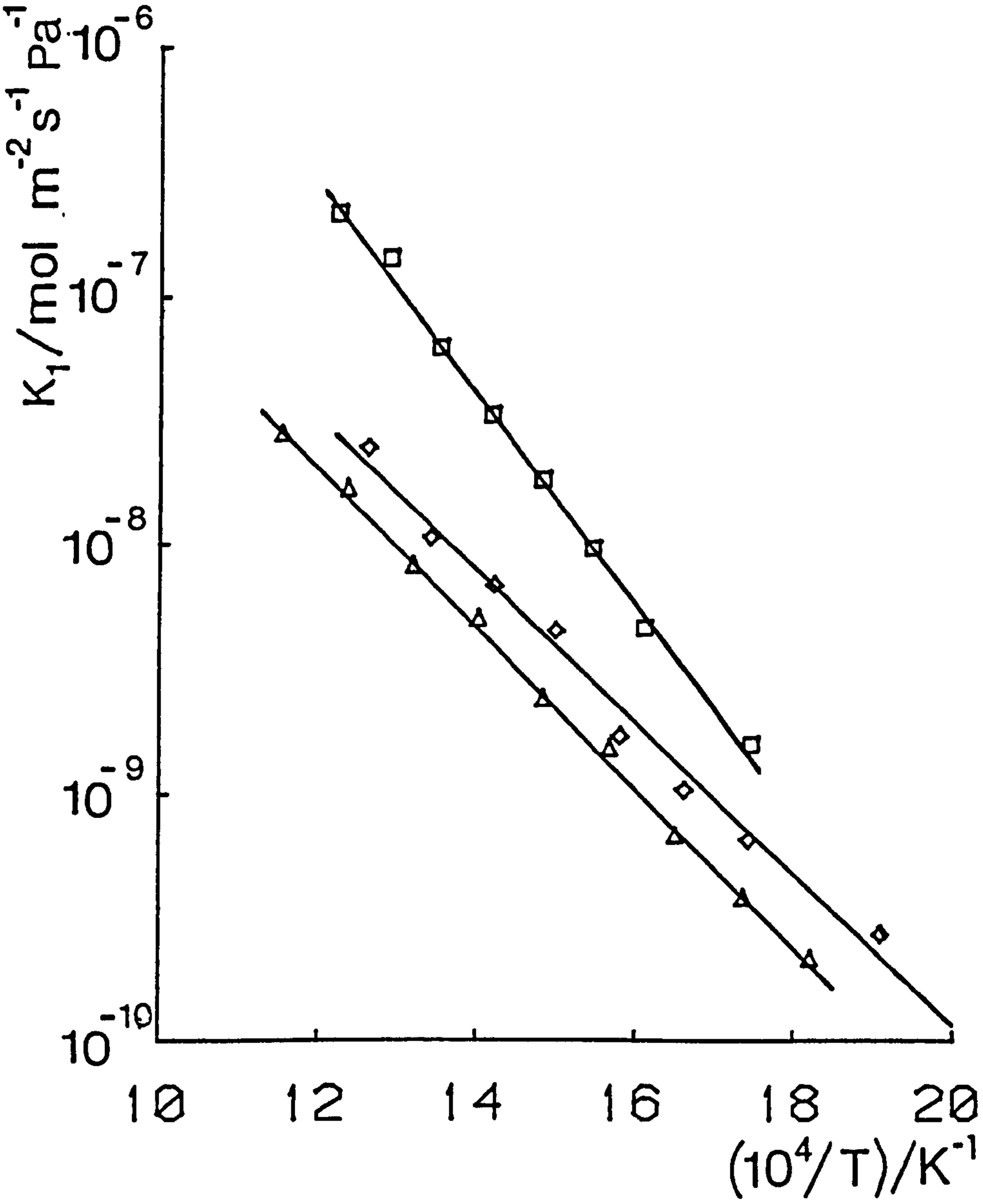

Fig 5.19 Variation of the rate constant k_1 with inverse temperature 1/T for AISI 316.

Upper curve: 5.0×10^{-5}m foil cleaned by an ion beam.

Middle curve: 5.0×10^{-5}m foil with symmetric oxide.

Lower curve: 1.0×10^{-4}m foil cleaned by an ion beam.

A least squares fit of these Arrhenius plots provides the following equations for D,P_m and k_1 for these clean AISI 316 foils.

For the ion beam cleaned AISI 316, 1.0×10^{-4}m foil:

$$D=(1.51\pm0.11)\times10^{-6}\exp\{-[(6.665\pm0.062)\times10^{3}/T]/K^{-1}\}m^{2}s^{-1} \quad [5.16]$$

$$P_m=(1.06\pm0.12)\times10^{-6}\exp\{-[(8.393\pm0.098)\times10^{3}/T]/K^{-1}\}molm^{-1}s^{-1}Pa^{-\frac{1}{2}} \quad [5.17]$$

$$k_1=(1.42\pm0.09)\times10^{-4}\exp\{-[(7.376\pm0.057)\times10^{3}/T]/K^{-1}\}molm^{-2}s^{-1}Pa^{-1} \quad [5.18]$$

For the ion beam cleaned AISI 316, 5.0×10^{-4}m foil:

$$D=(6.69\pm0.11)\times10^{-7}\exp\{-[(6.291\pm0.132)\times10^{3}/T]/K^{-1}\}m^{2}s^{-1} \quad [5.19]$$

$$P_m=(6.69\pm0.65)\times10^{-7}\exp\{-[(8.118\pm0.093)\times10^{3}/T]/K^{-1}\}molm^{-1}s^{-1}Pa^{-\frac{1}{2}} \quad [5.20]$$

$$k_1=(1.34\pm0.32)\times10^{-4}\exp\{-[(6.967\pm0.228)\times10^{3}/T]/K^{-1}\}molm^{-2}s^{-1}Pa^{-1} \quad [5.21]$$

Interestingly the values of k_1 are significantly smaller for the 1.0×10^{-4}m foil, fig 5.19. This and the values of D and P_m are discussed in chapter 6.

5.4.2 Oxidised surfaces

The 5.0×10^{-5}m thick foil descibed in the above sub-section was the subjected to a two stage oxidation process. First, it was oxidised on both sides *in* 0.9 torr of air at 1023K for 24 hours. The surface conditions on both surfaces of the foil were thus assumed similar so that once again, analysis is base on the assumption of $\mu = 0$. A

series of temperature , pressure and frequency runs were performed. For reference purposes this foil condition is referred to as the symmetric oxide.

The results for the 5.0×10^{-4}m foil symmetric oxide are tabulated in table 6. Figs 5.20 and 5.21 show the variation of D and P_m with 1/T for this symmetric oxide. The variation of k_1 with 1/T is shown in fig 5.19.

A least squares fit of these Arrhenius plots provides the following equations for D,P_m and k_1 for the symmetric and asymmetric foil oxides repectively.

For the symmetrically oxidised AISI 316, 5×10^{-4}m foil:

$$D=(1.34\pm0.10)\times10^{-7}\exp\{-[(5.227\pm0.070)\times10^{3}/T]/K^{-1}\}m^{2}s^{-1} \quad [5.22]$$

$$P_m=(3.73\pm0.27)\times10^{-7}\exp\{-[(7.590\pm0.067)\times10^{3}/T]/K^{-1}\}molm^{-1}s^{-1}Pa^{-\frac{1}{2}} \quad [5.23]$$

$$k_1=(3.22\pm0.34)\times10^{-2}\exp\{-[(9.712\pm0.097)\times10^{3}/T]/K^{-1}\}molm^{-2}s^{-1}Pa^{-1} \quad [5.24]$$

The reduction of k_1 after oxidation is considerably less dramatic than with stainless steel 304. This is in agreement with other work and is discussed more fully in chapter 6 along with the results for D and P_m.

Table 5.6 AISI 316, thickness ℓ = 5.0×10^{-5}m, cross-sectional area y = $5.0\times10^{-4}m^2$ and oxidised on both surfaces. Three pressures were investigated from 80.8 - 0.804torr. Frequency range at each temperature and pressure, expressed as a cycle time θ, was 160 - 990s for typically twelve frequencies.

T/K	D/m^2s^{-1}	$P_m/molm^{-1}s^{-1}Pa^{-½}$	$k_1/molm^{-2}s^{-1}Pa^{-1}$
793	***	2.20×10^{-11}	2.41×10^{-8}
746	1.45×10^{-10}	1.34×10^{-12}	1.05×10^{-8}
704	8.85×10^{-11}	6.28×10^{-12}	***
667	4.97×10^{-11}	3.18×10^{-12}	4.41×10^{-9}
633	4.06×10^{-11}	2.05×10^{-12}	1.67×10^{-9}
602	1.93×10^{-11}	9.78×10^{-13}	1.04×10^{-9}
574	1.21×10^{-11}	5.33×10^{-13}	6.48×10^{-10}
548	5.53×10^{-12}	2.22×10^{-13}	7.27×10^{-10}
524	3.44×10^{-12}	1.47×10^{-13}	2.68×10^{-10}
502	3.01×10^{-12}	5.20×10^{-14}	9.16×10^{-11}

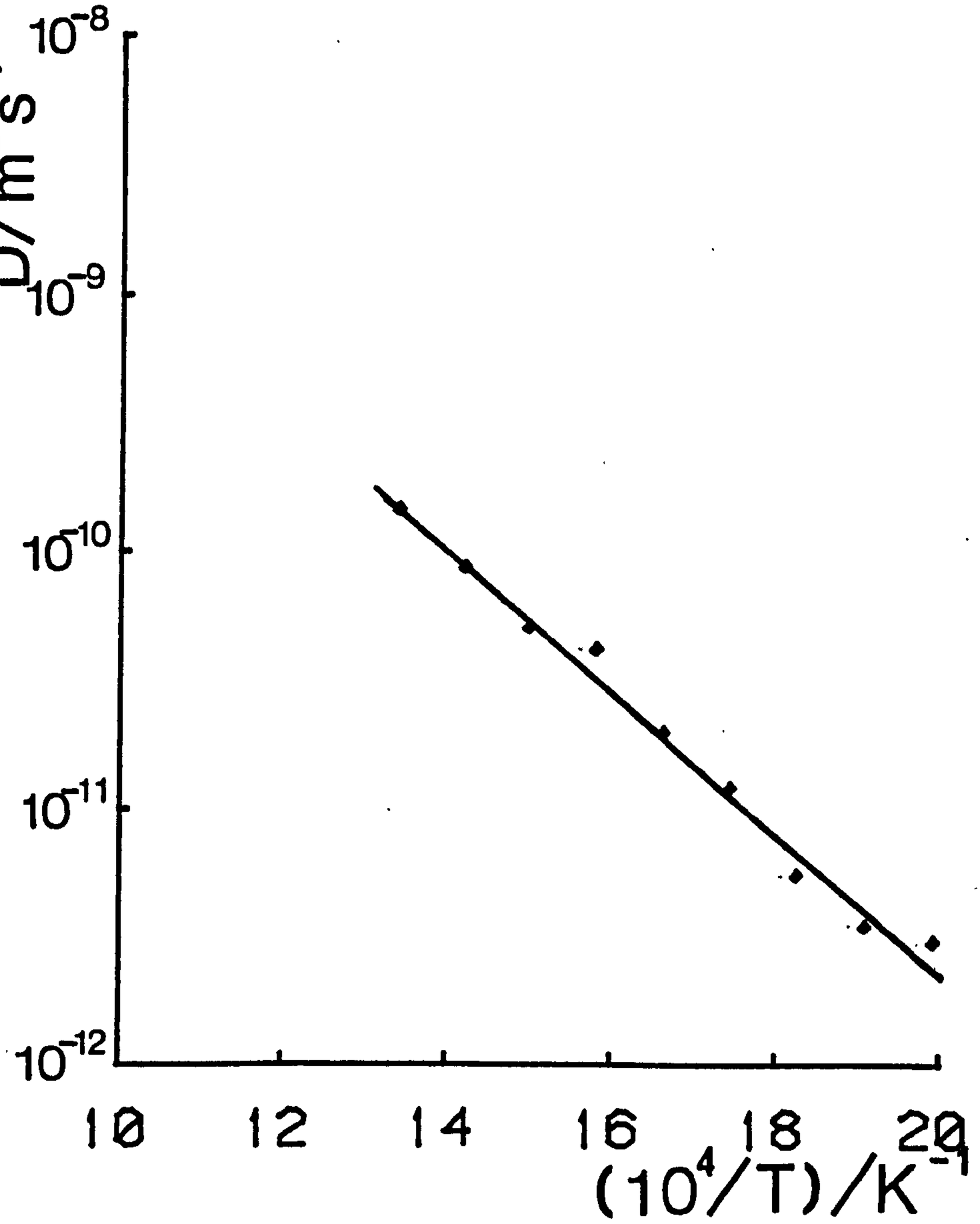

Fig 5.20 Variation of the diffusion coefficient D with inverse temperature 1/T for an AISI 316, 5.0×10^{-5}m, foil for a symmetric oxide.

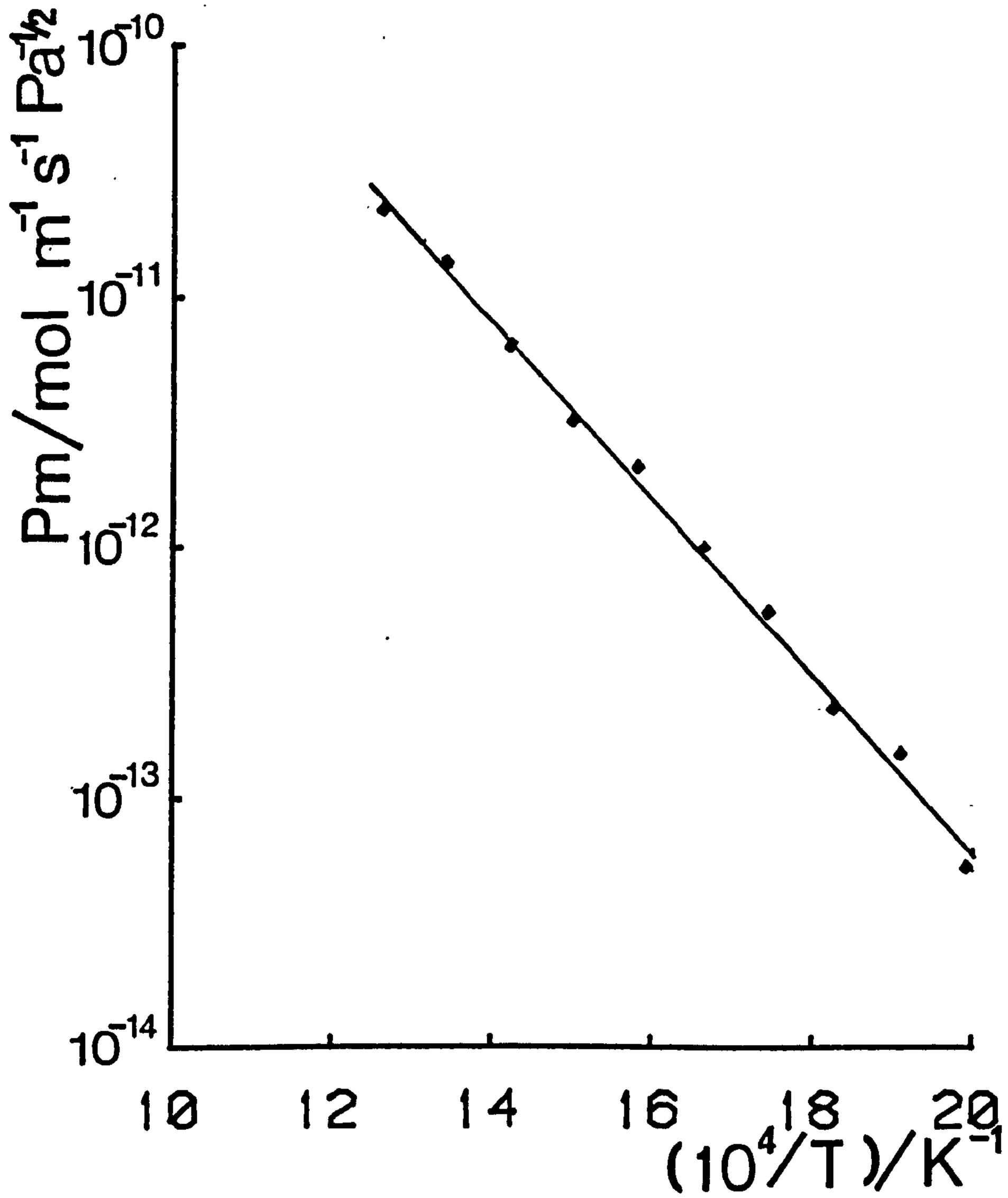

Fig 5.21 Variation of the permeation coefficient P_m with inverse temperature 1/T for an AISI 316, 5.0×10^{-5}m, foil for a symmetric oxide.

5.5 THE VARIATION OF PHASE LAG WITH PRESSURE

This section is concerned with the iso-frequency, iso-thermal variation of phase lag with input pressure. Data are provided for all the AISI 304 and 316 specimens and surface conditions. Three frequencies are used in each figure and are, in terms of Θ, 160, 280 and 990s. Temperatures were chosen such that ς, for the three frequencies, spanned the range 0.5 - 2. The precise values are given with each figure.

The points to note about the variation of phase lag with pressure are that limitations at a single surface may cause a phase lag varying by up to $\pi/4$ while limitations at the two surfaces has a limit of $\pi/2$. Examination of the data for the AISI 304, 2.5×10^{-4}m clean foil, fig 5.22, shows the higher pressures reaching the low plateau of the curves. This indicates that at these higher pressures conditions approached those of diffusion limited $p^{½}$ permeation. In contrast, the clean AISI 316 1.0×10^{-4}m and 5.0×10^{-5}m foils, fig 5.23 and 5.24, have clearly not reached the bottom plateau even at the highest pressure.

The theoretical curves indicate it would take a multiplier of about 100 in the pressure to bring the 316 foils to a condition of diffusion limited permeation. This may be because these specimens, being thinner, are less open to control by bulk diffusion. It should also be noted that the 2.5×10^{-4}m foil had the largest k_1 of any foil and was in effect the cleanest. It was therefore the foil most open to

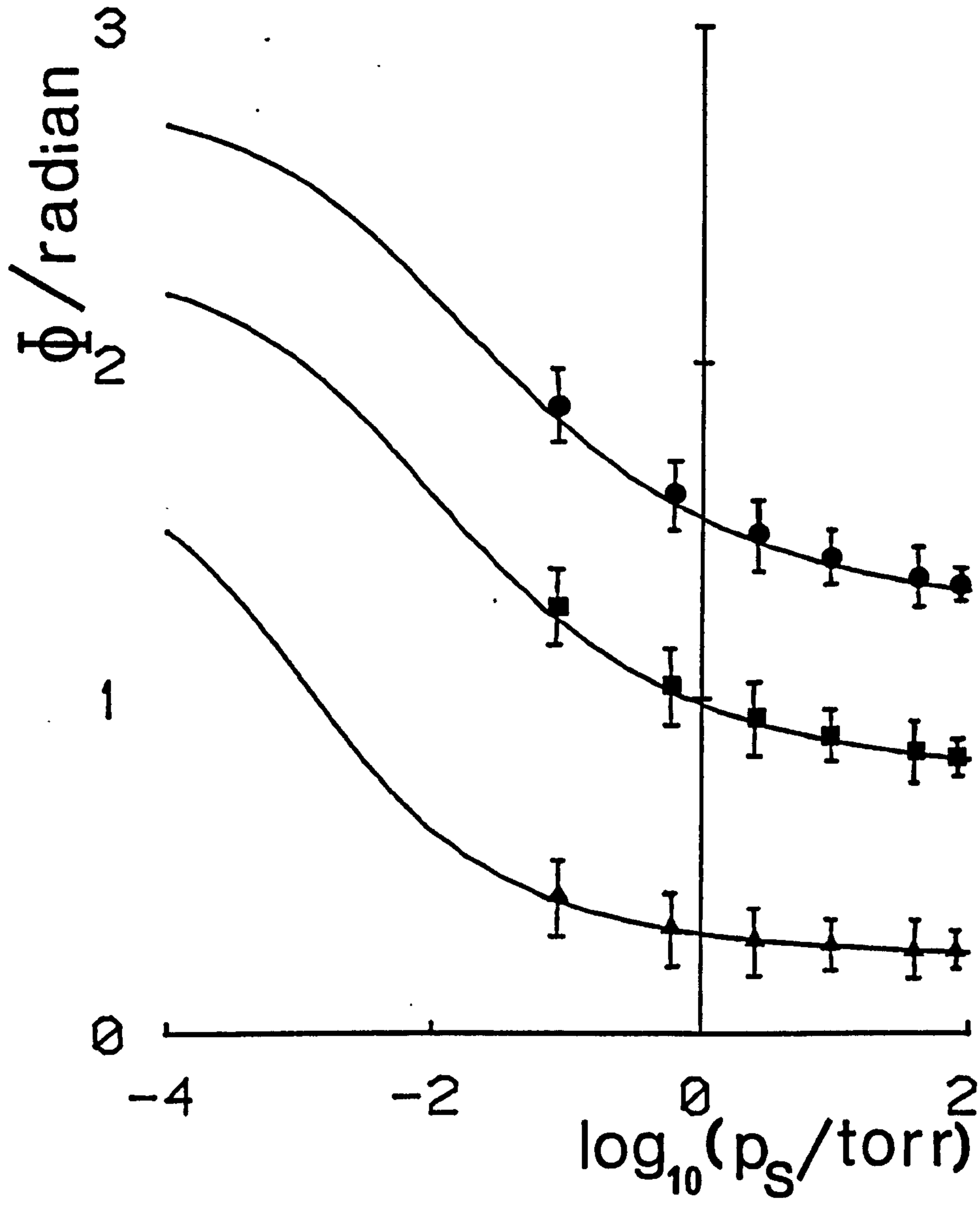

5.22 Iso-frequency, isothermal variation of the phase lag Φ with input pressure p_s. Temperature was 791K for an AISI 304, $\ell = 2.5\times10^{-4}$m, foil which was cleaned by an ion beam.

The upper to lower theoretical curves are for ζ equal to 2.050, 1.550 and 0.8241 respectively. This corresponds to cycle times, Θ, of 160, 280 and 990s.

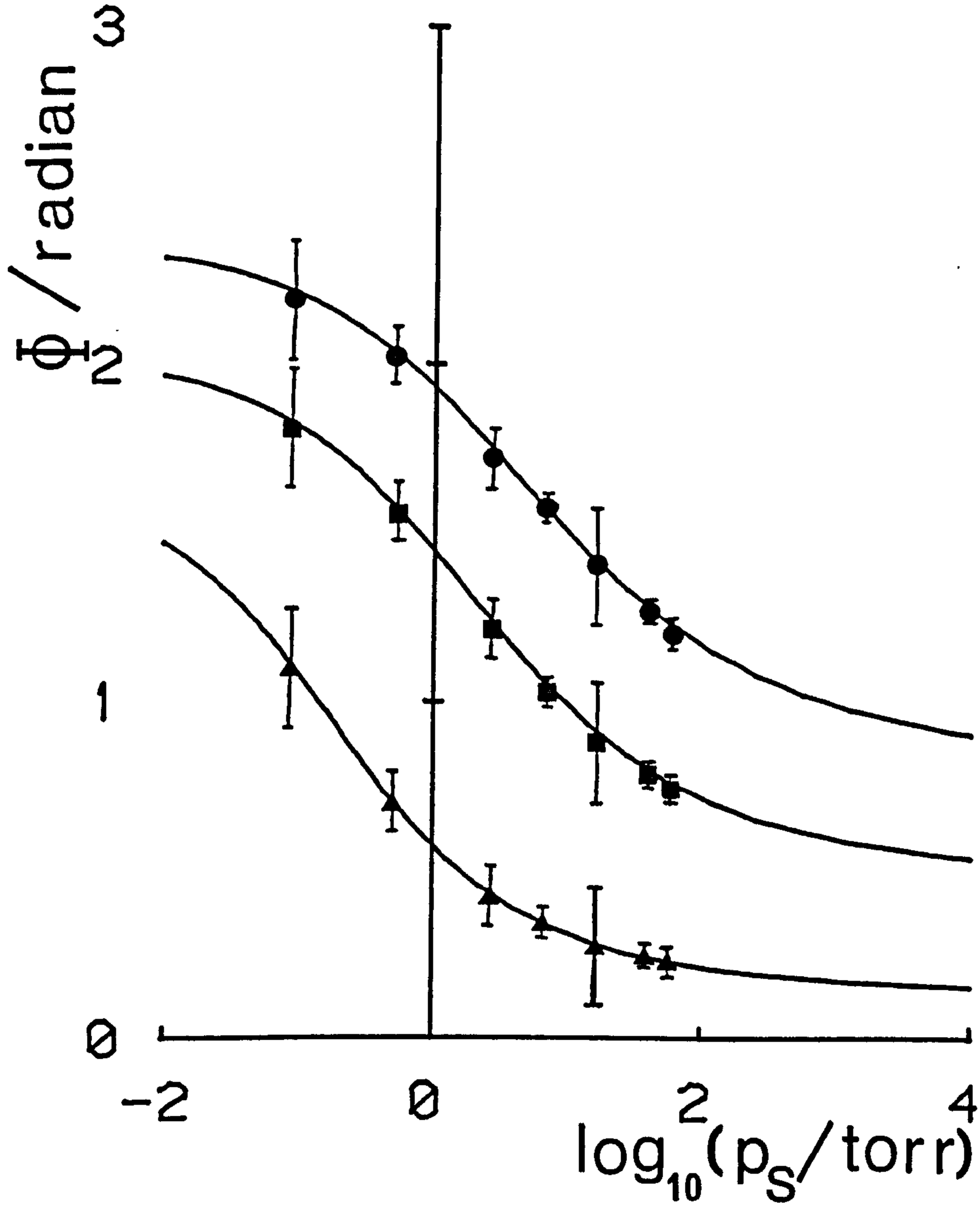

5.23 Iso-frequency, isothermal variation of the phase lag Φ with input pressure p_S. Temperature was 674K for an AISI 316, $\ell = 1.0\times10^{-4}$m, foil which was cleaned by an ion beam.

The upper to lower theoretical curves are for ζ equal to 1.590, 1.202 and 0.6391 respectively. This corresponds to cycle times Θ of 160, 280 and 990s.

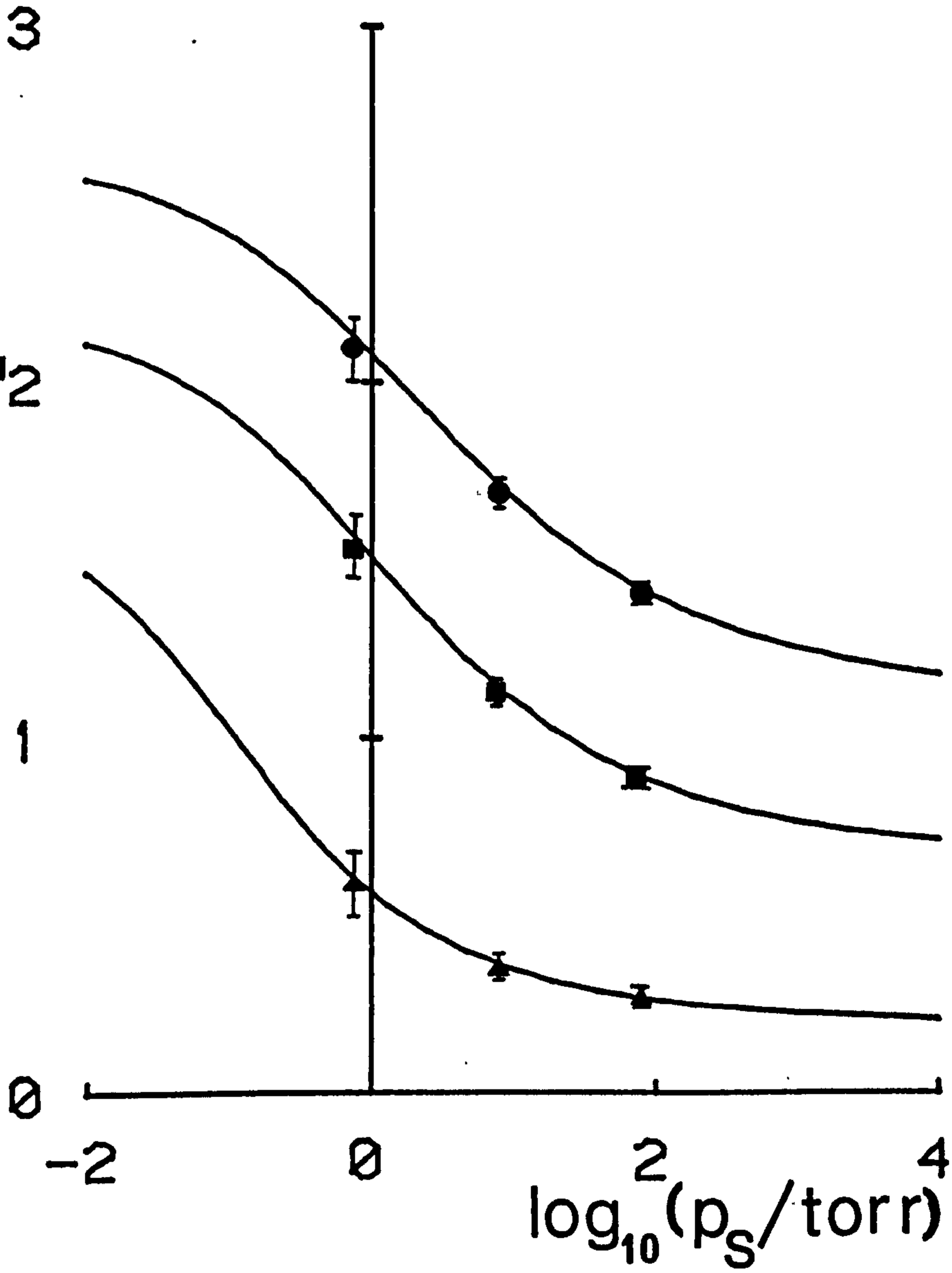

5.24 Iso-frequency, isothermal variation of the phase lag Φ with input pressure p_s. Temperature was 573K for an AISI 316, $\ell = 5\times10^{-5}$m, foil which was cleaned by an ion beam.

The upper to lower theoretical curves are for ζ equal to 1.879, 1.421 and 0.7555 respectively. This corresponds to cycle times, Θ, of 160, 280 and 990s.

diffusion control.

The results from the AISI304, 3.0×10^{-4}m foil, fig 5.29, are a poor fit, in comparison with those from the other foils. In part this is because the data covered just two pressures. Also, though it was the thickest foil it did not reach the lower diffusion limited plateau at the highest pressure. This is indicative that cleaning by the ion beam is a necessary technique when attempting to establish just how the transition from diffusion to surface limited permeation takes place.

A surface limited p^1 plateau was obtained for the lowest pressures using the 2.5×10^{-4}m single surface oxidised foil, fig 5.26. Notice that the increase in Φ with decreasing pressure is limited to a $+\pi/4$ phase as expected with single surface oxidation and the condition, $\mu = -1$. The 5×10^{-5}m symmetric oxide foil, fig 5.27, when compared with the 5.0×10^{-5}m clean foil, fig 5.24, shows a small increase in the phase lag at the same temperature and demonstrates why there is such a small decrease in k_1 between these two foil conditions.

Data taken at lower values of ς are illustrated in fig 5.28 for the 1.0×10^{-4}m foil using a higher temperature. Notice that high ς curves are parallel since for high values of ς the variation of phase lag Φ with ς becomes linear.

All the figures above illustrate the excellant agreement between

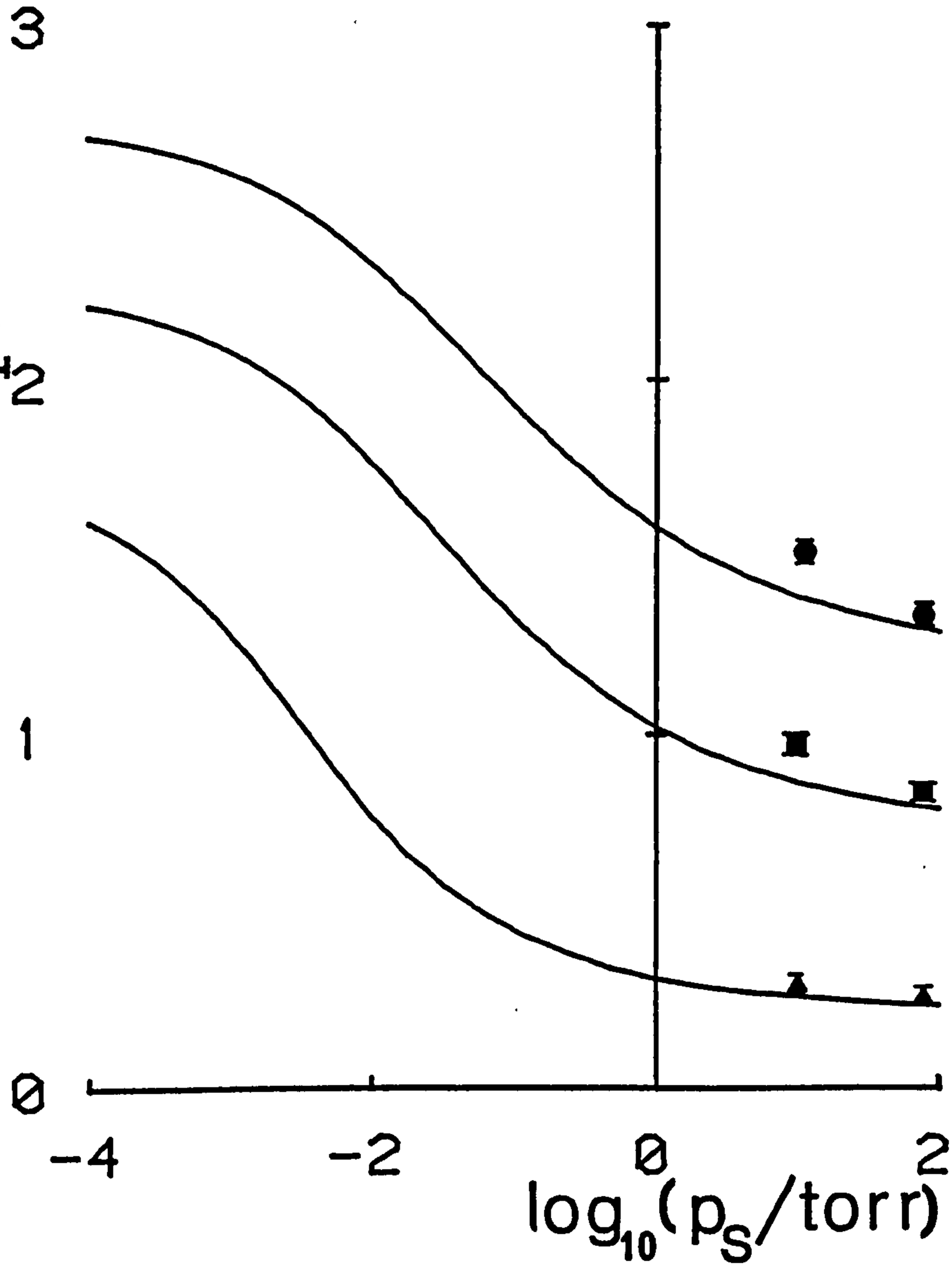

5.25 Iso-frequency, isothermal variation of the phase lag Φ with input pressure p_g. Temperature was 833K for an AISI 304, $\ell = 3.0\times10^{-4}$m, foil which was cleaned by activation.

The upper to lower theoretical curves are for ζ equal to 1.937, 1.464 and 0.7787 respectively. This corresponds to cycle times, Θ, of 160, 280 and 990s.

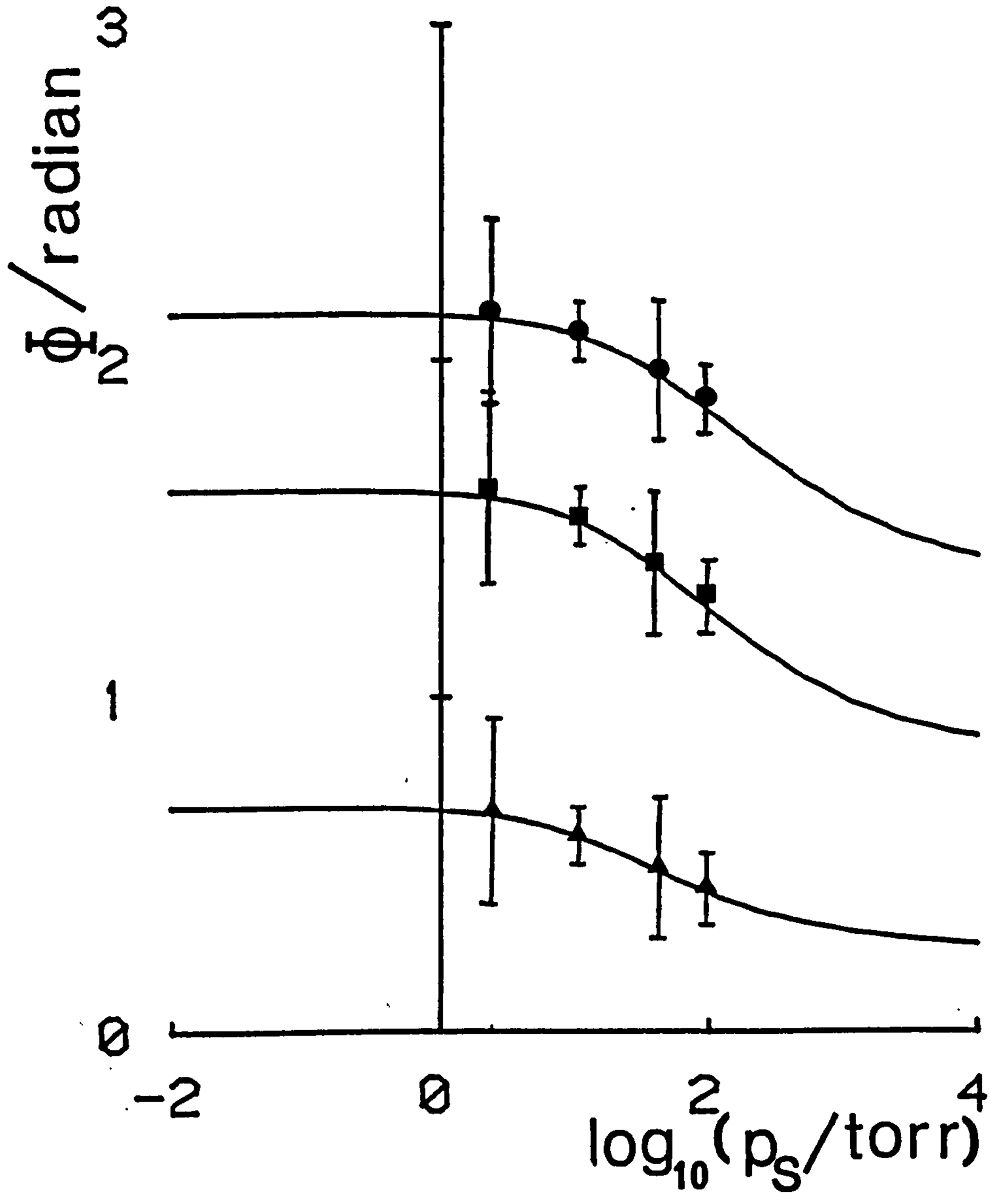

5.26 Iso-frequency, isothermal variation of the phase lag Φ with input pressure p_g. Temperature was 792K for an AISI 304, $\ell = 2.5\times10^{-4}$m, foil which was oxidised on the input surface only.

The upper to lower theoretical curves are for ζ equal to 2.156, 1.630 and 0.8668 respectively. This corresponds to cycle times, θ, of 160, 280 and 990s.

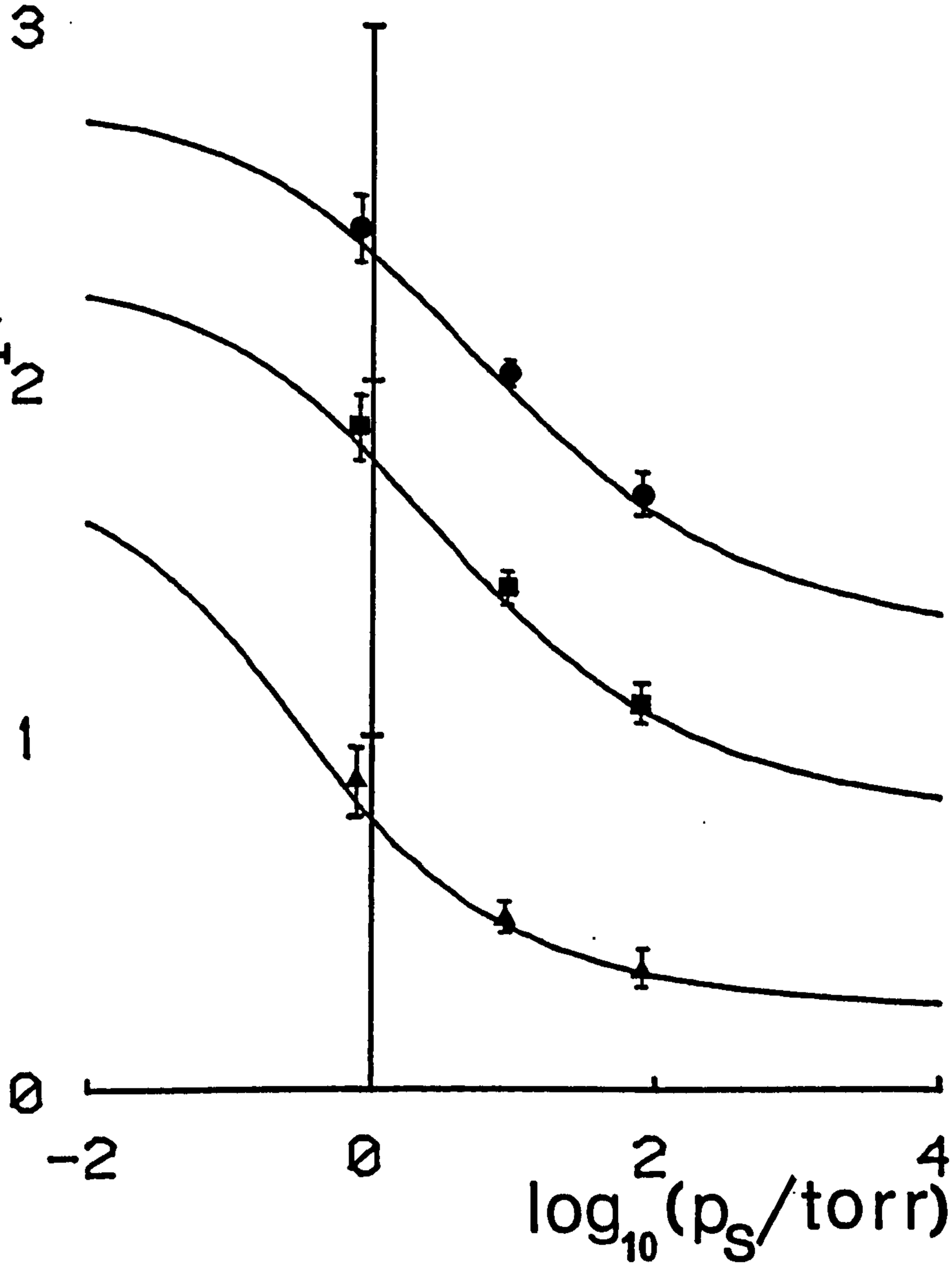

5.27 Iso-frequency, isothermal variation of the phase lag Φ with input pressure p_s. Temperature was 574K for an AISI 316, $\ell = 5.0\times10^{-5}$m, foil subjected to a symmetric oxidation.

The upper to lower theoretical curves are for ζ equal to 2.014, 1.523 and 0.8097 respectively. This corresponds to cycle times, Θ, of 160, 280 and 990s.

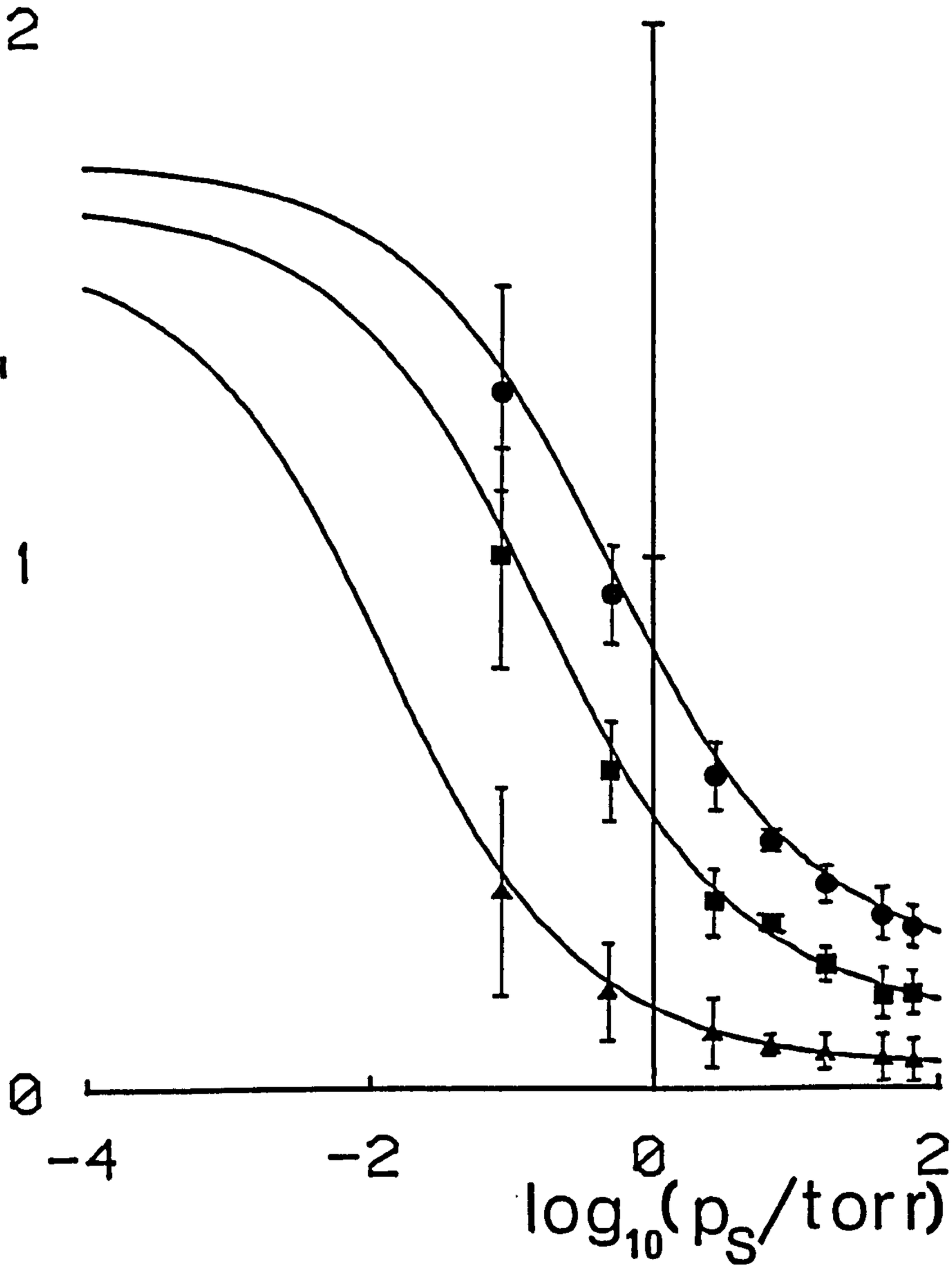

5.28 Iso-frequency, isothermal variation of the phase lag Φ with input pressure p_S. Temperature was 810K for an AISI 316, $\ell = 1.0\times10^{-4}$m, foil which was cleaned by an ion beam.

The upper to lower theoretical curves are for ζ equal to 0.7280, 0.5507 and 0.2929 respectively. This corresponds to cycle times Θ of 160, 280 and 990s.

theoretical and experimental values. All data shows at least part of the characteristic changeover, from the $p^{1/2}$ to the p^{1} permeation region. The process of finding this changeover region is extremely important, since it is the structure in this information that allows evaluation of the rate constant k_1.

5.6 FLUX MODULATION BY ION INJECTION RESULTS

To examine a different type of flux modulation one specimen was exposed to modulated current of hydrogen ions. The specimen of AISI 304, thickness 1.25×10^{-4}m, was mounted in the external furnace configuration and cleaned by an ion beam. The observed variation of phase lag Φ, with square root frequency $\nu^{1/2}$ at a temperature of 579K is plotted in fig 5.29

Theoretical curves for ion modulation and the corresponding one for pressure modulation, calculated from the data of section 5.2, are shown on the same plot. Both theoretical curves are calculated on the suppositions that surface reactions are fast and permeation is diffusion limited with zero backflow.

This sort of experiment gives the right general variation but its noise level was too high for it to be an effective alternative to the pressure modulation method, for the current design of gun.

5.7 PARALLEL DIFFUSION RESULTS

One AISI 304 specimen mounted in the internal configuration was used to investigate the parallel diffusion calculation of 4.7. To provide a good signal the input pressure was set at 83.5torr. To enable the frequency factor, ζ, to be kept low the relatively high temperature of 918K was chosen. This allowed the characteristic maximum and minimum, of the phase lag curve and the minimum of

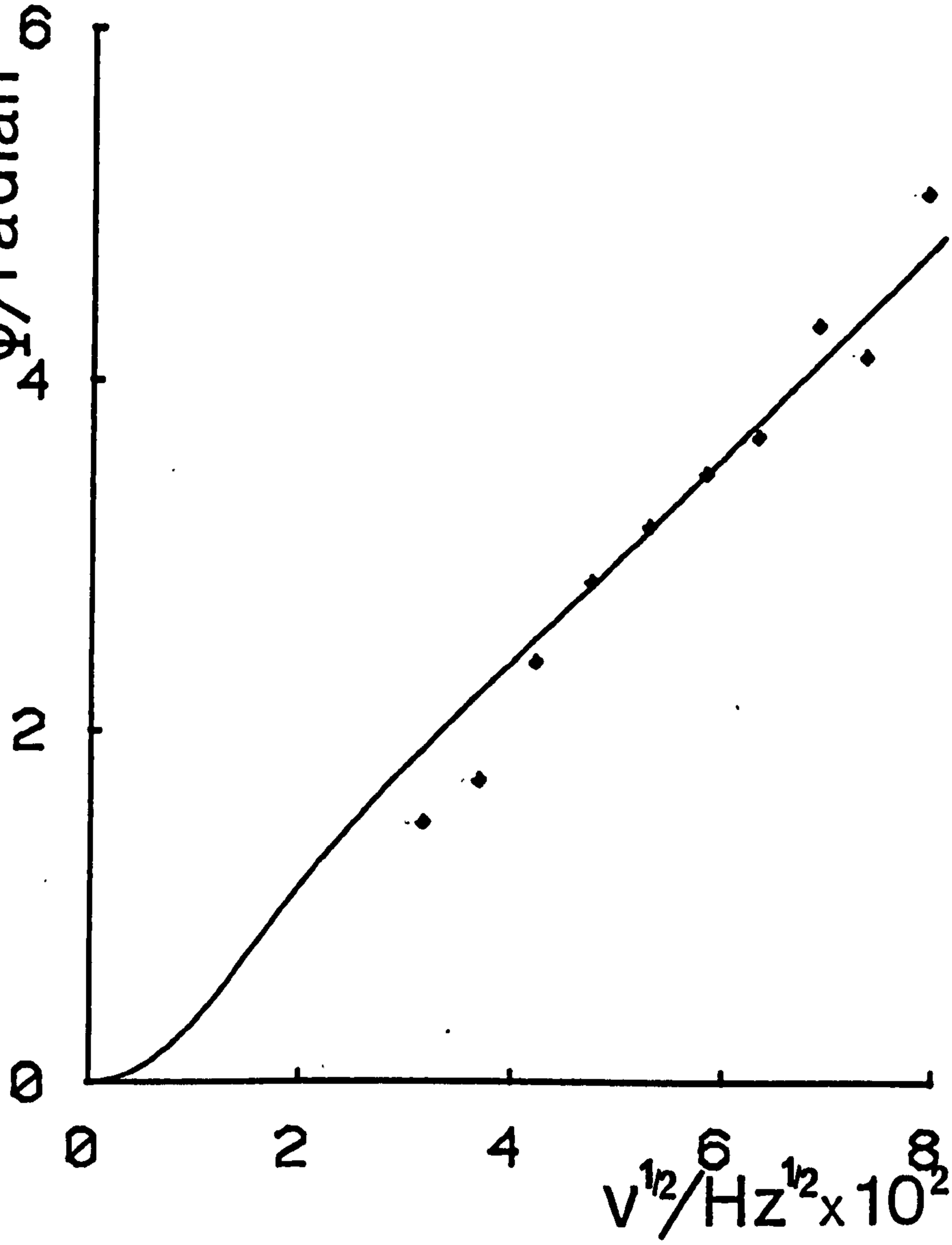

5.29 Variation of phase lag Φ with square root frequency $\nu^{1/2}$ for flux that is modulated by ion beam injection. The foil was AISI 304, 1.25×10^{-4}m, which was cleaned by an ion beam. The theoretical curve was obtained from considering diffusion limited conditions and using D obtained from the pressure modulation results for 304.

the relative amplitude modulation ratio curve to be held within reasonable experimental limits.

To map out these variations, fifty-eight frequency data points were run. The results are plotted on figs 5.30 and 5.31 with theoretical curves generated by a single parameter fit to the constant B introduced in 4.7. The other parameter A was set at 5.33 this being the known ratio of the specimen to tube wall thickness. The curves were derived subsequent to the assumptions that: permeation was diffusion limited, surface reactions were fast, and there was zero backflow.

The curves fitted well considering the assumptions made in 4.7. The deviations from the theoretical curves were consistent for a calculation made with no surface limitations.

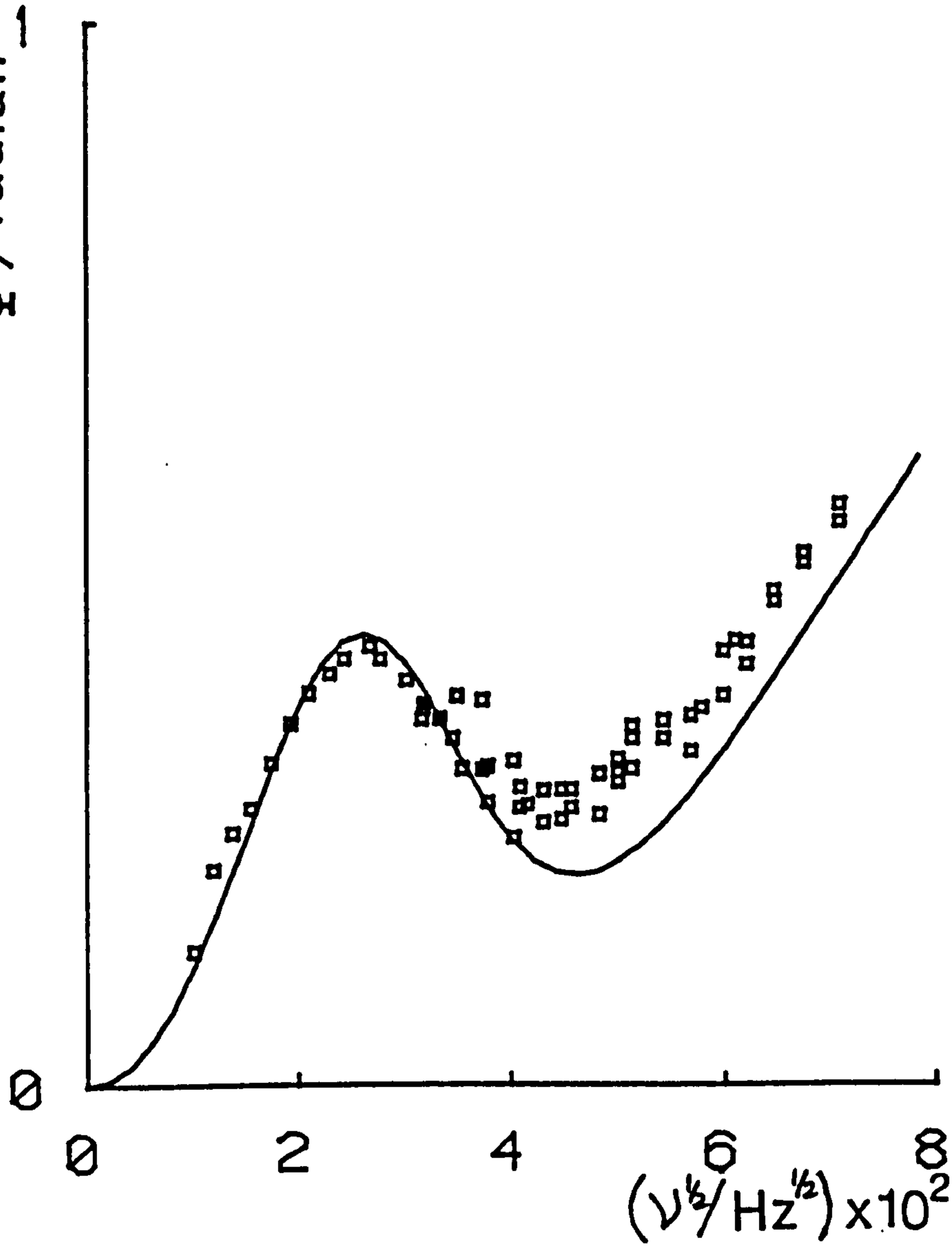

5.30 The variation of the phase lag Φ with square root frequency $\nu^{1/2}$ illustrating parallel diffusion. Notice the clear maximum and minimum characteristic of parallel diffusion. The parameters A and B for the theoretical curve, descibed in section 4.7, are 5.33 and 0.61 respectively.

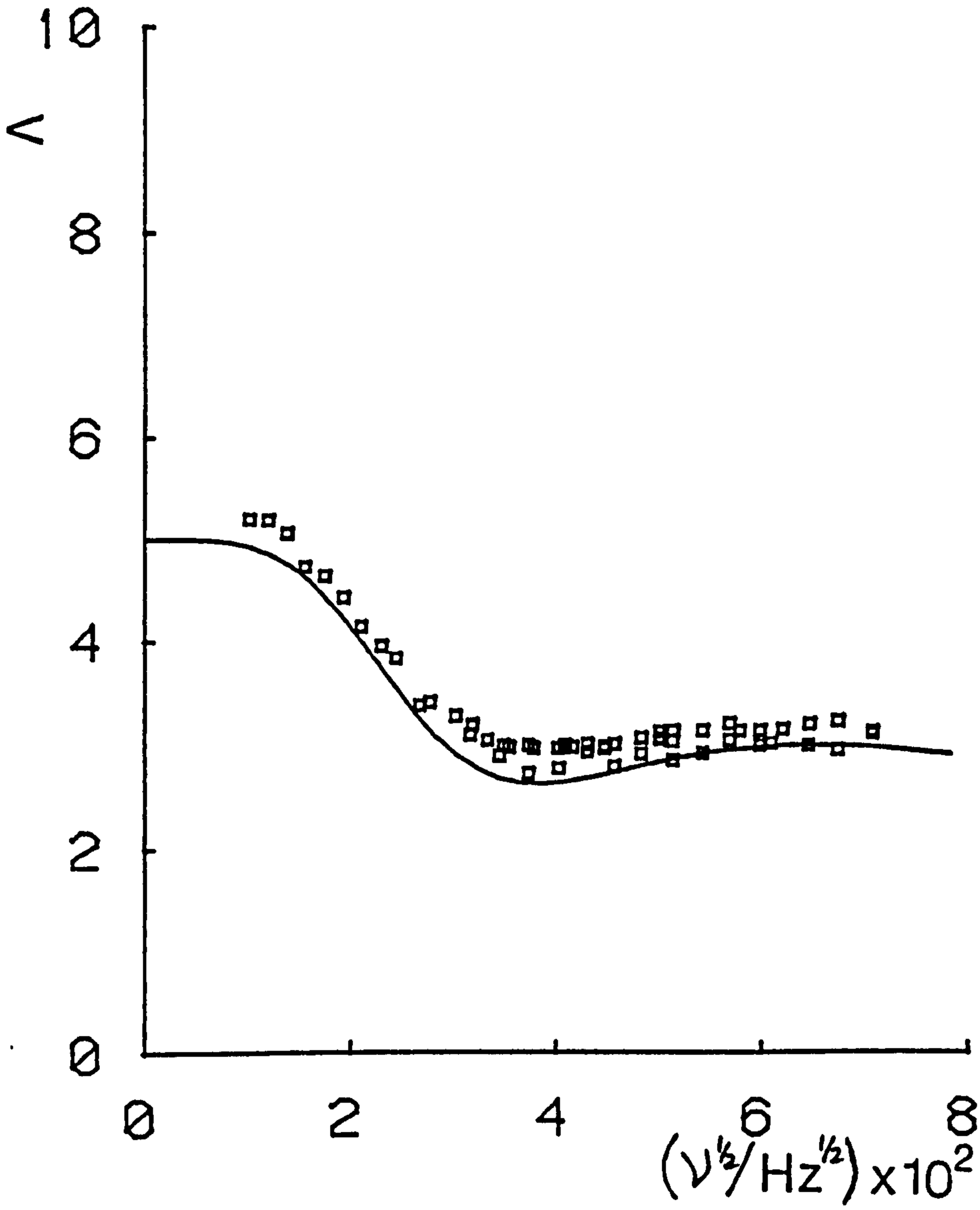

5.31 The variation of the relative amplitude modulation ratio Λ with square root frequency $\nu^{1/2}$ illustrating parallel diffusion. Notice the characteristic minimum of the curve. The parameters A and B for the theoretical curve, described in section 4.7, are 5.33 and 0.61 respectively.

5.8 OXIDE THICKNESS

To allow an interpretation of observed surface rates on oxidised foils, thickness measurements were made on two foils. The foils were AISI 304, 2.5×10^{-4}m single surface oxide and AISI 316, 5.0×10^{-5}m symmetric surface oxide. The method used to measure the oxide thickness was secondary ion mass spectroscopy, SIMS.

The SIMS instrument uses primary beam of oxygen or argon to give secondary ion emission from the sample surface. The resulting ionic species are identified by mass spectrometry and provides measures of the elemental composition. The progressive removal of the specimen during analysis allows the distribution in depth of a particular element in the specimen to be studied.

In the above two specimens the intensity of the elements of Fe^+,Mo^+,Cr^+ and Ni^+, were measured for a primary beam of oxygen, against depth. Depth measurement was obtained by mechanically measuring the depth of the eroded hole, using a stylus technique, after the experiment and calibrating the measured erosion rate. From these ion intensity curves an estimate of the oxide thickness can be made. For the above specimens they were estimated as:

(1) AISI 304, 2.5×10^{-4}m, single surface oxide depth = $1.0 \pm 0.2\mu$m

(2) AISI 316, 5.0×10^{-5}m, symmetric surface oxide depth = $0.4\pm0.2\mu$m

The large uncertainties were a product of the non-polished metal surfaces.

CHAPTER 6: DISCUSSION

This chapter is divided into the following sections: 6.1, deals with the results themselves, makes comparisons with other work, and examines compatibility of the analytic model with observed data; 6.2, details the rate constant k_1, presents a comparison with other work, discusses mechanisms of diffusant transport through oxide layers and describes diffusant flux in terms of the chemical potential; 6.3, discusses some alternative models for non-Richardson permeation; 6.4, details variations of the permeation power law index with diffusant flux and presents a means of adjusting reported non-half order permeation fluxes; 6.5, summarises the chapter.

6.1 DISCUSSION OF THE RESULTS PRESENTED IN CHAPTER 5 AND SUITABILITY OF ANALYSIS.

The topics considered in this section are:

6.1.1, the influence of surface reaction on flux, an assessment of the two rate constant model for the interpretation of data, the consistency of the data in terms of D,P_m, and the variation of the parameter k_1 with inverse temperature; 6.1.2, comparisons of D, P_m and k_1 with values reported elsewhere; 6.1.3, the sensitivity of interpretation of variations in the symmetry parameter μ.

6.1.1 Discussion of diffusion limited flux behaviour: an assessment of the two rate constant model for the interpretation of data.

From figs 5.22 - 5.28, it is clear that the phase lag Φ, increases as input pressure is reduced. When expressed in terms of the variation of phase lag with square root frequency, the extrapolated high frequency linear region intercepts the Φ-axis above $-\pi/4$. This deviation from the diffusion limited intercept of $-\pi/4$ increases with decreasing pressure.

It is evident, that in the experimental pressure range chosen, deviation from diffusion limited behaviour does occur and that some form of surface model incorporating finite rates of flow is required for the evaluation of the data. Whether the two rate constant model

is adequate to perform this role will be discussed in the next sub-section. In passing, it is interesting to note here that, as can be seen from fig 5.22, the diffusion limited analysis is a good approximation in some circumstances. For this example, greater than 100torr. This is a potential indicator in comparisons with other work since much of that depends on the time lag method which is relatively insensitive to the parameters of flux control and derives from a diffusion limited calculation.

The evaluation of surface limited fluxes in chapter 5 uses a simple two rate constant model of surface reactions. The independent parameters to be fitted, using this model, are D, P_m, k_1 and μ and they are expected to describe experimental data covering a pressure range of up to three decades. In question is whether the complexity provided by that model is adequate to describe the observed departure from diffusion limited behaviour.

On the basis of the experimental data reported earlier the answer to the above question must be: yes. This is so for the following three reasons.

(1) Despite differing surface conditions, imposed or otherwise, the diffusion and permeation coefficients obtained are reproducible to a high degree of consistency as shown by the aggregated results for 304 ,figs 6.1 and 6.2 and 316, figs 6.3 and 6.4, stainless steels. These aggregated results when fitted by a least squares analysis to an Arrhenius relationship are:

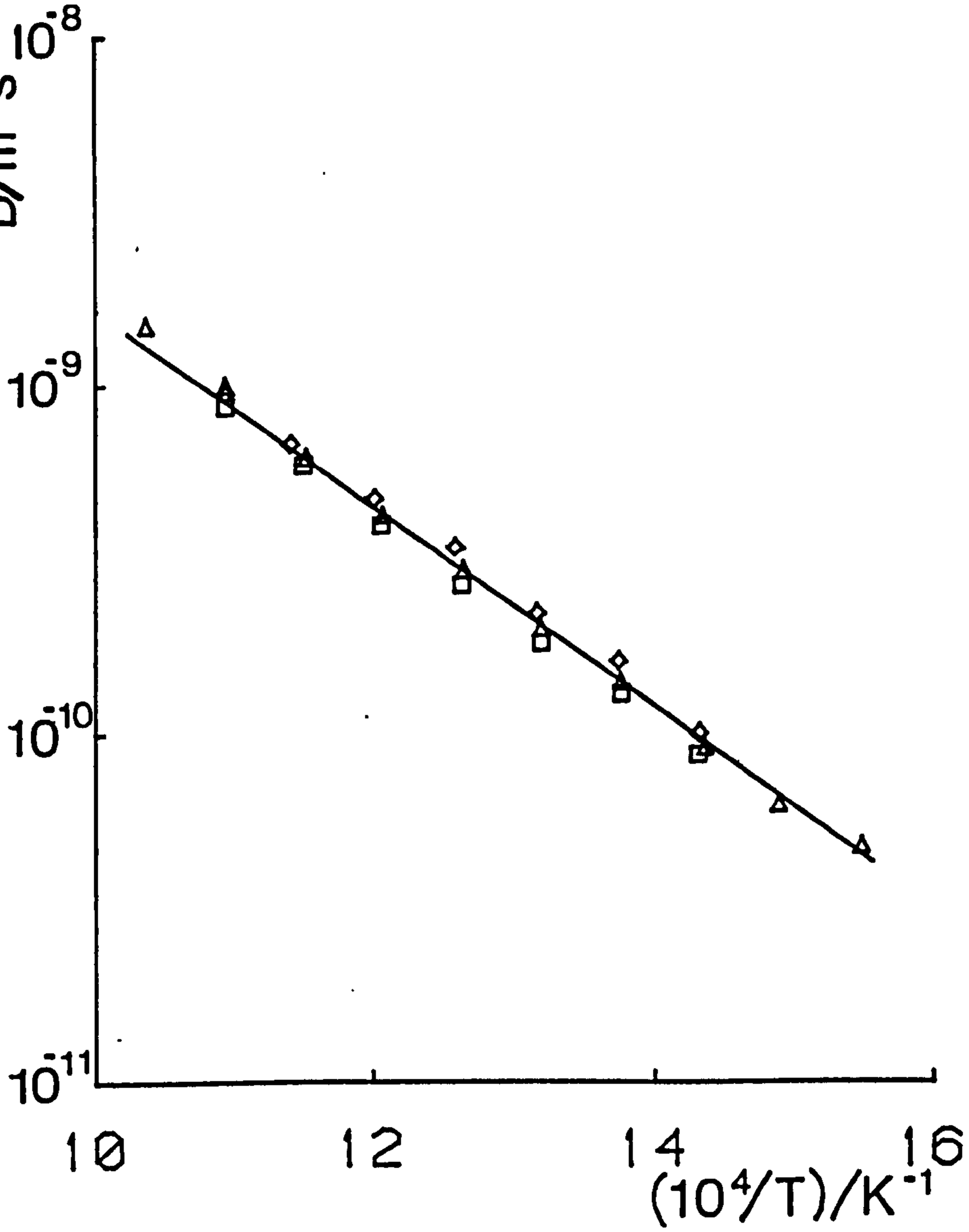

Fig 6.1 The variation of diffusion coefficient with reciprocal temperature for all 304 stainless steel data.

Key:

Triangle - 2.5×10^{-4}m, ion beam cleaned.

Square - 2.5×10^{-4}m, input surface oxidised.

Diamond - 3.0×10^{-4}m, cleaned by activation.

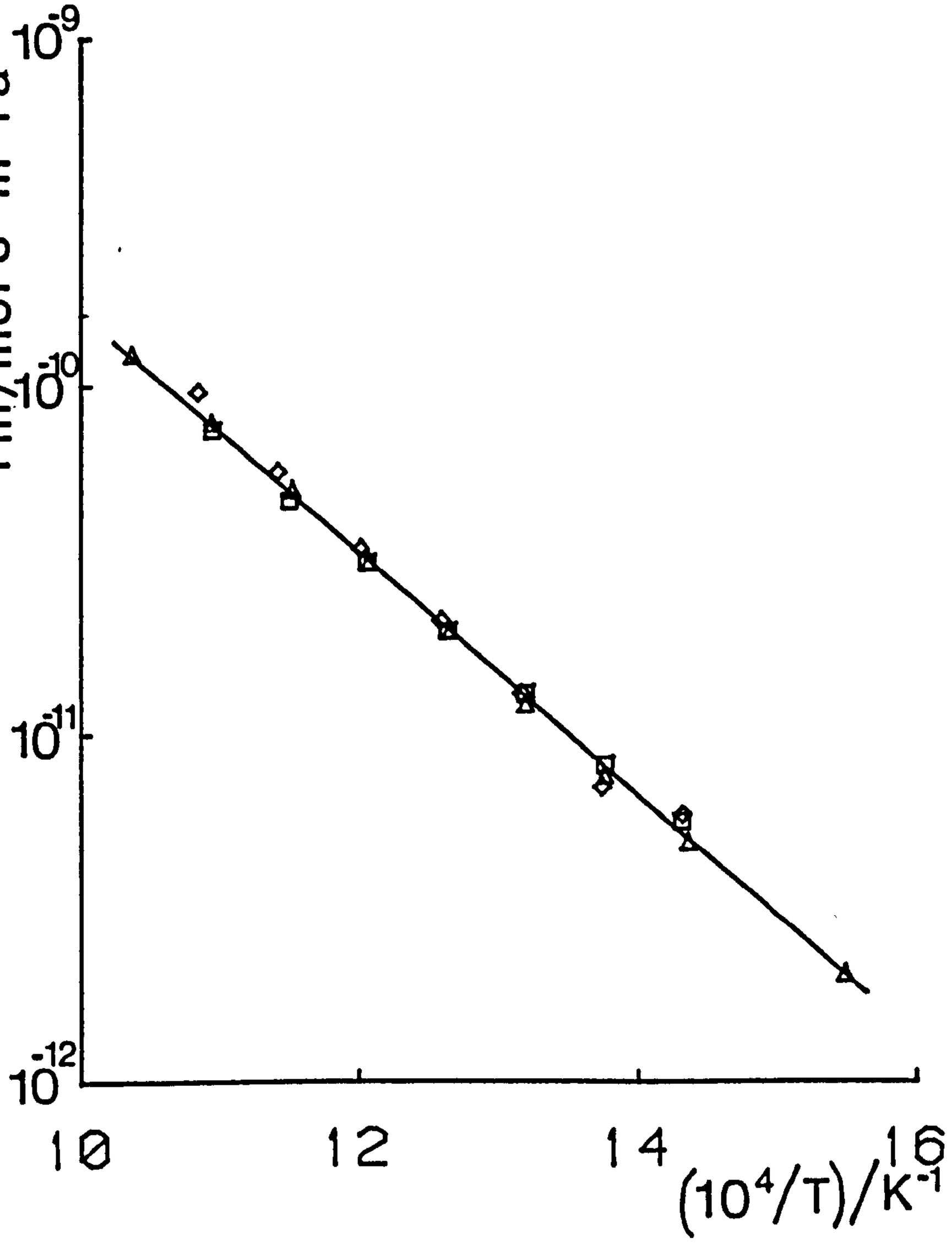

Fig 6.2 The variation of permeation coefficient with reciprocal temperature for all 304 stainless steel data.

Key:

Triangle - 2.5×10^{-4}m, ion beam cleaned.

Square - 2.5×10^{-4}m, input surface oxidised.

Diamond - 3.0×10^{-4}m, cleaned by activation.

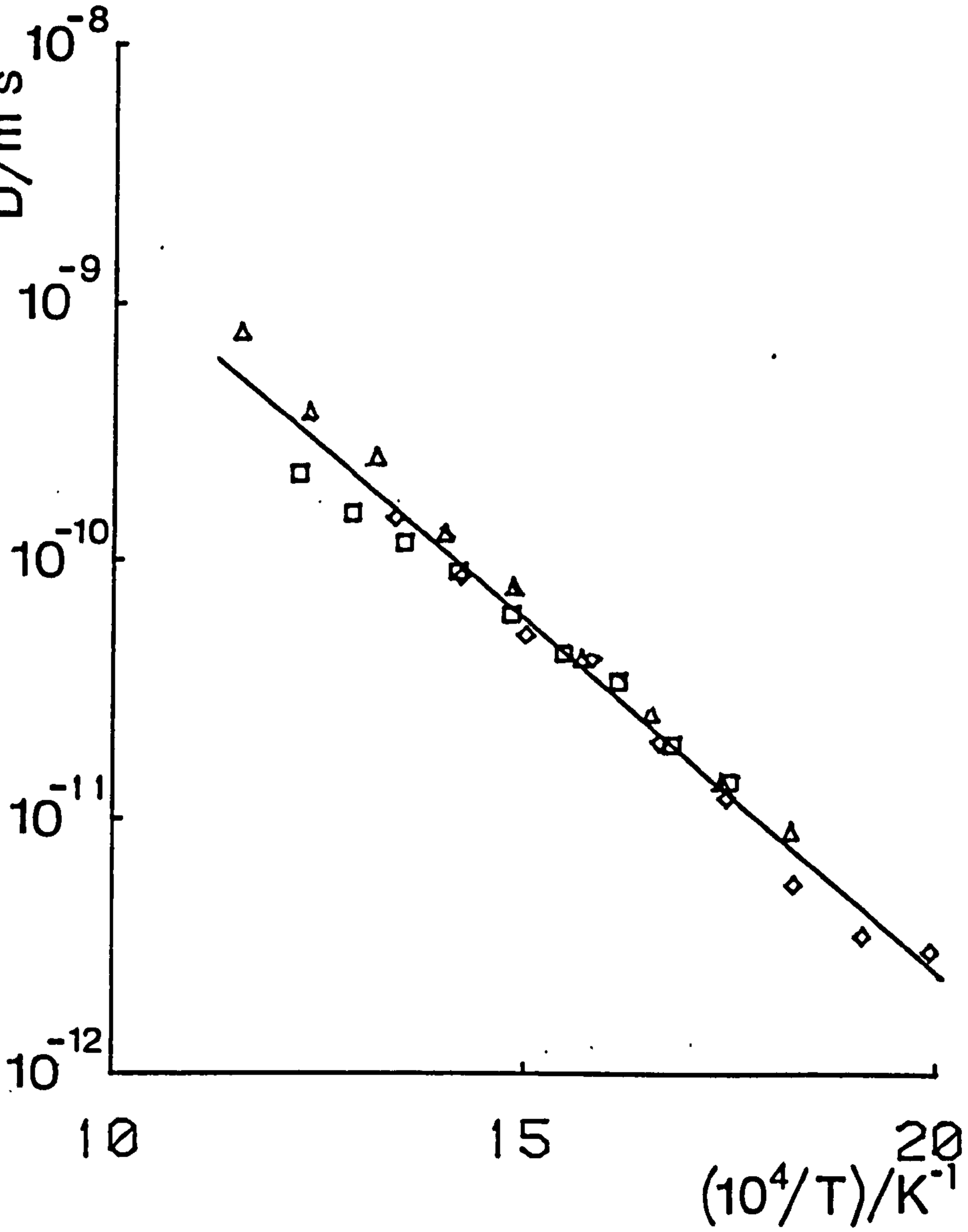

Fig 6.3 The variation of diffusion coefficient with reciprocal temperature for all 316 stainless steel data.

Key:

Triangle - 1.0×10^{-4}m, ion beam cleaned.

Square - 5.0×10^{-5}m, ion beamed clean.

Diamond - 5.0×10^{-5}m, oxidised on both surfaces.

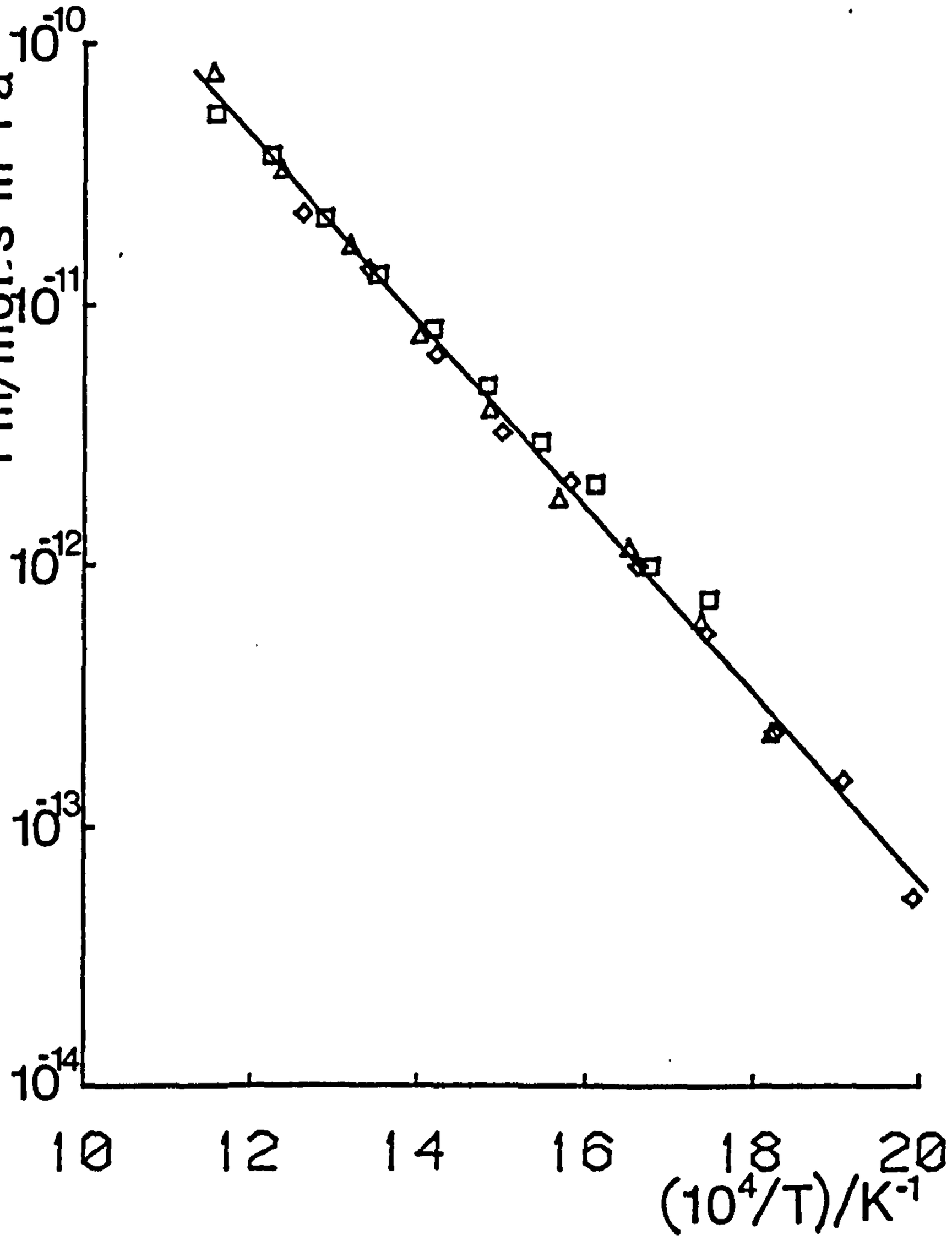

Fig 6.4 The variation of permeation coefficient with reciprocal temperature for all 316 stainless steel data. .

Key:

Triangle - 1.0×10^{-4}m, ion beam cleaned.

Square - 5.0×10^{-5}m, ion beamed clean.

Diamond - 5.0×10^{-5}m, oxidised on both surfaces.

$$D_{304}=(1.22\pm0.06)\times10^{-6}\exp\{[-(6.596\pm0.049)\times10^{3}/T]/K^{-1}\}\ m^{2}s^{-1} \quad [6.1]$$

$$P_{m304}=(4.82\pm0.21)\times10^{-7}\exp\{[-(7.990\pm0.044)\times10^{3}/T]/K^{-1}\}\ molm^{-1}s^{-1}Pa^{-\frac{1}{2}} \quad [6.2]$$

$$D_{316}=(7.28\pm0.94)\times10^{-7}\exp\{[-(6.296\pm0.109)\times10^{3}/T]/K^{-1}\}\ m^{2}s^{-1} \quad [6.3]$$

$$P_{m316}=(8.09\pm0.70)\times10^{-7}\exp\{[-(8.189\pm0.076)\times10^{3}/T]/K^{-1}\}\ molm^{-1}s^{-1}Pa^{-\frac{1}{2}} \quad [6.4]$$

The solubility K_{sm} is obtained by the simple product relationship, $P_m = DK_{sm}$, and is:

$$K_{sm304}=(0.395\pm0.033)\exp\{[-(1.394\pm0.066)\times10^{3}/T]/K^{-1}\}\ molm^{-3}Pa^{-\frac{1}{2}} \quad [6.5]$$

$$K_{sm316}=(0.81\pm0.08)\exp\{[-(1.902\pm0.133)\times10^{3}/T]/K^{-1}\}\ molm^{-3}Pa^{-\frac{1}{2}} \quad [6.6]$$

The data relate to the temperature domain $645 < T/K < 965$, for 304 stainless steel; $502 < T/K < 867$, for stainless steel 316; and for fluxes generated by driving pressures in the range $1.07\times10^{-5} < p_g/Pa < 10.7$ for both stainless steels.

(2) The iso-thermal, isofrequency variation of phase lag with pressure follows the theoretical curves extremely well, as shown in figs 5.22 - 5.28. Notice for the 2.5×10^{-4}m 304 stainless steel specimen, that the flux data derived from cleaned surfaces lies close to the $p^{\frac{1}{2}}$ variation, at the high end of the pressure range, characteristic of diffusion limited permeation. When the surface is oxidised the flux approaches the p^{1} variation, at the low end of the pressure range, characteristic of surface limited permeation.

(3) That the two rate constant model is an adequate one, is confirmed by the close Arrhenius dependence of k_1, for both clean and oxidised surfaces, over a large temperature range. This behavior is consistent with a model of surface reaction which involves a single activation energy. It indicates that the introduction of the further complication of a full six-rate constant surface reaction, which describes the adsorbed surface phase in a three stage mechanism, is not justified by the data taken from the accessible experimental phase space at the current signal to noise ratio.

6.1.2 Comparisons of D, P_m and k_1 with other work

The observed diffusion and permeation coefficients for 304 and 316 stainless steel are extremely close. From equations [6.1], [6.3], [6.2] and [6.4] the ratio D_{304}/D_{316} may be written $1.676\exp[(-0.3\times10^3/T)/K^{-1}]$ while that for P_{m304}/P_{m316} may be written $0.596\exp[(0.199\times10^3/T)/K^{-1}]$. Therefore, over the experimental range 549 - 965K the ratio for diffusion is $0.92 < D_{304}/D_{316} < 1.23$ while that for permeation is $0.89 < P_{m304}/P_{m316} < 0.73$. For this reason a single curve is used here as the basis for comparison of D with other work in stainless steel, as shown in fig 6.5.

For the diffusion coefficient this work is in excellent agreement with Kass and Andrejewski (6), Katsuta and Furukawa (9) and Phillips and Dodge (7). It is interesting to note that Kass and Andrejewski and

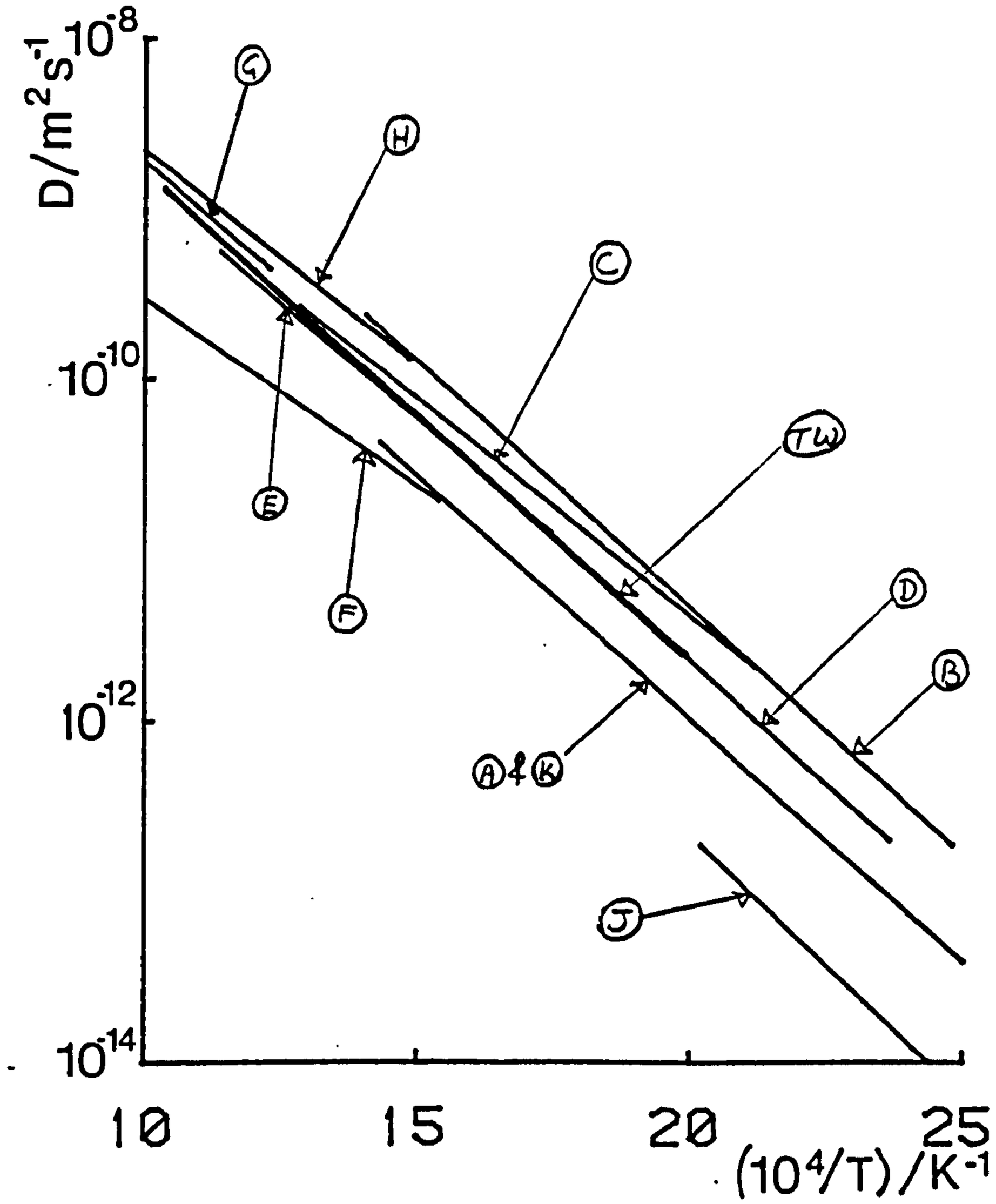

Fig 6.5 The variation of diffusion coefficient with reciprocal temperature in comparison with other work.

Key: H-hydrogen, D-deuterium, T-tritium, ()-reference number.

A - 304T (3), B - 304H (4), C - 310H (5), D - 309H (6), E - 321H (7), F - 304D (8), G - 304H (9), H - 347H (10), J - 304T and 316T (11), K - various steels (13).

Katsuta and Furukawa both sputter cleaned their specimens before coating with a thin layer of palladium, while Quick and Johnson (5) cleaned their specimen simply by activating it in a reducing atmosphere of hydrogen before coating it with palladium.

Phillips and Dodge used no more than mechanical polish to prepare their specimen but they made measurements at sufficiently high pressures, 100 - 8100torr, that diffusion was able to limit the permeation. This is confirmed by Earwaker *et al* who reported that an oxide thickness of 0.2μm, on the same 321 steel, still maintained a permeation power law index of one half, for a similar pressure range.

Both Quick and Johnson, and Outlaw and Peterson (10) present diffusion coefficients which agree with these of the present work at the high end of their respective temperature ranges. They do, however, report lower activation energies.

It can be argued that since surface effects hold up permeation through a foil, the highest reported diffusion coefficient, is likely to be the most precise. Nelson and Stein (4) report high values but are on their own with these. There is no obvious reason for this. Although it is not possible to verify from their report, their specimen configuration looks suspiciously susceptible to flux contamination through the support walls. The effect of this would be to generate a late flux and so seems likely to reduce the apparent diffusion coefficient. Their data does not fit well with that reported here and only unreasonable errors - such as overestimation of specimen

thickness – could bring it into line.

Austin and Elleman (11) found that "types 304 and 316 stainless steel yield essentially identical results". This is confirmed in this work for D and to a lesser extent P_m.

For the permeation coefficient, the best source of comparative data is made with the recent report by Le Claire (14) who obtained a mean curve from 40 investigators for the bulk of the stainless steel data. Results published since that recent report do not change the curve dramatically. As can be seen from fig 6.6, the present data for 304 and 316 stainless steel lies towards the upper limit of Le Claire's curve. His limits denote factors 1.5 and 1/1.5 from a mean and are shown by the dotted band.

For 304, $P_{m304}/P_{mLeClaire} = 1.475\exp[(-0.09\times10^3/T)/K^{-1}]$; for 316, $P_{m316}/P_{mLeClaire} = 2.476\exp[(-0.289\times10^3/T)/K^{-1}]$. Therefore, for the experimental temperature range, $1.25 < P_{m304}/P_{mLC} < 1.34$ and $1.39 < P_{m316}/P_{m3LC} < 1.82$. As expected this shows the permeation data to be relatively high. For comparable raw flux measurements this is inevitable since the present work is not evaluated in terms of diffusion limited permeation yet this is the basis for most evaluations reported elsewhere.

The few reported permeabilities lying above Le Claire's mean band are shown in fig 6.6. Among them, those from Nelson and Stein (4), and Perkins and Noda are notable. The validity of the data from

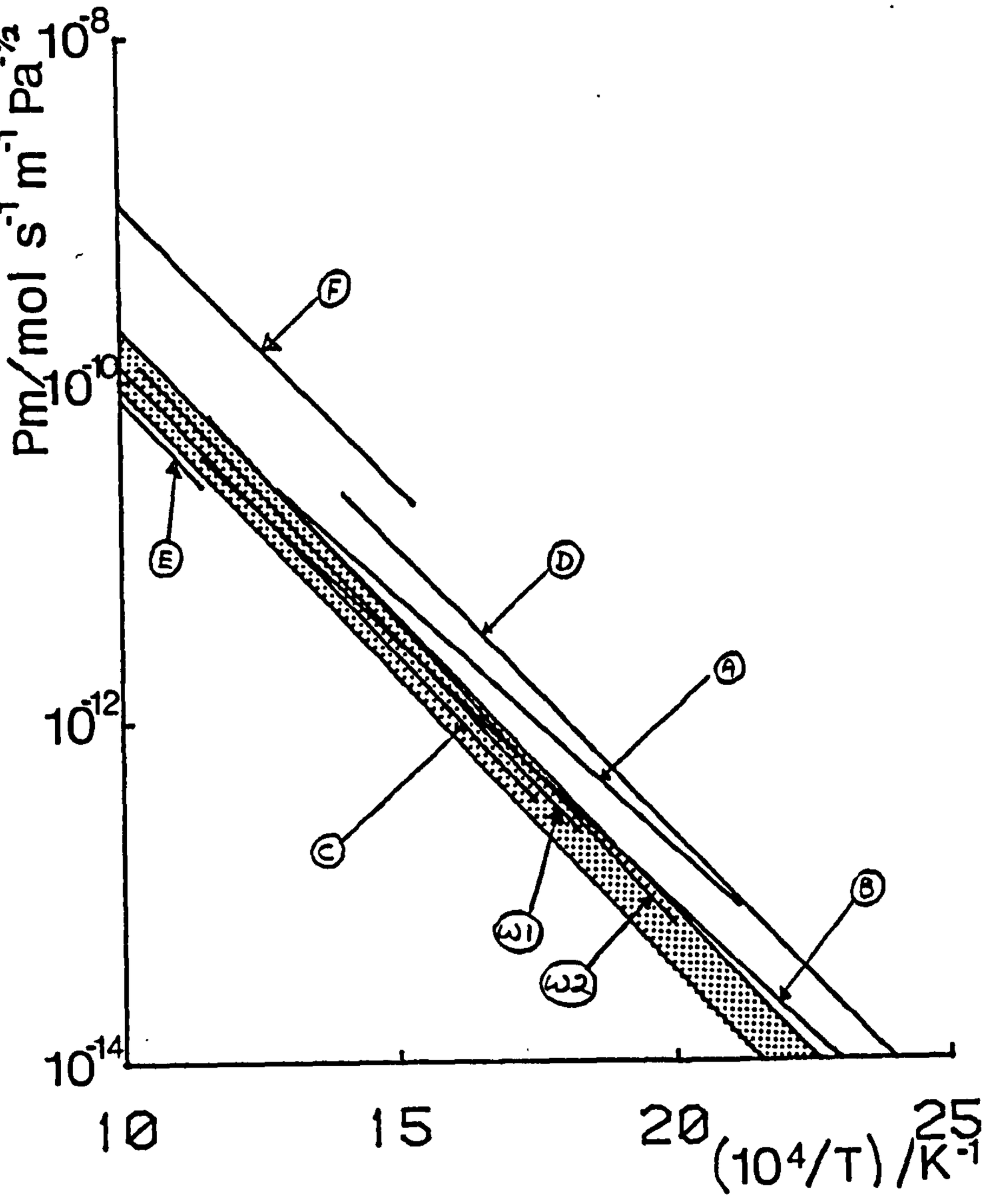

Fig 6.6 The variation of permeation coefficient with reciprocal temperature in comparison with other work.

Key: H-hydrogen, D-deuterium, T-tritium, ()-reference number.

A - 310H (5), B - 309H (6), C - 321H (7), D - 304H (4),

E - 304H (9), F - 304D (8).

Dotted band - limits of Le Claire's mean curve.

Nelson and Stein was questioned earlier but the work of Perkins and Noda is even more curious. Their diffusion coefficients were almost an order of magnitude down from other reported values yet their permeation values are an order of magnitude high. Further suspicion is aroused, in their reported power law index of 0.4 for 304 stainless steel. Examination of their specimen mount configuration reveals support walls which allow flux permeation into the output chamber. A rough calculation, using the values of wall thicknesses quoted, reveals that only 2.5×10^{-2}m of the length of the support tube would have to be at the the specimen temperature for the permeation to have doubled from its *real* value. Therefore the results from Perkins and Noda should be treated with some reserve.

Also shown in fig 6.6 are the permeation curves matching the diffusion coefficients that agree well with this present work. Notice Kass and Andrejewski (6), Phillips and Dodge (7) and Katsuka and Furukawa (9) all lie below this work while Quick and Johnson (5) lie above.

So far the data reported here shows excellent internal and external consistency in terms of diffusion and permeation coefficients for both 304 and 316 stainless steel. There remains the question of whether the surface parameter k_1, which was fitted simultaneously with D and P_m, can now provide interpretable data on the permeation characteristics of oxidised surfaces, data which have been hitherto largely unavailable. This question is treated in the next section following the sub-section below which concerns the symmetry

parameter, μ.

6.1.3 Sensitivity of the parameter μ

As stated earlier, the analysis of the variation of Φ and $|R|^{-1}$ with frequency was fitted for the parameters D, P_m and k_1. However the parameter μ was set *a priori*. In all but one case μ was set equal to 0 as identical treatment of clean and oxidised surfaces should have resulted in foils of symmetric surface conditions. The sole non-zero case was for a specimen with oxide on the input side. For this case μ was set equal to -1.

The purpose of this subsection is to demonstrate that this mathematical approach is a reasonable one and to asses whether it would be possible to add μ to the set of parameters D,P_m and k_1 which are directly determined from the experimental data.

The indicator of the quality of fit to the data is the normalised deviation, Δ, defined as:

$$\Delta^2 = \frac{\sum (\Phi_{obs} - \Phi_{calc})^2}{\left[\sum \Phi_{obs}\right]^2} + \frac{\sum (|R|^{-1}_{calc} - |R|^{-1}_{obs})^2}{\left[\sum |R|^{-1}_{obs}\right]^2} \qquad [6.7]$$

The variation of Δ with μ is shown in fig 6.7 for data from the 1.0×10^{-4}m, stainless steel 316 specimen at 633K, which has an

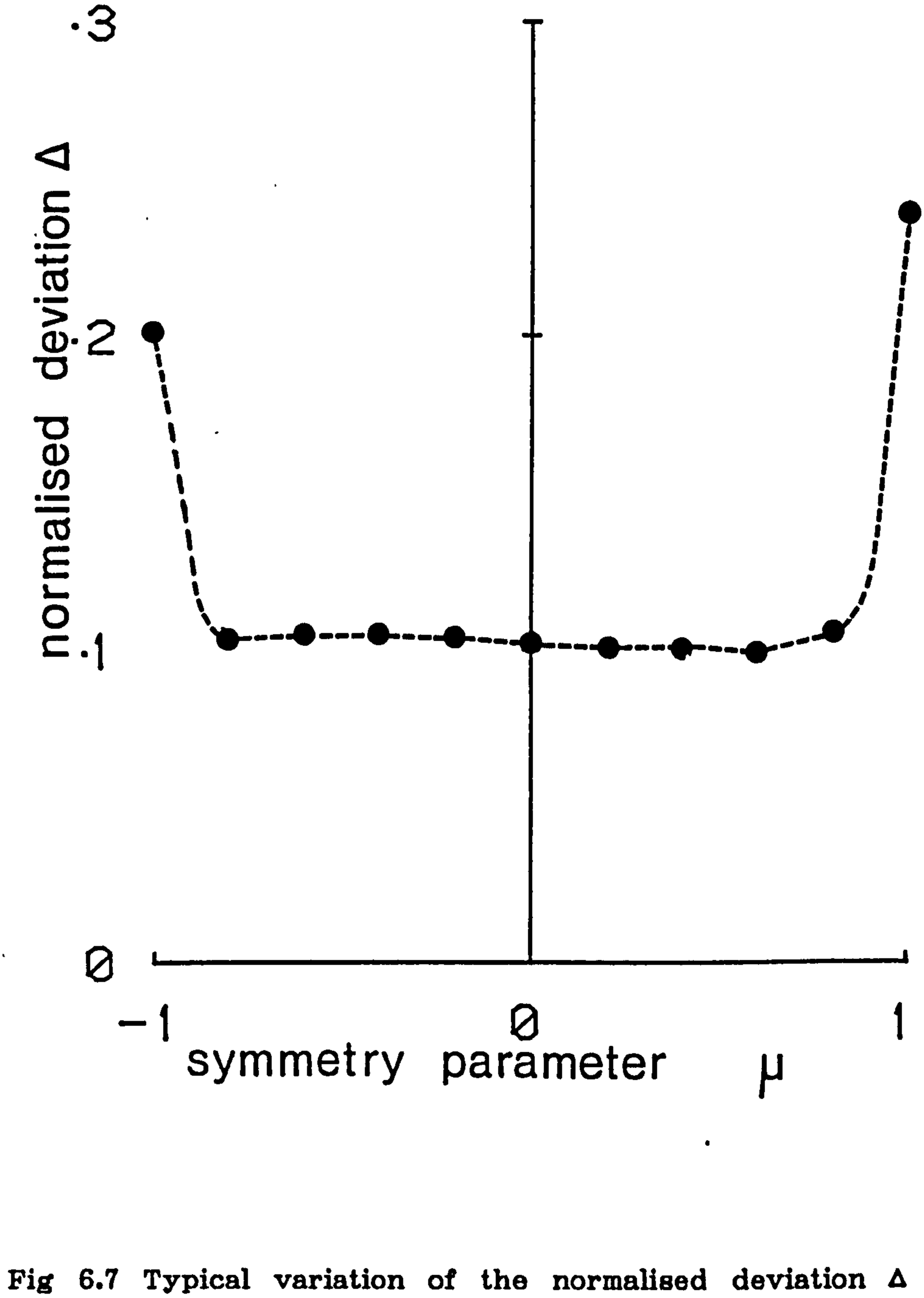

Fig 6.7 Typical variation of the normalised deviation Δ with symmetry parameter μ. Data is from the 1.0×10^{-4}m, 316 stainless steel at 633K for its range of pressures and frequencies. Notice the insensitivity of μ for most of the plot in this bucket shaped curve.

expected μ of 0. Notice the bucket shaped curve with greater than 90% of the plot effectively on a plateau.

It is clear that the fit is very insensitive to the parameter μ. This provides a general increase in confidence in the analysis, since the rate constants at the two surfaces would have to differ by greater than 20:1 before D,P_m and k_1 would be drastically affected. Specifically it shows the fixing of μ *a priori* to be a safe and valid proceedure.

Direct confirmation of μ was acheived with the 2.5×10^{-4}m stainless steel 304 foil. This foil was analysed with two surfaces clean, $\mu = 0$, and then with a single oxide on the input surface, $\mu = -1$. Thus, the values of k_1 and k_1' can be determined, for this surface configuration, and since $\mu = (k_1-k_1')/(k_1+k_1')$ then from the Arrhenius k_1 values it is found that $\mu = -0.98$. Hence, the assumption that was made in the analysis of a single-sided oxide, having a μ being equal to -1, was a good one. Even more so in view of the insensitivity of μ, as shown above.

6.2 THE RATE CONSTANT k_1 AND ITS PHYSICAL PROPERTIES

In sub-section 6.2.1 an internal and external comparison of k_1 data is made. To interpret the surface rate coefficient, k_1, it is first necessary to develop a physical model of the process by which hydrogen goes from the gas phase to solution in the metal; 6.2.2. That model allows the description of both, cleaned surfaces and adherent oxides and enables k_1 to be related to the oxide permeation coefficeint, P_{mox}. Finally, in section 6.2.3, a pictorial model illustating the variation of chemical potential across an oxide-metal-oxide foil is discussed.

6.2.1 Internal and external comparison of k_1

The Arrhenius plots of k_1 for the various surface conditions for both 304 and 316 stainless steel are illustrated in fig 6.8. Since the data was also shown in chapter 5, for reasons of clarity only the lines showing the fundamental relationships are drawn. Also on the figure are other reported direct dissociative chemisorption rate constant.

The pattern of the k_1 results seems to indicate a clear Arrhenius relationship although there does not seem to be any common activation energy.

In the present work a 1μm single surface oxide layer on 304 stainless

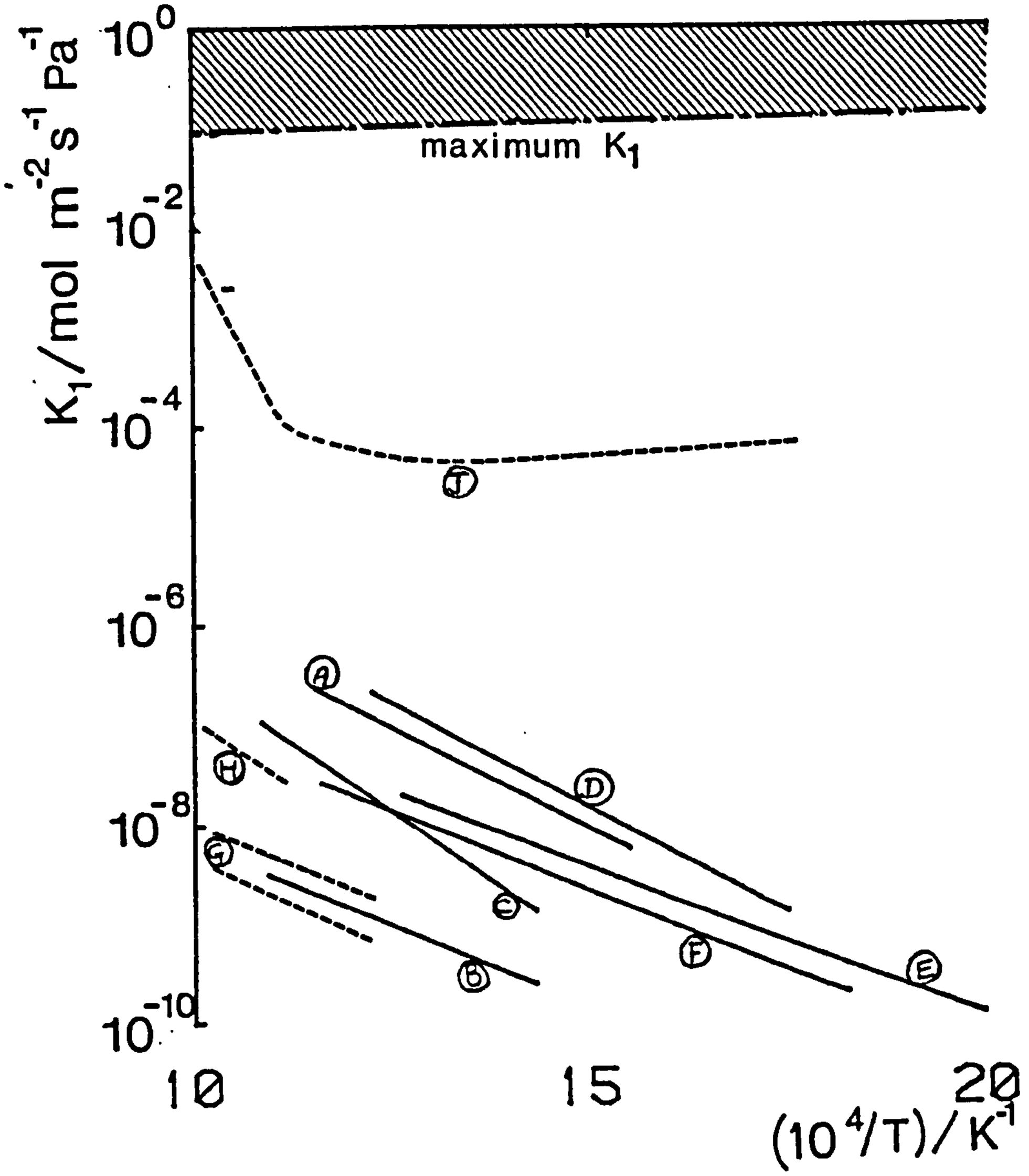

Fig 6.8 The variation of surface rate constant k_1 with reciprocal temperature for this and other work.
Key: H-hydrogen, D-deuterium, T-tritium, ()-reference number. This work 304: A - 2.5×10^{-4}m, ion beam cleaned; B - 2.5×10^{-4}m, input surface oxidised; C - 3.0×10^{-4}m, cleaned by activation. 316: D - 5.0×10^{-5}m, ion beam cleaned; E - 5.0×10^{-5}m, oxidised both surfaces; F - 1.0×10^{-4}m, ion beam cleaned. Other work: G - 347H and 347T (23); H - 304H (22); J - 304D (8).

steel was shown to cause a fall in k_1 by two orders of magnitude, while a double surface oxide of thickness 0.4μm, on 316 stainless steel had a much less dramatic effect. This lack of surface holdup in the permeation of hydrogen in stainless steel 316 is confirmed by Earwaker *et al* in a permeation oxide-thickness study.

Also of note is the foil cleaned by activation in a reducing atmosphere of hydrogen. This is a common practice used for example by the authors of (5), (22), (23), (49) and (50). The value of k_1 for this foil was an order of magnitude lower than that for the ion beam cleaned 2.5×10^{-4}m, 304, and 5.0×10^{-5}m, 316 stainless steel foils, indicative that ion beam cleaning is indeed a superior technique. Disappointingly, the 1.0×10^{-4}m 316 stainless steel was not ion cleaned for long enough to clear it of all oxide. This is attributable to inexperience this being the first specimen to be cleaned by such a technique. The specimen shows a low value of k_1.

In comparison with other work, the values obtained from Axtmann *et al* (22), and Randall and Salmon (23), agree with those given here for both activated and oxidised specimens. This is indicative again that ion beam cleaning provides higher rate coefficients and therefore implies that surfaces are cleaner. Since both investigators above report activation of their specimen prior to experiment the consistency with their data is reasonable.

As noted earlier, there is some doubt on the validity of the data provided by Perkins and Noda (8). That their surface rate constants

are 2-3 orders of magnitude greater than those shown here and show non-Arrhenius dependence do not help to reverse this view. Especially as their data shows flows near the theoretical maximum limits calculated from the Herz-Knudsen equation (48).

Braun *et al* (24) and Ali-Khan *et al* (51) provided data on surface recombination rate of deuterium in 304 stainless steel. To compare this work with the values presented here, k_1 was converted into k_2 using $K_{Sm} = (k_1/k_2)^{½}$. The results are presented in fig 6.9. As with the k_1 data, k_2 for this work, from ion-beam cleaned foils, is larger than the other reported work indicating, probably, the effectiveness of *in situ* ion-beam cleaning.

In conclusion, there is approximate agreement with the limited reported work on stainless steel surface rate coefficients. The good Arrhenius plots of this work cover a significantly larger temperature span than other reports. They also indicate, along with the excellent internal consistency of D and P_m, the adequacy of describing surface affects by a direct dissociative chemisorption model. To the precision of the present work a two rate constant model gives a good description of how surfaces limit permeation in stainless steels. There is no clear need for a more complex model, for example the six rate model of 6.3, incorporating such additional complexities of a surface phase.

To interpret the k_1 data further, the next sub-section questions the mode of diffusant transport through the oxide layer with a view to

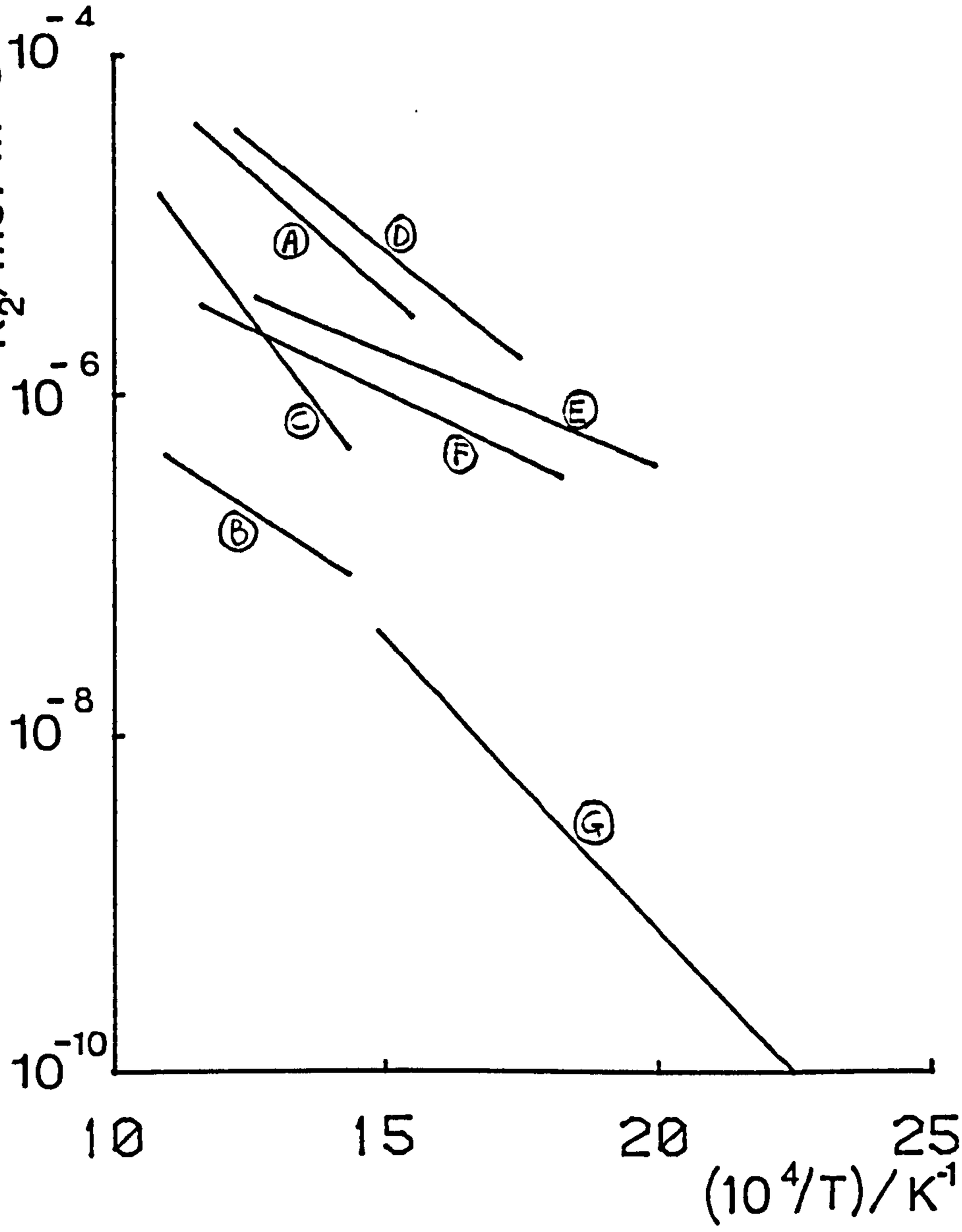

Fig 6.9 The variation of surface rate constant k_2 with reciprocal temperature for this and other work.

Key: D-deuterium, ()-reference number. This work, 304: A - 2.5×10^{-4}m, ion beam cleaned; B - 2.5×10^{-4}m, input surface oxidised; C - 3.0×10^{-4}m, cleaned by activation. 316: D - 5.0×10^{-5}m, ion beam cleaned; E - 5.0×10^{-5}m, oxidised both surfaces; F - 1.0×10^{-4}m, ion beam cleaned. Other work: G - 304D (24)

identifying these k_1 coefficients with a permeation coefficient for the oxide.

6.2.2 Molecular or atomic transport of hydrogen through oxide layers?

Le Claire (21) suggests that the oxide is capable of "molecule dissolving", that is, transport through the oxide layer is molecular. Whether this is indeed so can in principle, be confirmed by examination of how diffusant flux varies with pressure.

Following the line of argument developed in 4.4, it is easy to see that the effect on a surface layer may be described by:

$$R = Q(ZV_{ox}Z_{12})V_{mt}Z'Q' \qquad [6.8]$$

This may be written:

$$R = QZ_{eff}V_{mt}Z'Q' \qquad [6.9]$$

where Z_{eff} is an effective interphase matrix comparable with the matrix **Z** derived in the two rate constant model of section 4.4. Expressions for Z_{eff} will now be derived for atomic and molecular transport. They are based on the assumption that permeation is diffusion limited within the oxide. That is gas-oxide and oxide-metal rate constants are assumed infinite. In consequence each model uses an equilibrium equation to describe the gas-oxide interface but they differ in the form of equation used. The schematic diagram, fig 6.10, clarifies the coefficients in the surface and oxide layer for the two models.

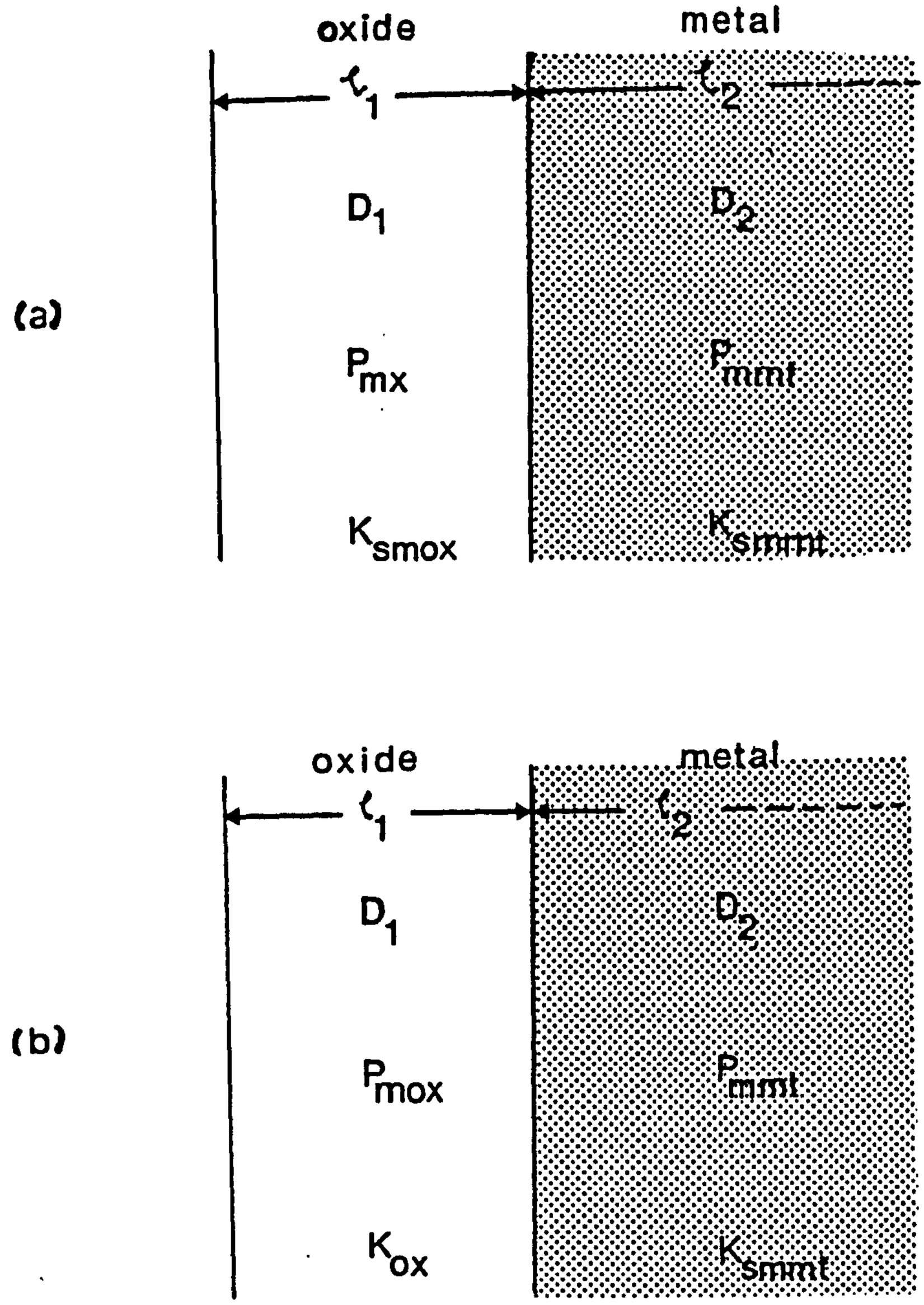

Fig 6.10 Schematic diagram clarifying coefficients used in determining two possible modes of transport through the oxide layer. (a) - atomic flow. (b) - molecular flow.

Mode (1): atomic transport

At equilibrium:

$$c_{ox} = K_{smox}p^{1/2} \qquad [6.10]$$

analogous with [4.45]. Then:

$$Z = \begin{bmatrix} 2\sqrt{p_s}/K_{smox} & 0 \\ 0 & 1 \end{bmatrix} \qquad [6.11]$$

and, from equation [4.35]:

$$W_{ox} = \begin{bmatrix} \cosh a_1 \ell_1 & (1/D_1 a_1)\sinh a_1 \ell_1 \\ D_1 a_1 \sinh a_1 \ell_1 & \cosh a_1 \ell_1 \end{bmatrix} \qquad [6.12]$$

which for a thin oxide can be simplified to:

$$W_{ox} = \begin{bmatrix} 1 & \ell_1/D_1 \\ i\omega\ell_1 & 1 \end{bmatrix} \qquad [6.13]$$

At equilibrium:

$$c_{mt} = K_{smmt}p^{1/2} \qquad [6.14]$$

where K_{smmt} and K_{smox} are the solubility coefficients of the metal and oxide respectively. Therefore:

$$Z_{12} = \begin{bmatrix} K_{smox}/K_{smmt} & 0 \\ 0 & 1 \end{bmatrix} \qquad [6.15]$$

By definition, Z_{eff} is the product $ZW_{ox}Z_{12}$ formed from [6.11],[6.13] and [6.15] and is:

$$Z_{eff} = \begin{bmatrix} \dfrac{2p_s^{1/2}}{K_{smmt}} & \dfrac{2\ell}{P_{mx}}\sqrt{p_s} \\ i\omega\ell_1 K_{smox}/K_{smmt} & 1 \end{bmatrix} \qquad [6.16]$$

where $P_{mx} = D_1 K_{smox}$.

Comparing Z_{eff} with [4.82], then:

$$k_1 \equiv P_{mx}/(2\ell_1 p_s^{1/2}) \qquad [6.17]$$

This result specifies that atomic transport of hydrogen through the oxide will result in a particular variation of diffusant flux with pressure.

Mode (2): molecular transport.

When there is equilibrium, the oxide concentration is:

$$c_{ox} = K_{ox}P \qquad [6.18]$$

where K_{ox} is the solubility in the oxide, supposing equilibrium to hold, then:

$$Z = \begin{bmatrix} 1/K_{ox} & 0 \\ 0 & 1 \end{bmatrix} \qquad [6.19]$$

and

$$V_{ox} = \begin{bmatrix} 1 & \varrho_1/D_1 \\ i\omega\varrho_1 & 1 \end{bmatrix} \qquad [6.20]$$

Supposing conditions to be at equilibrium:

$$c_{mt}^2 = K_{smmt}^2 c_{ox}/K_{ox} \qquad [6.21]$$

Therefore using boundary conditions then:

$$Z_{12} = \begin{bmatrix} 2K_{ox}/Ksmmt(P_s - \varrho_1 J_s/P_{mox})^{1/2} & 0 \\ 0 & 1 \end{bmatrix} \qquad [6.22]$$

where P_{mox} is defined by $P_{mox} = D_1 K_{ox}$. An expression for Z_{eff} may be derived by multiplying $ZV_{ox}Z_{12}$, [6.19],[6.20] and [6.22], to give:

$$Z_{eff} = \begin{bmatrix} 2/K_{smmt}(P_s - \varrho_1 J_s/P_{mox})^{1/2} & \varrho_1/P_{mox} \\ i\omega\varrho_1 2K_{ox}/K_{smmt}(P_s - \varrho_1 J_s/P_{mox})^{1/2} & 1 \end{bmatrix} \qquad [6.23]$$

Using [4.82], this expression for molecular transport, gives:

$$k_1 \equiv P_{mox}/\varrho_1 \qquad [6.24]$$

This is to be compared with the corresponding equation [6.17] for atomic transport.

The models have separate predictions: atomic transport through an oxide layer provides a k_1 which is pressure dependent, [6.17], while with molecular flow k_1 which is pressure independent, [6.24]. Clearly, the excellent Arrhenius plots of k_1 and the good fits of the iso-frequency, isothermal variation of phase lag with pressure, over a large range of values suggests k_1 is pressure independent, indicating molecular flow through the oxide layer.

The atomic and molecular transport models provide specific predictions about how flux varies with pressure. When a full analysis is made using [6.9] the molecular model provides estimates for P_{mox} which do not vary with pressure, while those derived for the atomic model, P_{mx}, are pressure dependent. On this basis it does seem that molecular flow takes place in the oxide. Using the SIMS analysis of the thickness of oxide on the oxidised 304 and 316 stainless steel foils and their respective equations for k_1, and $P_{mox} = k_1\varrho_1$ then:

$$P_{mox304}=(1.43\pm0.29)\times10^{-11}\exp([-7.661\pm0.081)\times10^{3}/T)/K^{-1}) \ molm^{-1}s^{-1}Pa^{-1} \qquad [6.25]$$

$$P_{mox316}=(5.36\pm2.68)\times10^{-11}\exp\{[-6.967\pm0.228)\times10^{3}/T)/K^{-1}\}\ molm^{-1}s^{-1}Pa^{-1} \quad [6.26]$$

These equations are shown in fig 6.11. Notice that P_{mox} for 316 is larger than 304. Again, this confirms that an oxide layer on 304 has a more dramatic affect on the bulk permeation than 316.

The ability to describe flows within the oxide layers makes it interesting to reassess flows generally. To help in this the following sub-section views the whole permeation process from a different perspective; that of the chemical potential of the system.

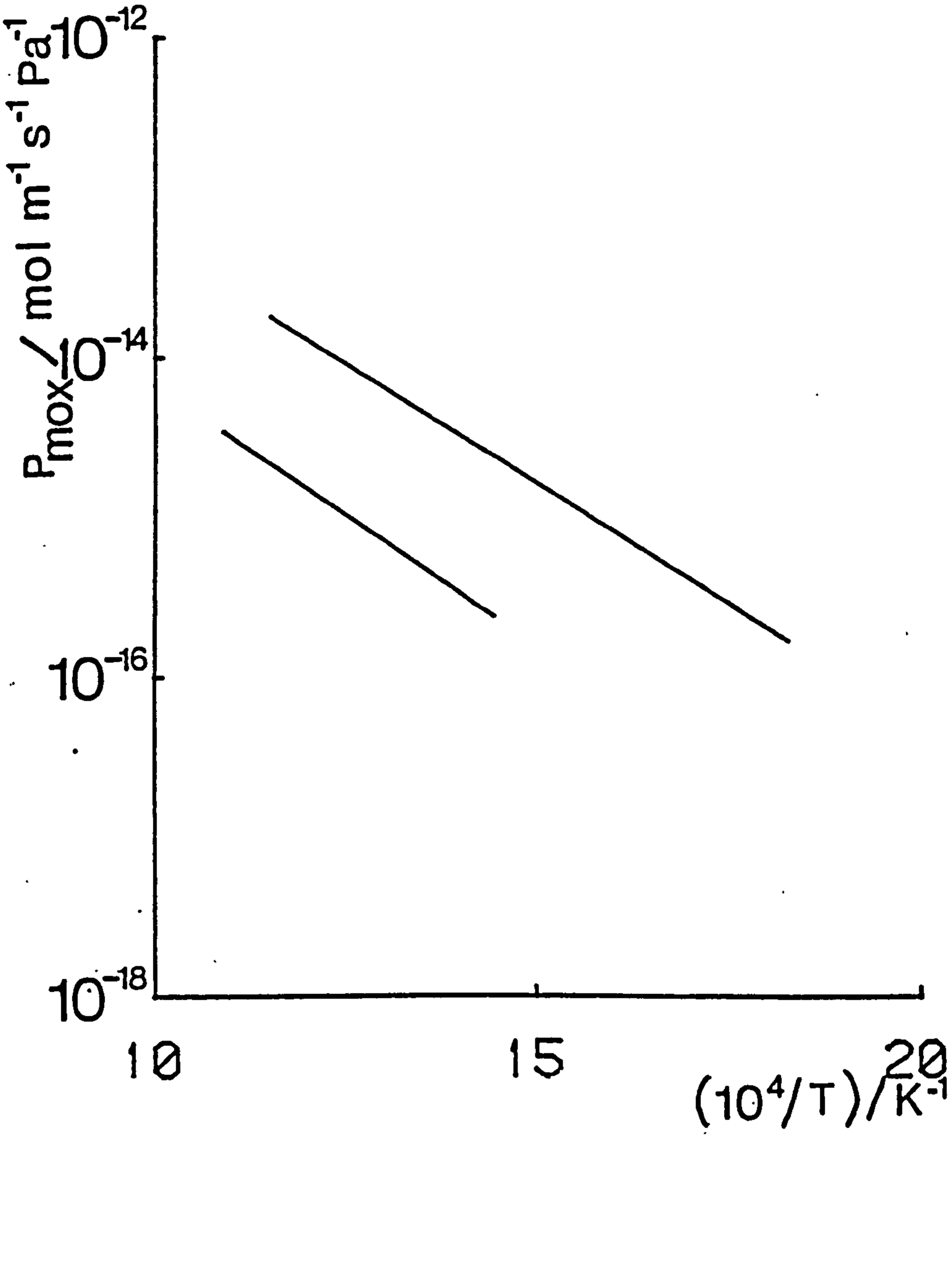

Fig 6.11 The variation of oxide permeation coefficient for molecular flow, P_{mox}, with reciprocal temperature.

Upper curve: 316 stainless steel.

Lower curve: 304 stainless steel.

6.2.3. The chemical potential μ_c

So far the gas-metal-gas system has been described by macroscopic flow rates. It may be interesting to briefly examine the thermodynamics of the system in terms of the chemical potential to obtain a different viewpoint on the process of permeation.

The reaction is:

$$H_2(gas) \rightleftharpoons 2H(solid) \qquad [6.27]$$

In a closed system the free energy of the system is: $G = n_2\mu_2 + n_2\mu_2$ where the subsript, $_2$, refers to hydrogen in the gas phase, molecular, and, $_1$, refers to hydrogen in the solid phase, atomic. Therefore at equilibrium:

$$dG = \mu_2 dn_2 + \mu_1 dn_1 = 0 \qquad [6.28]$$

Stoichiometry requires that:

$$dn_1 = -2dn_2 \qquad [6.29]$$

Therefore at equilibrium:

$$\mu_2 = 2\mu_1 \qquad [6.30]$$

Now:

$$\mu_2 = \mu_2^o + RT \ln(p/p^o) \qquad [6.31]$$

and

$$\mu_1 = \mu_1^o + RT \ln(c/c^o) \qquad [6.32]$$

where the superscript, ^{o}, refers to any arbitary state. When surface reactions are infinite, surface eqilibrium is maintained, $c(0) = K_{sm}p_s^{1/2}$,

$c(\ell) = K_{SM}p_S'^{½}$. *Thus:*

$$2\mu_1(0)-2\mu_1(\ell)= RT\ \ln(p_S/p_S') = \mu_2(g)-\mu_2(g') \qquad [6.33]$$

This allows a sketch of chemical potential versus position co-ordinate can now be drawn for this diffusion limited case, fig 6.11a.

By introducing surface rates which are finite, that is $J_S = k_1p_S - k_2c^2(0) = k_2'c^2(\ell) - k_1'p_S'$, the potential distribution is changed:

$$2\mu_1(0)-2\mu_1(\ell)= RT\ \ln\left[\frac{(k_1p_S - J_S)k_2'}{(k_1'p_S' + J_S)k_2}\right] \qquad [6.34]$$

A sketch of chemical potential versus position co-ordinates using finite surface rates is shown in fig 6.11b. All possible differences in chemical potential including, to avoid repetition, some not derived in this text are shown on this figure.

It is of interest to consider the x = 0 boundary to see how large this chemical drop is, $\mu_2(g) - 2\mu(0) = RT[k_1p_S/(k_1p_S - J_S)]$. Therefore, for the oxidised 316 stainless steel specimen at 633K, $\mu_2(g) - \mu_1(0) \approx 3.6\times10^2$ $Jmol^{-1}$; in comparison with $\mu_2(g) - \mu_2(g') \approx 8\times10^4$ $Jmol^{-1}$. Thus the chemical potential difference across the oxide layer is of the order of 0.5% of the total potential difference across the membrane.

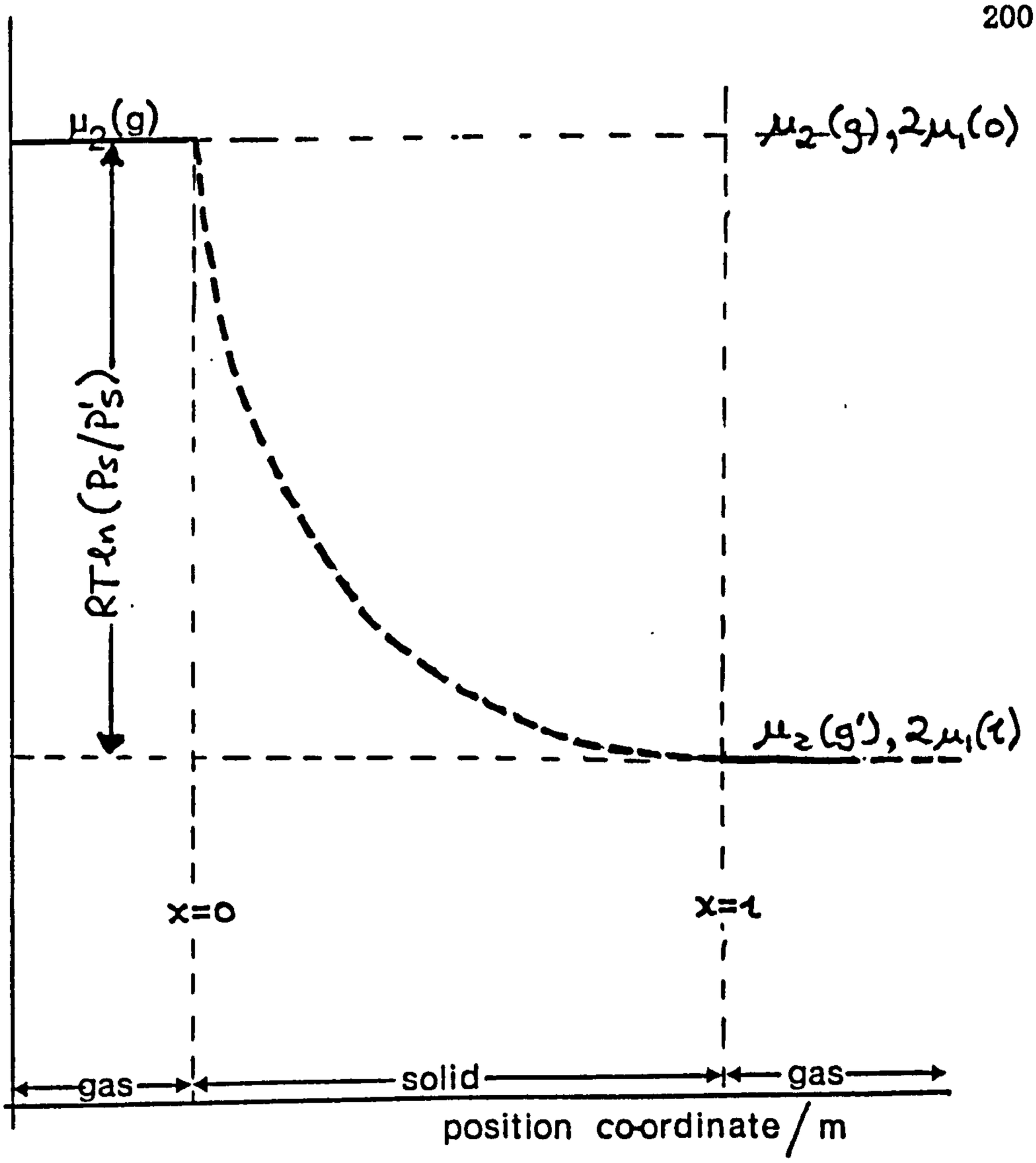

Fig 6.12a Sketch of the variation of chemical potential with position co-ordinate for diffusion limited permeation.

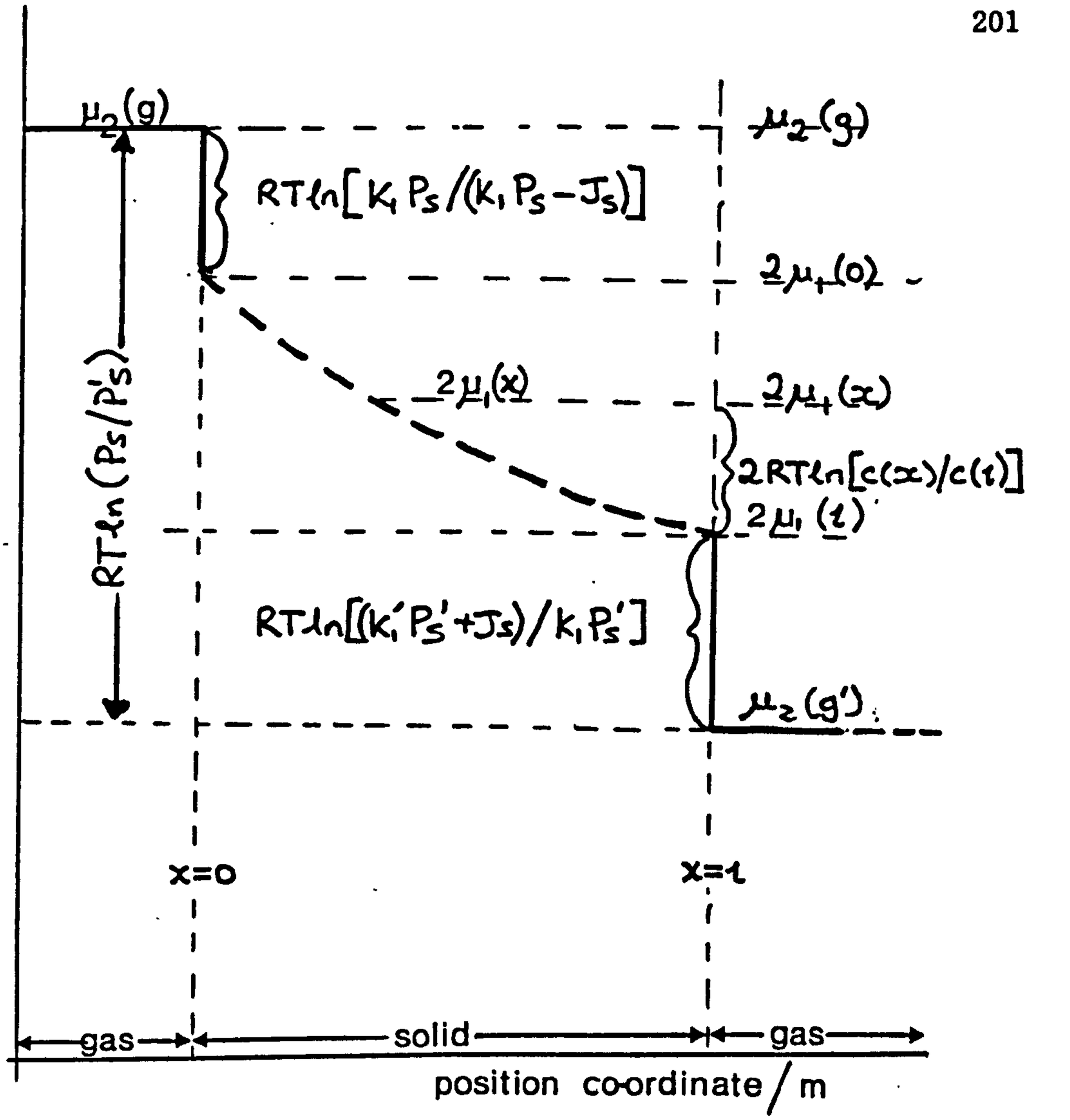

Fig 6.12b Sketch of the variation of chemical potential with position co-ordinate for permeation incorporating finite surface rates.

6.3 SOME POSSIBLE ALTERNATIVE MODELS

Slow surface reactions of a simple type or slow permeation through superficial layers are plausible causes of the observed hydrogen fluxes through stainless steel. There are other possibilities. These include the single reversible trap model and the six-reaction rate surface model. These are discussed in 6.3.1. and 6.3.2 respectively.

6.3.1 The single reversible trap model

Atoms of a species subject to trapping during diffusion may be supposed to follow random paths through the solid interrupted by occasional pauses in the locations which are traps. Traps which hold atoms of the diffusant species for long times relative to the time of an experiment are designated irreversible: traps which hold them for times comparable with the experiment time are designated reversible. Experiments using modulation methods are sensitive to trapping times comparable with the with period of the modulation, and it is this class of traps that is of interest.

Diffusant atoms subject to trapping may be seen as belonging to one of two species: they are free and mobile and so are part of the usual diffusant concentration, c, or they are restricted and immobile and so part of a separate concentration, z. Movement between the species is here described by the reversible reaction:

$$H(\text{mobile}) \underset{k_B z}{\overset{k_A c}{\rightleftharpoons}} H(\text{trapped}) \qquad [6.35]$$

where k_A and k_B are rate constants. The corresponding rate equation is:

$$\frac{dz}{dt} = k_A c - k_B z \qquad [6.36]$$

Since conservation of mass requires:

$$\frac{dc}{dt} = -\frac{\partial J}{\partial x} - \frac{dz}{dt} \qquad [6.37]$$

it follows from Fick's law that:

$$\frac{dc}{dt} + \frac{dz}{dt} = D\frac{\partial^2 c}{\partial x^2} \qquad [6.38]$$

Cummings and Blackburn (52) developed these equations for a pressure modulation case and found the following equations for Φ and Λ:

$$\tan\Phi = \frac{\xi\tan\chi - \chi\tanh\xi}{\xi\tanh\xi + \chi\tan\chi} \qquad [6.39]$$

$$\Lambda = \tfrac{1}{2}\left[\frac{(\xi^2 + \chi^2)}{\cosh^2\xi - \cos^2\chi}\right]^{\frac{1}{2}} \qquad [6.40]$$

where

$$Db = \frac{k_A\omega^2 + i\omega(\omega^2 + k_B + k_A k_B)}{(\omega^2 + k_B^2)} \qquad [6.41]$$

and

$$b\ell = \xi + i\chi \qquad [6.42]$$

To examine how, in general , trapping modifies the amplitude and phase of the transmitted pressure modulation it is useful to replace the rate constants k_A and k_B by the dimensionless parameters:

$$A = k_A\ell^2/2D \quad ; \quad B = k_B\ell^2/2D \qquad [6.43]$$

Figure 6.13 shows the variation of Φ with ς described by equation [6.45] for specified values of A and B, solid lines. There are two principal points of interest: the strong maxima which vary in position with B but are absent when B = 0, dotted lines, and the values of Φ at higher ς which show the curves describing flow through traps giving lower phase values than that for diffusion limited flow when A = B = 0.

Figure 6.14 shows the variation of Λ with ς described by equation [6.46]. General points to note are: Λ is greatest when A = B = 0; when B is small, Λ drops sharply from the value of ½ at ς = 0 to a plateau region before falling away again with increasing ς; and curves having a common value of A converge as ς increases.

Of particular relevance to this work is the striking similarity between these trapping curves and parallel diffusion. This is perhaps not so suprising if trapping is considered as a parallel process to the diffusion limited permeation. Happily there are determining features which enable the identification of either process. For the variation of Φ with ς , Φ recovers to simple diffusion limited curve for high ς while the trapping curve does not. For the variation Λ with ς parallel diffusion has a distinct minimum in the

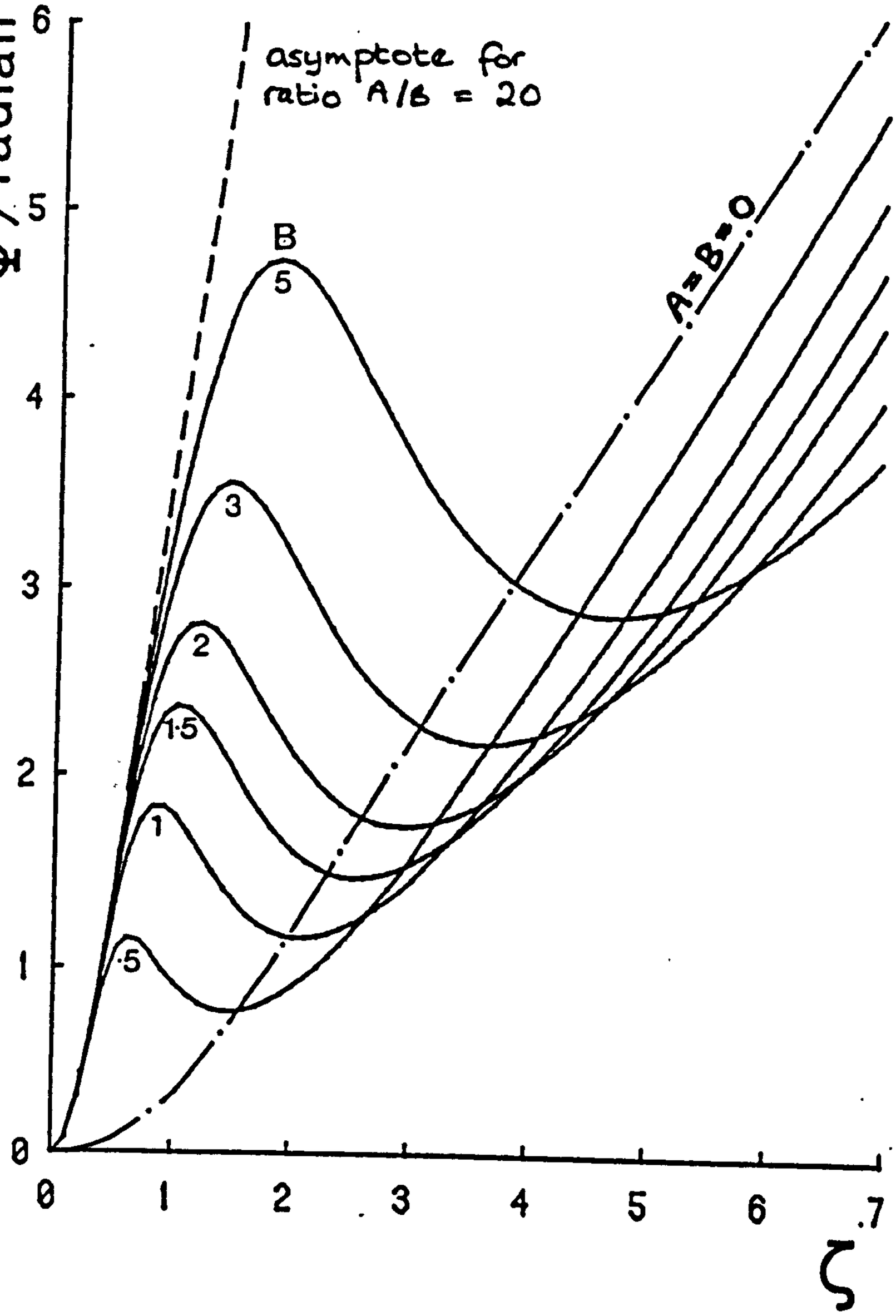

6.13 The variation of phase lag, Φ, with ζ for the reversible trap model, equation [6.45], and for specified values of A and B.

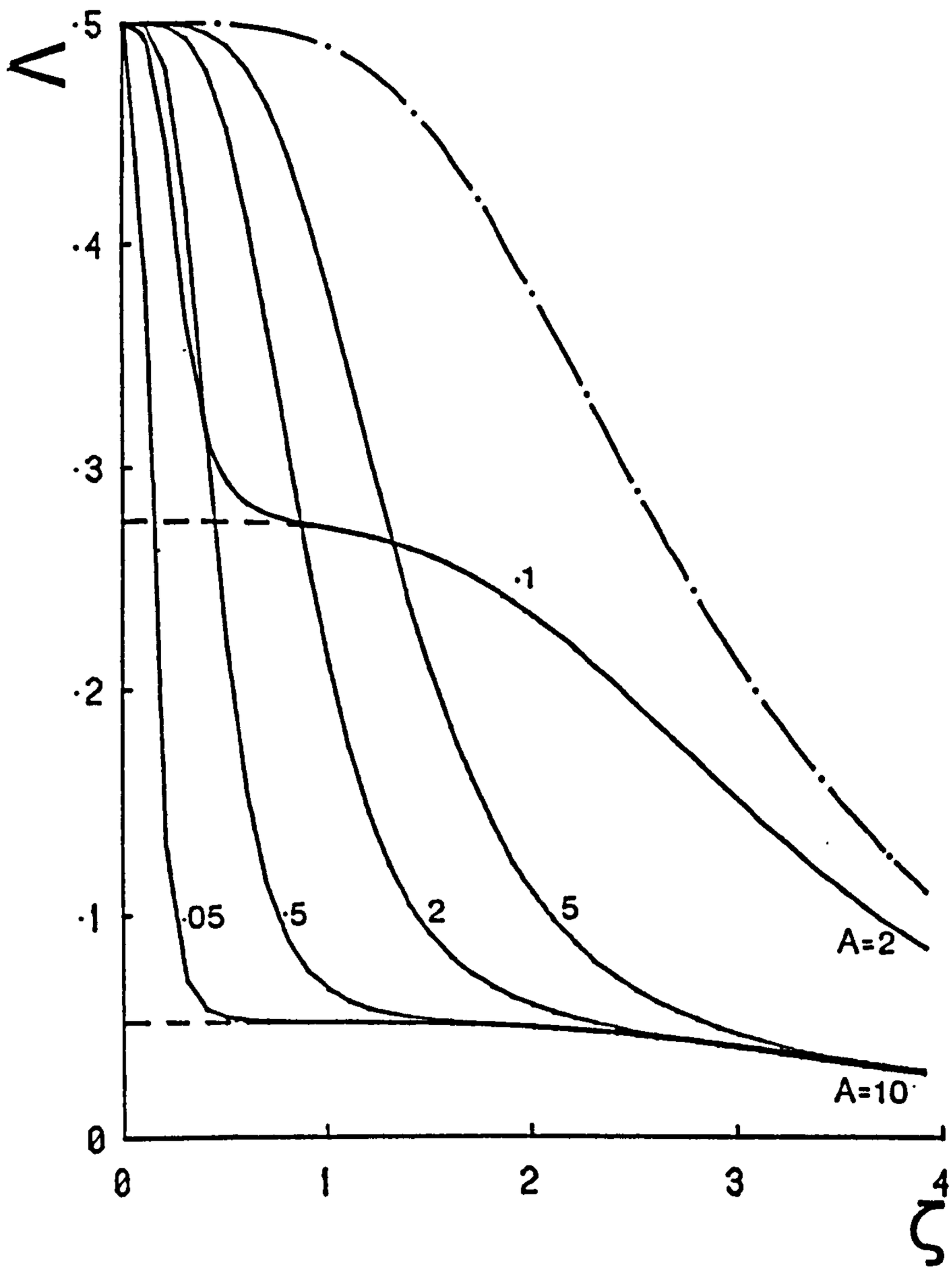

6.14 The variation of Λ with ζ for the reversible trap model, equation [6.46], and for specified values of A and B.

curve which does not exist in the trapping curve. In conclusion, although it cannot be said that trapping did not exist in the reported data, it certainly did not impart any great influence in the temperature and frequency range of the experiment.

6.3.2 The six-reaction rate surface model

The principal feature of the two-rate constant model used in this work is its ability to describe the changeover from high pressure, diffusion limited permeation, to low pressure, surface limited permeation. It takes no account, however, of any adsorbed surface phase of atoms or molecules. To investigate the possibility that such a surface layer might be detected in a modulation experiment a three stage process would have to be considered as shown in fig 6.14.

In this model of the surface processes, there are six independent rate constants defined by the following flow equations:

$$J(g) = k_1 p - k_2 \nu_m \qquad [6.44]$$

$$\frac{\partial \nu_m}{\partial t} = J(g) - k_3 \nu_m + k_4 \nu_a^2 \qquad [6.45]$$

$$\frac{\partial \nu_a}{\partial t} = k_3 \nu_m - k_4 \nu_a^2 - J(0) \qquad [6.46]$$

$$J(0) = k_5 \nu_a - k_6 c(0) \qquad [6.47]$$

where ν_m is the adsorbed molecules surface concentration and ν_a is the adsorbed atoms surface concentration. This set of relations

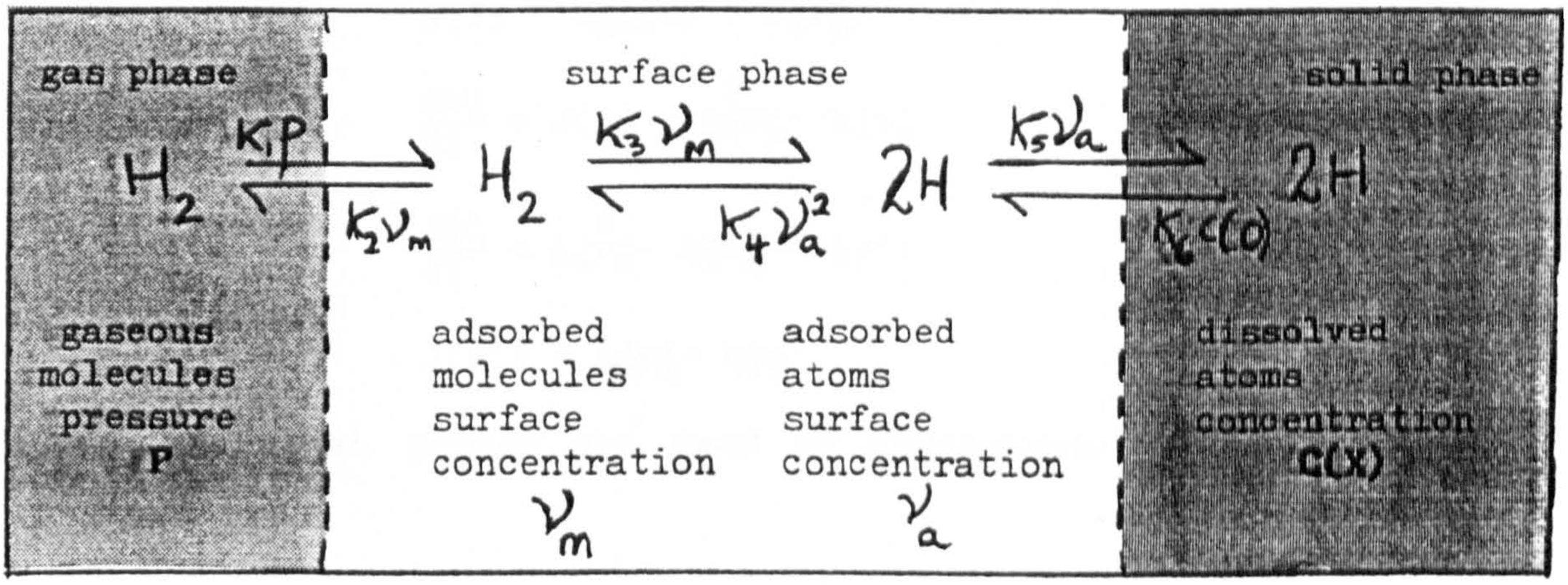

6.15 Schematic diagram of a three stage process involving a surface phase with six independent surface rate constants.

applies to the input surface; for the output surface, by analogy:

$$J(\ell) = k'_6 c(\ell) - k'_5 \nu'_a \qquad [6.48]$$

$$\frac{\partial \nu'_a}{\partial t} = J(\ell) - k'^2_4 \nu'_a + k'_3 \nu'_m \qquad [6.49]$$

$$\frac{\partial \nu'_m}{\partial t} = k'^2_4 \nu'_a - k'_3 \nu'_m - J(g') \qquad [6.50]$$

$$J(g') = k'_2 \nu'_m - k'_1 p' \qquad [6.51]$$

where, as usual, primes are used to distinguish exit surface rate constants.

It is apparent that the solution for this model would contain a large number of terms. Without evaluation, three limiting cases are listed here, which could enable this problem to be experimentally tackled. They are:

(1) Strongly bound molecules: the adsorbed molecules are supposed to lie in deep potential wells, requiring large activation energies either to evaporate, k_2, or dissociate, k_3; all other rate constants being fast relative to the diffusion process.

(2) Strongly bound surface atoms: atoms are considered to be strongly chemisorbed to the surface, so that the process of re-association, k_4, and solution in the bulk phase k_5, are necessarily much slower than any of the other reactions.

(3) Slow surface penetration: the transitions between the surface and solid phases, k_5 and k_6, are considered slow relative to the other

reactions.

There is effectively a fourth limiting case with k_1, k_1' as dominant parameters thus reverting to the two rate constant model described in 4.4. It must be re-emphasised, for stainless steel oxides, and current experimental phase space and signal to noise ratios, that evaluation of any of the extra parameters present in a more complicated surface model such as this one should not be expected. This is because of the excellence of fit of the data to the three parameters D, P_m and k_1, in the two rate constant model, noted earlier.

6.4 DISCUSSION OF THE FLUX AND THE POWER LAW INDEX

In this section other reported work will be discussed in relation to the flux and the permeation power law index. To do this a relationship between the permeation power law index n and the deviation from Richardson is derived in sub-section 6.4.1. This result is then used in 6.4.2. to assess reported deviations from the value of a half.

6.4.1 Flux reduction and the power law index

The steady state flow for a two-reaction rate surface model is given in [4.88] and is expressed in terms of j in [4.105]. Using [4.105] and defining the maximum possible flux as that corresponding to Richardson's permeation law, J_R, it follows that:

$$\frac{J_S}{J_R} = \frac{j^{½}}{\{1 + [2j(1+\mu)]^{½} + j\}^{½}} \qquad [6.52]$$

This can now be identified with n using [4.111]. This predicted variation of n with J_S/J_R was plotted for μ = -1,0,+1 in fig 6.10. This graph will now be used to estimate reduction of flux that corresponds to a particular power law index n. Notice from the graph that the effect is an important one. A 20% reduction in flux corresponds to n = 0.56.

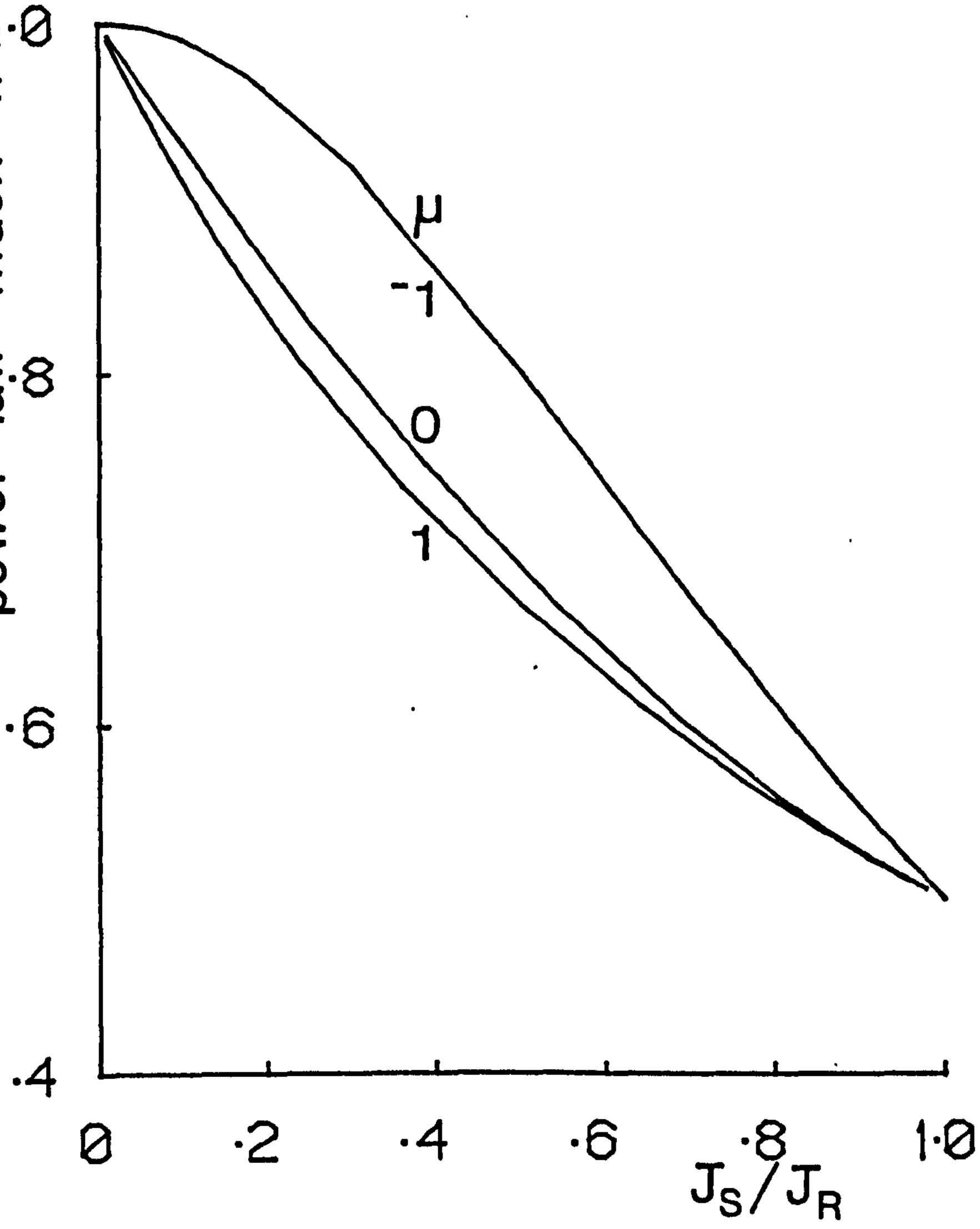

6.16 The variation of the permeation power law index with J_s/J_R, equation [6.52] for μ = 1,0 and -1.

6.4.2 Comparison of reported flux data.

To illustrate the use of these curves, available reported non-half order values of the permeation power law index for 304 stainless steel were compared with equation [6.52].

Matsuyama and Redman (26) measured a value for the permeation power law index, n, of 0.58. Comparing their permeation data with the present data, at 1000K, the calculated value should be ≈ 0.62. Repeating the process with Katsuka and Furukawa (9), a value of n of 0.67 is obtained in comparison with their measured 0.57.

It is not possible to justify a method of comparison on just two results but the good agreement with Matsuyama and Redman and to a lesser extent that with Katsuka and Furukawa, is encouraging and clearly suggests that their permeation data may be brought into line with the present work by making allowance for surface reactions of finite rate.

The way in which measurements of background pressure of the output chamber are introduced into calculations of the power law index, when using time lag experiments for diffusion coefficients, results in uncertainties in the power law index. This uncertainty is in a direction favourable to the above flux corrections and also illustates the importance of a pressure modulation technique, since it removes the millstone of background pressure from experimenters necks.

6.5 SUMMARY OF CHAPTER 6

All primary objectives of this work were met. The surface two reaction rate model developed in chapter 4, and the experimental rig described in chapter 3, provided internally and externally consistent data for the diffusion and permeation coefficients for 304 and 316 stainless steel. Also obtained were the two surface rate coefficients. These showed clear Arrhenius dependence and compared favourably with the limited data available.

From the k_1 coefficients a value for the permeability of the oxide, P_{mox}, describing molecular transport, on 304 and 316 stainless steel was obtained. As expected from surface inhibition of bulk material diffusion the value of P_{mox} for 304 was lower than that of 316.

Models incorporating internal trapping and the formation of a surface phase were considered as alternatives for the evaluation of data. That dealing with traps shows no interpretable effects within the range of the experiments. That using the more elaborate surface model was shown to be unnecessary for 304 and 316 stainless steels, at least to within the range and precision of the present work.

Permeation data drawn from other work was brought into line with this work by incorporating surface effects using an expression describing the flux dependence of the permeation power law index.

REFERENCES

(1) J.Volkl, G.Alefeld, *Hydrogen in Metals,* G.Alefeld, J.Volkl, eds., Springer Verlang,NY,1978,1,321

(2) K.Kiuchi, R.B.Mclellan, *Acta Metall,* 1983,31,961

(3) M.R.Louthan, J.A.Donovan,G.R.Caskey,*Nucl Tech,* 1975, 26,192

(4) H.G.Nelson, J.E.Stein, *N.A.S.A. Rep.*,TND-7265,1972

(5) N.R.Quick, H.H.Johnson, *Met trans,* 1979,10A,67

(6) W.J.Kass, W.J.Andrzejewski, *A.E.C.Rep.,* SC-DR/72/0136,1976

(7) J.R.Phillips, B.F.Dodge, *A.I.Chem.Eng.Jl.,* 1968.14,3

(8) H.K.Perkins, T.Noda, *J.Nucl. Mater.,* 1978,71,349

(9) H.Katsuta, K.Furukawa, *J.Nucl. Sci and Tech.,* 1981,18,143

(10) R.A.Outlaw, D.T.Peterson, *Metall. Trans. A,* 1983,14A,1869

(11) J.H.Austin, T.S.Elleman, *J. Nucl. Mater,* 1972,43,119

(12) T.Tanabe *et al, J. Nucl. Mater,* 1984,122,1568

(13) M.R.Louthan, R.Derrick, *Corrosion Sci,* 1975,15,565

(14) A.D. Le Claire, *Diffusion and defect data,* 1983,34

(15) L.G.Earwaker, D.K.Ross, J.P.G.Farr, *IEEE Trans on Nucl Sci,* 1981, NS-28,1848

(16) F.H.Heubaum, B.J.Berkowitz, *Scripta Metall,* !982,16,323

(17) M.R.Piggott, A.C.Siarsowski, *J.Iron and Steel. Inst.,* 1972,907

(18) A.J.Kummick,H.HJohnson, *Metall Trans.,* 1975,6A,1087

(19) W.A.Swansiger, R.Bastasz, *J. Nucl. Mater.,* 1979,85&86,335

(20) W.A.Swansiger *et al, J. Nucl. Mater.,* 1974,53,307

(21) A.D. Le Claire, *Diffusion and defect data,* 1983,33

(22) R.C.Axtmann *et al, Radiation effects for fusion reacors, Proc Intl. Conf - Gatlinburg, USA,* 1975,IV,361

(23) O.N.Salmon, D.Randall, *Knolls Atomic Power Lab Rep.*, KAPL - 984, 1954

(24) M.Braun *et al*, *J.Nucl Mater*, 1980,93&94,861

(25) O.Richardson, *Phil. Mag.*, 1904,7,266

(26) M.Matsuyama,J.D.Redman, *Metal TransA*, 1983,14A,498

(27) W.J.Kass, W.J.Andrzejewski, *A.E.C.Rep.*, SC-DR/72/0136,1976

(28) E.H.Van Deventer, V.A.Maroni, *Materials poster session*.1

(29) A.S.Zarchy,R.C.Axtman, *J.Nucl. Mater*, 1979,79,110

(30) R.A.Strehlow,H.C.Savage,*J.Nucl. Mater.*, 1974,53,323

(31) T.Tanabe *et al*, *Trans, J. Inst. Met.*, 1984,25,1

(32) J.S.Wang, *Proc. Cam. Phil. Soc*, 1936,32,657

(33) H.A.Daynes, *Proc. Roc. Soc.*, 1920,A97,286

(34) R.M.Barrer, *Phil. Mag.*, 1939,28,148

(35) Shah *et al*, *Metall. Trans. A*,1975,6A,373

(36) N.Boes, H.Zucher,*J. less-common Metals.*, 1976,49,223

(37) H.M.Morrison, D.A.Blackburn, K.M.Chui, *J.Nucl. Mater*, 1978,68&69,598

(38) W.M.Robertson, *Proc. 2nd Int.Conf, Enviromental degradation of Engineering Materials in Hydrogen,Blacksburg, Virginia*, eds. Louthan, McNeil, Sisson, 1981.

(39) Y.Hayashi, A.Tahara, *J.Japan Inst. Met.*, 1983,47,180

(40) D.L.Cummings, R.L.Reuben, D.A.Blackburn,*Metall trans.*, 1984,14A,639

(41) P.Kedzierzawski *et al*, *Bull Polonaise Sciences*, 1976,XXIV,595

(42) J.Volkl, G.Alefeld, *Diffusion in solids, Recent developments*,eds Nowick, Burton,Academic Press,NY,1975

(43) R.Sherman, H.K.Birhaum, *Metall Trans.A*, 1983,14A,203

(44) Dennis,Heppell, *Vacuum System Design.*

(45) J.Franks, *Vacuum,* 1974,10,487

(46) A.H.McIlraith, *J.Vac. Sci. Tech.*,1972,9,209

(47) H.S.Carslaw, J.C.Jaeger, *Heat Conduction in Solids, Clarendon Press*,1976.

(48) F.C.Thompkins, *Chemisorption of gases on metals,* Academic Press,1978,20

(49) E.H.Van Deventer, V.A.Maroni, *Trans Amer. Nucl. Soc.*,1978,28,199

(50) E.H.Van Deventer, V.A.Maroni, *J. Nucl. Mater.,* 1980,92,103

(51) Ali Khan *et al, J. Nucl. Mater.,* 1978,76&77,337

(52) D.Cummings, D.A.Blackburn, in press.